Mechanics of Micro- and Nano-Textured Systems: Nanofibers, Nanochannels, Nanoparticles and Slurries

BY

SUMAN SINHA RAY
BME, Jadavpur University, Kolkata, India, 2007.

THESIS

Submitted as a partial fulfillment of the requirements
for the degree of Doctor of Philosophy in Mechanical Engineering
in the Graduate College of the
University of Illinois at Chicago, 2011

Chicago, Illinois

Defense Committee:

Alexander L. Yarin, Chair
Constantine M. Megaridis
Farzad Mashayek
Kenneth Brezinsky
Alan W. Nicholls, Research Resources Center, UIC

This Thesis is dedicated to my mother (Manashi Sinha Ray) and my father (Sukumar Sinha Ray) without whose dreams and hard work I would not have reached the place, where I am currently standing.

ACKNOWLEDGEMENTS

I would like to acknowledge the individuals without whose inspirations and contributions I would have never accomplished this work and achieve my dream and goal. I would like to thank on my knees (an Indian way of saying is to offer my *PRANAM*) my parents, Smt. Manashi Sinha Ray (Ma- mother) and Sri Sukumar Sinha Ray (Baba- Father), who stood by my decision of pursuing higher education. In my childhood days I never liked to study and never thought that I will come that far. It was always my mother's dream, which wanted me to "make a mark of my own", which brought me here.

If parents' blessing is one of the pillars of the building, obviously the other pillar is those people, who have not only taught but also inspired me to think out of the box and introduced me into this beautiful world of science. I would like to thank and offer my humble 'pranam' to my advisor Dr. Alexander Yarin, who has always guided my work not only as an advisor but also as a guardian. His parental guidance has always shaped my thoughts and aspirations. I would like to thank Dr. Abhijit Chanda and Dr. Achintya Mukhopadhyay of Jadavpur University, who inspired me to take up higher education. I would also like to acknowledge my high school teacher Mr. Dulal Bhattacharya, whose blessings and hard work are some of the most important primary building blocks of my life.

I would like to thank Dr. Alan Nicholls and Dr. Ke-bin Low, who always answered all my questions regarding electron microscopy and helped me to understand it properly. I owe a lot to Mr. Eric Schmidt and Mr. David Mecha for their help and significant

contributions to make my experiments successful. I would also like to thank Dr. Manish K. Tiwari for his help like my elder brother. I am really thankful to God for having a friend as Zankar Vakil, who helped me to sail through the tough phase at the beginning at the start of my PhD work, when I went through a road accident. I would also like to thank Miss Yiyun Zhang for being the most helpful labmate and a good friend. I want to express my gratitude to my lab mates for shaping up and perfecting my idea of professionalism.

I would like to express my gratitude to all my thesis committee members (Dr. Alexander L. Yarin, Dr. Constantine M. Megaridis, Dr. Farzad Mashayek, Dr. Kenneth Brezinsky and Dr. Alan Nicholls) for their support and assistance, which helped me achieving my research goals.

TABLE OF CONTENTS

LIST OF TABLES

TABLES **PAGE**

LIST OF FIGURES

FIGURE **PAGE**

LIST OF FIGURES(CONTINUED)

FIGURE **PAGE**

LIST OF FIGURES(CONTINUED)

FIGURE **PAGE**

LIST OF FIGURES(CONTINUED)

FIGURE **PAGE**

LIST OF FIGURES(CONTINUED)

FIGURE **PAGE**

LIST OF FIGURES(CONTINUED)

FIGURE **PAGE**

LIST OF FIGURES(CONTINUED)

FIGURE **PAGE**

LIST OF FIGURES(CONTINUED)

FIGURE **PAGE**

LIST OF FIGURES(CONTINUED)

FIGURE **PAGE**

LIST OF FIGURES(CONTINUED)

FIGURE **PAGE**

SUMMARY

This work is devoted to the experimental and theoretical/numerical investigation of several important problems of mechanics of micro- and nano-textured systems, namely, it is related to nanofibers, nanochannels, nanoparticles and slurries.

Carbon nanochannels were fabricated by drop casting polymer solutions of Polyacrylonitrile (PAN) onto parallel arrays of electrospun Polycaprolactone (PCL) nanofibers followed by carbonization and removal of PCL nanofibers. The latter resulted in carbon nanochannels of 300-500 nm in diameter and length on the order of 1 cm. These nanochannels were used for for pressure-driven nanofluidics experiments. In these experiments it was found that it is possible to deliver more liquid through a nanochannel if it is partially filled with air than through the same nanochannel with the entire bore being filled with liquid. This paradoxical result was explained and attributed to a previously unknown phenomenon of a giant pseudo-slip. In the following part of the present work these nanochannels were also used to produce thermoresponsive PNIPAM hydrogel nanoparticles at a very high rate (10^7 nanoparticles/sec), with the sizes in the therapeutic range (~400 nm in diameter). These hydrogel nanoparticles represent themselves potential novel drug carriers, which can release drug on demand in response to thermal clues. In the thesis, that was demonstrated by loading these nanoparticles were loaded with low molecular weight fluorescent dyes and studying their release kinetics both experimentally and theoretically.

Another type of electrospun nanofiber with negative thermoresponsive effect developed by coworkers was studied by the present author using electron microscopy, which revealed the island-like nano-structures consisting of thermoresponsive hydrogel

(PNIPAM) embedded in the nanofibers. That was the origin of the negative thermoresponse of such nanofibers.

In the following part of the thesis, a realistic model of meltblowing, an important industrial process used for mass production of polymer microfibers and nonwovens was proposed. As a first step, the role of turbulent eddies has been elucidated both experimentally and theoretically by using blowing of a solid flexible threadline in a high-speed gas jet. Using this information, a linear stability theory of small perturbations on polymer viscoelastic jets and fully nonlinear theoretical/numerical model and description of the large amplitude bending perturbations of a single polymeric viscoelastic jet in meltblowing were developed. Both 2D and 3D cases of isothermal and non-isothermal meltblowing were investigated. That was generalized to simulate numerically multiple jets accounting for their deposition on a screen moving normally to the direction of blowing. The model allowed predictions of 3D configurations of bending polymeric jets in meltblowing, tapering profile, the velocity distribution, as well as the onset length of the strong bending instability (flapping), full configuration of jets undergoing nonlinear bending instability, fiber-size distributions and breakup of jets in flight. It also sheds light on fly formation, shot formation and pattern formation, and in general, rises our understanding of meltblowing from the previous purely empirical level to the framework of physical sciences, which allows further optimization ond development of novel approaches. One of such approached proposed and demonstrated in the present work is solution blowing of monolithic and core-shell nanofibers. In addition, this method allowed formation of monolithic and core-shell soy protein nanofibers.

At the following stage of the present work electrospun metal-plated polymer nanofibers were used for spray cooling. That led to dramatically high cooling rates of the order of 1 kW/cm^2 and eliminated the Leidenfrost effect at high substrate temperatures.

The intercalation of Phase Change Material (waxes) into carbon nanotubes was developed next. It was shown that using blends of different waxws and butter it is possible to widen the working temperature region of such PCMs.

In addition to the rheologically complex viscoelastic polymeric liquids used in the other parts of this work, the rheological behavior of gypsum slurries was studied using the elongational rheometer. It was demonstrated that the rheological behavior of such slurries is consistent with the power-law Ostwald-de Waele rheological constitutive equation.

1. INTRODUCTION

Nanotechnology is currently one of the most popular fields in science and engineering. The ability of nano-science of affecting our daily life and widening our horizons is enormous. According to different predictions, the US National Science Foundation (NSF) estimated a world market for nanotechnological products being of USD 1 trillion in 2015. Other forecast predicts USD 2.6 trillion in 2014 (Lux Research). Predictions vary according to the definition of nanotechnology and, as well as the experts' degree of optimism (http://www.nanowerk.com/news/newsid=1140.php).

The meaning of "nano" is 10^{-9} of the unit, which means that 1 nm=10^{-9} m. For comparison, a human hair (~100 μm in diameter) is 10^5 times bigger than 1 nm. However, the definition and domain of nanotechnology is not so well-defined and varies in different sources. According to a generally accepted view, notion nanotechnology is defined as a part of science which deals with objects of the order of 100 nm as a minimum in one direction.

The history of nanotechnology is almost 4000 years old. The alloying of different metals to make stronger weapons, which dates back to the Metal Age, can be considered as one of the first steps towards nanotechnology. Also, vulcanization of rubber, strain hardening of metals, etc. represent themselves the additional steps which followed. During the early 1900s the famous Austrian chemist Richard Adolf Zsigmondy came up with the methods of making gold sol of 10 nm in diameter. In 1926 Irving Langmuir and Katherine Blodgett introduced the famous Langmuir-Blodgett trough, where they found that when a solid surface is inserted into an aqueous solution containing monolayers of organics, a monolayer will be deposited homogeneously over the surface. For this work

in 1932 Langmuir was awarded the Nobel Prize in Chemistry. However, all these efforts and achievements were not termed nanotechnology per se, although they were of significant contributions to the field.

In his famous talk on December 29, 1959 titled “There’s Plenty of Room at the Bottom”, Richard Feynman envisioned the idea of modern nanotechnology. However, even after two decades after his seminal talk there were only a few works which were invigorated with the idea. Only in 1981, when scanning tunneling microscope was invented by Gerd Binnig and Heinrich Rohrer at IBM Zurich Research Laboratory, for which they were awarded Nobel Prize in Physics in 1986, first practical developments followed. The additional important building blocks emerged with the discovery of fullerene by Harry Kroto, Richard Smalley, and Robert Curl in 1985 and carbon nanotubes by Ijima in 1991.

An exponential growth in the number of publications and patents in the field of nanotechnology followed. According to Thomson Reuters from 2002-2010 there has been a total of 54,312 publications with the percentage steadily increasing from 3.44% of the total publications in 2002 to 14.99% of the total publications in 2010.

In spite of such a tremendous increase in the scientific efforts, Feynman’s vision is far from being realized for various reasons. Some of the reasons are as follows. (a) The existing methods are very expensive and involve rather cumbersome steps, which precludes their scale-up and wide-spread usage. (b) The lack of detailed understanding of some basic principles in certain areas of technology.

In this thesis several methods for producing nanostructures are proposed (Chapters 4 to 6 and 10 to 13). These nanostructures were used for making stimuli

responsive systems, which can be used in different applications, namely biomedical, structural, etc. (Chapter 5 and 6). These nanostructures also resulted in special nano-textured surfaces used to intensify spray cooling (Chapter 12) and carbon nanotubes of macroscopic length for nanofluidic application. They were also implemented as novel electrode materials for the alternative energy approaches (microbial fuel cells, Chapter 10), for making soy protein-based nanofiber nonwoven (Chapter 11), and smart tunable phase change materials (Chapter 13). In addition to the extensive experimental efforts, special attention was devoted to developing thorough theoretical understanding of nano-scale stimuli responsive systems (Chapter 5), meltblowing of nanofibers (Chapter 7 to 9) and spray cooling using metalized nanofibers (Chapter 12). Rheological studies of the gypsum slurries comprised of microscopic stucco particles were also conducted (Chapter 14) to elucidate and characterize the dynamics of their flows. The author expects that this thesis will be able to provide its unique contribution to nanotechnology and widening its applications.

2. BACKGROUND AND LITERATURE REVIEW

2.1 Micro and Nanofluidics

Micro- and nanofluidics hold great promise in the fields of medicine, chemistry, drug delivery, DNA segregation, DNA stretching, capillary electrophoresis and electrokinetic microchannel batteries (Dersch et al., 2005; Kohli et al., 2004; Ewing et al., 1989; Guo et al., 2004). Microfluidic devices can be based on either flow-generation mechanisms or diffusion. In addition, researchers were also interested in studying different cell migration mechanisms. In particular, receptors on the plasma membrane in cells can activate signal transduction pathways that change the mechanical behavior of cells by reorganizing motion-related organelles, while cancer cells can change their migration mechanism widely based on different stimuli. Therefore, to develop novel therapeutic approaches to immobilize cancer cells via inhibition of the related signal transduction pathways, a better understanding of cell migration mechanisms is required (Huang et al., 2011). One such approach is illustrated in Fig. 2.1.

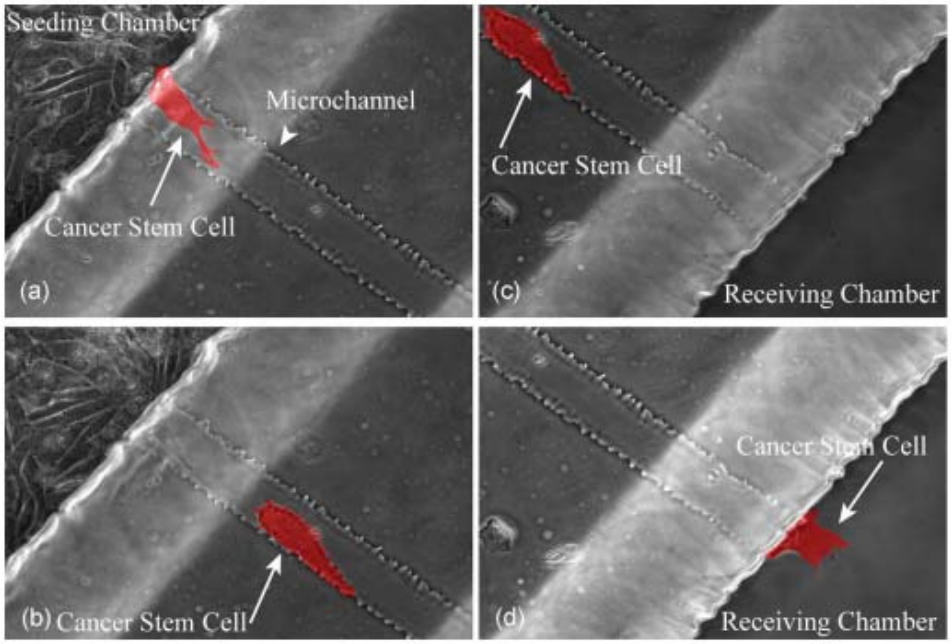

Fig. 2.1 Brain Tumor Stem Cell (BTSC) migration through a microfluidic device. Real time microscopy demonstrating a BTSC (highlighted in red) migrating from seeding chamber to the receiving chamber through a bridging microchannel. (Huang et al., 2011).

There are three different methods used to produce nanotubes, which employ: (i) self-assembly (Fig 2.2a), (ii) templates (Fig 2.2b) and (iii) co-electrospinning (Fig 2.2c) (Whitesides et al., 2002; Ijima 1991; Chen et al, 2009; Bazilevsky et al., 2007b; Zussman et al., 2006). Self-assembly results in crystalline close-ended, single- or multi-wall carbon nanotubes with cross-sectional diameters in the range of 1-100 nm not longer than several microns. Template-based methods use as templates either porous alumina where carbon deposition on the pore walls is achieved using chemical vapor deposition (CVD), or electrospun nanofibers. In the latter case, CVD, electroplating or atomic layer deposition (ALD) lead to core-shell fibers, and the core is eliminated during post-processing using chemical or thermal means. Co-electrospinning yields a one-step way of creating core-

shell fibers, which are made hollow during post-processing using chemical or thermal means. Carbon nanotubes made via CVD deposition inside pores have cross-sectional diameters of the order of 50-300 nm and are several microns long. As possible candidates for nanofluidics applications, close-ended nanotubes are inappropriate, while short micron-long nanotubes produced via CVD make it extremely difficult to incorporate them in nanofluidic devices. Hollow carbon nanotubes fabricated via electrospinning or co-electrospinning can be macroscopically long (of the order of 1 cm) and could have diameters in the range from 100 nm to several microns. However, so far only such carbon tubes with diameters of the order of 1 μm were employed in fluidic devices (Bazilevsky et al., 2008a). Using those carbon tubes it was also shown that for delivery of homogeneous solutions through the carbon tubes the delivery soon changes from fast convection dominated flow to slow jammed diffusion dominated flow (Srikar et al., 2009b).

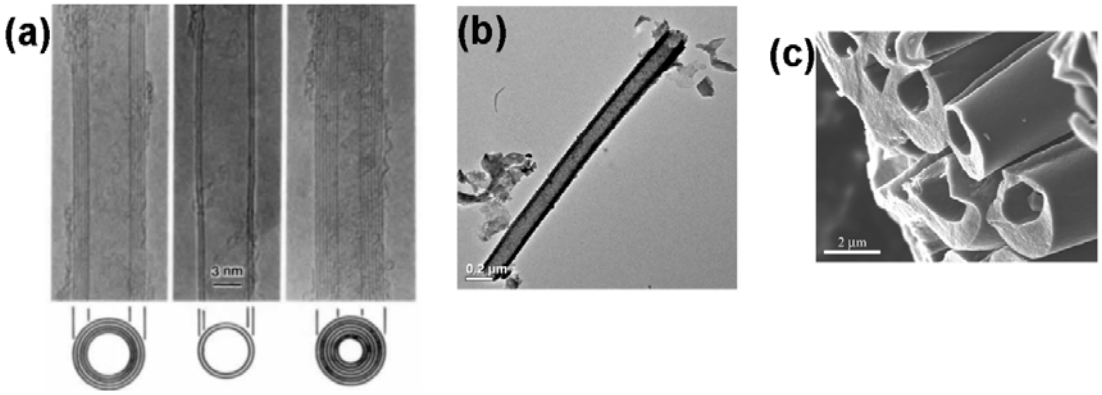

Fig. 2.2 (a) TEM images of carbon nanotubes obtained from self-organization (Ijima 1991), (b) TEM images of an isolated $BaTiO_3$ nanotube obtained using AAO membrane as template, (c) aligned array of carbonized hollow nanofibers obtained from core-shell fiber of PMMA/PAN (Zussman et al., 2006).

2.2 Stimuli Responsive Polymer System

External stimuli dependent, namely temperature, pH, magnetic, solvents/irons, mechanicaland electric field, reversible volume phase transition (VPT) - swelling/shrinkage- in aqueous surroundings characteristic of certain polymers are considered as promising features for such applications as drug delivery, materials with controlled wettability and micro- and nanofluidics (Hoffman et al., 1987; Duracher et al., 2000; Kondo et al., 1994). These materials might be used to eliminate many undesirable characteristics of traditional drug carriers and introduce new, beneficial traits, e.g capability of pulsatile, site-specific and/or externally triggered release. In the class of materials responsive to the external stimuli, stimuli-responsive hydrogels have attracted the most attention due to their versatilely adjustable properties. Hydrogels are polymer networks which can take up water causing them to swell dramatically. They can also expel water when shrinking. If hydrogel swelling/shrinkage in water can also be controlled by an external stimulus, such as temperature or pH, the term smart hydrogel is adopted. For example, poly(N-isopropyl acrylamide) (PNIPAM) shrinks above its lower critical solution temperature (LCST) at 32.8 °C. The shrinkage occurs owing to the release of the water entrapped in the polymer coils due to the increased attractive segmental interactions between the hydrophobic isopropyl groups of the PNIPAM chain. This unique capability of hydrogels are utilized to the fullest extent by various workers with different hydrogels to come up with an array of wide variety of stimuli responsive polymer network to achieve different objective. To enhance the treatment of Diabetes Mellitus membranes consisting of hydrogels to make a biosensor that can release insulin with proper control (Brahim et al., 2002). In this work the researchers fabricated the

membrane of the biosensor by combining cross-linked poly(2- hydroxyethyl methacrylate) with polypyrrole (PPy) (Fig 2.3a) . Then to control the release of insulin the device employed cross-linked poly(2-hydroxyethyl methacrylate-co-dimethylaminoethyl methacrylate) (p(HEMA –co- DMA)) (Fig 2.3b). Some workers have fabricated smart hydrogel, random copolymers composed of poly(acrylic acid) and poly(vinyl sulfonic acid) (Kim et al., 2004), which can be stimulated externally with pH, temperature and electric field (Fig 2.4). However, this shows there ample possibility of development of nanoparticles and nanofibers using these smart hydrogels using their smart behaviour.

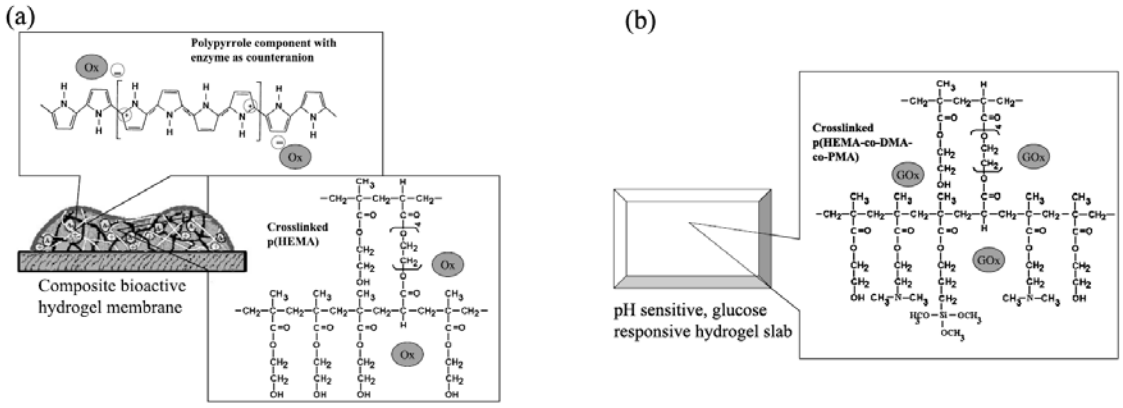

Fig. 2.3 Schematic representation of the three components of the novel hydrogel composite matrix-the cross-linked hydrophilic hydrogel, the positively charged electroactive PPy component and the negatively charged (net) oxidase enzyme. (b) Partial structure of the hydrogel network used for the fabrication of engineered devices for the controlled release of insulin. (Brahim et al., 2002).

.

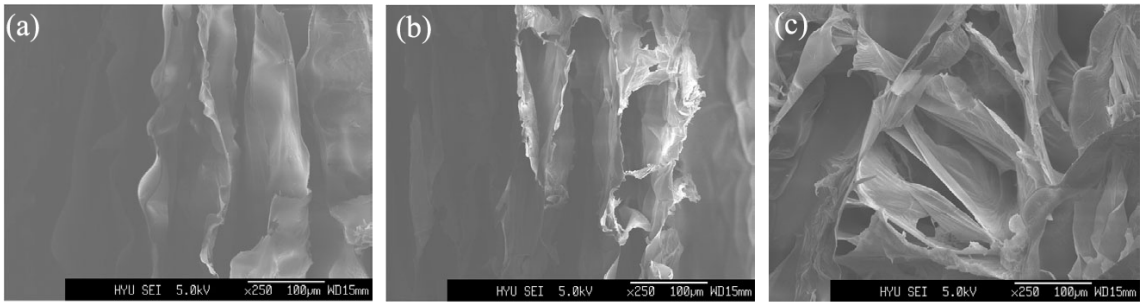

Fig. 2.4 Series of cross-sectional SEM micrographs of the freeze-dried hydrogels with different ratio of Polyacrylic Acid (PAAc) and Poly(Vinyl Sulfonic Acid) (PVSA) , with PAAc:PVSA being (a) 3:1, (b) 5:1, (c) 11:1. (Kim et al., 2004).

Nanoemulsions and nanoparticles attracted significant attention in relation to self-healing materials and controlled drug and gene delivery (Tong et al., 2007; Ferrari 2005; Heath et al., 2005; Alexis et al., 2008; Blaiszik et al., 2008; Solans et al., 2005; El-Aasser et al., 1997; Antonietti et al., 2002; Asua 2002; Gutiérrez et al., 2008). Formation of oil-in-water nanoemulsions can be achieved using: (i) PIT (Phase Inversion Temperature) (Kunieda et al., 1981, 1996; Izquierdo et al., 2002, 2004, 2005), (ii) microfluidics and sonication (Jafari et al., 2006), and (iii) centrifugation (Graves et al., 2005). Except PIT, the other methods rely on a high energy input and high shear rates in stirring. Polymer nanoparticles can also be produced using nanoemulsions as nanoreactors (Antonietti et al., 2002; Asua 2002; Gutiérrez et al., 2008; Kim et al., 2007) . In oral drug delivery, sub-micron diameter polymer spheres (nanoparticles) offer significant advantages over conventional microsphere formulations (Mathiowitz et al., 1997), with nanoparticles in the 200-1000 nm dia. range having the greatest potential therapeutic benefit (Laulicht et al., 2008). Despite the critical need for nanoparticles in this size range, methods for encasing sensitive therapeutics (proteins, biologics, etc.) within biocompatible polymer

nanoparticles, especially at room temperature and pressure and at relatively low shear stresses, are currently lacking both in the literature and in commercial practice.

Electrospinning is a unique straightforward process to produce polymer nanofibers of the order of several hundreds of nanometers in diameter (Reneker et al., 2007, 2008). Among many possible applications of electrospun nanofibers that are being investigated is their use as drug delivery systems. A possible advantage of nanofibers as drug carriers is that the smaller the dimensions of the drug carrier, the better the drug can be absorbed by the human body. Also, nanofiber mats containing, for example, camptothecin (an anticancer drug) are very flexible and could be set into spaces near a brain tumor without damaging the surrounding healthy tissue. Recent work by (Srikar et al., 2008) fully described desorption limited release mechanism from electrospun nanofiber mat in full detail both theoretically and experimentally. Modifying the release rate from PNIPAM-containing nanofibers on demand is not only a goal but also a tool to probe the intrinsic physical mechanisms of the process. In particular, the theoretical model described by (Yarin 2008) assumed that PNIPAM is distributed as nanogel islands in a polymer matrix. At T>LCST, these nanogel islands shrink and stretch the surrounding polymer matrix, which creates new nanopores/nanocracks in it. As a result, drug release rate increases, even though PNIPAM shrinks.

2.3 Meltblowing

Meltblowing is one of the most popular methods of manufacturing polymer microfibers in the diameter range of 1 to 20 μm from a variety of polymers. In this

process polymer melt is extruded through a row of fine capillaries and exposed to high velocity gas flow field, which stretches the polymer jets and forms polymer laydowns. The schematic of the process is shown in Fig. 2.5.

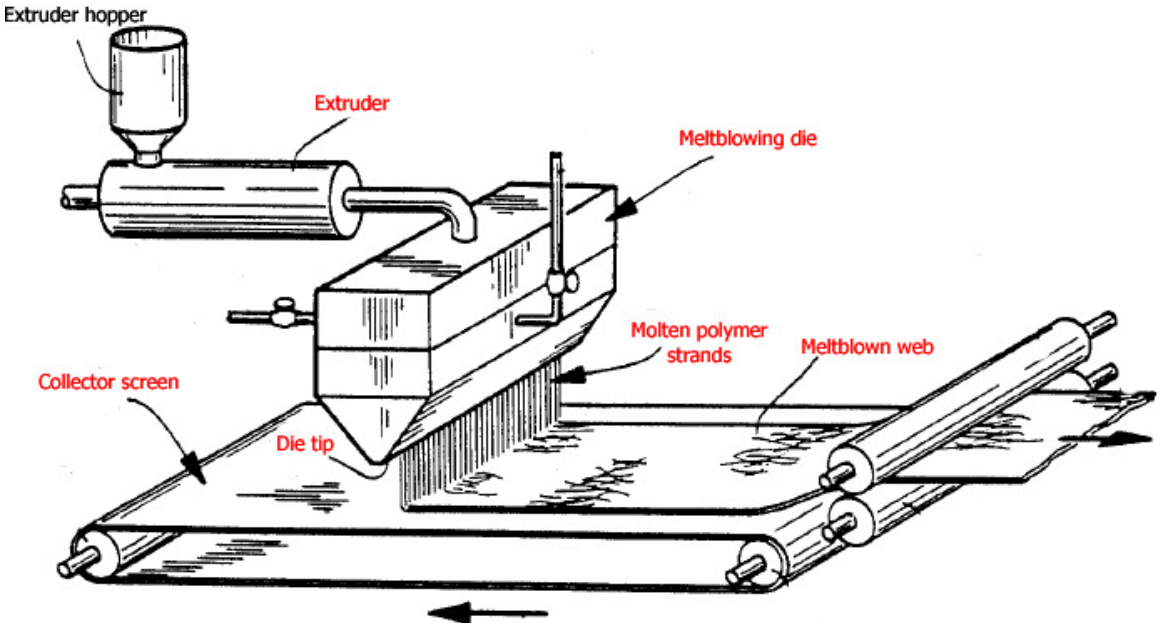

Fig 2.5 Schematic of the meltblowing process (Begenir 2008).

Historically the work on meltblowing dates back to the work of V.A. Wente (Wente 1956), who developed the method of producing micron-sized fibers for capturing radioactive airborne particles, while working at Naval Research Laboratories. In 1960s the work was appreciated by Exxon Corporation and was soon put into practice. After that over the last two decades several companies have started working on manufacturing meltblowing dies, like Hollingsworth and Vose, Kimberly-Clark, 3M, Fleetguard Filter, PGI Nonwovens, BBA Nonwovens, etc. However, the most important developments are mostly done by Exxon Corporation. The value of the current nonwoven industry is estimated to be of the order of billions of dollars. This unique and apparently

straightforward, but intrinsically complex process, is still poorly understood scientifically, stays practically empirical, which hinders further development and innovations. For example, the complex interplay of turbulent flow field with rheological properties of polymer melts and polymer jet dynamics has not been understood, even though that is the key element of meltblowing.

A brief survey of the recent works devoted to meltblowing reveals the following. Several important experimental works (Breese et al., 2003; Pinchuk et al., 2002). and references therein demonstrate that polymer jet configurations in meltblowing are extremely transient and non-straight at already several centimeters from the hole exits in die nosepiece, the jet-jet interactions are significant and merging of neighboring jets is quite possible. Thermal regimes and polymer rheology have a strong effect. Also, turbulence of the surrounding gas flow can have a very significant effect on the final characteristics of the meltblown nonwovens. However, it is improbable that polymer jet characteristics in meltblowing are determined by turbulent eddies alone. Indeed, the results of the experiments (Breese et al., 2003) show that the initial sections of the jets in meltblowing (of the order of 4 cm) are straight, even though the turbulent pulsations are the strongest in the surrounding high-speed gas flow. The jet bending pattern is thus inconsistent with the one driven solely by turbulent eddies. Therefore, rheological behavior of polymeric liquid is expected to have a significant effect on jet dynamics. Also, the interaction with the surrounding gas flow cannot be reduced to only the effect of turbulent eddies, and the interaction with the mean flow can be very significant. In addition, a realistic description of the dynamics of bending perturbations should account

for the interplay of the above-mentioned factors, which determine the pattern of bending perturbation propagation over polymer jets.

The theoretical works on meltblowing initially concentrated on the simplest model of a single straight jet (Uyttendaele et al., 1990). However, later on, the first steps were done in the direction of the quasi-one-dimensional equations of polymer non-straight jets moving in gas (Marla et al., 2003; 2004) even though these works were seemingly unrelated to any preceding works on such jets discussed below, and did not result in a comparable model. Some preliminary steps were taken to mimic turbulence (Chhabra et al., 2004). In a series of publications (Marheineke et al., 2006, 2007; Gotz et al., 2007; Bonilla et al., 2007)the idea that stretching and bending of liquid jets in meltblowing is due exclusively to the turbulent pulsation field in the surrounding gas, which is responsible for the fluctuating gas drag force acting on the jet, was developed in full detail. Nevertheless, the predicted jet configurations can hardly be considered in agreement with the experimental observations. Neither the realistic (viscoelastic) rheological behavior of polymeric liquids was accounted for in the meltblowing context.

The above-mentioned works dealt with meltblowing. Blowing of polymer solutions is also possible and was recently studied in the experiments in (Medeiros et al., 2009).

Flapping flags and ropes in gas or water flows attracted some interest in fluid mechanics as an example of flow-induced vibrations of deterministic (non-turbulent) character (Paidoussis 1966; Triantafyllou 1992; Shelley et al., 2005; Farnell et al., 2004; Argentina et al., 2005; Williamson et al., 2004; Connell et al., 2007). These works targeted a detailed deterministic description of flows about flapping ropes and flags, even including lateral forces resulting from shedding the von Karman vortex street in one case.

In the other cases, the von Karman street-related forces were neglected as insignificant for the overall dynamics. All these works also accounted for bending stiffness of flexible flags and ropes, even though in most cases it was relatively small in reality. This approach resulted in the fourth order PDE governing flag or rope dynamics, which does not allow an easy insight in the physical reasons of flapping, even though the obstruction comes from the higher order term which is negligible in many cases.

It was mostly overlooked that meltblowing is kindred to propagation of high speed liquid jets in gas environment and the latter process has been understood in full detail in the 1980th. The works on high speed jets propagating in gas environment represent a good guidance for the study of meltblowing. Friction and heat transfer coefficients for straight cylindrical bodies (threadlines) moving in gas were measured experimentally and calculated theoretically in the framework of the boundary layer theory in numerous papers and monographs (Ziabicki 1976; Ziabicki et al., 1985; Yarin 1993), which contain many empirical correlations and/or theoretical formulae for the corresponding friction coefficient and Nusselt number. They were successfully applied to calculate the drag force and heat flux on straight liquid jets moving in gas in the melt, dry or wet spinning processes. These correlations can be equally used locally in studies of meltblowing when the velocity determining drag and heat transfer should be understood as a relative velocity between rapidly moving gas and slower polymeric jet.

It is emphasized that the dynamics of liquid jets rapidly moving in gas is much richer than just propagation and thinning of straight jets characteristic of melt spinning, and so should be the dynamics of meltblowing. Indeed, the theoretical study of high speed liquid jets moving in gas began with the seminal works of Weber and Debye and

Daen (Weber 1931; Debye et al., 1959). In this case a rather complicated, three-dimensional problem on dynamic interaction of liquid jet and gas stream arises, where coupled evolution of the jet shape (which can become non-straight) should also be determined. In Ref. (Debye et al., 1959) in the framework of the linear stability theory it was shown that inviscid liquid jets of circular cross-section are prone to planar bending if the jet velocity is sufficiently high. Such bending instability leads to an exponential growth of small bending perturbations. The instability is determined by a peculiar gas pressure distribution over the jet surface: gas pressure on the convex parts of the jet is lower than on the concave ones, which results in a distributed lateral lift force promoting further bending. The resulting distributed lift force is related rather to the potential (or mean) flow aerodynamics than to turbulent eddies and was not accounted for in [7-10] and several works on flag or rope flapping. The linear theory of Debye and Daen (Debye et al., 1959) did not account for viscosity or viscoelasticity of liquid in the jet, possible large amplitudes of bending perturbations and their three-dimensional (as in the experiments) rather than planar shape. It is practically impossible to address any of these factors in the framework of the Navier-Stokes equations or the corresponding 3D equations for the rheologically complex liquids due to a huge geometric complexity of the problem and complicating physical factors. That was the reason for the development of the general quasi-one-dimensional equations of liquid jets moving in gas in (Yarin 1993; Entov et al., 1984). These equations were successfully used to describe the bending instability threshold and the whole nonlinear bending process of such jets including incorporation of the rheological effects and, in particular, viscoelasticity characteristic of

polymer solutions and melts. In the present work this approach is applied to description of melt and solution blowing and prediction of the characteristics of this process.

An additional process which is formally kindred to meltblowing is electrospinning of polymer nanofibers, where jet bending results from the electric Coulombic repulsion force (Reneker et al., 2000, 2007; Yarin et al., 2001). The latter is proportional to the local curvature of the jet axis, which is similar to the distributed aerodynamic lift force (Yarin 1993; Entov et al., 1984).

2.4 Solution Blowing: A unique method of making nanofibers

Nanofibers hold a great potential for their high surface area to volume ratio. Among different nanofibers, polymer nanofibers are the most popular because of the ease of producing long nanofibers with or without different functionalities. Different precursors can be incorporated into polymer nanofibers, whose post-treatment can result in various nanostructures relatively easily (Sigmund et al., 2006; Dersch et al., 2005). This versatility highlights different methods for making polymer nanofiber- meltblowing (Shaumbugh 1988), electrospinning (Reneker et al., 2000, 2007; Yarin et al., 2001), force spinning (Sarkar et al., 2010) and solution blowing (Medeiros et al., 2009; Sinha-Ray et al., 2010b).

In meltblowing polymer melt is stretched by surrounding turbulent non-isothermal air flow field as explained in section 2.3. Although recent developments in meltblowing technologies can produce polymer nanofiber, they are accompanied by various problems. For example, (a) precise machining to make ultrafine die holes increases the cost of manufacturing to a great extent, (b) requires very high pressure to

operate, (c) ultra-fine capillary increases propensity to the intermittent clogging and problems in de-fouling. Also, (d) the high-temperature range of operation does not allow an addition of various functional materials. All these factors require better understanding of the physical foundations of the process. Electrospinning is one of the most popular methods to make nanofibers for its ease and controllability on lab scale. In electrospinning polymer solution is supplied into an electric field, which stretches, bends, flaps the polymer jet resulting in polymer nanofiber. However, on the industrial scale this method is still limited to a great extent for the following reasons. Firstly, the process is dependent on solution charge. Those solutions which can hardly be characterized as leaky dielectrics, cannot be electrospun. This also limits the incorporation of functional materials. Secondly, electrospinning has a relatively low throughput. Also, the use of high electric field (~1 kV/cm) also limits electrospinning on the industrial scale. Lastly, the presence of the electric field can limit loading of biologically-active materials in nanofibers.

In forcespinning polymer solution or melt is issued through a spinneret disk, which is rotated at an angular speed of about ~20000 rpm. This method does not use electric field and can give a very high throughput but implementing this technology in nonwoven industry is hindered by difficulty in collecting a useful laydown.

In solution blowing, polymer solution is subjected to a turbulent flow field of air (at room temperature), that results in the jet stretching and bending. As a result of an enormous elongation, after solvent evaporates, polymer nanofiber mat are collected at a very high throughput. The process does not involve the electric charge and field, which

facilitates a whole range of additives to achieve a plethora of functionalities. Also, solution blowing proceeds at room temperature air in distinction from meltblowing.

2.5 Spray Cooling

Modern electronics has the capability of achieving various goals. However, the increase of the operation speed is associated with miniaturization. According to Moore's Law, doubling up of transistors on a chip is expected almost twice every year. This poses a severe problem of heat dissipation, which limits chip capabilities. Zhirnov et al., (2003) stated that "even if entirely different electron transport models are invented for digital logic, their scaling for density and performance may not go much beyond the ultimate limits obtainable with CMOS technology, due primarily to limits on heat removal capacity". Due to the unavoidable high heat fluxes, cooling by liquid becomes unavoidable. Among various types of liquid cooling, spray cooling is one of the most efficient methods (Kim 2007).

In spray cooling liquid is forced through small orifices, breaks into smaller droplets, which then impact heated surface (Fig. 2.6). After the impact, droplets spread over the surface. Individual droplets evaporate, whereas excessive droplets form liquid film, which involves pool boiling. Heat transfer from high-heat-flux surfaces is severely limited by the Leidenfrost effect, which results in liquid levitation over the surface, with a severe reduction in heat removal. Taylor (1950) used a first order perturbation analysis to find the critical wavelength that is supposed to grow and disrupt a horizontal smooth surface. Based on that, different authors proposed various models to find the minimum

temperature for pool boiling (Berenson 1961; Yao et al., 1978; Bernardin et al.,1999).

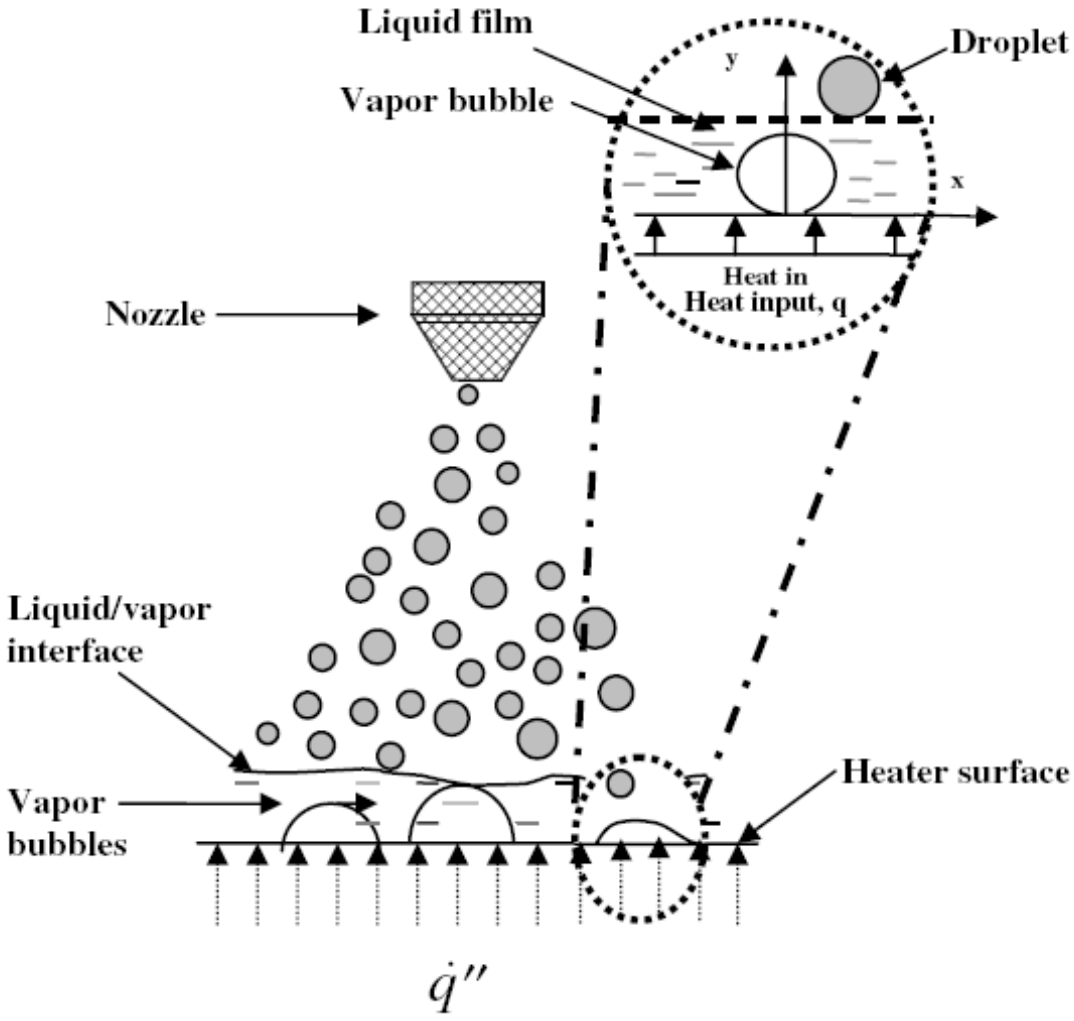

Fig. 2.6 Schematic of spray cooling process. (Silk et al., 2008).

In spray cooling there is a significant number of parameters, which critically influence the heat transfer rate. Namely, the angle of impact, droplet diameter, sprayer type, surface finish of the target plate, surface roughness of the target plate, type of

coolants, pattern of sprayer, nozzle spacing, etc. (Silk et al., 2004, 2006, 2008; Mudawar et al., 1996). In addition to the advantages of spray cooling, its disadvantages include need for pumps, filters, and the need to transport the excess liquid and vapor to a condenser.

2.6 Phase Change Materials

The energy problems became more aggravated over the last three decades. There has been a growing concern on how to save the excess energy and/or use natural energy sources, e.g. solar energy, which otherwise would have been wasted. Phase change materials (PCMs) seem to be a possible approach to the latter problem. In PCMs, a material undergoes phase change and stores a certain amount of energy owing to its high heat capacity. After that, when needed, PCM can release that energy. This unique capability was first explored by Telkes and Raymond in the 1940s (Telkes et al., 1949). However, until the 1970s and 1980s there were only a few following works. The most significant modern usages of PCMs are associated with storing solar energy for drying agricultural produce (Bal et al., 2011; Mahapatra et al., 1990; Ekechukwu et al., 1999; Zhiqiang et al., 2005), dwelling construction (Schossig et al., 2005; Kuznik et al., 2011) and cooling power electronic devices (Sabbah et al., 2009).

For dwelling construction several different PCMs were explored. An ideal PCM should satisfy the following criteria (Abhat et al., 1983): (a) to possess a melting point in the desired operating temperature range (temperature range of application) and (b) to possess high latent heat of fusion per unit mass, so that a small amount of material stores a given amount of energy. Also, it should possess (c) a high specific heat to provide

additional significant sensible heat storage effects, (d) a high thermal conductivity, so that the temperature gradients for charging and discharging the storage material are small and the response time is short. In addition, it should have (e) small volume changes during phase transition, so that a simple container and heat exchanger geometry can be used, (f) exhibit small or no subcooling during freezing, and (g) possess chemical stability, no chemical decomposition and corrosion resistance to construction materials. Due to some additional restrictions, it should (h) contain non-poisonous, non-flammable and non-explosive elements/compounds, and (i) be available in large quantities at low cost. To achieve these goals, different research groups used different PCMs: ice slurry in chilled water (Inaba 2000), solid hexadecane (Choi et al., 1995), n-eicosane (Goel et al., 1993), paraffin wax (Schossig et al., 2005; Kuznik et al., 2011, Wu et al., 2010; Akgun et al., 2008) and Capric–myristic acid/vermiculite composite (Karaipekli et al., 2009).

2.7 Rheological Characterization of Gypsum Slurries

Gypsum is one of the most used materials in construction engineering. Gypsum is a naturally occurring mineral, which is also referred to as calcium sulfate dihydrate. The sources of gypsum are (a) natural and (b) synthetic. Synthetic gypsum is recovered via flue gas desulfurization at some coal-fired electric power plants. It can be used interchangeably with natural gypsum in some applications. Gypsum in the form of stucco, when mixed with water at sufficient concentrations, constitutes concentrated slurries. Such slurries represent themselves a key element of gypsum processing in industry to wet-form gypsum products, e. g. wallboards. In addition, gypsum slurries

solidify due to rapid hydration of gypsum and evaporation of water. Rheology of gypsum slurries is an uncharted area and is tremendously important for gypsum processing.

Generally speaking, gypsum slurries belong to a wide class which can be loosely termed as muddy materials, materials with a complex internal structure, or construction materials. Complicated rheological behavior of such materials is currently in focus (Barnes 2007; Tiwari et al. 2009, Chalencon et al. 2010; Ferraris 1999; Banfill 2003; Shenoy et al. 2005; Egres et al. 2005, 2006; Alexandrou et al. 2010).

The term stucco used below is understood as a shorter term applied to this form of gypsum, namely, $CaSO_4 \cdot (1/2)H_2O$. Rehydration of stucco in water proceeds according to the following reaction (Kuntze 2009).

$$CaSO_4 \cdot (1/2)H_2O + H_2O \rightarrow CaSO_4 \cdot 2H_2O + Q \qquad (2.1)$$

in which β-hemihydrate transforms into dehydrate [$CaSO_4 \cdot 2H_2O$] by binding more water, whereas its molecular weight increases from 145.15 Da to 172.17 Da. The reaction is exothermic with the heat release Q=111.9-173.3 J/g. The transformation (Kuntze 2009) is not only chemical but also structural. In particular, mixing of stucco with water for 60 s can result in complete disintegration of stucco particles, which is accompanied by reduction of the median particle size from 24 to 1.4 μm (Kuntze 2009). Moreover, the transformation (1) is accompanied by three-stage solidification process: (1) a true crystalline in growth where ions are shared within the particles; (ii) a gel-like network formation with crystalline outgrowth through water-filled spaces between the particles, and (iii) hydrogen bonding of touching crystals.

Rheology of stucco slurries can be treated as time-independent for sufficiently short time intervals (of the order of minutes from the moment of preparation). Longer

than that, the effect of the reaction (1) and the accompanying solidification should be already felt. This short time of reaction is on one hand very beneficial for the wallboard industry as it reduces processing time and high heat resulting from exothermic reaction gets rid of excess water to some extent but on the other hand the short time of reaction makes it extremely challenging and difficult to study its rheological properties leading to the optimization of the process.

3. RESEARCH DESIGN AND OBJECTIVE

Nano-textured systems, namely nanofibers, nanochannels, nanoparticles and nanotubes find various applications in different fields, such as biomedical engineering, electronics, alternative energy sources, structural engineering, spray cooling, etc. it is quite imperative and instructive to study their properties and modus operandi in the framework of the mechanics of these systems. The objective of the present work is divided into the following categories. (a) Preparation of macroscopically long carbon nanochannels and nanofluidics based on them. (b) Generation of thermo-responsive polymer nanoparticles and theoretical and experimental studies on release kinetics of dye (model drug) from them. (c) Experimental study of polymer nanofiber scaffolds with negative thermo-sensitivity (d) Theoretical study of meltblowing. (e) Production of turbostatic carbon naotubes, carbon nanofiber and soy protein-based nanofiber mats using novel method of solution blowing. (f) Experimental and theoretical study of spray cooling using nano-textured surfaces-electroplated metal nanofiber mats. (g) Production of smart, tunable phase change material. (h) Rheological characterization of gypsum slurries.

3.1 Macroscopically Long Carbon Nanochannels

There have been significant efforts in producing nanotubes and/or nanochannels. However, their usage in nanofluidic devices is significantly hindered because of the following reasons: (a) high cost of manufacturing leaves a very little room for error; (b) most of the processes produce closed ended nanotubes; (c) the small sizes (lengths of ~1-

10 μm) precludes manual handling, and (d) most of the methods require significant prior expertise in manufacturing.

In this work a novel solution for production of macroscopically long carbon nanochannel is provided using electrospun nanofiber as template. Parallel array of electrospun nanofibers were collected on aluminum holders with a rectangular whole at the middle. Then solution of Poly-acrylonitrile (PAN) is drop cast on them. They were dried, cut into rectangular pieces followed carbonization, which destroyed the polymer nanofiber core and left behind carbon strips with series of nanochannels (length ~1 cm). These nanochannels were installed in homemade microfluidic device and their release kinetics was studied.

During the experiments it was found that that it is possible to deliver more liquid through nanochannels if it is partially filled with air than the whole bore being filled with liquid (giant quasi-slip). This apparently paradoxical result is not only a fundamental fluid mechanics problem but also might find significant practical applications. In particular, the most efficient desalination plants reject 4-8 gallons of water to produce 1 gallon of potable water. This increases costs and causes huge waste of energy. This work shows that if air bubbles would be added to the brine before the reverse osmosis membrane, the output of potable water can be increased.

3.2 Generation of Thermoresponsive Nanoparticles and Theoretical and Experimental Study of Their Release Kinetics

Most of the standard methods used for generation of micro- and nanoparticles have different drawbacks. For example, PIT (Phase Inversion Temperature) (Kunieda et

al., 1981, 1996; Izquierdo et al., 2002, 2004, 2005) relies on a wide variation of temperature for generation of nanoparticles. This produces thermal shock to the encapsulated materials, which are mostly drugs and/or proteins. Besides the temperature shocks, this method subjects the encapsulated materials to the temperature range beyond the denaturization temperature. Another method, sonication and centrifugation (Jafari et al., 2006; Graves et al., 2005) relies on high shear rate, which can also physically damage the encapsulated materials and produces highly polydisperse nanoparticles. Microfluidics-based devices (Kim et al. 2007) require expensive setups, which leaves very little room for error. Besides that, the particles thus produced are bigger than 5 μm in diameter, which is higher than the therapeutically relevant size (~1 μm), as well as the production rate is relatively low (~10^2-10^3 Hz).

In this work macroscopically long straight carbon nanopores produced by the nanofiber template method are used to polymerize sufficiently monodisperse thermo-responsive Poly(N-isopropyl acrylamide) (PNIPAM) nanoparticles of the order of 400 nm dia. at the rate of 10^7 particles per sec. During their formation, the nanoparticles were loaded with fluorescent dye Rhodamine 6G. The dye release kinetics from the nanoparticles was studied experimentally and theoretically under the conditions of thermal stimulation, and thermo-responsive release was demonstrated.

This work not only addresses some existing problems but also provides a theoretical framework, which was lacking in the literature. The modeling elucids the experimental results obtained in our experiments with thermoresponsive systems.

3.3 Thermoresponsive Polymer Nanofiber Scaffold

Electrospinning is a unique straightforward process to produce polymer nanofibers of the order of several hundreds of nanometers in diameter (Reneker et al., 2007, 2008). Among many possible applications of electrospun nanofibers that are being investigated is their use as drug delivery systems. A possible advantage of nanofibers as drug carriers is that the smaller the dimensions of the drug carrier, the better the drug can be absorbed by the human body. Also, nanofiber mats containing, for example, camptothecin (an anticancer drug) are very flexible and could be set into spaces near a brain tumor without damaging the surrounding healthy tissue. Modifying the release rate from PNIPAM-containing nanofibers on demand is not only a goal but also a tool to probe the intrinsic physical mechanisms of the process. In particular, the theoretical model (Yarin 2008) assumed that PNIPAM is distributed as nanogel islands in a polymer matrix. At T>LCST, these nanogel islands shrink and stretch the surrounding polymer matrix, which creates new nanopores/nanocracks in it. As a result, drug release rate increases, even though PNIPAM shrinks.

The elucidation of the intrinsic physical mechanism of PNIPAM swelling/shrinkage in nanofibers submerged in water has immense practical consequences as well. Recently it was shown (Srikar et al., 2008; Gandhi et al., 2009) that solid-state diffusion can hardly be the mechanism responsible for dye/drug release from nanofibers, while dye/drug desorption from nanopore surfaces plays the main role. This poses a crucial question whether PNIPAM “raisins” can indeed be distributed in nanofibers and create new nanopores without global shrinkage/swelling of nanofiber mats? An affirmative answer to this question was given in this work.

3.4 Theoretical Study of Meltblowing

Meltblowing is one of the leading methods in the field of nonwoven industry starting from medical application to the apparels that we wear and this industry is worth billions of dollars. This is intrinsically immensely complex process for complex interaction of various physical parameters namely the rheology of the polymer melt, jet-jet interaction, geometry of the melt blowing die etc. A number of defects in the melt-blown mats and drawbacks of the technology in general are rooted in the process fluid- and aeromechanics. Currently, the so-called *roping* (formation of streak-like structures in the webs and mats) is typically attributed to an uncontrolled turbulence. Such drawbacks of the process as the so-called *fly* (contamination of the surrounding gas by short and extremely thin fibers which do not connect to the fiber network) are generally attributed to too violent blowing conditions. These assumptions have, however, never been substantiated by either theoretical of experimental elucidation of the physical mechanisms of the process. The appearance of the so-called *shots* most probably results from the excessively high temperatures, when capillary breakup sets in (this situation is also insufficiently understood in the literature). The experimental data available in the literature are mostly descriptive and did not allow full recognition of the underlying physics and delineation of different effects responsible for the final parameters of melt-blown fabrics.

This part of work is devoted in filling the gaps in present day literature to understand this process and thus get away with the defects. The work is divided in three parts. In the first part solid flexible sewing threadlines are subjected to parallel high speed

gas jet. The mechanism of threadline flapping blowing is elucidated via the analysis of the effect of turbulent fluctuations, bending perturbation propagation over threadlines. Blown threadlines appear to be capable of extracting both turbulent pulsation and mean flow energy, which makes flapping vigorous. This helped in elucidating the role of ill understood turbulence in meltblowing. In the second part using this knowledge of turbulent pulsation first growth of small perturbations in the framework of the linear stability theory is developed. Then, the fully nonlinear case of large-amplitude planar bending perturbations of polymer jet is solved numerically. Both isothermal and non-isothermal cases are considered. The cooling of the surrounding gas jet results in cooling of the polymer jet inside, and to the arrest of the bending perturbation growth due to melt solidification. In the third part a comprehensive model of three-dimensional configurations of polymer jets in meltblowing from die exit to deposition screen is developed. In addition, multiple jets were modeled simultaneously, as well as deposition on a screen moving normally to the principal jet direction was accounted for. The results include prediction of the fiber deposition patterns and fiber-size distributions in the resulting nonwovens. Comparisons with the experimental data suggest that the model captures main trends rather accurately.

3.5 Solution Blowing of Carbon Nanotubes and Carbon Nanofiber

Carbon nanotubes and carbon nanofibers hold a great potential for different application. In this work a novel method, Solution Blowing, has been proposed to produce amorphous CNTS and carbon nanofibers at mass scale. For amorphous CNTS core-shell drops of Polymethyl Methacrylate (PMMA) and Polyacrylonitrile (PAN) and

for carbon nanofibers solution of PAN and PAN with carbon black are subjected to a high speed gas jet that results in their stretching and bending. As a result of this enormous elongation, after solvent evaporates, core-shell and monolithic nanofiber mats are deposited on a screen. Heat treatment allows complete elimination of the core and carbonization of the shell for the core-shell nanofiber mats yielding carbon tubes with an inner diameter 50-150 nm and outer diameter 400-600 nm and complete carbonization of monolithic nanofiber mats. These carbon nanofiber mats were used as microbial fuel cells, which showed enhanced activity than regular polycrystalline graphitic felt.

3.6 Solution Blowing of Soy Protein Nanofiber Mats

Modern technology is experiencing a significant shift toward biodegradable, or renewable, or just "green" agricultural biomolecular materials. The shift is driven by consumer awareness, stringent regulations regarding synthetic waste and a necessity to reduce dependence on synthetic materials. As a result, significant efforts are directed toward production of biodegradable materials from cotton, corn, potato (Kanczler et al., 2009; Yu et al., 2008; Greene 2007; Kim et al., 2005, 2006) and soy protein and development of biodegradable composites (Huang et al., 2007, 2008; Chabba et al., 2005). In particular, there is a growing emphasis on making soy-based "green materials". The reason behind the drive towards soy-based materials can be attributed to the fact that soy protein is one of the cheapest and most widely grown vegetable products with a wide range of uses. Booming SoyDiesel production (Klass 1998; Ahmed et al., 1994) facilitates increasing production of soy, while using only soy oil, and leaving behind abundant residual soy protein. In addition to the use of soy protein as a nutrient, it has

great industrial value too. Soy protein contains sialic acid (Springer et al., 1969), which is able to inhibit and/or capture influenza virus as receptor. Soy protein can be used as plastics, adhesives and fire retardants (Johnson et al., 1984; Kalapathy et al., 1995; Hettiarachchy et al., 1995). As a result of all these advantages, there is a growing need and market for nanofibers containing soy protein isolates, utilizing their high surface area to volume ratio, which facilitates their functionality. Several attempts were undertaken to produce such fibers through electrospinning (Phiriyawirut et al., 2008; Alemdar et al., 2008; Fung et al., 2010; Vega-Lugo et al., 2009; Cho et al., 2010) or wet spinning (Zhang et al., 2003). In these works electrospinning mostly relied on blends with a fiber forming polymer and soy protein since pure soy protein fibers are not flexible and it is very hard to achieve submicron fibers. Moreover, in such solution-based methods as electrospinning and wet spinning, dissolution of soy protein can be facilitated by denaturation by means of thermal treatment (Zhang et al., 2003; Rangavajhyala et al., 1997), alkali, for example NaOH, sodium sulfite and urea (Rangavajhyala et al., 1997; Lee et al., 2003), as well as pH and ionic strength variation (Lee et al., 2003). Note also, that to improve tensile strength of protein/polymer fibers, cross-linking was applied (Zhang et al., 2003).

In this work solution blowing of soy protein (sp)/polymer blends was used to form monolithic nanofibers. The monolithic fibers were blown from blends of soy protein and nylon-6 in Formic Acid. The sp/nylon-6 ratio achieved in dry monolithic nanofibers formed using solution blowing of the blend was equal to 40/60. In addition, solution blowing of core-shell nanofibers was realized with soy protein being in the core and the supporting polymer in the shell. The shells were formed from nylon-6. The sp/nylon-6

ratio achieved in dry core-shell fibers was 32/68. The nanofibers developed in the present work contain significant amounts of soy protein and hold great potential in various applications of nonwovens.

3.7 Spray Cooling Using Metalized Nanofiber Mats

Spray cooling is one of the most effective and aggressive methods of cooling compared to the other air- or liquid cooling systems (Mudawar 2001; Briones et al., 2010; Yarin 2009). It was discovered recently that the efficiency of spray cooling can be enhanced still more if a high-heat flux surface is covered by a nano-textured layer, namely, an electrospun polymer nanofiber mat of the thickness about 100 μm (Srikar et al., 2009b). Such an approach where a hot surface is cooled more effectively through a "furry overcoat", almost 90-95% of which is filled with air, is rather paradoxical. It triggered a deeper fluid mechanical study in the following work (Lembach et al., 2010) where it was shown that the texture of the electrospun nanofiber mats facilitates penetration of water into their pores and simultaneously prevents receding motion of the contact line of spread-out drops, as well as eliminates bouncing. All these phenomena are greatly beneficial for spray cooling through nanofiber mats.

However, polymer nanofibers have a relatively low thermal diffusivity of their own, as well as the individual fibers are pretty smooth. Therefore, a further enhancement of spray cooling through nanofiber mats might probably be achieved if they would be metalized and made as rough as possible, as a means to further increase the effective surface area of nanofiber-coated hot surfaces. In this context, our attention in this work is

attracted to electroplating of electrospun nanofiber mats deposited on high-heat flux surfaces to facilitate their cooling.

Electroplating is a process that coats conductive or semi-conductive objects with a thin metal layer. The process uses the electrical current to reduce cations of a desired metal from a solution. It is used to deposit various metals on targeted surfaces (Schlesinger et al., 2000; Graham 1971). The process is technologically stable and attractive for growing thin films and/or nanostructures with potentially superior thermoelectric and microelectronics properties (Feng et al., 2007; Li et al., 2009; . There is a significant body of previous research on electroplating and many examples of its successful application in microelectronics and automotive and aerospace industries (Sikder et al., 1999; Aruna et al., 2005; Xu et al., 2008; Vaezi et al, 2008). However, studies on electroplating of metal coatings on nano-textured non-conductive polymer nanofibers are scarce (Pinto et al., 2004; Ochanda et al., 2005, 2007).

In the present work the electrospun nanofiber mats were made metallic using electroplating. Then, their cooling capabilities in the case of drop cooling were studied, which revealed heat removal rates up to 0.6 kW/cm^2. The experimental results on the rate of drop evaporation inside metallic nanofiber mats are also supported by the theoretical estimates.

3.8 Smart Tunable Phase Change Materials (PCMs)

PCMs offer unique capabilities to thermal management. Different combinations of paraffins seem to be the best possible approach to PCMs due to the melting temperatures of the individual paraffins being distributed over a wide temperature range,

high heat of fusion, nontoxicity, stability and resistivity to corrosion. However, the organic PCM met with several problems: (i) each of these materials taken separately undergoes phase transition in a narrow temperature range; (ii) due to their very low thermal conductivity, their thermal response time might be too long; (iii) they solidify on heat exchanger surfaces. A partial remedy to problem (ii) might be in the encapsulation in PCM of copper nanoparticles (Wu et al., 2010) or impregnating porous materials (Karaipekli et al., 2009), albeit an ultimate simultaneous solution of all these problems lies within nano-encapsulation of PCM.

In this work a mass scale process of intercalation of different types of paraffins and their mixtures with triglycerides inside carbon nanotubes (CNTs) followed by a proper cleaning procedure , which cleaned the nanotubes from outside only leaving the inside of the CNTs completely filled as shown in TEM, was achieved. Then these filled CNTs were studied using Differential Scanning Calorimetry and it was found that using different mixtures there phase change can be widened over a wider temperature range thus answering to the problem (i). Due to their smaller size the characteristic time frame of response was estimated to be $\sim 10^{-7}$ s solving the problem (ii). The encapsulation technique did away with the problem (ii).

3.9 Rheology of Gypsum Slurries

Manufacturing of gypsum wallboards resulted a multi-billion-dollar industry. To manufacture gypsum wallboards, water is mixed with gypsum powder (stucco) to form slurry, which solidifies eventually to in the form of a wallboard. The field is mostly

empirical. Its further optimization and development depend significantly on the understanding of rheology of gypsum slurries.

In this work concentrated gypsum slurries used for wallboard production are studied using elongational rheometers, which was substantiated by shear rheometry conducted by Dr. R. Srikar. It is shown that the rheological behavior of different slurry compositions can be sufficiently accurately described in the framework of the Ostwald–de Waele power law, which reproduces both shear and elongational experimemtal data with sufficiently close values of the consistency and flow behavior indexes for each slurry composition studied.

4. ENHANCED RELEASE OF LIQUID FROM CARBON NANOTUBE BUNDLES/ NANOCHANNELS

4.1 Introduction

In Chapter 4 a nanofiber-derived nanofluidic device is realized. It is shown that bi-layered (liquid-air) flows through nanochannels can result in a higher flow rate of liquid release as compared to the case when the same liquid flows through the same channels occupying the whole bore and subjected to the same pressure drop.

Section 4.2 describes the theoretical background of the work. Section 4.3 illustrates the experimental method. Section 4.4 contains the results and discussion. The concluding remarks are drawn section 4.5.

4.2 Theoretical Background

Pressure-driven flows through carbon tube bundles were studied experimentally in (Bazilevsky et al., 2008a). The results for flows of pure liquids or gases occupying the whole bore were found to be in agreement with the Poiseuille law affected by cross-sectional size distribution in the bundle. Bi-layer liquid-gas flows were also recorded but no analyzed. Bi-layer (liquid-gas) laminar flows in nano- and microchannels, albeit classical, yield some surprises. Consider, for example, a planar bi-layer fully-developed pressure-driven flow in a slit described by the following problem:

$$\frac{d^2 u_i}{dy^2} = \frac{1}{\mu_i}\frac{dp}{dx}, \quad i = 1, 2, \tag{4.1}$$

$$y = 0 \quad u_1 = 0; \quad y = H \quad u_2 = 0, \tag{4.2}$$

$$y = h \quad u_1 = u_2, \quad \mu_1 \frac{du_1}{dy} = \mu_2 \frac{du_2}{dy}, \tag{4.3}$$

where i=1 and 2 correspond to liquid and gas, respectively; u is the axial velocity; μ viscosity, H the channel width; h (<H) the interface lateral coordinate y; dp/dx is a constant longitudinal pressure gradient, which is the same in both liquid and gas. Equation (4.1) is the appropriate form of the Navier-Stokes equations in the present case; the no-slip conditions at the walls are given by Eqs. (4.2). At the interface, continuity of velocity and shear stresses in both phases is assumed, Eqs. (4.3). Gas flow is considered as incompressible because it was shown(Bazilevsky et al., 2008a) that at pressure drop of the order of 1 bar, which is of interest in the present work, compressibility effects are still negligibly small.

Solving Eqs. (4.1) with the boundary conditions (4.2) and (4.3), one can find the velocity profiles $u_1(y)$ and $u_2(y)$. They, in turn allow calculation of the volumetric flow rate of liquid Q_1. Rendering it dimensionless by the corresponding volumetric flow rate of pure liquid when its flow occupies the whole bore (Yarin et al. 2005), $Q_{1,pure} = -H^3/(12\mu_1)dp/dx$, one can find the following dimensionless volumetric flow rate in the bi-layer flow

$$R = \frac{Q_1}{Q_{1,pure}} = -2\bar{h}^3 + 3\frac{\bar{h}^2 - \bar{h}^4(1-\mu_2/\mu_1)}{1-\bar{h}(1-\mu_2/\mu_1)}, \tag{4.4}$$

where $\bar{h} = h/H$.

The dependence $R = R(\bar{h})$ is plotted in Fig. 4.1.

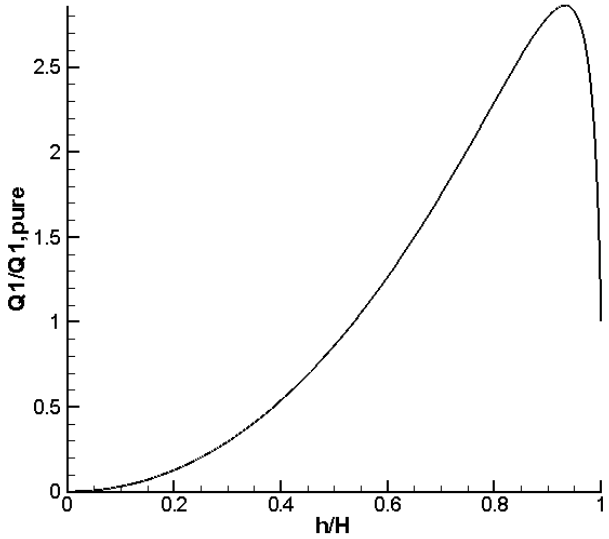

Fig. 4.1. Dimensionless volumetric flow rate versus liquid layer thickness for n-decane/air flow (μ_2/μ_1=0.019565).

The striking feature visible in Fig. 4.1 is that liquid flow rate can be larger in a bi-layer flow than in the corresponding pure liquid flow occupying the whole bore and subjected to the same pressure drop, i.e. R can be larger than 1 (almost 3 at the maximum). This is related to the fact, that the less viscous air layer can flow much faster than the underlying liquid layer and pull the latter via a significant shear stress. For n-decane/air system, the velocity profile in a channel cross-section is shown in Fig. 4.2, which clearly illustrates how a very fast air flow (at $0.8 \le y/H \le 1$) pulls the n-decane layer (at $0 \le y/H \le 0.8$). In Fig. 4.2 the velocity profile u is rendered dimensionless by the maximal velocity in pure liquid flow, $u_{max,pure}= -(H^2/8\mu_1)dp/dx$.

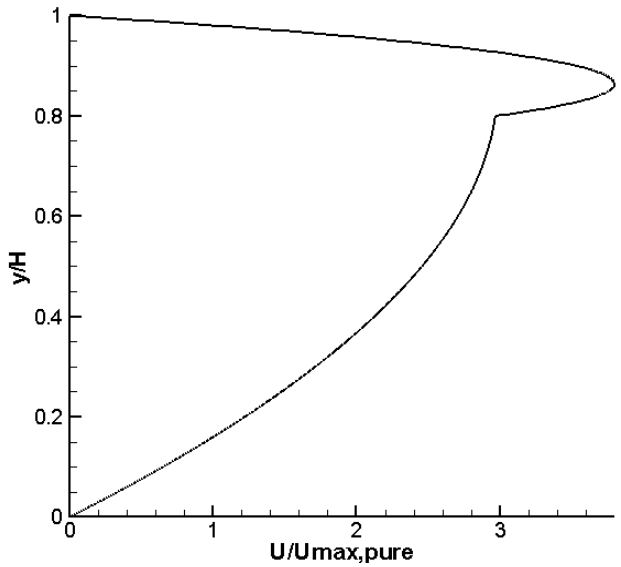

Fig. 4.2. Velocity profile for n-decane/air flow (μ_2/μ_1=0.019565) with h/H=0.8. The velocity profile is rendered dimensionless by the maximal velocity in pure liquid flow, $u_{max,pure}$.

The theory outlined above for a slit flow cannot be easily extended to flows in cylindrical channels. However, it is clear that in cylindrical channel flows the same physical reasons exist for an enhanced liquid release due to pulling by relatively fast gas layer. Therefore, the results for a slit can be used as a qualitative guide for bi-layer flows in cylindrical channels which were studied experimentally.

4.3 Experimental Section

Polyacrylonitrile (PAN; M_w=150 kDa) was purchased from Polymer Inc.). Polycaprolactone (PCL; - M_w=80 kDa), N,N-Dimethyl Formamide (DMF) anhydrous-99.8% and DichloroMethane (MC), N-Decane all purchased from Sigma-Aldrich.

Quickset epoxy and aluminum foil were purchased from local store. All materials were used as received.

For electrospinning of PCL nanofibers, PCL solution of 12 wt% concentration (in w/w 60:40 DMF:MC) was prepared. For drop casting, PAN solution of 12 wt% concentration in DMF was used.

An aluminum holder with a sparse parallel array of electrospun polycprolactone (PCL) nanofibers collected on the holder as in (Theron et al 2001) were fixed on a glass slide. Drops of polyacrylonitrile (PAN) solution were deposited with a syringe on the nanofibers located on the slide. The drops spread and formed a uniform PAN film. The PCL nanofibers floated up and were surrounded by PAN solution in their central, freely suspended part. The PAN film with the PCL nanofibers embedded in it was dried in open air overnight. Then strips were cut from it in the nanofiber direction. These PAN strips continued to be dried in open air until had become hard (cf. Fig. 4.3a). Then they were carbonized in an oven at elevated temperature following the routines of Refs. (Theron et al; 2001; Zussman et al., 2006) used to carbonize core-shell poly(methylmethacrylate)-polyacrylonitrile (PMMA-PAN) nanofibers. The PCL nanofibers inside the strips were eliminated, while PAN was carbonized. The resulting carbonized strips contained parallel tubes inside with diameters of the order of 300-500 nm (Fig. 4.3b).

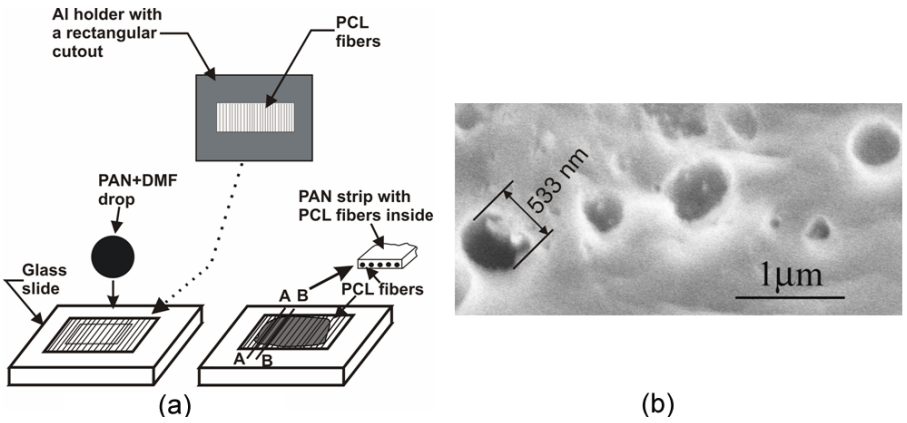

Fig. 4.3 (a) Schematic showing steps for preparation of carbon nanochannels; (b) SEM image showing nanotube exits from the end of a carbon strip (a small part of the strip cross section is shown: the full cross-sectional size of the strip is of the order of several hundred microns and it encases thousands of nanotubes). Tube diameters are of the order of 300–500 nm; the sample is slightly tilted in the image. Therefore, some nanotube cross sections look a bit elliptical rather than circular.

For the pressure driven flow the flow through carbon nanochannels were realized using setup described in (Bazilevsky et al., 2008a). In particular, the strips were installed at the end of a glass capillary and fixed by epoxy. Pure n-decane was supplied through the glass capillary. Pure n-decane was released through the nanotubes into a Petri dish filled with water (Fig. 4.4 a). One such case is shown in Fig. 4.4b. It can be seen that the n-decane droplets merged and made a larger droplet. It can be also seen that along with n-decane air is also supplied, which can be seen inside the merged n-decane droplet.

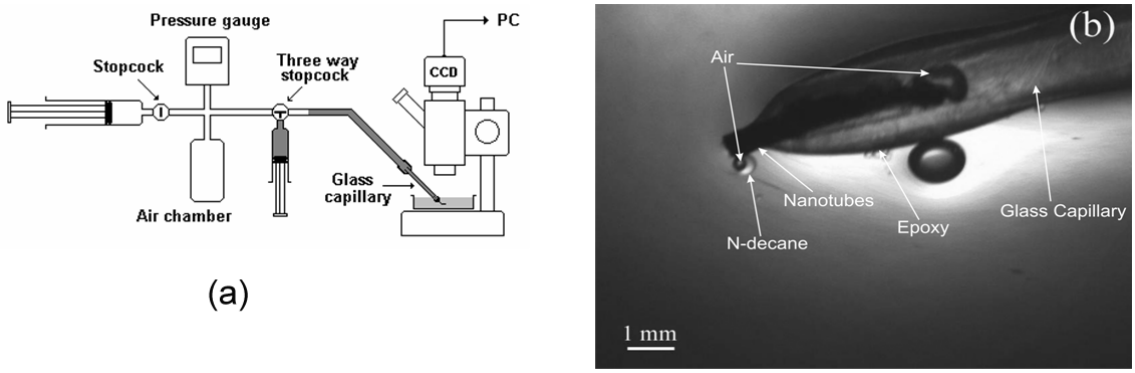

Fig. 4.4 (a) Sketch of the experimental apparatus. A carbon strip was secured by epoxy cement at the exit of the glass capillary (of the order of 1 mm i.d.) and submerged in water. The fluid supply system consisted of two standard plastic syringes of volumes 10 and 1 ml, a digital pressure meter, a 7 ml plastic air chamber and two stopcocks connected by thin silicon tubing. The air chamber was used to maintain pressure at a nearly constant level during a test. After pressurizing the air chamber by means of the 10 ml syringe (on the left in the figure), the one-way stopcock was closed. The second syringe (vertical in the figure), which was connected directly to the three-way stopcock, was used to fill (with n-decane) the silicon pipe leading to the glass capillary.; (b) Carbon strip with nanotubes fixed by epoxy at the end of a glass capillary. The air bubble seen inside the glass capillary is located at the inlets of the nanotubes in the carbon strip (the latter is seen as a long black strip inserted in the class capillary from the left).

4.4 Results and Discussions

Pure n-decane was released through the nanotubes into Petri dish filled with water. As it was observed in a microscope, the tiny n-decane droplets from different nanotubes immediately merged at the tube exits and formed the n-decane drop submerged

in water shown in Fig. 4.5a. If air was present in the glass capillary, as in Fig. 4.4b, it penetrated the nanotubes. In this case, the merged drop attached to the strip end and submerged in water contained merged air bubble in the middle (Fig. 4.5b).

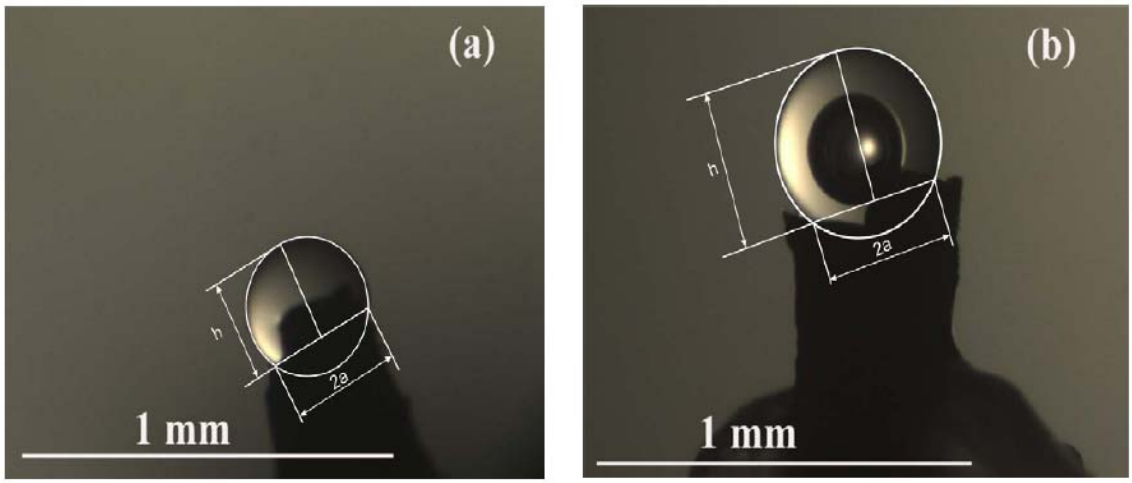

Fig. 4.5. (a) Release of n-decane without air at pressure drop of 1.143 bar. (b) Release with air: air penetrates the tubes and accumulates at the center of the merged drop of released n-decane at 1.133 bar.

The released volumes of air and n-decane were measured from the images at different time moments as shown in Fig. 4.6 a and b. In particular, the geometric parameters a and h measured in the cases with and without air, were used to find the overall volume V of pure n-decane or compound n-decane/air drops considering them as spherical segments, $V=\pi h(3a^2+h^2)/6$. Note that a small part of n-decane released from the nanotubes and staying near their exit is not accounted for in this procedure, so that V is slightly underestimated. Volume of the central air bubble V_{air}, which was always fully visible, was also measured from images similar to that of Fig. 4.6b approximating it as a sphere. In presence of the central air bubble, the volume of pure n-decane was found as $V_d=V-V_{air}$. The images in Fig. 4.6 show that the exit surface of the carbon slit is not

necessarily plain because cutting slits led to some fence-like debris left on the periphery of the area with nanotube exits. In Figs. 4.6 a and b such fence-like debris shield the drop lower part on the right. The cumulative volumetric flow rates of n-decane through the nanotubes Q_1 were found as dV_d/dt, evaluating the derivative using the values of V_d recorded for two successive images with an interval 4 s between them. The results are depicted in Fig. 4.7 for bi-layer (n-decane/air) and pure n-decane flows through the same carbon nanotube bundle. The volumetric flow rates are of the order of 1 nL/s which agrees with the results on (Bazilevsky et al., 2008a). Figure 4.7 shows that the volumetric flow rate of n-decane in the n-decane/air case (when a part of the bore might be occupied by air) Q_1 is always larger than the volumetric flow rate of pure n-decane through the same tubes $Q_{1,pure}$ with the ratio being in average $Q_1/ Q_{1,pure}=2.188$, i.e. approaching the maximal possible value in Fig. 1, even though the value of Q_1 is slightly underestimated.

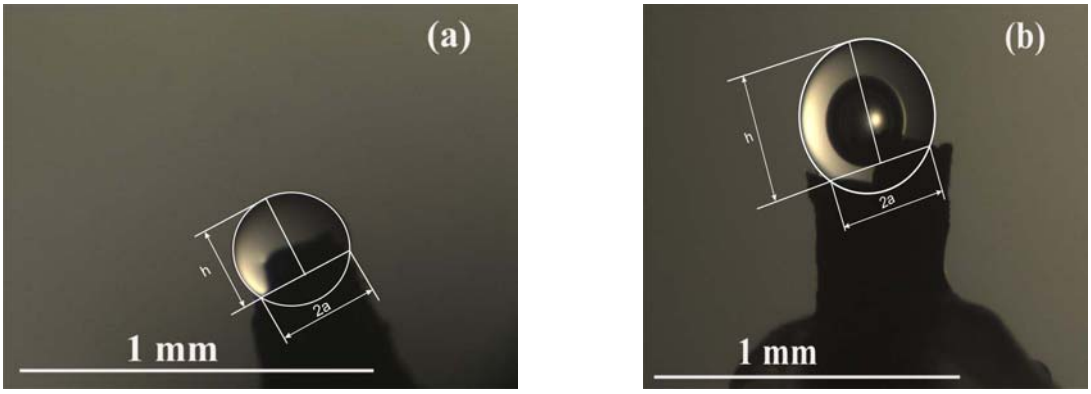

Fig. 4.6. Measurement of n-decane volume from the images.

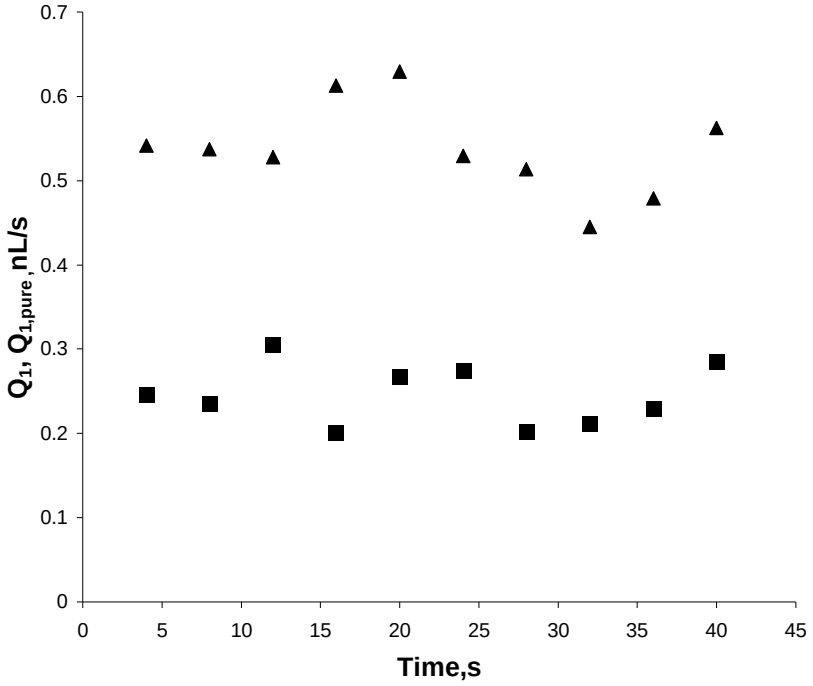

Fig. 4.7. Volumetric flow rates of bi-layer flow (Q_1, triangles) and pure n-decane ($Q_{1,pure}$, squares) through the same carbon nanotube bundle. of n-decane with and without air with respect to air.

The character of the flow deserves, however, an additional analysis. Indeed, it is not immediately clear that the n-decane/air flow we are dealing with is a truly bi-layer flow, since air could be simply partially dissolved in n-decane before the nanotube entrance at elevated pressure, whereas at the nanotube exits at a lower pressure an excessive air could be desolubilized. Applying Henry's law, one can find the mole fractions of nitrogen and oxygen $x_{nitrogen}$ and $x_{nytrogen}$ (relative to n-decane), which will be desolubilized in response to a pressure drop Δp

$$x_{nitrogen} = \frac{\Delta p}{K_{nitrogen}}, \quad x_{oxygen} = \frac{\Delta p}{K_{oxygen}}. \tag{4.5}$$

The values of the corresponding Henry's constants are found using the data from (Ashcroft et al., 1997) as $K_{nitrogen}$=152.8046 atm/mole/lt and K_{oxygen}=89.72 atm/mole/lt. Then, the desolubilized volumes of nitrogen and oxygen $\Delta V_{nitrogen}$ and ΔV_{oxygen} are found as

$$\Delta V_{nitrogen} = \frac{x_{nitrogen,hp} - x_{nitrogen,lp}}{C_{nitrogen}} V_d, \tag{4.6}$$

$$\Delta V_{oxygen} = \frac{x_{oxygen,hp} - x_{oxygen,lp}}{C_{oxygen}} V_d \tag{4.7}$$

where $C_{nitrogen}$=0.01105 and C_{oxygen}=0.0416 and hp and lp in the subscripts denote the corresponding values at high pressure (at the nanotubes entrances) and at low pressure (at the nanotubes exits in water). Then, the desolubilized volume of air is $\Delta V_{air} = \Delta V_{nitrogen} + \Delta V_{oxygen}$.

Equations (4.5) – (4.7) show that in the present case $\Delta V_{air} = 0.168 V_d$. Note that Henry's law is strictly valid for infinitely dilute systems. Therefore, in the present case of a finite dilution, the value of ΔV_{air} might be even slightly overestimated. Figure 4.8 demonstrates the total volume of the released air V_{air} as well as the desolubilized volume of air ΔV_{air} versus time. It shows that most of air in the bubble at the center of n-decane drops in cases similar to that of Fig. 4.6b was brought by convection rather than desolubilization, which supports the idea that the flow inside carbon nanotubes is a bi-layer one in such cases.

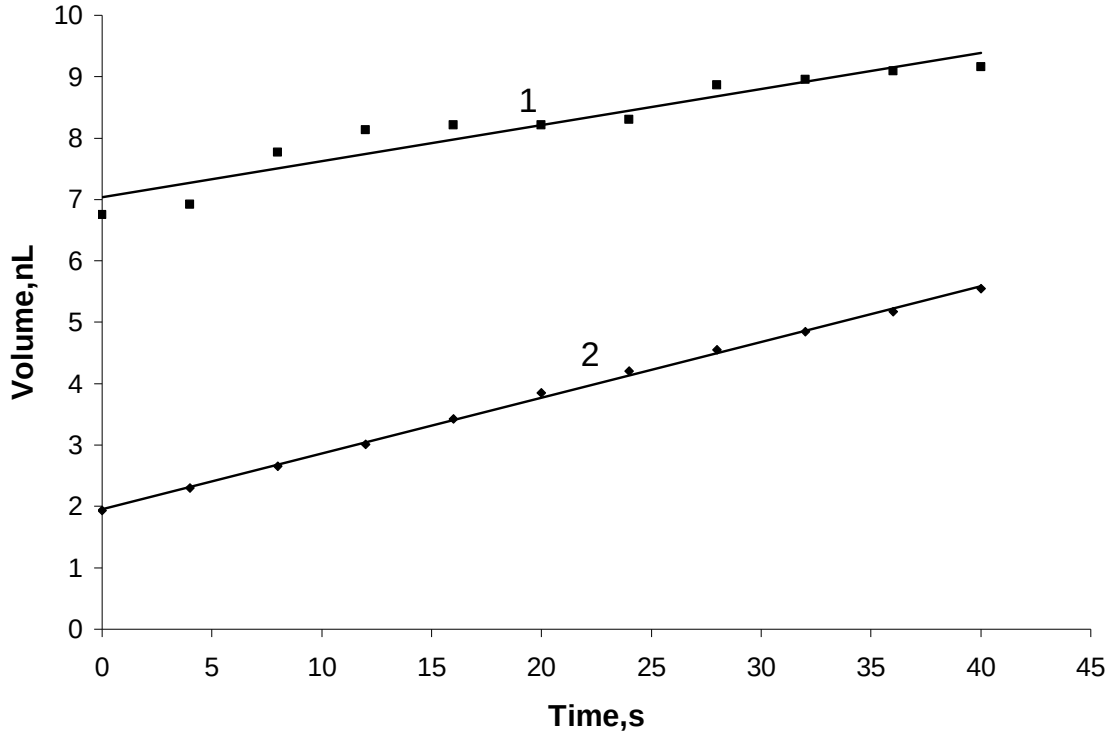

Fig. 4.8. Total (V_{air}; 1) and desolubilized (ΔV_{air} ; 2) volumes inside the merger drop.

Some additional structures of liquid/air flows in nanochannels can be imagined. For example co-annular (ring-like) flows were observed in microchannels (Yarin et al.,2009) and should also be considered as a possibility. There are two possible ring-like configurations: (i) the flow with a liquid ring attached to thechannel wall, while air is in the core, (ii) and the flow with an air ring near the wall, while liquid is in the core. Both flows can be readily described using Poiseuille-like solutionsof the Navier–Stokes equations for co-annular cases. Then, the corresponding formulae for the liquid volumetric flow rate in cases (i) and (ii) are given by equations (4.8) and (4.9):

$$\frac{Q_1}{Q_{1,pure}} = 1 + \bar{h}^4 - 2\bar{h}^2 \qquad (4.8)$$

$$\frac{Q_1}{Q_{1,pure}} = \bar{h}^4 + \frac{2}{\mu_2/\mu_1}\left(\bar{h}^2 - \bar{h}^4\right) \tag{4.9}$$

In equations 4.8-4.9 $\bar{h} = h/R$, where R is the bore cross-sectional radius, and $Q_{1,pure} = -(\pi R^4/8\mu_1)\,(dP/dx)$.

Equation (4.8) shows that $Q_1/Q_{1,pure} \leq 1$ for $0 \leq \bar{h} \leq 1$, which means that liquid flow in the ring-like case (i) can never be entrained strong enough to have the volumetric flow rate higher than in the whole-bore case. On the other hand, the ratio $Q_1/Q_{1,pure}$ can become larger than 1 according to equation (4.9) and the maximal value which can be reached is $(Q_1/Q_{1,pure})_{max} = (\mu_1/\mu_2)(2-\mu_2/\mu_1)^{-1}$.For the case of n-decane/air flow, the ratio $(Q_1/Q_{1,pure})_{max} = 25.88$, whichis much larger than the experimental one, 2.188. In the ring like case (ii), where a liquid cylinder is strongly entrained by an air ring, in the nanoscale characteristic of the present work, capillary (Rayleigh) instability will almost immediately break it up (Rayleigh 1945; Yarin 1993). Therefore, case (ii) is unstable, cannot be realized and will almost immediately result in a two-phase flow. In the case of liquid phase dominating, this means a two-phase flow containing air bubbles in a liquid matrix. Such a flow can never have $Q_1/Q_{1,pure} > 1$, which means that neither core–shell n-decane/air flow (case (ii)) nor its immediate two-phase 'descendant' are relevant for the current experiments. Moreover, core–shell air/*n*-decane flow (case (i)) is also prone to capillary instability (Yarin et al.,1993), which is clearly seen in the images taken in the experiments with transparent microchannels (Yarin et al, 2009). Therefore, that case is also unstable and can never lead to $Q_1/Q_{1,pure} > 1$. Therefore, the only plausible flow configuration left is the one similar to the model (4.1)-(4.3), Namely, a bi-layer liquid/air flow where the two phases each occupy its own part of the bore cross-section.

4.5 Conclusion

The experimental and theoretical results of this paper show that liquid/air flows in carbon nanotube channels of cross-sectional diameters of the order of 300–500 nm can self-organize as a bi-layer structure. Liquid and air layers each occupy its own part of the channel bore. Moreover, air motion can become relatively fast due to its low viscosity. As a result, the air layer entrains the liquid layer. The entrainment results in such a significant enhancement of liquid flow that its flow rate becomes larger than it would be if the same liquid occupied the whole bore at the same pressure drop. It is interesting to note that slip in nanochannel flows is typically expected in the diameter range of the order of 10 nm, i.e. in much smaller channels. In larger scales, slip in some cases is rather apparent than real, and is related to the possibility of liquid flow over gas pockets (Lauga et al., 2007). The present results show that some enhanced liquid flows through nanotubes, which could also be interpreted as a deviation from the no-slip condition, in reality are entrained by a rapidly moving gas layer in bi-layer liquid/gas flows.

5. FLOW FROM MACROSCOPICALLY LONG STRAIGHT CARBON NANOPORES FOR GENERATION OF THERMO-RESPONSIVE NANOPARTICLES

5.1 Introduction

In the present work the proposed approach relies on multi-channel pressure-driven nanofluidic device as shown in chapter 4. It was manufactured via the nanofiber template method (cf. chapter 4) and used for delivery of chemical components needed for *in situ* polymerization of thermo-responsive biocompatible polymer nanoparticles encasing model substances and suspended in water. Thermo-responsive polymer, Poly(N-isopropyl acrylamide) (PNIPAM) is one of the best candidates for creating smart nanogels. Its lower critical solution temperature (LCST) is about 32 °C. At temperatures T>LCST, PNIPAM shrinks in water, whereas at T<LCST it swells until reaches an equilibrium volume. This behavior results from the disruption of hydrogen bonding between water molecules and the amide side groups of PNIPAM macromolecules, which is a fully reversible process. The aim of the present work is to develop a novel nanofluidic polymerization reactor based on macroscopically long straight carbon nanopores for mass production of relatively monodisperse nanoemulsions and/or nanoparticles of thermo-responsive polymers.

Section 5.2 describes the experimental part. Section 5.3 contains results and dscussions. Section 5.4 outlines the theoretical model. Concluding remarks are drawn in section 5.5.

5.2 Experimental Section

Polycaprolactone (PCL) - M_w=80 kDa was used to electrospin the template nanofibers using the following solvents: N,N-Dimethyl Formamide (DMF) anhydrous-99.8% and DichloroMethane (MC), all purchased from Sigma-Aldrich. In particular, PCL solutions of 12 wt% concentration (in w/w 60:40 DMF:MC) were used to electrospin nanofibers using a standard setup described elsewhere (Reneker et al., 2007) . The elrectrospun fibers were collected as ordered parallel arrays on hangers made from domestic heavy duty aluminum foil located over a cut in a rotating grounded sharpened wheel, which served as an electrostatic lens similar to those inroduced in (chapter 4; Reneker et al., 2007; Theron et al., 2001; Zussman et al., 2003) . Parallel PCL nanofiber arrays were encased in Polyacylonitrile (PAN; M_w=150 kDa purchased from Polymer Inc.) strips by dripping and drying a drop of PAN solution (12 wt% in DMF). The strips were heat treated as described in chapter 4, which led to complete elimination of template PCL nanofibers and carbonization of PAN strips. The resulting turbostratic carbon strips contained thousands of hollow straight nanopores of the order of 300-500 nm dia. The strips were installed at the exit of a glass microcapillary and fixed by Quick Set Epoxy. The capillary was installed in the pressure-driven setup described in detail in (Chapter 4; Bazilevsky et al., 2008a), which allowed pressure-driven flows through the parallel nanopore arrays in the carbon strips.

The following compounds were used to polymerize thermo-responsive nanoparticles using the nanofluidic setup based on pressure-driven flows through parallel nanopores in carbon strips. N-Isopropyl acrylamide (NIPAM)-97%, N,N′-Methylenebisacrylamide (BIS)≥ 99.5% (cross-linker), N,N,N’,N’-

tetramethylethylenediamine-99% (accelerator), [2-(methacryloyloxy) ethyl] trimethyl ammonium chloride (METAC)-75% (to facilitate NIPAM polymerization at room temperature), ammonium persulfate (APS) (initiator), N-decane anhydrous ≥ 99% , Brij-30 (surfactant), and fluorescent dye Rhodamine 6G (used in the release experiments), all purchased from Sigma-Aldrich.

To form Poly(N-Isopropyl acrylamide) (PNIPAM) nanoparticles, a series of solutions were made. Solution A was an aqueous solution of NIPAM (15.5% w/v), BIS (1.5% w/v), METAC (2 vol%) and APS (3% w/v). Solution B was prepared by dissolving surfactant (6 wt%) in n-decane. Solution C was prepared by adding accelerator (2 vol%) to solution B. Solution D was prepared by adding Rhodamine 6G (4 mg/mL) to solution C. Solutions C and D were used to prepare thermo-responsive PNIPAM nanoparticles. Solution E was prepared by adding accelerator (2 vol%) to n-decane. The solution list is given in Table 5.1.

Table 5.1. Solution list

Solution Name	**Aqueous Solution**				**N-decane Solution**		
	NIPAM (%w/v)	**BIS (%w/v)**	**METAC (vol%)**	**APS (%w/v)**	**Brij-30 (wt%)**	**Accelerator (%vol)**	**Dye (mg/mL)**
A	15.5	1.5	2	3	-	-	-
B	-	-	-	-	6	-	-
C	-	-	-	-	6	2	-
D	-	-	-	-	6	2	4
E	-	-	-	-	-	2	-

All TEM observations of PNIPAM nanoparticles were made using JEOL JEM-3010, a 300 kV transmission electron microscope with a LaB_6 electron source. All SEM observations of PNIPAM nanoparticles were made using JEOL JSM-6320F, a scanning

electron microscope with a cold field emission source. Dynamic light scattering (DLS) was done by DLS Wyatt Technology instrument to evaluate nanoparticle size distribution.

Fluorescence was measured by Spectrophotometer Spectra-Max Gemini to follow the kinetics of dye release from nanoparticles.

5.3 Results and Discussion

Formation of n-decane nanoemulsions

Parallel straight carbon nanopores were first used to produce nanoemulsion of n-decane droplets in water. Release of pure n-decane into water from nanopores results in formation of tiny n-decane droplets which merge to produce a single macroscopic drop attached to carbon strip edge similarly to Refs. (Chapter 4; Bazilevsky et al., 2008a). On the other hand, in the current case the presence of 6 wt% of surfactant reduced the interfacial n-decane/water tension, which prevented merging of n-decane droplets produced by the release of solution B (n-decane and surfactant) and facilitated formation of fine emulsion of n-decane in water contained in a Petri dish (Fig. 5.1). It is emphasized that we found that 6 wt% of surfactant in n-decane is the minimum (and thus, optimal) concentration needed to prevent droplet merging, since at 2 and 5 wt% macroscopic merger drops were observed. The presence of surfactant also allowed operation at lower pressure drops. The observations of droplet formation in comparable microchannel flows might suggest that capillary instability is the main mechanism determining droplet size (Saeki et al., 2008). N-decane droplet diameter in the emulsion stabilized by surfactant can be estimated using the Rayleigh-Weber theory (Yarin 1993) as

$$D = D_0(3\pi/2)^{1/3}[2(1+3\sqrt{Oh/2})]^{1/6} \quad (5.1)$$

where D_0 is the nanotube diameter, and $Oh=2\mu^2/(\rho D_0\alpha)$ the Ohnesorge number, with ρ, μ and α being the n-decane density, viscosity and interfacial tension, respectively. Take for the estimate the parameter values corresponding to n-decane in water (Chapter 4; Bazilevsky et al., 2008a): $\rho=0.73$ g/cm^3, $\mu = 0.925\times10^{-2}\,\mathrm{g/(cm\,s)}$ and $\alpha=53$ g/s^2. Then, the estimate shows that $D=2.04D_0$. However, then for $D_0 \approx 1\,\mu\mathrm{m}$, the droplet size is $D \approx 2$ μm, which is 5 times larger than in reality (cf. Fig. 5.2, where the droplet-size distributions obtained using dynamic light scattering are plotted). In the presence of surfactant, taking the interfacial tension $\alpha=5.3$ g/s^2, one finds $D=2.25D_0 \approx 2.25$ μm, i.e. a larger disparity with the experimental data. Therefore, the Rayleigh-Weber capillary instability seems to be inapplicable in the present case. In addition, a magnetic stirrer was rotating at 700-1000 rpm in the Petri dish, which might be the mechanism determining n-decane droplet sizes via the effect of shear stresses. Then, the diameters of the order of $D=\sigma/(\mu_w\dot{\gamma})$ are expected, where μ_w is water viscosity and $\dot{\gamma}$ the shear rate in water (Taylor 1934). The latter yields $D \approx 5$ cm, which is definitely out of scope. Therefore, the magnetic stirrer effect on the droplet size should be considered negligibly small. The magnetic stirrer was used to minimize the effect of clustering, which might occur if the produced n-decane droplets are not removed from the source. Detachment of n-decane droplets from the nanotube exits due to buoyancy could also be a mechanism responsible for the droplet sizes. Then, $D=[6\sigma/(\Delta\rho g)]^{1/2}$, where $\Delta\rho$ is the density difference of water and n-decane, and g gravity acceleration. The latter estimate yields $D \approx 1$ cm, too large in the light of the data in Fig. 5.2.

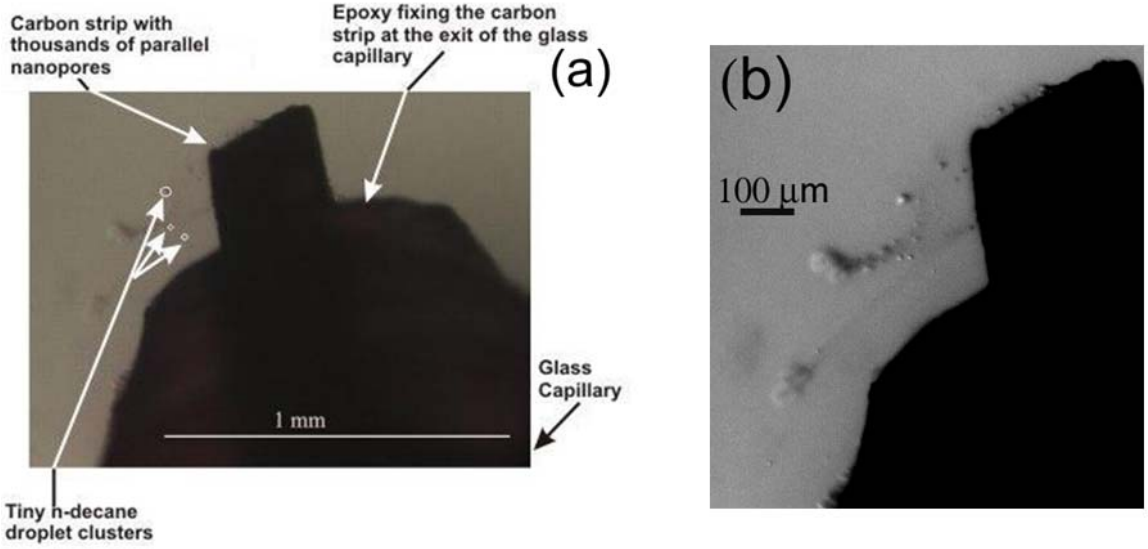

Fig. 5.1. Release of pure n-decane in water at 1.19 bar. Formation of clusters of small n-decane droplets stabilized by surfactant is seen. (a) The carbon strip containing thousands of parallel carbon nanopores is seen as a black vertical strip above the glass capillary. (b) Cluster clouds and individual droplets which are big enough to be seen using optical microscope.

Given the estimates above, the most probable scenario of the droplet formation looks as follows. N-decane drips from the nanotube exits producing tiny droplets of the order of $D_0 \approx 100$ nm. These droplets almost immediately make clusters or cluster clouds visible in Fig. 5.1. The clusters stabilized by surfactant and restricted in size by stirring are still tiny compared to huge merger n-decane drops originating without surfactant-related stabilization and stirring as in (Chapter 4; Bazilevsky et al. , 2008a).

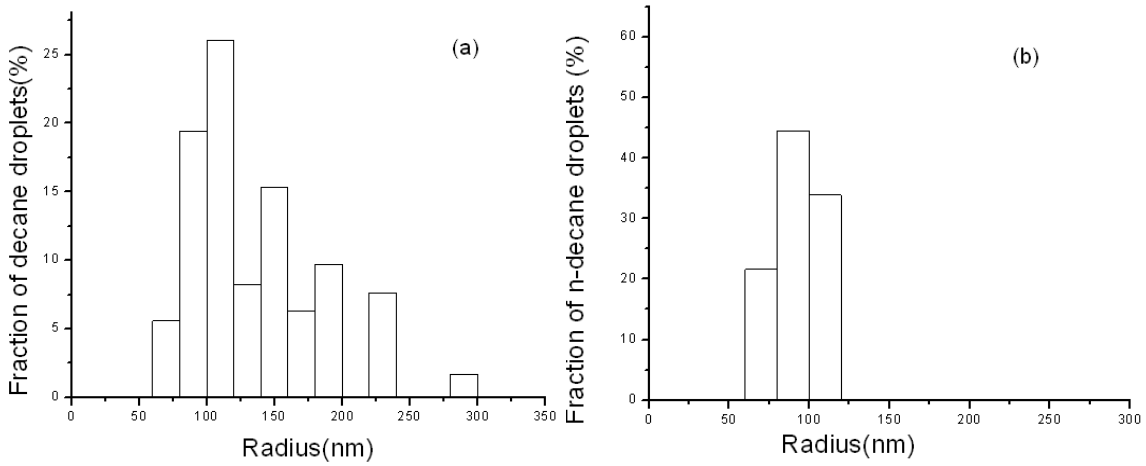

Fig. 5.2. (a) and (b) Droplet-size distributions in n-decane/water emulsions produced by two different nanopore strips. The distributions in (a) and (b) correspond to emulsions produced from two different nanopore strips with a different number of channels and channel-size distributions in two separate experiments.

Formation of PNIPAM nanoparticles

The same nanofluidic setup which was used to form nanoemulsions of n-decane in water was also applied to form PNIPAM nanoparticles. For this purpose, solution C (also containing accelerator for PNIPAM polymerization reaction in n-decane) was released through carbon strips with parallel straight nanopores into a Petri dish filled with solution A (containing NIPAM monomers and initiator in water) as shown in Fig. 5.3. It was expected that as soon as n-decane droplet clusters containing the accelerator supplied through carbon nanopores come in contact with the aqueous solution of NIPAM monomers and the initiator in the bath, polymerization of

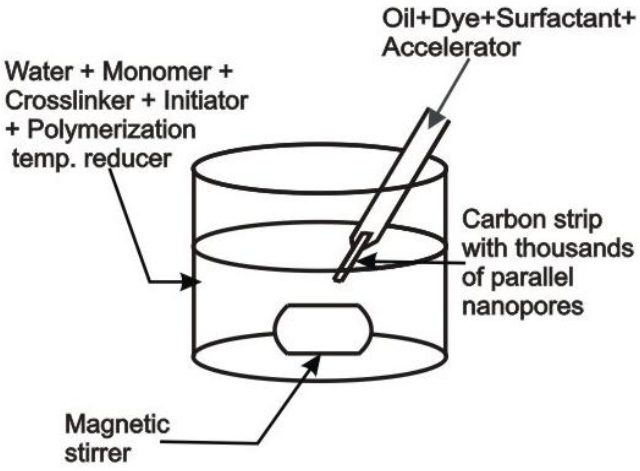

Fig. 5.3. Polymerization of PNIPAM nanoparticles using carbon strip with straight nanopores.

PNIPAM will proceed at the droplet/cluster surface encapsulating n-decane in PNIPAM shell and forming core-shell nanoparticles (Fig. 5.4). If fluorescent dye is supplied in n-decane through carbon nanopores (solutions D is used instead of C), it should also be encapsulated in the nanoparticle core, as well as can probably also diffuse into the shell. It is emphasized that in the case of PNIPAM polymerization, the presence of a stirrer is important, since otherwise the nanopore exits will be clogged by the polymer.

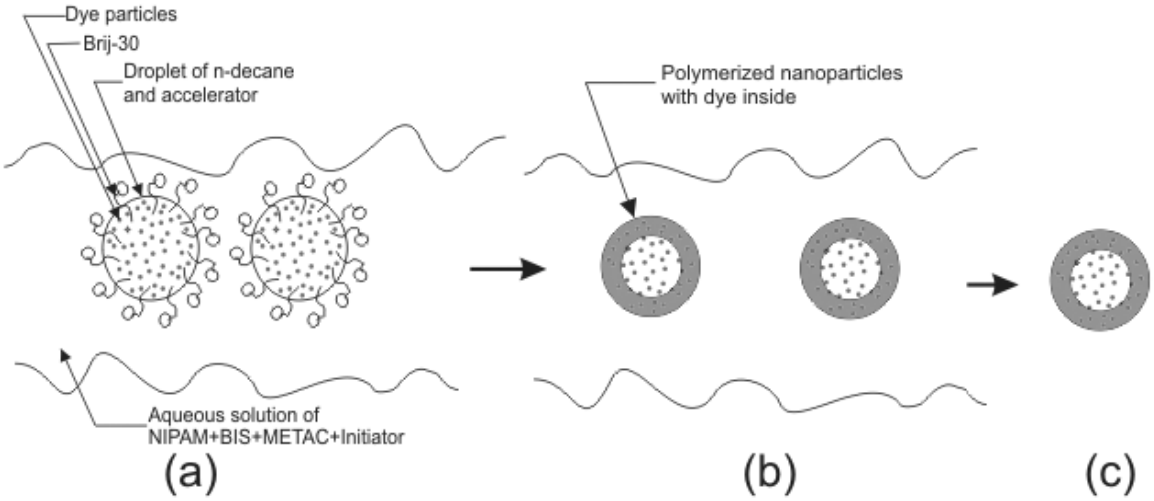

Fig. 5.4. Sketch of formation of PNIPAM nanoparticles. (a) N-decane nanodroplet with dye, surfactant and accelerator delivered into the aqueous solution of NIPAM, BIS, METAC and the initiator. (b) Formation of PNIPAM nanoparticles. (c) Collected PNIPAM nanoparticles after filtration.

For comparison, the polymerization reaction described above was realized first without flow through nanopores, just taking 3 mL of solution A in the bath and adding to it 200 μL of solution C. The resulting blend was shaken manually for 15 min and then rinsed in water (to eliminate the excess of n-decane) and filtered to collect the polymerized PNIPAM particles. The SEM images of the particles formed by this method (without carbon nanopores) demonstrated that they are quite big (of the order of 10 μm). This shows that batch emulsification and polymerization do not allow formation of submicron PNIPAM particles, which led us to employ carbon nanopores as described.

Using flow through carbon nanopores as in Fig. 5.4, solution C was supplied to a bath (Petri dish) filled with solution A for 5 minutes. Then, the aqueous solution was

filtered through a 200 nm filter paper purchased from Cole-Parmer. After that, the filter paper was suspended in water and, as a result, PNIPAM nanoparticles were rinsed from the filter and suspended in pure water. TEM images of the PNIPAM nanoparticles formed using one of the carbon strips with nanopores are shown in Fig. 5.5. These PNIPAM particles are all sub-micron in size. Some of them have a well-defined core-shell structure, whereas some others contain multiple small cores. The existence of multiple cores can be attributed to the preceding droplet clusters.

TEM images similar to the one in Fig. 5.5 cover the area of 0.192×10^{-7} cm^2 and contain in average 24 nanoparticles. TEM grids used to collect samples for such images were disc-like of diameter of 0.3 mm, i.e. their surface area was 0.0707 cm^2. Assuming a uniform distribution of nanoparticles over a grid, we find in average $24\times0.0707/0.192\times10^{-7}=8.84\times10^{7}$ nanoparticles on a grid. These nanoparticles were deposited with a sample of 100 μL extracted from a Petri dish with 100 mL of nanoparticle suspension. Therefore, there should be 8.84×10^{9} nanoparticles in the dish, which were produced in 300 s. This corresponds to the production rate of the order of 2.95×10^{7} nanoparticles per second.

TEM observations can also be used for a rough evaluation of the ratio of core-shell to monolithic nanoparticles produced. Unfortunately, TEM beam cannot be focused too much for observations inside larger nanoparticles (above 400 nm in dia.), since they begin to evaporate. TEM images acquired with smaller nanoparticles show that the ratio of core-shell (including multiple cores) to monolithic nanoparticles is about 5:4 for the optimal surfactant concentration range.

Size distribution of PNIPAM nanoparticles produced while releasing solutions C or D through carbon strips with nanopores into a bath filled with solution A were analyzed using dynamic light scattering and found to be log-normal (Fig. 5.6). The radii of PNIPAM nanoparticles belong to the range 50-300 nm, which are quite comparable to those in the image in Fig. 5.5. The observed polydispersity of PNIPAM nanoparticles is partially rooted in the size distribution of the nanopores in the carbon strips[35]. The largest particles in the radius range of 450-600 nm are most probably formed via clustering of the preceding n-decane droplets.

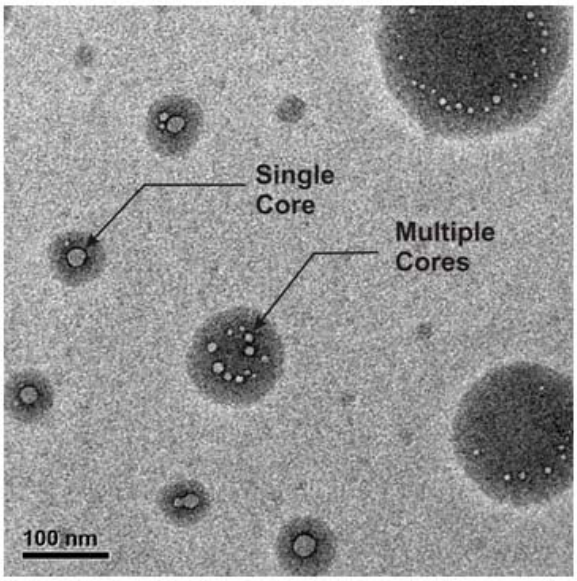

Fig. 5.5. TEM images of dye-containing PNIPAM nanoparticles (produced by releasing solution D through carbon nanopores into a bath filled with solution A).

As a control, dynamic light scattering of DI water, which had been used to rinse out the polymer nanoparticles from the filter paper, was conducted. It was found that DI water contains impurities of 30 nm radius, which are clearly distinguishable from PNIPAM nanoparticles in Fig. 5.6 (the less-than 50 nm range is not included in Fig. 5.6).

In Fig. 5.5 some nanoparticles are quite small (radius ~25 nm). However, their texture is similar to that of the bigger particles in the image, so these smallest nanoparticles are most probably not the impurities and consist of PNIPAM.

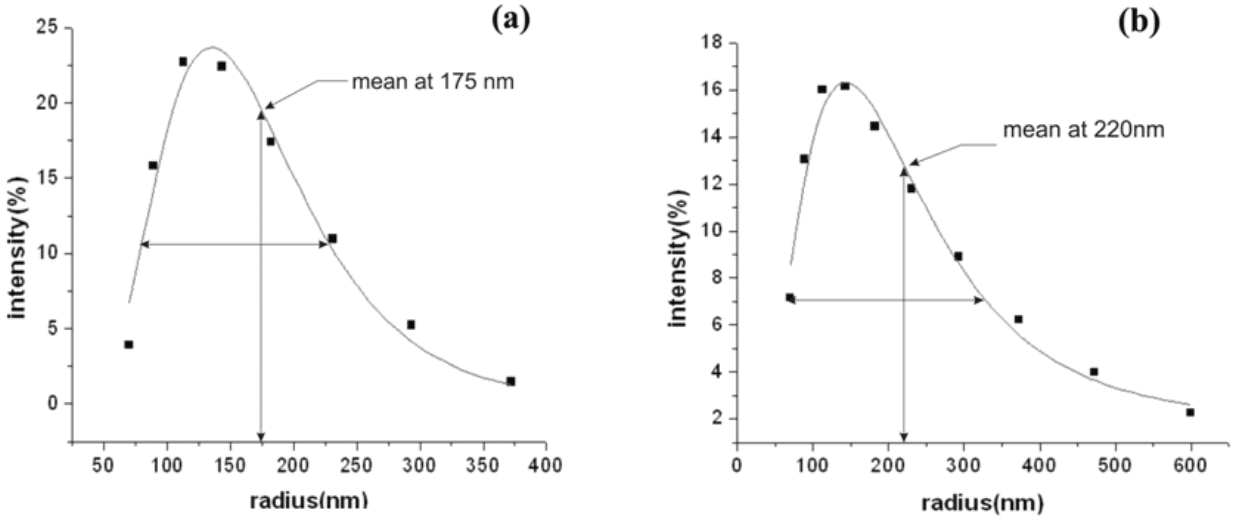

Fig. 5.6. Size distributions of PNIPAM nanoparticles (formed using two different carbon strips with nanopores) obtained using dynamic light scattering. Symbols show the experimental data, lines - the corresponding log-normal distributions fitted using Originpro 7.5 software. The mathematical expectation and variance in (a) are μ_m=175 nm and σ=75 nm, respectively; in (b) μ_m=220 nm and σ=136 nm, respectively. The distributions in (a) and (b) correspond to nanoparticles produced from two different nanopore strips with a different number of channels and channel-size distributions in two separate experiments.

To estimate the nanoparticle production rate, consider the mechanism of nanoparticle formation. As the solution of n-decane, surfactant and accelerator is supplied through carbon nanopores, it breaks up into tiny droplets, which almost immediately form bigger clusters as discussed above. The clusters are in contact with the bath filled with

solution of NIPAM, BIS, METAC and APS in water. Therefore, polymerization reaction begins at the n-decane cluster surface. Due to the diffusion supply, the polymerized layer widens outward and inward the cluster. The reaction can be stopped when all n-decane is squeezed from a cluster by polymerized PNIPAM and a monolithic nanoparticle is formed, or the polymerized shell has become so thick that the diffusion-driven reagent supply is practically disrupted, and thus an n-decane-filled or hollow PNIPAM nanoparticle is formed. In such a process, the number of nanoparticles formed is equal to the number of n-decane clusters. If we assume that the cluster size roughly corresponds to that of a PNIPAM nanoparticle replacing it (even though some PNIPAM deposition has been in the outward direction), then the average cluster volume V_c can be evaluated, for example, from Fig. 5.6, which yields $V_c=22.4\cdot10^{-15}$ cm^3. The supplied volume V of solutuion of n-decane, surfactant and accelerator increases linearly in time t (Bazilevsky et al., 2008a), with V/t~1 nL/s. Therefore, the frequency of nanoparticle production is estimated as $\nu=V/(tV_c)$, which yields $\sim10^7$ nanoparticles per sec, which is quite high in comparison to the production rate ($10^2-10^3\,\mathrm{sec}^{-1}$) described in Ref. (Mathiowitz et al., 1997).

Thermo-responsive dye release from PNIPAM nanoparticles

In the experiments with dye release from PNIPAM nanoparticles suspended in DI water in Petri dish, several different stages can be recognized. In experiment I, stage (i) is the immersion stage (5 min) when nanoparticles had been suspended in water at room temperature of about $T_\infty = 25$ °C, and swelled due to their "elastic diffusion" into water and released dye in parallel. The notion of "elastic diffusion" was introduced in the

seminal work of Tanaka et al. (Tanaka et al., 1979) In the present context the "elastic diffusion" is discussed in section 5.4. Stage (ii): the heating stage (6 min) when the surrounding temperature was instantaneously increased to $T_\infty = 65$ °C. Stage (iii): the cooling stage when the surrounding temperature has been reduced to $T_\infty = 25$ °C once again for 12 min. Stage (iv): the second heating stage at $T_\infty = 65$ °C for 6 min. At each stage, once or twice 200 μL samples were taken from the Petri dish (1.7 mL) without replenishment for fluorescence measurement, to evaluate the amount of dye released. The number of nanoparticles in the dish is enormous and they are inevitably uniformly distributed through its volume. When the release rate is constant, sampling without replenishment does not affect concentration reading. On the other hand, when the release rate decreases at the end of the process, this can introduce an additional inaccuracy in the readings. In experiment II, the immersion stage (i) at the room temperature lasted for 7 min. It was followed by the heating stage at $T_\infty = 65$ °C for 7 min, then by the cooling stage (iii) at the room temperature for 14 min, and then, by a succession of one more heating (iv) ($T_\infty = 65$ °C for 7 min) and cooling (v) (at the room temperature for 7 min) stages.

The experimental data for both experiments are presented in Fig. 5.7.

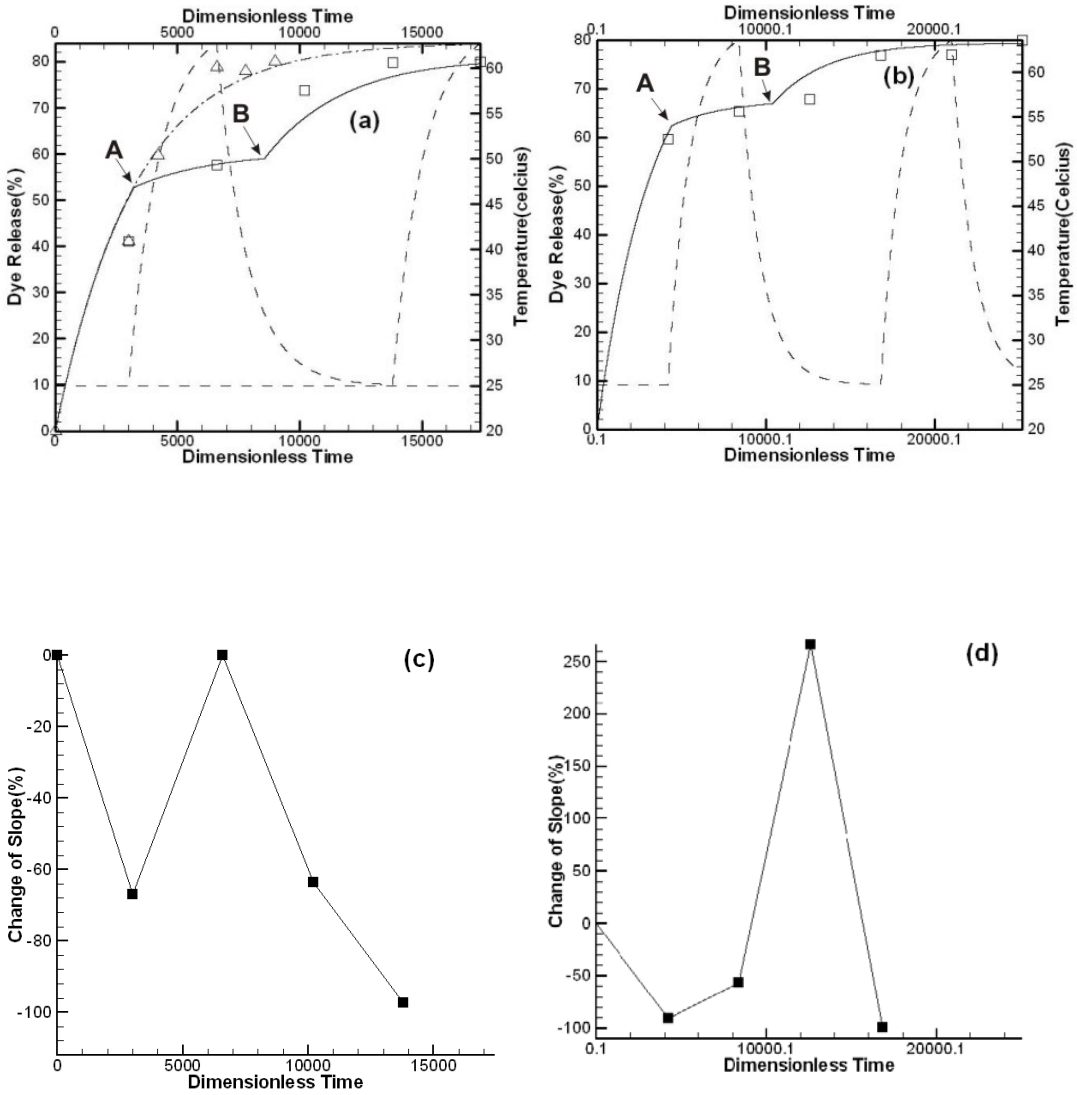

Fig. 5.7. (a) and (c) Experiment I. (b) and (d) Experiment II. The experimental data is depicted by symbols in (a) [squares for the non-isothermal experiment, whereas triangles show data for an isothermal experiment for comparison] and (b) [squares for the non-isothermal experiment]. Solid lines in (a) and (b) present the theoretically predicted release history in the non-isothermal experiments. The dashed-dotted line in (a) shows the prediction for the isothermal case. The dashed lines in (a) and (b) depict the thermal history. Point A corresponds to the moment when temperature exceeds LCST=32 °C and

point B –to the moment when temperature decreases below 32 °C. Time is rendered dimensionless by $\tau_{swelling}$= 0.1 s**.** In (c) and (d) only experimental data is shown.

The theoretical model described in section 5.4 was used for comparison with the experimental data in Fig. 5.7. In the simulations described below, in accordance with the experimental procedure, a three-stage process was considered: immersion, heating and cooling. The particle radius at every stage was rendered dimensionaless by the initial radius at that stage. In addition, equilibrium particle sizes should be determined for T<LCST and T>LCST and the nanoporosity coefficient (Srikar et al., 2008) at room temperature α_0 found. This was done as described in section 5.4. The results depicted in Fig. 7 correspond to the interplay of three simultaneous processes, desorption(Srikar et al., 2008) with $\tau_{desorption} \approx$ 400 s, swelling/shrinkage with $\tau_{swelling} \approx$ 0.1 s, and heating/cooling with $\tau_{heating} \approx 115$ s. Therefore, swelling/shrinkage of PNIPAM nanoparticles can be considered almost instantaneous compared to dye desorption and heating/cooling of water in Petri dish, as it might be expected for microgels. As a result of the interplay of only two processes (dye desorption and heating/cooling), the rate of dye release abruptly changes in concert with heating/cooling cycles, which is manifested by salient points in the dependence of Dye Release % on time (locations A and B in Fig. 5.7). The following heating/cooling cycles have a lesser effect on the release curve, since a significant amount of dye had already been released from the nanoparticles. It can be seen from Fig. 5.7 that the agreement of the predictions with the experimental data is good.

The established value of the characteristic desorption time of PNIPAM/dye pair $\tau_{desorption} \approx$ 400 s can be used to evaluate the corresponding desorption enthalpy(Srikar et al., 2008) E. Since $\tau_{desorption} \sim L^2/D_{eff}$, where L is the characteristic nanopore length, taking L~300 nm, we evaluate that $D_{eff} = 2.25 \times 10^{-12}$ cm^2/s corresponds to $\tau_{desorption} \approx 400$ s. The dye desorption rate is given by (Srikar et al., 2008)

$$k_0 \exp(-E/RT) = \rho_p 2aD_{eff} / D_w \delta \qquad (5.2)$$

With $D_w = 10^{-5}$ cm^2/s for the diffusion coefficient of dye in water, ρ_p =1.386 gm/cm^3 for the polymer density, $2a = 10^{-8}$ cm for the molecular size, and the nanopore diameter δ=10 nm, the desorption enthalpy E for PNIPAM/dye pair is evaluated as E=31.411 kJ/mol. For comparison, according to Ref. 44 for the polycaprolactone/dye pair E=37-38 kJ/mol, whereas for polymethyl methacrylate/dye pair E=45-46 kJ/mol.

5.4 Theoretical Model

Swelling/shrinkage of PNIPAM particles

Understanding of thermally controlled dye release from PNIPAM nanoparticles involves evaluation of the "elastic diffusion" coefficient introduced in the seminal work of Tanaka (Tanaka et al., 1979). For a spherical particle, its swelling/shrinkage in water is given by the following expression (Tanaka et al., 1979)

$$\frac{a(t)}{a_{eq}} = 1 - \frac{6}{\pi^2}\left(1 - \frac{a_0}{a_{eq}}\right)\sum_{n=1}^{\infty}\frac{\exp\left(-\pi^2 n^2 tD / a_{eq}^2\right)}{n^2}, \qquad (5.3)$$

where a denotes the particle radius, t denotes time, n is integer, subscript eq denotes an equilibrium value of the radius corresponding to a certain temperature, while subscript 0 denotes the initial value. The "elastic diffusion" coefficient D is defined as

$D=(K+4\mu/3)/f$, where K and μ denote, respectively, the bulk and shear modulus of PNIPAM network, and f is the coefficient of friction between the network and the fluid (water) medium.

The observations of swelling/shrinking PNIPAM particles in water allow for evaluation of the value of D. However, it cannot be done directly with nanoparticles. There is no indication that swelling/shrinkage behavior of particles with sizes of the order of $d_m=10^{-2}$ cm is physically different from that of the nanoparticles with $d_n=10^{-5}$ cm, which makes macroscopic particles a useful observation tool (Cho et al., 2008). The characteristic times are definitely different, as $(d_n/d_m)^2<<1$, as it is expected from the macroscopic Tanaka's theory. That is the reason that microgels and nanogels are so attractive compared to hydrogels. No significant deviations from the continuum-like behavior are observed in multiple situations encountered in micro- and nano- fluid mechanics, heat and mass transfer, electrohydrodynamics and micro-elasticity (Reneker et al., 2007; Theron et al., 2001; Zussman et al., 2003; Bazilevsky et al., 2008a; Cho et al., 2008; Yarin et al., 2007). Therefore, to evaluate D, macroscopic PNIPAM spheres were prepared by dripping solution E into solution A by an injection syringe. After the formation of PNIPAM spheres, water was added to dilute the suspension. Then, a portion containing several PNIPAM spheres was taken into a Petri dish and observed under optical microscope. An example of the observed PNIPAM spheres is shown in Fig. 5.8. It was found that larger spheres possessed, in fact, a core-shell structure (as is the case of sphere 1 in Fig. 5.8). On the other hand, smaller spheres consisted of monolithic PNIPAM, as, for example, sphere 2 in Fig. 5.8. The observed swelling of the smaller monolithic spheres is depicted in Fig. 5.9. The diffusion coefficient D was evaluated for

a number of PNIPAM spheres fitting Eq. (5.3) to the data as in Fig. 5.9. It was found that $D \sim 10^{-6}$ mm^2/s (Fig. 5.10). This value of D is used in the evaluations of dye release from PNIPAM nanoparticles in the following section. In the observations of swelling behavior of macroscopic spheres in the experiments to determine D, it was found that a_0/a_{eq} varies in the range 0.9-0.95. Therefore, in the simulations described below, the value of a_0/a_{eq} =0.925 was used.

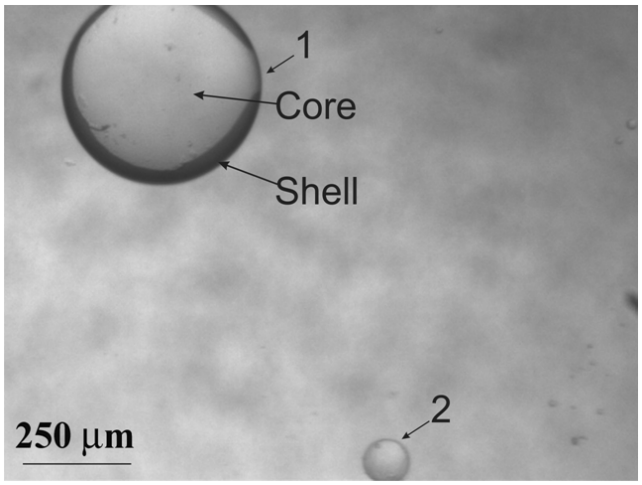

Fig. 5.8. Macroscopic PNIPAM spheres observed for determining the "elastic diffusion" coefficient D.

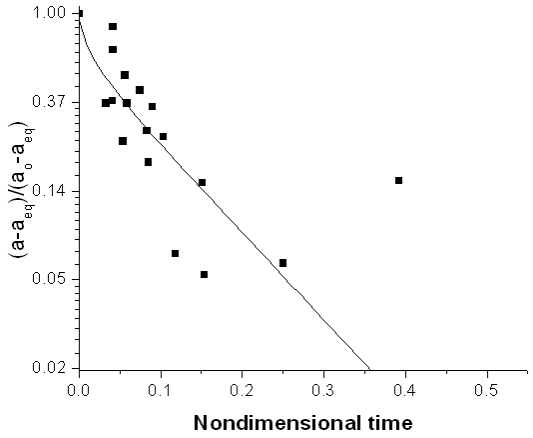

Fig. 5.9. Swelling dynamics of monolithic PNIPAM sphere brought in contact with water at room temperature. The experimental data is presented by symbols, the curve corresponds to Eq. (5.3). The nondimensional time is defined as tD/a_{eq}^2.

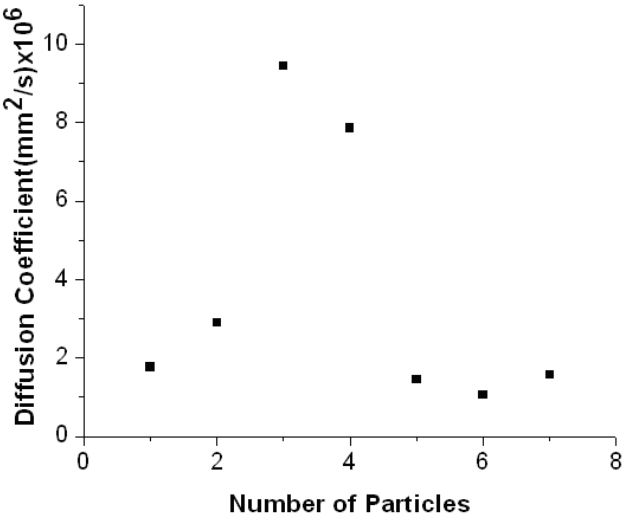

Fig. 5.10. Elastic diffusion coefficient D obtained for several macroscopic PNIPAM spheres.

Dye release model

The recent works (Srikar et al., 2008; Gandhi et al., 2009)demonstrated that dye/drug release from polymeric nanostructures is limited by dye/drug desorption from

nanopore surfaces. The release rate is given by the following expression(Srikar et al., 2008)

$$\frac{d}{dt}\left(\text{Dye Release \%}\right) = \frac{\pi^2}{8\tau_{desorption}}\alpha_0 \frac{S}{S_0}\exp\left(-\frac{\pi^2}{8\tau_{desorption}}t\right), \tag{5.4}$$

where S denotes specific surface area of the nanopores in a nanoparticle; $S=S_0$ at t=0; and the nanoporosity coefficient(Srikar et al., 2008) α_0 at time t=0 is a physical characteristic of nanoparticles determined by their formation process. The characteristic dye/drug desorption time(Srikar et al., 2008) $\tau_{desorption} \sim L^2/D_{eff}$, where L is the characteristic nanopore length and the effective diffusion coefficient $D_{eff}=D_w\delta k_0/(2\rho_{sp})\exp(-E/RT)$ with D_w being the dye/drug diffusion coefficient in the surrounding medium, ρ_{sp} the surface density of polymer at the nanopore surface, and δ the nanopore diameter. The pre-exponential factor, k_0, and the desorption enthalpy, E, characterize the intermolecular forces binding the admixture (dye/drug) molecules on the polymer surface in presence of the surrounding media, i.e. water; R is the absolute gas constant. Therefore, $\tau_{desorption}$, k_0 and E manifest the chemical nature of PNIPAM-admixture interactions responsible for sorption-desorption processes in the presence of water.

Denote the nanopore concentration inside nanoparticles as ν. Then, the nanoparticle porosity $m=\pi\delta^3\nu/6$. The surface area of nanopores is given by $S=\pi\delta^2\nu=6m/\delta$. On the other hand, $m=1-(a_p/a)^3$ where a_p is the volume-equivalent radius of the polymeric content of a nanosphere. Therefore,

$$\frac{dS}{dt} = \frac{18a_p^3}{a^4(t)\delta}\frac{da}{dt}, \tag{5.4}$$

At the very beginning of the process t=0, and (Dye Release %)=0, $S=S_0$, $a=a_0$. On the other hand, beginning from any moment $t=t_{change}$ when the surrounding temperature

has been changed, Eqs. (B1) and (B2) are solved using the initial conditions at $t=t_{change}$: (Dye Release %)=(Dye Release %)$_{change}$, $S=S_{change}$, where the values at $t=t_{change}$ were calculated at the preceding stage.

The surrounding temperature T varies as

$$T = T_\infty + (T_{change} - T_\infty)\exp[-(t - t_{change})/\tau_{heating}], \quad (5.5)$$

where $\tau_{heating}=\rho_w c_w V_P/(hS_P)$, with ρ_w and c_w being water density and specific heat, V_P and S_P are the volume and surface area of water in the Petri dish where the dye release experiment is conducted, and h is the heat transfer coefficient. Naturally, at t=0, the initial temperature $T=T_{change}=T_0$. The surrounding air temperature is denoted by T_∞. In the experiments described below, $\tau_{heating} \approx 115$ s.

The equilibrium radius of PNIPAM nanoparticles is given by the following expression

$$a_{eq}(T) = a_{below} + (a_{above} - a_{below})H(T - LCST), \quad (5.6)$$

where $H(\cdot)$ denotes the Heaviside step function, a_{below} denotes the equilibrium nanoparticle radius at T<LCST, and a_{above} – at T>LCST.

The characteristic swelling/shrinkage time of PNIPAM nanoparticles is of the order of $\tau_{swelling} \sim (2a)^2/D$. With $a \sim 300$ nm and $D \sim 4 \cdot 10^{-6}$ mm^2/s, we find that $\tau_{swelling} \sim 0.1$ s.

Swelling/shrinkage ratio and nanoporosity coefficient

The equilibrium particle sizes can hardly be evaluated using nanoparticles suspended in liquid, since they are invisible in optical microscopes. Observations were done with a macrscopically large cylindrical specimen (Fig. 5.11) of the same material formed by adding 300 μL of solution C to 3 mL solution of A. The top and side views of

the cylindrical PNIPAM specimen in the images in Figs. 5.11a and d were taken at room temperature. Then the specimen was transferred into a larger vial and submerged in water. After that, heating was started. During the heating process the cylindrical specimen could change its shape freely similarly to PNIPAM nanoparticles suspended in water. For two hours the specimen was sustained at T>LCST, which guaranteed that an equilibrium shape at the elevated temperatures had been achieved. Then the specimen was extracted from the vial and the images in Fig. 5.11b and e were taken. After that, the warm water inside the vial was replaced by water at room temperature and the cylindrical specimen was submerged in it for two hours at T<LCST. In that way the specimen retained its equilibrium shape corresponding to T<LCST. Then, it was extracted once again and the images in Figs. 5.11c and f were taken. The images in Fig. 5.11 allowed evaluation of the values of the volume-equivalent radii for each stage. In particular, the average values of a_0, a_{above} and a_{below} were found. The corresponding radii ratios were $a_{above}/a_0=0.8$ for the first heating stage (shrinkage) and for the following heating/cooling transition (swelling) it was $a_{cooling}/a_{heating}=1.3$. These values were used in the calculations with the nanoparticles.

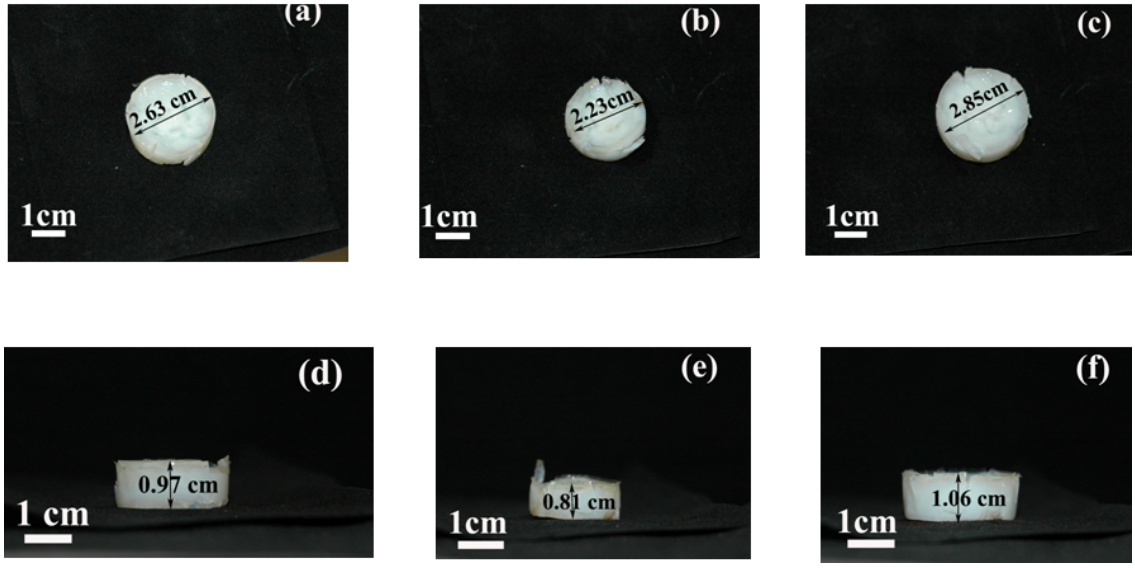

Fig. 5.11. Top and side views of cylindrical PNIPAM specimen at room temperature (a and d), at T>LCST (b and e), and at T<LCST (c and f).

An additional parameter required for the calculations is the nanoporosity coefficient at room temperature α_0. To determine it in a separate experiment, we used release profile from a cylindrical specimen similar to the one in Fig. 5.11, which was formed by adding solution D to solution A. The dye release profile was obtained at room temperature (Fig. 5.12) and revealed the value of $\alpha_0 \approx 0.8$. This value signifies the proportion of dye molecules which are exposed to the surrounding water in contact with nanopore surfaces in the macroscopic specimen. As it was shown in (Srikar et al., 2008), saturation of the release process below 100% means that the release process is desorption-limited: dye is released from the nanopore surfaces, whereas the dye embedded in the polymer bulk cannot be released. The same value of $\alpha_0 \approx 0.8$ is expected in the nanoparticles (cf. Fig. 5.7).

The characteristic desorption time corresponding to the release profile in Fig. 5.12, is 90 min (Srikar et al., 2008). In nanoparticles the nanopore length L~300 nm. The characteristic desorption time $\tau_{desorption}$ decreases as L^2 (Srikar et al., 2008), and thus using desorption times for L=1μm found in (Srikar et al., 2008) , we can estimate that in the present case the desorption time for the nanoparticles is $\tau_{desorption} \approx 400$ s.

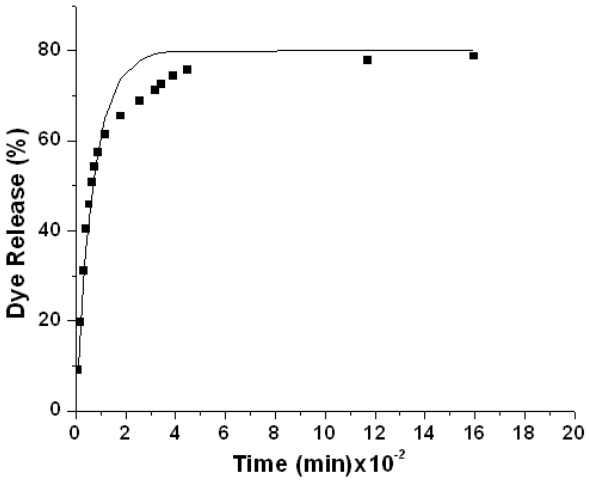

Fig. 5.12. Dye release profile from a macroscopic cylindrical specimen of PNIPAM. The experimental data are shown by symbols, the theory of (Srikar et al., 2008)-by the curve.

An additional parameter needed to be specified in the calculations is the ratio $\varsigma = (a_p / a_{eq})^3 / \left\{1 - \left[(a_p / a_{eq})/(a_0 / a_{eq})\right]^3\right\}$ which is related to the nanoparticle porosity. Its value is mostly determined by the fact that the original aqueous solution which was used, had 15.5 wt% of NIPAM. The corresponding initial value of the ratio ς was estimates as 1.15. At the following stages, this value was updated according to the variation of a_0 for them.

5.5 Conclusion

Nanofluidic polymerization reactor based on parallel arrays of thousands of macroscopically long straight carbon nanopores allows formation of rather monodisperse PNIPAM particles of about 400 nm dia. at a rate of 10^7 nanoparticles per sec. The nanoparticles were loaded with fluorescent dye, and thermally stimulated dye release was demonstrated experimentally, with release rate being controlled by the surrounding temperature. The desorption enthalpy of dye from PNIPAM was evaluated as E=31.411 kJ/mol. It was shown that swelling/shrinkage of PNIPAM nanoparticles can be considered as almost instantaneous compared to dye desorption and heating/cooling of water in Petri dish. As a result, dye release process can be viewed as an interplay of only two processes - dye desorption and heating/cooling.

6. RESINS WITH "NANO-RAISINS"

6.1 Introduction

Thermosensitive hydrogels are materials which globally shrink/swell in water when the surrounding temperature crosses the lower critical solution temperature (LCST). A novel class of cross-linked polymeric materials, which do not shrink/swell in water globally, but nevertheless reveal a hydrogel-like, stimuli-responsive behavior, was developed by Dr. D. Placke. For nano-scale observations, these fibers were stained with copper by Ms. Yiyun Zhang. Using the stained samples, the present author applied transmission electron microscopy and energy dispersive X-ray analysis and found, as predicted in Yarin (2008), nanogel "raisins" dispersed in such materials (e.g., polymer nanofibers). Shrinkage of individual nanogel "raisins" at elevated temperatures increases nanoporosity via increased exposure of the existing nanopores to water, or formation of new nanopores/nanocracks in the overstretched polymer matrix in the vicinity of shrinking nanogel "raisins". As a result, the release rate of the embedded dye from the nanofibers increases at elevated temperatures. It has been suggested that similar functional materials with embedded nanogel "raisins" will find applications in nanofluidics and as drug carriers for controlled drug release (Yarin 2008).

In Section 6.2 the experimental methods are described. The proof of the island-like PNIPAM structures using transmission electron microscopy and energy dispersive X-ray analysis is discussed in section 6.3. Conclusions are drawn in section 6.4.

6.2 Experimental

All TEM observations were made using a JEOLJEM-3010 300KV transmission electron microscope with LaB_6 electron source. For TEM observation, two different TEMgrids were used- a copper (Cu) grid with lacey carbon and a molybdenum (Mo) grid. For energy dispersive X-ray analysis (EDX) in TEM, theMo grid was used in conjunction with a double-tilt holder made of beryllium, whereas the diffraction pattern was determined using the Cu grid in conjunction with a single-tilt holder made of copper. For TEM sample preparation, the nanofibers stained with copper sulfate were sonicated in isopropanol (IPA) using an ultrasonicator before very small drops of IPA with nanofiber fragments were deposited on grids of both types. All the diffraction pattern data were matched with the standard data from JCPDS;International Centre for Diffraction Data.

6.3 PNIPAM Nano-"Raisins" Revealed by Staining, Transmission Electron Microscopy (TEM), and Energy Dispersive X-ray (EDX) Analysis

The results of D. Placke described in Sinha-Ray et al. (2010c) indirectly suggest that PNIPAM might be agglomerated in the mats in the form of "raisins". Staining with copper sulfate (CuSO4) and coordination of Cu^{2+} with PNIPAM, as proposed by Y. Zhang (Sinha-Ray et al., 2010c) makes this polymer visible (and distinct from PAA and PVA) in TEM images. Two different types of holders and grids in TEM were used due to the following reasons. The nanofibers were stained with copper coming from copper sulfate ($CuSO_4$). Using EDX to prove unambiguously the existence of copper stained "raisins" in nanofibers alone, one needs to avoid any signal of copper coming from the

grid and holder, which can be a source of a false signal. Therefore, a molybdenum (Mo) grid was used with a double-tilt holder made of beryllium for determining EDX. However, the double-tilt holder had an insufficiently tight fixture and itwas hard to focus the electron beam on a single “raisin” to obtain the diffraction pattern. Therefore, a Cu grid was used with a single-tilt holder to obtain the diffraction pattern.

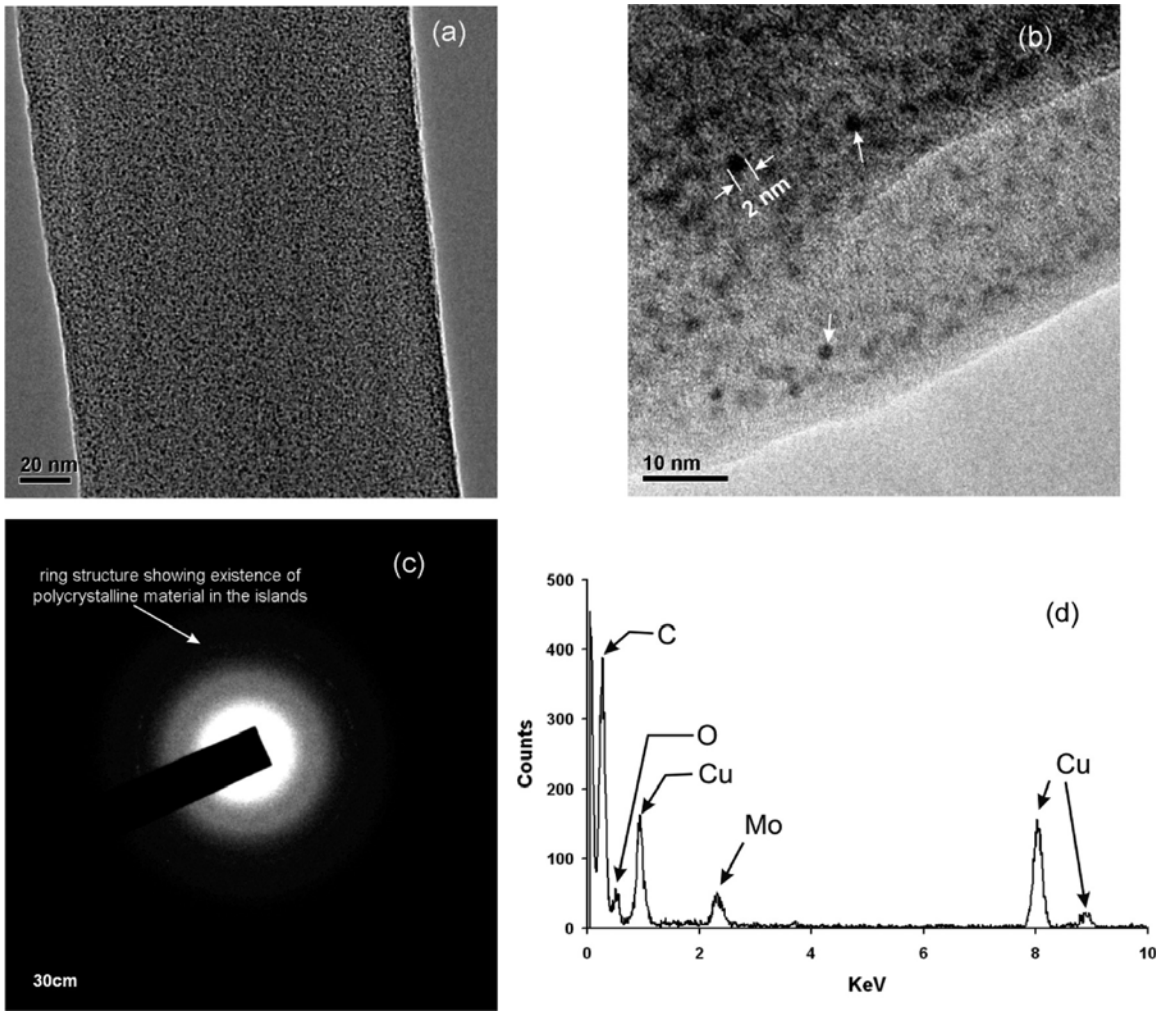

Fig. 6.1. PNIPAM “raisins” in nanofibers. (a) TEM image of a single nanofiber. (b)Azoomed-in area of the nanofiber shown in part a. The black “raisins” shown by arrows are of the order of 2 nmin diameter. (c)Diffraction pattern obtained from one of

the “raisins”, which proves unequivocally the presence of a crystalline material. Moreover, the ring sharpness reveals crystals different from possible polymer crystallininty, since the latter is short-range and random, which would result in an integrated diffusive ring unlike the one in the image, which is characteristic ofmetals (in this case). The value of 30cmin the image indicates the camera distance required to measure the d-spacing. (d)EDX spectrum obtained from a nanofiber with “raisins”,which shows the presence of Cu. The peak of Mo arises from the TEM grid made of Mo and used for EDX.

The nanofiber samples were studied using TEM revealed identical structures. A set of representative images is shown in Fig. 6.1 a, b. The overall view of a single nanofiber in Fig. 6.1a reveals black dot-like objects. Zooming-in (Figure 6.1b) showed that these objects are “raisins” of about 2 nm in diameter. These “raisins” are expected to be PNIPAM islands stained by Cu from $CuSO_4$. To prove that, diffraction pattern of the “raisins” was studied. An example of the diffraction pattern is depicted in Fig. 6.1c. For several such images the d-spacing corresponding to the sharp crystalline ring was measured using the following formula

$$\textit{d-spacing (in } \overset{0}{A}\textit{)= (camera constant} \times \textit{2)/ diameter of the ring in pixel} \qquad (6.1)$$

The corresponding value of the d-spacing was found to be 0.148 nm. This value is close to the d-spacing for cuprite (Cu_2O), where for the (h,k,l) plane the interplanar d-spacing in the (2,2,0) direction is 0.151 nm. The measured value of the d-spacing is also close to the one for cupric oxide (CuO) whose d-spacing of the in the $(\bar{1},1,3)$ direction is 0.15 nm. However, if the island material would be CuO, there should be seen several rings

corresponding to the d-spacing of the $(\bar{3},1,1)$, (1,1,3) and (3,1,1) directions, namely 0.14 nm, 0.138 nm and 0.13 nm, respectively. The absence of these rings suggests that the islands consist predominantly of Cu_2O. The presence of a single ring in Fig. 6.1c corresponding to a single d-spacing suggests that sonication flattened the nanofibers. To prove the presence of Cu on the "raisins", EDX spectra were observed (Fig. 6.1d). The spectra indeed demonstrated a significant amount of Cu on the "raisins".

6.4 Conclusion

The "raisin"-like distribution of PNIPAM in the PAA/PVA/ PNIPAM nanofiber mats corresponds to the structural model (Yarin 2008) and explains the main reason for their lack of shrinkage/swelling behavior compared to that of such ordinary hydrogels as poly-(methyl methacrylate/N-isopropylacrylamide) copolymers developed in (Zhang et al.,2009). The "raisin"-like distribution of PNIPAM in the present case is associated with its low molecular weight and thus an elevated mobility at the annealing temperature. These nano-"raisins" alone are sufficient for positive thermoresponsive dye release according to the mechanism proposed in (Yarin 2008). Namely, contraction of these "raisins" at elevated temperatures results in elastic stresses and strains in the surrounding material, which can lead to nanocracking. The latter brings more dye in contact with water and facilitates dye release in those areas. This is indirectly corroborated by the positive thermosensitivity observed experimentally. The nanofiber mats studied in this work represent a novel class of resins with nano hydrogel "raisins". Bulk materials of this type can also be obtained.

7. MELTBLOWING: BASIC PHYSICAL MECHANISMS AND THREADLINE MODEL

7.1 Introduction

Meltblowing is an aerodynamically-driven process, in which polymer jets are accelerated and stretched by high speed gas streams (planar or axisymmetric, in general non-isothermal, subsonic turbulent jets). The aerodynamics of the mean flow in such jets is fairly well understood in the framework of the classical semi-empirical turbulence models (Reneker et al., 2007; Pai 1954; Abramovich 1963) and will be accounted for in the theoretical approach developed below.

The present work is devoted to basic physical mechanisms responsible for meltblowing. To concentrate on the aerodynamic forces and the corresponding small (linearized) bending perturbations, a model situation of blowing of a solid, non-stretchable and flexible threadline is treated here. Meltblowing of polymer jet under isothermal and non-isothermal conditions with the account for polymer viscoelasticity and large (finite) perturbations is tackled in the following description. Section 7.2 describes model experiments with solid flexible threadlines with the goal to elucidate the important physical aspects relevant in the context of meltblowing. In particular, we elucidate experimentally the peculiarities of turbulent fluctuations transmitted to the threadline where they result in visible bending perturbation. Propagation of these perturbations over the threadline is also studied in the experiments of Section 7.2, which reveal a blow-up flapping region. A linearized theoretical model dealing with propagation of small bending perturbations over threadlines is given in Sections 7.3. Some comments

on comparison of the theoretical predictions with the experimental data for threadlines are given in Section 7.4. Conclusions are drawn in Section 7.5.

7.2 Experiments with Flexible Threadlines

A sketch of the experimental setup is shown in Fig. 1. It consists of a compressed gas (nitrogen at 25-40 bar) cylinder used to create blowing jet. High pressure tubing led to the nozzle (500 μm inner diameter) issuing the gas jet. A sewing threadline (mean diameter 110 μm, straightened by ironing before the experiments) was attached to the nozzle (Fig. 7.1). Blowing was directed downward and the nozzle positioning was adjusted using a moving stage with a ruler relative to the CCD camera which was fixed (Fig. 7.1). An electronic CCD camera (MotionScope-Redlake Imaging Corporation) was used for high speed imaging. It was operated at 500 fps using a shutter speed of 1/8500 – 1/10000 s. When gas was blowing and the threadline was flapping, the high speed imaging was conducted for a number of segments of the threadline. At any new elevation of the threadline suspension point, a delay of 5 mins (sufficient for the transients fading) was adopted before data acquisition at that location. The images recorded with the high speed CCD camera were processed using the interface of MATLAB- R2007A. In addition, an electronic DSLR Nikon D70s camera was used at a very high shutter speed (1/4 – 1/6 s) to record the whole envelope of the flapping threadline at a single still image.

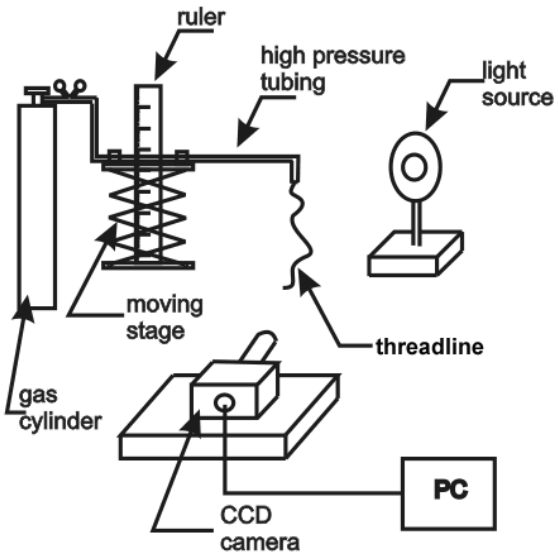

Fig. 7.1. Schematic of the experimental setup.

Gas flows from a high pressure cylinder to open atmosphere (where it comes in contact with polymer jet) through a long uniform pipe of cylindrical cross-section. Pressure drops are of the order of several tens of bars, i.e. we are dealing with an adiabatic compressible gas flow with friction. An approximate theory of such flows in uniform cylindrical pipes based on the compressible Bernoulli equation with friction can be found in Ref. (Yarin 2007) (p. 138) supplemented by standard isentropic formulae for gas flows (Sun et al 2003). The theory reduces to the following three equations

$$\frac{1}{\lambda_1^2}-\frac{1}{\lambda_2^2}-2\ln\left(\frac{\lambda_2}{\lambda_1}\right)=f\frac{2\kappa}{\kappa+1}\frac{L}{d_0} \tag{7.1}$$

$$\frac{p_{01}}{p_2}=\frac{\lambda_2}{\lambda_1}\frac{1}{\left[1-\lambda_2^2(\kappa-1)/(\kappa+1)\right]}\frac{1}{\left[1-\lambda_1^2(\kappa-1)/(\kappa+1)\right]^{1/(\kappa-1)}} \tag{7.2}$$

$$u_2=\left(\frac{2}{\kappa+1}\right)^{1/2}\lambda_2 a_{01} \tag{7.3}$$

In Eqs. (7.1) - (7.3), λ_1 and λ_2 are the velocity coefficients at the pipe entrance and exit, respectively, which are both less than 1 in the subsonic flows we are dealing with, κ is the ratio of the specific heat at constant pressure to the specific heat at constant volume, L and d_0 are the pipe length and cross-sectional diameter, respectively, f is the friction factor, p_{01} is the stagnation pressure of gas in the cylinder, p_2 is the atmospheric pressure, u_2 is the gas velocity at the pipe exit and a_{01} the adiabatic speed of sound in stagnant gas in the cylinder. For the friction factor in smooth pipes, the following expression (the Unwin formula) can be used (Menon 2005)

$$f = 0.0025(1 + 3.6/d_0) \tag{7.4}$$

where the pipe diameter d_0 is taken in inches. In the present case d_0=0.02" and thus f=0.45.

Equations (7.1)-(7.2) define the velocity coefficient at the pipe exit λ_2 through the pressure ratio p_{01}/p_2 for any pipe length. After that Eq. (7.3) is used to find the corresponding gas velocity u_2. As the ratio p_{01}/p_2 increases, the value of λ_2 increases until λ_2=1 is inevitably reached at a certain value of $(p_{01}/p_2)_c$, which corresponds to flow choking. At $p_{01}/p_2>(p_{01}/p_2)_c$ velocity u_2 does not change and is equal to $u_{2c}=[2/(\kappa+1)]^{1/2}a_{01}$.

The predicted exit velocity of gas is plotted in Fig. 7.2 versus pressure difference. The utmost right point of about u_2=310.38 m/s at p_{01}/p_2=47.91 corresponds to chocking. At the pressure ratios $p_{01}/p_2>47.91$ the exit velocity will stay the same u_2=310.38 m/s due to chocking. The experimental data in Fig. 7.2 were acquired using two flow measuring devices: one for the lower pressures $p_{01}/p_2<25$ with a higher accuracy (digital flow meter FMA-5610 from Omega), and another one for the higher pressures $p_{01}/p_2>25$ (Dwyer

Instruments rotameter with a float; with a lower accuracy). The agreement of the predicted and measured velocities is very good practically in the whole range.

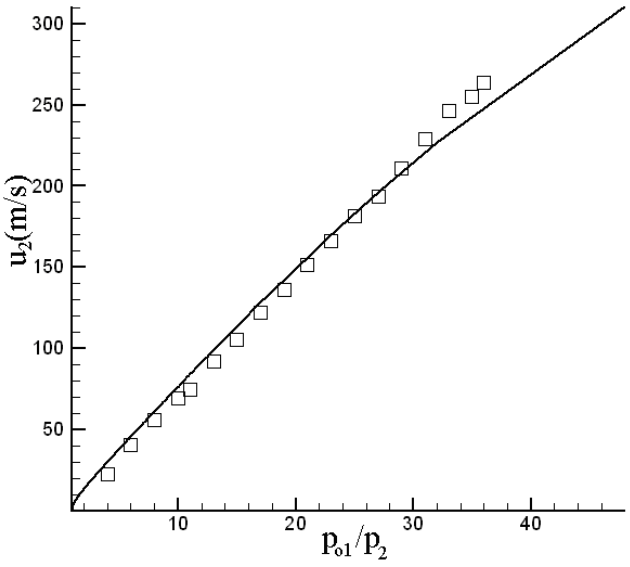

Fig. 7.2. Exit velocity versus pressure ratio for κ=1.4, L/D=3000 and a_{01}=340 m/s. The predicted velocity is shown by the curve, the experimental data-by symbols.

As a basic variant, a L=19.3 cm-long threadline was used with gas blowing at 35 bar (263.9 m/s-Fig. 7.2). The threadline was vigorously flapping under such conditions. The time series for the lateral threadline displacements at two locations are depicted in Fig. 7.3. Two specific positions were chosen for illustration. Figure 7.3-a shows the evolution at x=10.4 cm and Fig. 7.3-b shows the evolution at x=14.82 cm. It is emphasized that the dc part of the lateral displacement caused by a slight uncontrolled tilt of the gas jet axis relative to the vertical was subtracted from the data in Fig. 7.3 using Fast Fourier Transformation (FFT) of the recorded signal.

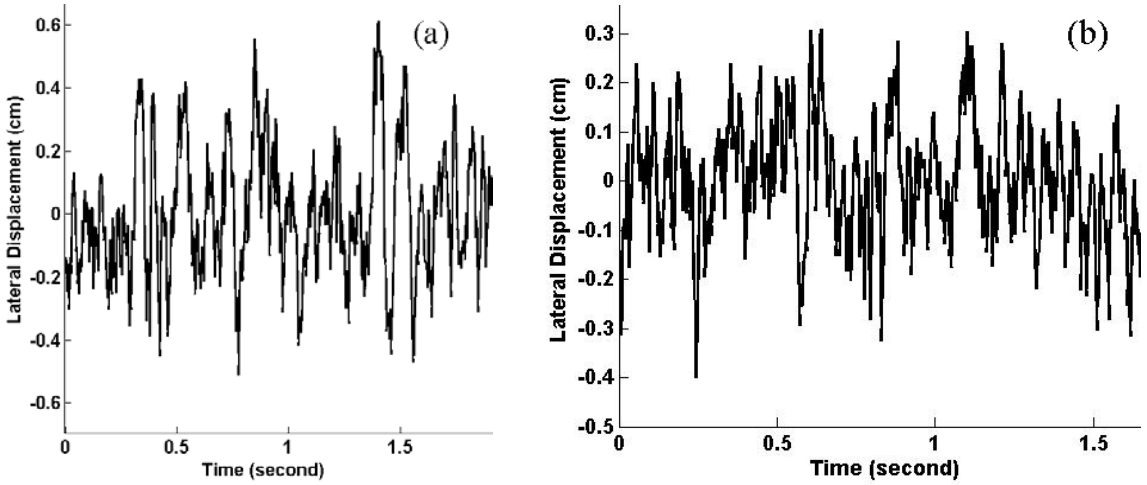

Fig. 7.3. Lateral displacements of the threadline at two locations: (a) x= 10.4 cm and at (b) x= 14.82 cm from the nozzle.

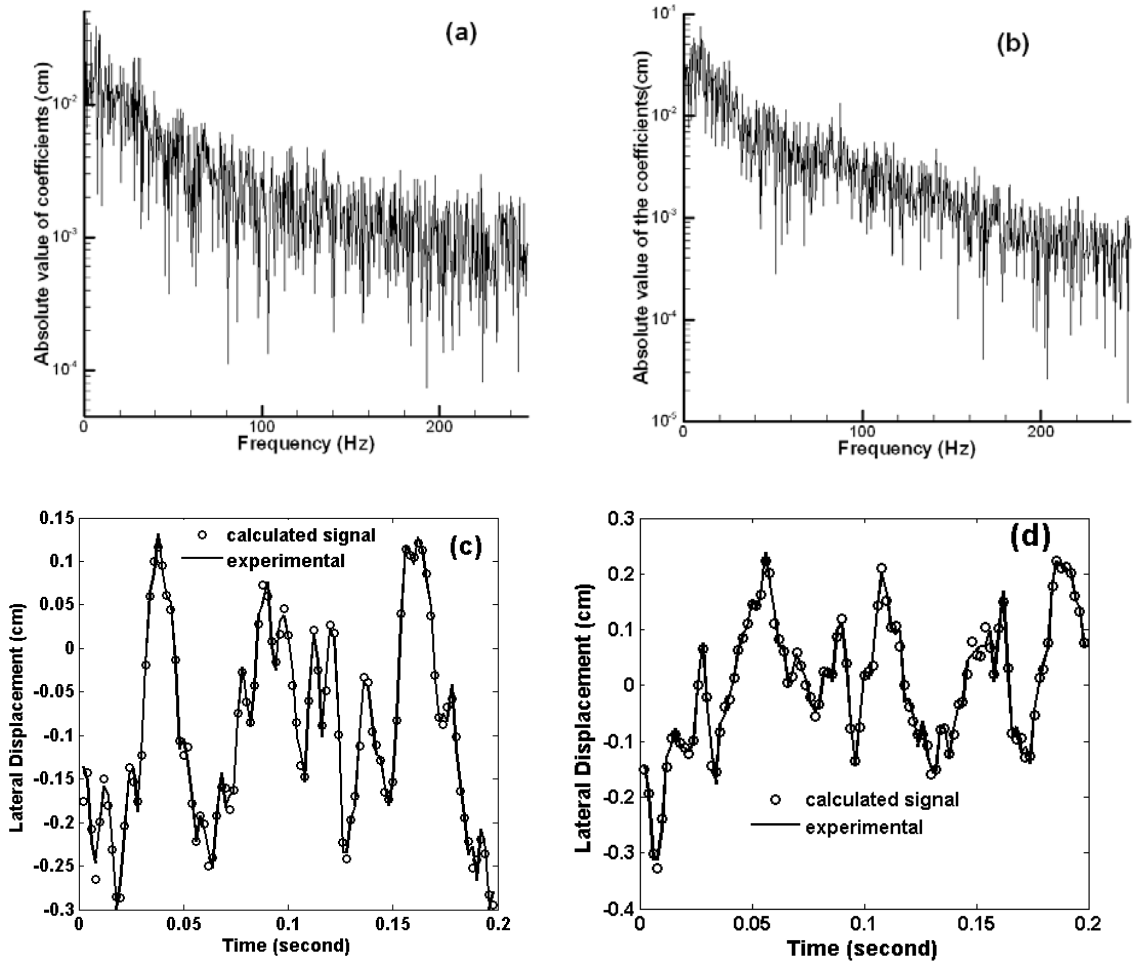

Fig. 7.4. Absolute values of the Fourier coefficients corresponding to the lateral displacement of the threadline at (a) x= 10.4 cm (Fig. 7.3a) and (b) x=14.82 cm (Fig. 7.3b). (c) Lateral displacement at x=10.4 cm reconstructed using the Fourier series with the truncated spectrum. The calculated displacement is shown by symbols, the experimental data by solid line. (d) Same as (c) but at x=14.82.

FFT of the time series for the lateral displacements of the threadline corresponding to the time intervals of 3 s (two shorter sections of the data of about 1.5 s are shown in Fig. 7.3) was done using the corresponding MATLAB routine. The absolute values of the

Fourier coefficients obtained are plotted against frequency in Figs. 7.4a and b. It is seen that the spectral band covered was up to 250 Hz, with the spectrum being continuous. It is emphasized that the recorded signal obtained from the CCD operated at 500 fps, as well as its processing with FFT involving frequencies up to 250 Hz, precluded probing frequencies higher than those in Figs. 7.4a and b (up to 250 Hz). However, a very significant and gradual decrease in the signal amplitudes for the high-frequency harmonics allows one to assume that there are no significant higher frequency modes. Indeed, Figs. 7.4a and b show that above the frequency of about 167 Hz, the Fourier coefficients become negligible compared to those with frequencies less than 167 Hz, and thus, the importance of the whole high-frequency range in the compound signal is expected to be small. This is illustrated in Figs. 7.4c and d where the Fourier series with a truncated spectrum with frequencies less than 167 Hz (and the cut-off of the spectral band with frequencies above 167 Hz) and the corresponding Fourier coefficients from Figs. 7.4a and b are plotted versus experimental data. It is clearly seen that the experimental data are reproduced fairly well in spite of the truncated spectrum.

It is emphasized that the unperturbed threadline is vertical in the experimental setup of Fig. 7.1, i.e. potentially represents itself a kind of a pendulum. The eigenfrequency of the pendulum-like oscillations $\omega_p = (2\pi)^{-1}\sqrt{g/L}$, with g being gravity acceleration and the factor $(2\pi)^{-1}$ included for comparison with the frequency in Figs. 7.4 a and b. Taking the pendulum length within the range $L \approx$ 1-20 cm (since any part of the threadline can be excited), we find $\omega_p \leq 5$ Hz. These are to low frequencies to cause resonances with the oscillations in Figs. 7.3 and 7.4, and thus can be excluded from consideration.

The character of the time series for lateral displacements of the threadline depicted in Fig. 2 can be also elucidated using the corresponding autocorrelation functions. The latter were calculated using standard MATLAB routine and are plotted in Fig. 7.5. It is clearly seen that the autocorrelation function rapidly decays and approaches zero-a clear sign of a chaotic process.

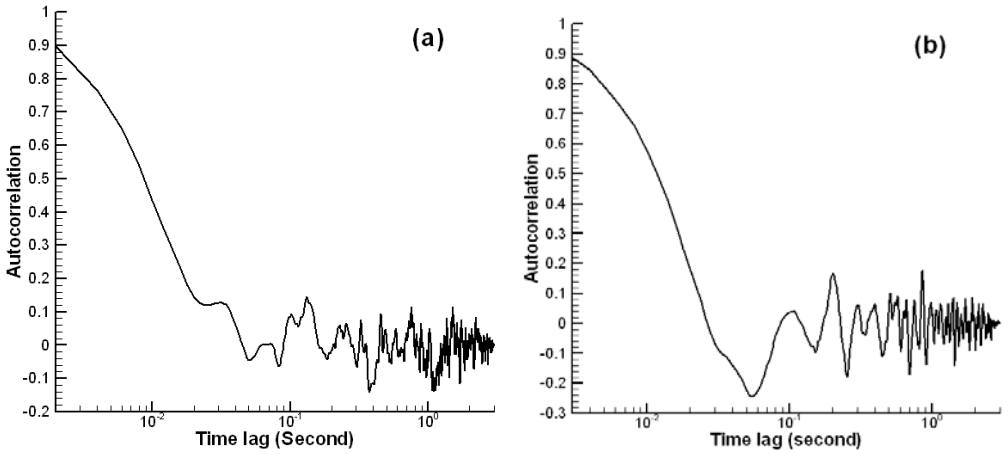

Fig. 7.5. Autocorrelation function for the time series for the lateral displacements of the threadline in Figs. 2a and b at (a) x= 10.4 cm and (b) x=14.82 cm.

The threadline is subjected to turbulent perturbations of the surrounding turbulent gas jet. Denote by $U_g(0)$ the exit velocity of the gas jet, by d_0 the nozzle diameter, and by ν_g the kinematic viscosity of gas. Define the Reynolds number as $Re_d= U_g(0)d_0/\nu_g$. Then, the turbulence Taylor microscale in the axisymmetric gas jet according to (Pope 2000) is equal to $\lambda=1.23Re_d^{-1/2}x$. Take for the estimate $U_g(0)=230$ m/s and $d_0=0.05$ cm. Then, for air $Re_d=7667$. Therefore, at x=1 cm, turbulent eddy scales are of the order of $\lambda=0.014$ cm, and at x=10 cm, they are of the order of $\lambda=0.14$ cm. The corresponding frequencies are of the order of (Pope 2000) $\omega=U_g(0)/\lambda$, which is 10^5-10^6 Hz, well above the frequency band

characteristic of the threadline oscillations (Fig. 7.4). On the other hand, the large eddies in the system gas jet/threadline are of the order of L=10 cm, and their frequencies $\omega=U_g(0)/L$ are 10^3 Hz. This is still significantly higher than the frequency band in Fig. 7.4.

Local interactions of random, high-frequency (compared to those of the threadline) turbulent eddies in gas with massive threadline resembles those responsible for the Brownian motion. In the latter case, multiple simultaneous tiny impacts in different directions produce macroscopic displacement of massive (submicron) particles on time scales much larger than those of the individual impacts. In the turbulence context this idea was developed by G.I. Taylor. In particular, a lateral averaged displacement in time t produced by turbulent eddies is (Pope 2000; Frost 1977) $<A>=[2<v'^2>\tau t]^{1/2}$, where $<v'^2>$ is the correlation of the lateral velocity pulsation and τ the characteristic time scale of large eddies. In turbulent jets all the pulsation velocity components, in particular, v' (lateral) and u' (longitudinal) are of the same order. Thus, $<v'^2>=<u'v'>$. The characteristic time scale of the large eddies is $\tau=\left(\partial u/\partial y\right)^{-1}$, where u is the mean longitudinal velocity component, and y is the lateral coordinate. Therefore, $<v'^2>\tau=<u'v'>/\partial u/\partial y=\nu_t$, where ν_t is the kinematic eddy viscosity which plays here the role of the diffusion coefficient. In axisymmetric turbulent jets the kinematic eddy viscosity is constant over the jet and with a good accuracy is given by (Frost 1977) $\nu_t=0.015U_g(0)d_0$. Turbulent eddies can push a threadline element at a certain location only for the time of the order of the characteristic time τ_r of propagation of a bending perturbation over the threadline (which plays the role of relaxation in this case). After that, the excursion leaves the previous location and propagates along the threadline. Therefore, we can estimate the amplitude of the

threadline lateral displacements as $<A_{threadline}>=(2\nu_t\tau_r)^{1/2}$. The speed of propagation of bending perturbations along a stretched threadline is of the order of $[P/(S\rho)]^{1/2}$, where P is the tensile force in the threadline cross-section, S is the cross-sectional area ($\sigma_{xx}=P/S$ is the longitudinal stress in the threadline cross-section) and ρ the threadline density. Therefore, the characteristic time of propagation of a bending perturbation over a threadline is $\tau_r = L[P/(S\rho)]^{-1/2}$. The tensile forces P is evaluated as $q_\tau L$ where q_τ is the longitudinal air drag imposed on the unit length of the threadline. An appropriate expression for the drag force is given by Refs. (Ziabicki 1976; Ziabicki et al 1985) as

$$q_\tau = 0.65\pi a_0 \rho_g U_0^2 \left(\frac{2U_0 a_0}{\nu_g}\right)^{-0.81} \tag{7.5}$$

where ρ_g and ν_g are the gas density and kinematic viscosity, U_0 is the gas velocity relative to the unperturbed threadline, and $a_0= d_0/2$ is the cross-sectional radius of the threadline.

Taking for the estimate L=10 cm, $S=\pi d_0^2/4=1.96\times10^{-3}$ cm^2 (for d_0=0.05 cm), $U_0= U_g(0)$=230 m/s and ρ = 0.786 g/cm^3, we find for air $\nu_t=0.015U_g(0)d_0$=17.25 cm^2/s, q_τ=23.5 g/s^2 and τ_r =0.0256 s (the value is in a very good agreement with the main threadline frequencies in Fig. 7.4, which are of the order of τ_r^{-1}=39 Hz). Therefore, $<A_{threadline}>$=0.94 cm, in a reasonable agreement with the experimental data in Fig. 7.3. The result confirms that the lateral threadline oscillations are imposed by multiple impacts of large turbulent eddies and restricted by propagation of bending perturbations along the threadline. Another parameter of interest is the length of the threadline where flapping is the most vigorous. This requests a definition of vigorous flapping in the experiment. Two different definitions and methods based on them were used in the present work. In the first one, the images of the free-end part of the threadline were

analyzed using CCD records. The threadline cross-sections from which large lateral displacements of the free-end part were visible are denoted by arrows in the images (Fig. 7.6).

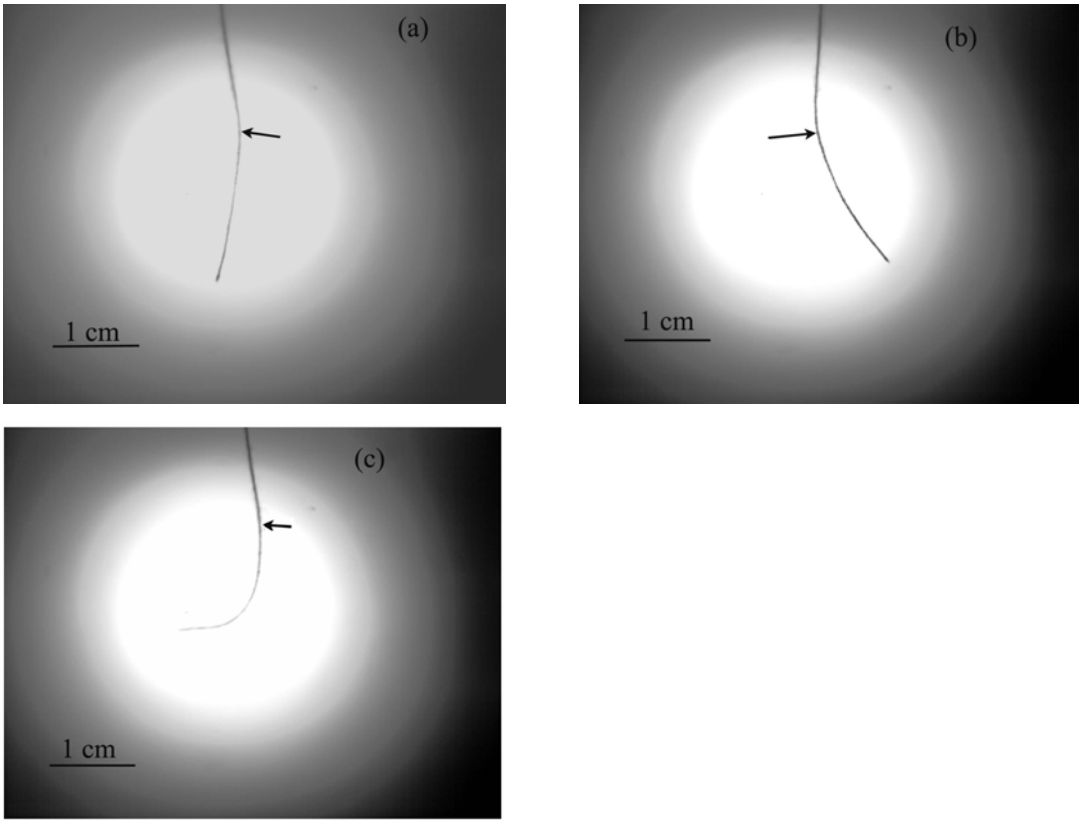

Fig. 7.6. Flapping of a 19.3 cm-long threadline, which was subjected to gas jet issued at 35 bar recorded by CCD. The arrows show the beginning of the flapping part of the threadline. (a)-(c): Three different snapshots from the same experiment are shown to illustrate the different configurations recorded.

The flapping region depicted in Fig. 7.6 shows that propagation of bending perturbations along the threadline serves as a relaxation mechanism for lateral oscillations imposed by turbulent eddies only in the strongly stretched part at the beginning of the threadline, which supports practically the whole air drag force. On the

other hand, the free end of the threadline is almost unloaded and imposes weak restrictions on the lateral excursions driven by turbulent eddies. Moreover, bending perturbations entering there from the upper part of the threadline can amplify with practically no restriction, delivering their whole energy parcel into such lateral motion. That is one of the reasons of the strong amplification of the bending perturbations of the threadline close to the free end, which results in flapping. Another reason for strong amplification will be in the appearance of the distributed lift force, which also diminishes the restricting effect of the threadline tension and is discussed in detail in Section 7.3.

Another method of determining a vigorously flapping part of the threadline was based on the threadline envelope photographed by DSLR Nikon D-70s camera (Fig. 7.7). This method is capable of observations of almost the whole threadline length (in distinction from the first method based on CCD images), which allows an easy recognition of the flapping part of the threadline (Fig. 7.7).

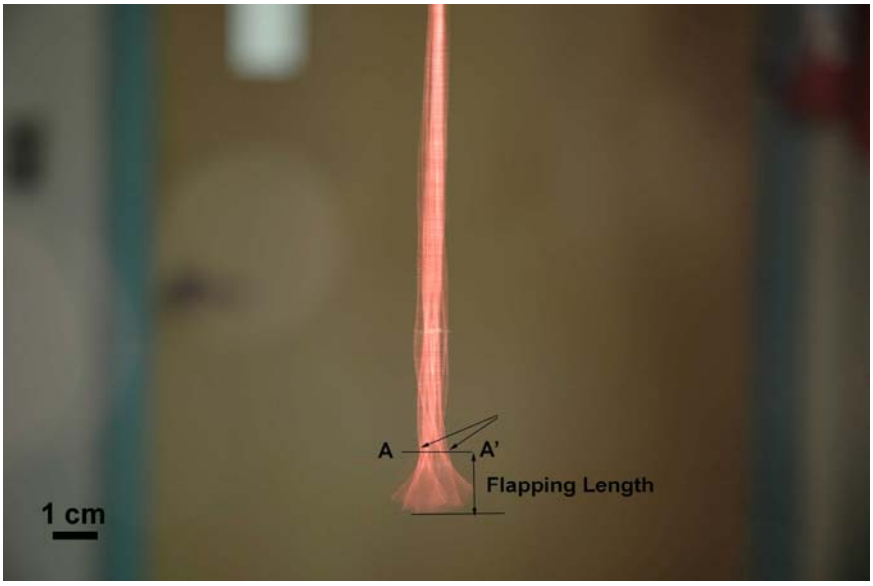

Fig. 7.7. Determination of the flapping part of the threadline. The beginning of the flapping section is indicated by the inclined arrows. Experiment with a 19 cm-long threadline subjected to gas jet issued at 28 bar.

Comparison between the results of the two methods of measuring the flapping part revealed the following. In the experiment with a 18.5 cm-long threadline subjected to blowing at 35 bar (263.9 m/s), the flapping length found averaging the data recorded by CCD camera was 1.82 cm. On the other hand, the application of the method of Fig. 7.7 based on the data recorded by DSLR camera revealed the length of the flapping end of the threadline as 1.76 cm. Therefore, the results obtained by the two different methods are sufficiently close. The slight difference in the values of the flapping length found by the two methods can be attributed to the following reasons: (i) the pixel resolution of the images obtained by DSLR camera is not sharp enough; (ii) due to the three-dimensional nature of flapping, the actual beginning cross-section of the flapping part might be off by a few pixels from the one in the images; (iii) in spite of the fact that the threadlines were

ironed and straightened prior to the observations, they always possessed some local non-zero curvatures along their length; (d) a certain inhomogeneity of the threadlines.

The method illustrated in Fig. 7.7 was applied to determine flapping lengths of threadlines of different lengths subjected to the same blowing speed. The experiment began with a 21 cm-long threadline subjected to parallel gas jet flow issued at 35 bar (263.9 m/s). After the transient effects had faded, the corresponding flapping length was measured as in Fig. 6. Then, blowing was ceased and the threadline was cut shorter. Then, blowing was turned on once again and the corresponding flapping length was measured. After that, the procedure was repeated again and again until the threadline length of 10.1 cm. The results are shown in Fig. 7.8a. It can be seen that the experimental points are clearly subdivided into two groups-one for shorter threadlines (10 to 16 cm long) and the other one-for the longer ones (16 to 21 cm long). In the "shorter" group the data suggest some variation of the flapping length L_f versus threadline length L, albeit it might be caused by data scatter. Note that the shorter threadlines might be significantly affected by such end effects as shedding vortices forming the von Karman street, as it was suggested in (Argentina et al., 2005). On the other hand, in the "longer" group the flapping length is practically independent of the threadline length L.

Using the well-known analytical solution for the axisymmetric turbulent gas jets (Abramovich 1963; Frost 1977), it is easy to evaluate the ratio $u_{gA}/U_g(x)$ where u_{gA} is the gas velocity value at points A and A' in Fig. 7.7, and $U_g(x)$ is the local axial velocity of the gas jet. The results are shown in Fig. 7.8b. They demonstrate that the part of the threadline preceding the flapping part is located within the core of the surrounding gas jet

corresponding to the range of $u_{gA}/U_g(x)$ from 0.78 to 0.87, i.e. to the gas velocity values of 78-87% of the local axial gas jet velocity in cross-section A A′.

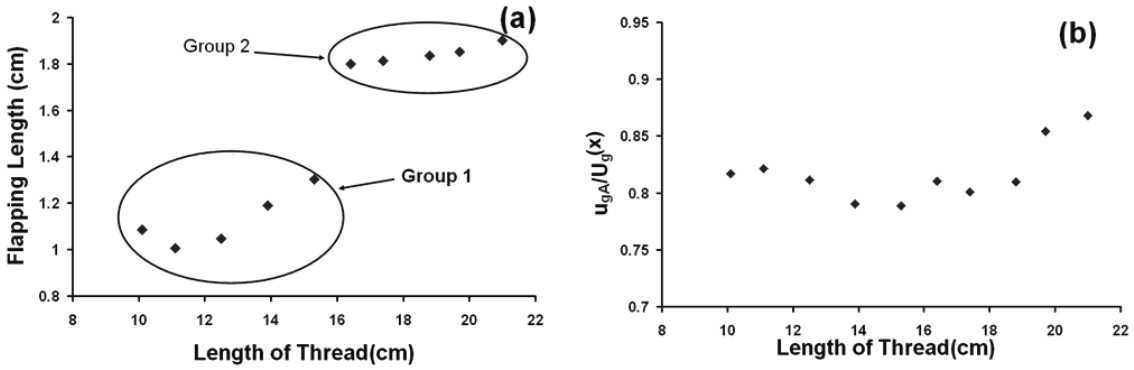

Fig. 7.8. (a) Flapping length versus threadline length. (b) Gas velocity at points A and A′ in Fig. 7.7 relative to the local axial velocity value $U_g(x)$ for different threadlines.

In an additional experiment a 19 cm-long threadline was subjected to gas jets issued at different pressures from 24 to 40 bar with a step of 2 bar (blowing velocities $U_g(0)$ =181.6-274.1 m/s) and the flapping length was measured using the method of Fig. 7.7. The results are depicted in Fig. 7.9a in logarithmic scales. They reveal the scaling $L_f \sim U_g(0)$ at $U_g(0) \leq 230$ m/s. At $U_g(0)>230$ m/s the scaling changes to $L_f \sim U_g(0)^{2.42}$. The values of the ratio $u_{gA}/U_g(x)$ in the cross-sections corresponding to points A and A′ in Fig. 6 for all different blowing velocities are shown in Fig. 7.9b. They demonstrate that the part of the threadline part preceding the flapping part is located within the core of the surrounding gas jet corresponding to the range of $u_{gA}/U_g(x)$ from 0.75 to 0.95, i.e. to the gas velocity values of 75-95% of the local axial gas jet velocity in cross-section A A′.

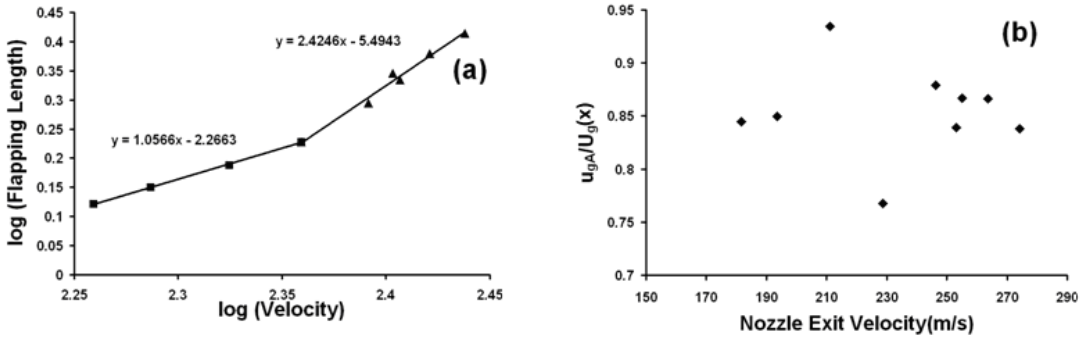

Fig. 7.9. (a) Flapping length versus the gas jet velocity at the nozzle exit. (b) Gas velocity at points A and A′ in Fig. 6 relative to the local axial velocity value $U_g(x)$ for different blowing velocities.

7.3 Theoretical: Solid Flexible Threadline in Parallel High Speed Gas Flow

Consider a solid flexible threadline subjected to parallel high speed gas flow. The threadline is assumed to be non-stretchable and with negligible bending stiffness. Its cross-sectional radius a_0 is constant. In the unperturbed state the threadline is straight and aligned in the flow direction and does not move. The force balance in the threadline in this state reads

$$\frac{dP}{dx} + q_\tau = 0 \qquad (7.6)$$

where $P=\sigma_{xx}\pi a_0^2$ is the longitudinal force acting in the threadline cross-section (with σ_{xx} being the normal stress), and q_τ is the distributed aerodynamic drag force acting on a unit length of the threadline. An appropriate expression for the drag force is given by Eq. (7.5) in Section 7.2. The longitudinal axis Ox is directed along the unperturbed threadline, with x=0 corresponding to a certain "initial" cross-section which is discussed in detail below.

The normal stresses in the threadline cross-sections are of the elastic origin. Since the threadline stretchability is assumed to be very low (which means that its Young's modulus is sufficiently high), the static (and, further on, dynamic) threadline elongation is assumed to be negligible, even though the stress σ_{xx} might be large.

The threadline length is L, and at the free end x=L the normal stress vanishes, i.e. $\sigma_{xx}\big|_{x=L} = 0$. Then, Eq. (7.6) is integrated to yield the normal stress distribution along the unperturbed threadline

$$\sigma_{xx} = \frac{q_\tau (L - x)}{\pi a_0^2} \tag{7.7}$$

In particular, the largest stress is achieved in the "initial" cross-section of the threadline at x=0, which is $\sigma_{xx0}=\sigma_{xx}(0)=q_\tau L/(\pi a_0^2)$, since it supports practically the whole aerodynamic drag applied to the threadline.

The solid flexible threadline is subjected to bending perturbations, which can result in lateral threadline motions due to the appearance of the normal component q_n of the aerodynamic force per unit threadline length related to the mean flow (Yarin 1993; Weber 1931; Debye et al., 1959; Entov et al., 1954). This component is of the inviscid origin and resembles a distributed lift force, which originates from the unsteady Bernoulli equation for gas motion. Obviously, it is not alone, since the unsteady Bernoulli equation in addition produces the force component associated with the added mass. However, in high speed flows the lift force is the dominant one compared to the added mass effects, since only it is proportional to U_0^2, whereas the additional force components are only linear in U_0. It is emphasized, that we do not include here the effect of the turbulent pulsations in the gas flow, which will be accounted for separately.

As it is shown in (Yarin 1993; Weber 1931; Debye et al., 1959; Entov et al., 1954), the distributed lift force is proportional to the local curvature of the threadline axis, and in the linear approximation (for small bending perturbations) is given by

$$q_n = -\rho_g U_0^2 \pi a_0^2 \frac{\partial^2 H}{\partial x^2} \qquad (7.8)$$

where H=H(x,t) represents the curved threadline axis. Note that planar bending is considered here for simplicity, whereas the generalization to the three-dimensional bending is straightforward (Yarin 1993; Weber 1931; Debye et al., 1959; Entov et al., 1954). The distributed drag and lift forces acting on a perturbed threadline subjected to gas flow are shown schematically in Fig. 7.10. Random force imposed by turbulent pulsations is also shown in Fig. 7.10 for completeness.

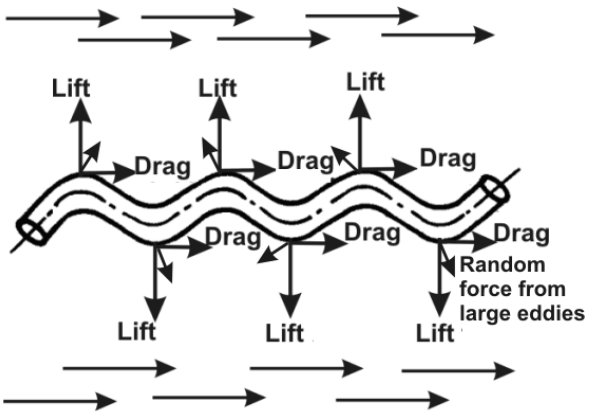

Fig. 7.10. Distributed forces acting on perturbed threadlines (and polymer jets) subjected to high speed gas flow.

The linearized lateral momentum balance for the perturbed threadline in a high speed gas flow reads

$$\rho\pi a_0^2 \frac{\partial V_n}{\partial t} = kP + q_n \tag{7.9}$$

where ρ is the threadline density, $V_n = \partial H / \partial t$ is the lateral local velocity of the threadline and $k = \partial^2 H / \partial x^2$ is the local curvature.

Accounting for Eq. (7.8), Eq.(7.9) takes the following form

$$\frac{\partial^2 H}{\partial t^2} + \frac{\left[\rho_g U_0^2 - \sigma_{xx}(x)\right]}{\rho} \frac{\partial^2 H}{\partial x^2} = 0 \tag{7.10}$$

where $\sigma_{xx}(x)$ is given by Eq. (7.7).

Equation (7.10) is rather peculiar. It shows that in regards to the lateral motion of the threadline, the distributed lift force diminishes the effect of stretching imposed by the aerodynamic drag. Correspondingly, if $\sigma_{xx0}>\rho_g U_0^2$, this equation is hyperbolic at $0 \le x \le x_*$ where $\sigma_{xx}>\rho_g U_0^2$, and elliptic at $x_* \le x \le L$ where $\sigma_{xx}<\rho_g U_0^2$, since according to Eq. (7.7) the normal stress decreases along the threadline. The transition cross-section x_* according to Eq. (7.7) is determined by the condition

$$\rho_g U_0^2 - \frac{q_\tau (L - x_*)}{\pi a_0^2} = 0 \tag{7.11}$$

which yields the length of the "elliptic" (flapping) part of the threadline L_f as

$$L_f = L - x_* = \frac{a_0}{0.65}\left(\frac{2U_0 a_0}{\nu_g}\right)^{0.81} \tag{7.12}$$

Equation (7.12) shows that the length of the "elliptic" part of the threadline does not depend on its length L. On the other hand, it increases with blowing speed as $U_0^{0.81}$.

The fact that Eq. (7.10) changes type at $x=x_*$ makes it kindred to the Tricomi equation, albeit different from it.

The general solution of Eq. (7.10) with σ_{xx} given by Eq. (7.7) is readily found by the method of characteristics as

$$\mathbf{H}(x,t) = \mathbf{\Phi}\left[\int_0^x \frac{dx}{[q_\tau(L-x)/\pi a_0^2 - \rho_g U_0^2]/\rho} - t\right] + F\left[-\int_0^x \frac{dx}{[q_\tau(L-x)/\pi a_0^2 - \rho_g U_0^2]/\rho} - t\right] \tag{7.13}$$

where $\mathbf{\Phi}(\cdot)$ and $F(\cdot)$ are arbitrary functions.

Perturbations on the threadline are imposed by turbulent pulsations in the surrounding turbulent gas jet. The experimental data discussed in Section 7.2 show that significant perturbations of the threadline configuration are visible at some distance from the suspended end of the threadline. In the first approximation, it is assumed that at a certain relatively small distance from the suspended end perturbations of frequencies and amplitudes corresponding to the local turbulent pulsation structure of the mixing layer in the gas jet are imposed on the threadline, whereas down the threadline no new perturbations are imposed, since the gas jet widens. This cross-section of the threadline where bending perturbations are imposed is considered to be the "initial" one, and x=0 there. In this cross-section it is assumed that the threadline is subjected to small lateral perturbations generated in the mixing layer of the gas jet, so that

$$\mathbf{H}\big|_{x=0} = \mathbf{H}_{0\omega}\exp(i\omega t), \quad \partial\mathbf{H}/\partial x\big|_{x=0} = 0 \tag{7.14}$$

where $H_{0\omega}$ (which is a complex number in the general case) and real ω are the corresponding mode amplitude and frequency, and i is the imaginary unit.

The boundary conditions (10) fully determine the functions $\mathbf{\Phi}(\cdot)$ and $F(\cdot)$ in the "hyperbolic" part and reduce Eq. (9) to the following threadline configuration

$$\mathbf{H}(x,t) = \mathbf{H}_{0\omega} \exp(i\omega t)\cos[\omega I(x)] \tag{7.15}$$

The real function I(x) results from the evaluation of the integrals in Eq. (7.13) as

$$I(x) = \frac{2\rho\pi a_0^2}{q_\tau}\left\{\left[\left(\frac{q_\tau L}{\pi a_0^2} - \rho_g U_0^2\right)/\rho\right]^{1/2} - \left[\left(\frac{q_\tau (L-x)}{\pi a_0^2} - \rho_g U_0^2\right)/\rho\right]^{1/2}\right\} \tag{7.16}$$

Note that

$$I(0) = 0, \quad I(x_*) = \frac{2\rho\pi a_0^2}{q_\tau}\left[\left(\frac{q_\tau L}{\pi a_0^2} - \rho_g U_0^2\right)/\rho\right]^{1/2} \tag{7.17}$$

The physically relevant solution for the threadline shape in the "hyperbolic" part is given by the real part of Eq. (7.15).

On the other hand, in the "elliptic" part the characteristics are imaginary, and Eq. (9) reduces to

$$\mathbf{H}(x,t) = \exp(i\omega t)\left\{A\exp\left[-i\omega I(x_*)\right]\exp\left[-\omega J(x)\right] + B\exp\left[i\omega I(x_*)\right]\exp\left[\omega J(x)\right]\right\} \tag{7.18}$$

where A and B are constants and

$$J(x) = \frac{2\rho\pi a_0^2}{q_\tau}\left[\frac{q_\tau x}{\rho\pi a_0^2} - \frac{q_\tau L/(\pi a_0^2) - \rho_g U_0^2}{\rho}\right]^{1/2} \tag{7.19}$$

Note that

$$J(x_*) = 0, \quad J(L) = \frac{2\rho\pi a_0^2}{q_\tau}\left(\frac{\rho_g U_0^2}{\rho}\right)^{1/2} \tag{7.20}$$

The constants are found via matching of Eq. (7.18) to Eq. (7.15) at $x=x_*$, which yields $A = B = \mathbf{H}_{0\omega}/2$. Then, the threadline shape in the "elliptic" part is given by

$$\mathbf{H}(x,t) = \mathbf{H}_{0\omega} \exp(i\omega t)\left\{\cosh\left[\omega J(x)\right]\cos\left[\omega I(x_*)\right] + i\sinh\left[\omega J(x)\right]\sin\left[\omega I(x_*)\right]\right\} \tag{7.21}$$

As in the "hyperbolic" part, the physically relevant result for the "elliptic" part is given by the real part of Eq. (7.21). It is emphasized that since $dI/dx\big|_{x=x_*} = dJ/dx\big|_{x=x_*} = \infty$, the transition from the "hyperbolic" part to the "elliptic" part occurs in the cross-section $x=x_*$ where $d\mathbf{H}/dx\big|_{x=x_*} = \infty$, i.e. the threadline is oriented perpendicularly to the gas flow.

Four dimensionless snapshots of the threadline shape calculated using Eqs. (7.15), (7.16), (7.19) and (7.21) are plotted in Fig. 7.11. It is clearly seen that the wavelength of the standing perturbation wave in the "hyperbolic" part becomes shorter as approaching to the transition cross-section $x=x_*$ (= 0.695 in the present case). In the "elliptic" part after the transition the perturbation amplitude increases very rapidly, which in fact, rapidly violates the assumption of small perturbations. A fully realistic prediction of the threadline shape in this part can be achieved only in the framework of the fully nonlinear theory which is our future goal. However, a practical approximation is probably the one where the calculation is truncated at a cross-section $x> x_*$ where the perturbed threadline length reaches the value of the order of L (i.e. 1 in the dimensionless case).

The "explosive" behavior of the solution in the "elliptic" part is a clear manifestation of the fact that the elliptic problem is solved there as an initial value problem. This results from the matching condition imposed only at one side of the interval at the transition from the "hyperbolic" part at $x=x_*$. That means that in the "elliptic" part we are dealing with an Hadamard-like problem, which is inevitably prone to fast perturbation growth. Situations where physical problems reduce to the ill-posed Hadamard-like problems are not unique. For example, the well-known capillary Rayleigh instability, if treated in the quasi-one-dimensional, linearized approximation for small

perturbations (Yarin 1993) immediately reveals an Hadamard-like initial value problem for the Laplace equation with surface-tension-related regularization for the short waves.

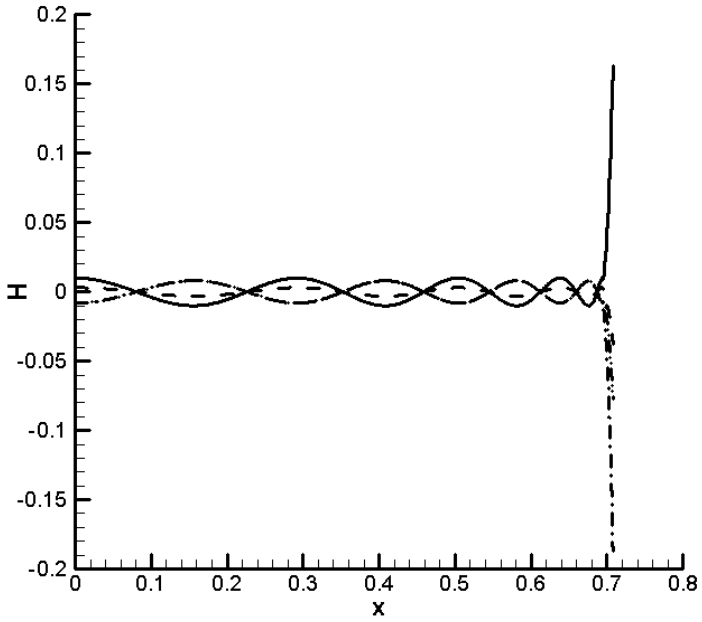

Fig. 7.11. Four snapshots of the threadline shape (shown by lines with different patterns) corresponding to the case with $R=\rho_g/\rho=0.00122$, $L/a_0=100$, the Reynolds number $Re=2U_0a_0/\nu_g=40$, $\mathbf{H}_{0\omega}=0.01$, and the dimensionless perturbation frequency $\Omega=\omega L/U_0=0.01$ (for $L=10\,\text{cm}$ and $U_0=10^4\,\text{cm/s}$, $\omega=10\,\text{Hz}$). The perturbation amplitude $\mathbf{H}$ and the longitudinal coordinate x are rendered dimensionless by L.

Strong amplification of bending perturbation waves as they pass from the "hyperbolic" (stretched) to the "elliptic" (almost unstretched) part of the threadline is partially related to the fact that the wave brings with itself a parcel of mechanical energy delivered to it by turbulent eddies in the "initial" cross-section x=0. In the almost unloaded part, this energy is released as kinetic energy of lateral excursions unrestricted by longitudinal stretching and manifesting themselves as flapping. Also, the distributed

lift force strongly amplifies bending perturbations in the unloaded part of the threadline. This effect also significantly contributes to flapping.

In reality turbulent pulsations can affect threadline not only at the "initial" cross-section but over a certain length. Considering the effect of distributed turbulent pulsations on threadlines separately from the effect of the distributed lift force, we apply the formula for the oscillation magnitude $<A_{threadline}>$ derived in Section 7.2 accounting for the fact that the restrictive longitudinal tension diminishes in the x direction. Therefore, $<A_{threadline}(x)>=[2\nu_t\tau_r(x)]^{1/2}$, where $\nu_t=0.015U_0d_0$, $\tau_r(x)= L[\sigma_{xx}(x)/\rho)]^{-1/2}$ and $\sigma_{xx}(x)$ is given by Eqs. (1) and (3). As a result, we find the threadline envelope as

$$< A_{threadline}(x) >= 0.16\left(\frac{\rho}{\rho_g}\right)^{1/4}\left(\frac{U_0 d_0}{\nu_g}\right)^{0.2025}\left(\frac{d_0}{L}\right)^{1/4}\sqrt{d_0 L}\,\frac{1}{(1-x)^{1/4}} \qquad (7.22)$$

where x is rendered dimensionless by L. The result shows that the shape of the threadline envelope should follow the dependence $< A_{threadline} > \sim (1-x)^{-1/4}$ if only turbulent pulsations are accounted for, whereas distributed aerodynamic lift force disregarded.

The theoretical predictions of this Section are compared to the experimental data in Section 7.4.

7.4 Discussion: Some Theoretical Predictions versus Experimental Data

The results for longer threadlines in Fig. 7.8a show that the length of the flapping region L_f does not vary with the threadline length L. This is in agreement with the theoretical prediction of Eq. (7.12).

The experimental data in Fig. 7.9 reveal the scaling $L_f \sim U_g(0)$ at $U_g(0) \leq 230$ m/s, which is close to the scaling $L_f \sim U_g(0)^{0.81}$ expected from Eq. (7.12). On the other hand, at

$U_g(0)$>230 m/s the scaling changes to $L_f \sim U_g(0)^{2.42}$, which deviates significantly from the predictions of Eq. (7.12). A much stronger dependence of the aerodynamic drag on the gas jet velocity at such high values of $U_g(0)$ most probably corresponds to a strong increase in the eddy turbulent viscosity at higher blowing rates. The experiments in Ref. 19, which established the expression for the aerodynamic drag (7.5) used to derive Eq. (7.12) were conducted with threadlines moving in stagnant air, which does not involve high levels of the eddy turbulent viscosity in blowing jets. Therefore, deviations from Eqs. (7.5), (7.12) and (7.25) are thus expected at higher blowing velocities, and it is remarkable that these equations work rather accurately up to 230 m/s.

The comparison of the prediction of the effect of the distributed turbulent pulsations to the experimentally observed threadline envelope shown in Fig. 7.12 reveals the following. In the upper, hyperbolic part of the threadline where bending is strongly restricted by longitudinal stretching and the aerodynamic lift cannot be large, the envelope profile is rather accurately described by the predicted dependence of Eq. (7.22) $< A_{\text{threadline}} > \sim (1 - x)^{-1/4}$. On the other hand, in the lower, elliptic part of the threadline the effect of turbulent pulsations alone is insufficient to describe the observed flapping amplitudes, which are mostly determined by the distributed aerodynamic lift force.

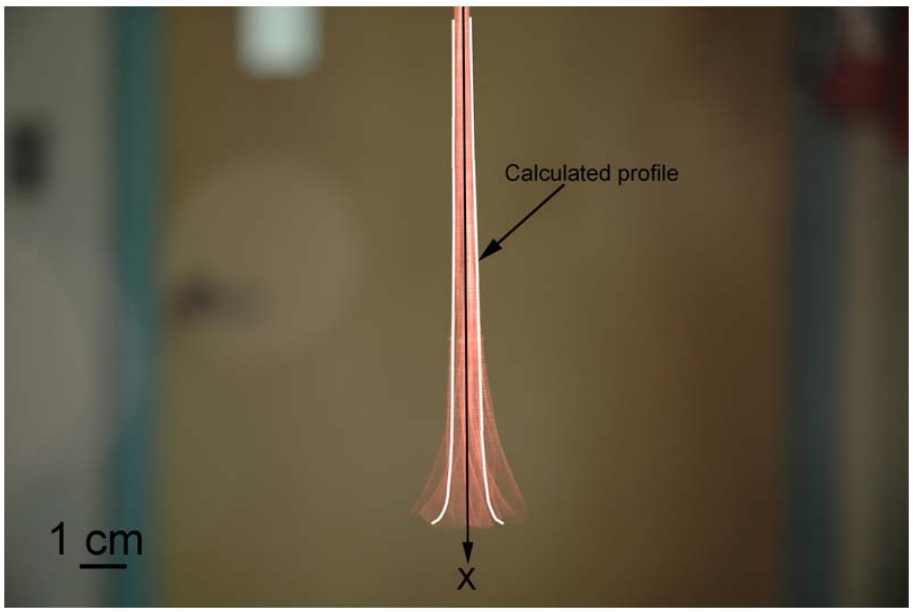

Fig. 7.12. The envelope observed in the experiment with a 19 cm-long threadline subjected to gas jet issued at 28 bar versus the prediction accounting for only the effect of turbulent pulsations and disregarding distributed aerodynamic lift force.

7.5 Conclusion

The experimental and theoretical study of threadline blowing in this work revealed the following mechanism of the process. Large turbulent eddies in the high speed gas jet with the eddy frequencies of the order of 10^3 Hz impact the threadlines introducing bending perturbations. It takes multiple rapid eddy impacts on a massive threadline to cause a visible lateral excursion. The bending amplitude achieved locally by the eddy bombardment is controlled by a much slower (with the frequencies of about 10-100 Hz) propagation of bending perturbations along the stretched (by the aerodynamic drag) threadline. Bending perturbations propagate along the threadline and reach lower regions which are practically unstretched/unloaded, since they do not support the whole aerodynamic drag imposed on the threadline. There, the restrictions on large amplitude

bending imposed by strong stretching are removed. Then, turbulence energy stored in the bending perturbations of the threadline can be released as the kinetic energy of a further bending. Moreover, bending perturbations of the unloaded threadlines are strongly amplified by the distributed aerodynamic lift force. As a result, the whole region close to the free unloaded threadline end experiences flapping of high amplitude. Blowing threadlines are capable of simultaneous extracting kinetic energy from both mean flow and turbulent pulsations in it.

8. MELTBLOWING-LINEAR AND NONLINEAR WAVES ON VISCOELASTIC POLYMER JETS

8.1 Introduction

Polymer jet stretching in meltblowing results not only from direct action of aerodynamic drag force but also due to the amplification of the bending perturbations triggered by turbulent eddies in gas and growing due to the distributed lift force. Certain experimental aspects of meltblowing have already been revealed in the literature, and some first steps were done in the direction of developing a comprehensive theory of the process. However, several key elements of such a theory are still lacking. Namely, the whole spectrum of the aerodynamic forces acting on polymer jets in meltblowing is not fully accounted for, and the true rheological behavior of polymer melts, their viscoelasticity, has never been included.

The present work aims at closing these gaps. It adopts several findings described in Chapter 7 regarding the aerodynamic interactions revealed in the model situation of threadline blowing, and also incorporates viscoelasticity of polymer jet. The approach used in the present work is based on the quasi-one-dimensional equations of free liquid jets-the technique which had already been successfully applied to the description of bending perturbations of polymer liquid jets moving with high speed in air or in the electric field in electrospinning (Yarin 1993; Entov et al., 1984; Reneker et al., 2000; Yarin et al., 2001; Reneker et al., 2007).

Section 8.2 describes the unperturbed flow in polymer viscoelastic jets in meltblowing, while Section 8.3 covers the linear stability theory of meltblown polymer

jets with small bending perturbations. Section 8.4 is devoted to the governing equations in the case of the fully nonlinear, large amplitude perturbations for the isothermal blowing. Their generalization on the non-isothermal blowing is given in Section 8.5. The numerical solutions of the nonlinear equations and discussion are presented and discussed in Section V. Conclusions are drawn in Section 8.6.

8.2 Unperturbed Straight Polymeric Viscoelastic Liquid Jet in Parallel High-speed Gas Flow

In the case of polymeric liquid jet stretched by surrounding parallel high speed gas jet, flow in the former should be calculated in distinction from the case of solid flexible threadline described in Chapter 7. Steady-state flow in an unperturbed straight polymer jet is governed by the following quasi-one-dimensional continuity and momentum balance equations (Yarin 1993)

$$\frac{dfV_\tau}{dx} = 0, \quad f = \pi a^2 \tag{8.1}$$

$$\rho \frac{dfV_\tau^2}{dx} = \frac{d\sigma_{xx} f}{dx} + q_\tau \tag{8.2}$$

where f (x) and a(x) are the cross-sectional area and radius, respectively, and $V_\tau(x)$ is the unperturbed absolute axial velocity of the polymeric liquid in the jet. In Eq. (8.2) surface tension and gravity effects are neglected as insignificant compared to the dominating inertial and internal (rheological) stresses (σ_{xx} is the longitudinal stress) and the aerodynamic drag q_τ (per unit jet length). As in Chapter 7, the effect of turbulent pulsations in gas is considered to be localized at the "initial" cross-section where they are

assumed to impose bending perturbations (in the perturbed case considered in the following Sections).

The stretching aerodynamic drag force q_τ depends on the relative velocity between the gas stream and polymer jet (U_g-V_τ). Therefore, similarly to Chapter 7, the following expression is used in the present case to calculate the local value of the drag force $q_\tau(x)$

$$q_\tau = 0.65\pi a\rho_g(U_g - V_\tau)^2\left[\frac{2(U_g - V_\tau)a}{\nu_g}\right]^{-0.81} \tag{8.3}$$

where a is the cross-sectional radius, ρ_g and ν_g are the gas density and kinematic viscosity, respectively.

Equation (8.1) is readily integrated, which yields

$$\pi a^2 V_\tau = \pi a_0^2 V_{\tau 0} \tag{8.4}$$

where subscript zero designates the cross-sectional radius and longitudinal velocity values at the "initial" cross-section. This expression allows one to exclude the cross-sectional radius from the consideration, as is done below.

In thin liquid jets the normal stress in the cross-section can be always presented as a difference between the normal and radial deviatoric stresses, τ_{xx} and τ_{yy}, respectively, i.e. as(Yarin 1993) $\sigma_{xx}= \tau_{xx}- \tau_{yy}$. The deviatoric stresses should be related to the flow kinematics via a rheological constitutive equation (RCE). For polymeric liquids experiencing strong uniaxial stretching as, for example, in melt blowing, an appropriate RCE is the viscoelastic upper-convected Maxwell model (Astarita 1974) (UCM), which is substantiated by direct statistical consideration of macromolecular stretching and the corresponding entropic elasticity (Yarin 1993). In the present case, the RCE of the Maxwell model reduces to the following axial and radial (lateral) projections

$$V_\tau \frac{d\tau_{xx}}{dx} = 2\frac{dV_\tau}{dx}\tau_{xx} + \frac{2\mu}{\theta}\frac{dV_\tau}{dx} - \frac{\tau_{xx}}{\theta} \tag{8.5}$$

$$V_\tau \frac{d\tau_{yy}}{dx} = -\frac{dV_\tau}{dx}\tau_{yy} - \frac{\mu}{\theta}\frac{dV_\tau}{dx} - \frac{\tau_{yy}}{\theta} \tag{8.6}$$

where μ and θ are the liquid viscosity and relaxation time, respectively.

Combining Eqs. (8.2)-(8.6), we can transform them to the following system of dimensionless equations

$$\frac{dV_\tau}{dx} = \frac{\left[-E(\tau_{xx} - \tau_{yy})/(DeV_\tau^2) + q_\tau\right]}{\left[1 - E(\tau_{xx} + 2\tau_{yy} + 3)/V_\tau^2\right]} \tag{8.7}$$

$$\frac{d\tau_{xx}}{dx} = \frac{1}{V_\tau}\left(2\frac{dV_\tau}{dx}\tau_{xx} + 2\frac{dV_\tau}{dx} - \frac{\tau_{xx}}{De}\right) \tag{8.8}$$

$$\frac{d\tau_{yy}}{dx} = \frac{1}{V_\tau}\left(-\frac{dV_\tau}{dx}\tau_{yy} - \frac{dV_\tau}{dx} - \frac{\tau_{yy}}{De}\right) \tag{8.9}$$

where

$$q_\tau = 0.65R\ell / V_\tau^{1/2}(U_g - V_\tau)^2\left[Re(U_g - V_\tau)/V_\tau^{1/2}\right]^{-0.81} \tag{8.10}$$

The equations are rendered dimensionless by the following scales: $V_{\tau 0}$ for V_τ and U_g, the distance between the "initial" cross-section and deposition screen L for x, a_0 for a, μ/θ for τ_{xx} and τ_{yy}, and further on, $L/V_{\tau 0}$ for time t. The primary dimensionless groups involved in Eqs. (8.7)-(8.10) are given by

$$R = \frac{\rho_g}{\rho}, \quad \ell = \frac{L}{a_0}, \quad Re = \frac{2V_\tau^0 a_0}{\nu_g}, \quad De = \frac{\theta V_{\tau 0}}{L} \tag{8.11}$$

with Re and De being the Reynolds and Deborah numbers, respectively; the secondary dimensionless groups are

$$E = \frac{2R}{De\ell\,Re\,M}, \quad M = \frac{\mu_g}{\mu} \tag{8.12}$$

In Eq. (8.12) μ_g denotes gas viscosity.

The system of three ordinary differential equations (8.7)-(8.9) is subjected to the following dimensional conditions at the “initial” cross-section of the polymer jet

$$x = 0: \quad V_\tau = 1, \quad \tau_{xx} = \tau_{xx0}, \quad \tau_{yy} = 0 \tag{8.13}$$

The fact that all boundary conditions for Eqs. (8.7)-(8.9) can be imposed at x=0 stems from the hyperbolicity of this system of equations, which holds if the dimensional initial velocity $V_{\tau 0}$ is larger than the dimensional speed of the "elastic sound"(Yarin 1993; Entov et al., 1987; Joseph 1990) $(\sigma_{xx}/\rho)^{1/2}$. Accounting for Eq. (8.13), the latter corresponds to the following dimensionless condition

$$1 > E\tau_{xx0} \tag{8.14}$$

This means that even though polymeric liquids can develop rather significant longitudinal deviatoric stresses in flow inside the die and carry a significant part of it as τ_{xx0} to the “initial” cross-section (Han et al., 2000), the convective effects in the polymeric jet are initially stronger than propagation of the "elastic sound". Therefore, the information in such a jet is convected downstream, even though the "elastic sound" can propagate not only down- but also upstream (i.e. against the flow, but swept by it). In such cases all boundary conditions are imposed at the beginning of the polymer jet as in Eq. (8.13).

The system of equations (8.7)-(8.9) subjected to the conditions (13) was solved numerically using the Kutta-Merson method.

The solution of Eqs. (8.7)-(8.9) for the unperturbed jet is illustrated in Figs. 8.1-8.2 for the following values of the parameters: M=0.001, R=0.00122, $\ell = 83000$, De=0.01,

Re=40, the dimensionless velocity of the gas flow assumed to be constant in the present case is $U_g=U_g(0)=10$, $\tau_{xx0}=10^4$, $\mathbf{H}_{0\omega}=0.01$, and the dimensionless perturbation frequency $\Omega=\omega L/V_{\tau 0}=1500$. These values of the dimensionless groups correspond to plausible values of the physical parameters partially taken from (Marheineke et al., 2007): $a_0=3\times10^{-3}\,\mathrm{cm}$, L=250 cm, $\rho_g=1.22\times10^{-3}\,\mathrm{g/cm^3}$, ν_g=0.15 $\mathrm{cm^2/s}$, $V_{\tau 0}=10^3\,\mathrm{cm/s}$, the dimensional $U_g(0)=10^4$ cm/s, $\theta=0.25\times10^{-2}\,\mathrm{s}$ and $\omega=6\times10^3$ Hz.

Figure 8.1 depicts the unperturbed longitudinal velocity $V_\tau(x)$ and radius a(x) distributions, and Figs. 8.2a and b-the unperturbed distributions of the longitudinal and lateral deviatoric stresses, $\tau_{xx}(x)$ and $\tau_{yy}(x)$, respectively. It is seen that the polymeric jet is gradually accelerated by the aerodynamic drag imposed by the gas stream, and simultaneously thins (Fig. 8.1). The longitudinal deviatoric stress τ_{xx}, which is rather high at the die exit due to the prior strong stretching in the die channel, decreases along the jet because the elongation rate due to the gas flow there is insufficiently high to overcome the viscoelastic relaxation (the so-called, weak flow; cf. Fig. 8.2a). Comparison of Figs. 8.2a and b shows that the lateral deviatoric stress τ_{yy} is negligibly small compared to the lateral one, τ_{xx}, as expected in the uniaxial elongational flows.

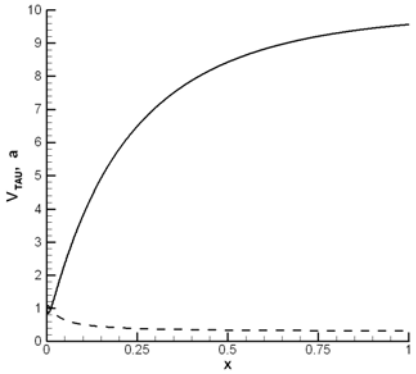

Fig. 8.1. The unperturbed distributions of the longitudinal velocity (solid line) and cross-sectional radius (dashed line) along polymer jet stretched by high speed gas jet.

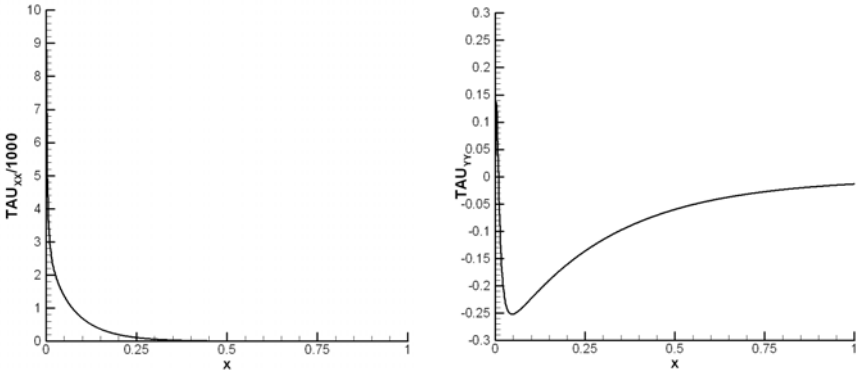

Fig. 8.2. The unperturbed distributions of the longitudinal (a), and lateral (b) deviatoric stresses (τ_{xx} and τ_{yy}, respectively) along polymeric jet stretched by high speed gas jet.

8.3 Small Perturbations of Polymeric Viscoelastic Liquid Jet in Parallel High-speed Gas Flow

Bending perturbations of polymeric jets stretched by high speed gas jet will be studied using the quasi-one-dimensional equations of the dynamics of free liquid jets (Yarin 1993). In the momentless approximation (neglecting the bending stiffness) and assuming small bending perturbations (linearizing), one can reduce Eqs. (4.19) on p. 49

in (Yarin 1993) to the normal projection of the momentum balance equation in the following dimensional form

$$\frac{\partial^2 H}{\partial t^2} + 2V_\tau \frac{\partial^2 H}{\partial x \partial t} + \left[V_\tau^2 + \frac{\rho_g (U_g - V_\tau)^2 - \sigma_{xx}}{\rho} \right] \frac{\partial^2 H}{\partial x^2} = 0 \qquad (8.15)$$

Rendering this equation dimensionless using the scales listed above in Section 8.2, the following dimensionless equation is obtained

$$\frac{\partial^2 H}{\partial t^2} + 2V_\tau \frac{\partial^2 H}{\partial x \partial t} + \left[V_\tau^2 + R(U_g - V_\tau)^2 - E\sigma_{xx} \right] \frac{\partial^2 H}{\partial x^2} = 0 \qquad (8.16)$$

where L is also used as a scale for the perturbation amplitude H. Equations (8.15) and (8.16) are kindred to Eq. (8.6) in Chapter 7 for the bending perturbations of a solid flexible threadline.

It is emphasized that in the linear approximation, perturbations of the longitudinal flow do not affect small bending perturbations, i.e. the latter are completely uncoupled from the former ones, since the coupling could happen only via nonlinear terms. Therefore, in Eq. (8.16) the factors multiplying the derivatives in the second and third terms on the left depend on the unperturbed distributions of $V_\tau(x)$ and $\sigma_{xx}(x)=\tau_{xx}(x)-\tau_{yy}(x)$, which are found from Eqs. (8.7)-(8.9).

The general solution of Eq. (8.16) can be found using the characteristics

$$\frac{dx}{dt} = V_\tau \pm \left[E\sigma_{xx} - R(U_g - V_\tau)^2 \right]^{1/2} \qquad (8.17)$$

Equation (8.16) is hyperbolic if $E\sigma_{xx}-R(U_g-V_\tau)^2>0$ and the characteristics are real, and elliptic if $E\sigma_{xx}-R(U_g-V_\tau)^2<0$ and the characteristics are complex. This means that if at x=0, the inequality $E\tau_{xx0}>R[U_g(0)-1]^2$ holds, the initial part of the jet is "hyperbolic".

Given Eq. (8.14), the conditions that the initial part of the jet is "hyperbolic" in both unperturbed and perturbed states are

$$1 > E\tau_{xx0} > R[U_g(0) - 1]^2 \tag{8.18}$$

The transition cross-section $x=x_*$ is found from the following equation

$$K(x) = E\sigma_{xx}(x) - R[U_g(x) - V_\tau(x)]^2 = 0 \tag{8.19}$$

The general solution of Eq. (8.16) is given by

$$\begin{aligned} \mathbf{H}(x,t) = \Phi\left[\int_0^x \frac{dx}{V_\tau + \sqrt{E\sigma_{xx} - R(U_g - V_\tau)^2}} - t\right] \\ + F\left[\int_0^x \frac{dx}{V_\tau - \sqrt{E\sigma_{xx} - R(U_g - V_\tau)^2}} - t\right] \end{aligned} \tag{8.20}$$

where $\Phi(\cdot)$ and $F(\cdot)$ are arbitrary functions.

Assume that the inequalities (8.18) hold. Then, the initial part of the polymeric jet $0 \le x \le x_*$ is "hyperbolic", whereas the following part $x_* \le x \le 1$ –"elliptic".

Here again, as in the case of the threadline described in Chapter 7, we apply the conditions for the perturbation wave at the "initial" cross-section of the polymer jet in the following form

$$\mathbf{H}\big|_{x=0} = \mathbf{H}_{0\omega}\exp(i\omega t), \quad \partial\mathbf{H}/\partial x\big|_{x=0} = 0 \tag{8.21}$$

which corresponds to the overall effect of the turbulent pulsations being combined there.

Then, we can find the functions $\Phi(\cdot)$ and $F(\cdot)$ and reduce Eq. (8.20) to the following solution for the "hyperbolic" part at $0 \le x \le x_*$

$$\mathbf{H}(x,t) = \frac{\mathbf{H}_{0\omega}}{1-\delta}\exp(i\omega t)\left\{-\delta\exp[-i\omega I_1(x)] + \exp[-i\omega I_2(x)]\right\} \tag{8.22}$$

where the two real functions $I_1(x)$ and $I_2(x)$ are given by

$$I_1(x)=\int_0^x \frac{dx}{V_\tau(x)+\sqrt{E\sigma_{xx}(x)-R[U_g(x)-V_\tau(x)]^2}} \tag{8.23}$$

$$I_2(x)=\int_0^x \frac{dx}{V_\tau(x)-\sqrt{E\sigma_{xx}(x)-R[U_g(x)-V_\tau(x)]^2}} \tag{8.24}$$

and

$$\delta=\left.\frac{dI_2/dx}{dI_1/dx}\right|_{x=0} \tag{8.25}$$

The corresponding solution for the "elliptic" (in regards to bending perturbations) part of the polymer jet at $x_* \le x \le 1$ is also obtained from the general solution (8.20). After it is matched to the "hyperbolic" solution at the transition point $x=x_*$, it reads

$$\begin{aligned}\mathbf{H}(x,t)=&\frac{H_{0\omega}}{1-\delta}\exp\{i\omega[t-J_1(x)]\}\\ &\times\left\{-\delta\exp[-i\omega I_1(x_*)]\exp[-\omega J_2(x)]+\exp[-i\omega I_2(x_*)]\exp[\omega J_2(x)]\right\}\end{aligned} \tag{8.26}$$

In Eq. (8.26) the two additional real functions $J_1(x)$ and $J_2(x)$ are defined as

$$J_1(x)=\int_{x*}^x \frac{V_\tau(x)}{V_\tau^2(x)+R[U_g(x)-V_\tau(x)]^2-E\sigma_{xx}(x)}dx \tag{8.27}$$

$$J_2(x)=\int_{x*}^x \frac{\sqrt{R[U_g(x)-V_\tau(x)]^2-E\sigma_{xx}(x)}}{V_\tau^2(x)+R[U_g(x)-V_\tau(x)]^2-E\sigma_{xx}(x)}dx \tag{8.28}$$

It is emphasized that the dimensional gas stream velocity at the outer boundary of the boundary layer near the liquid jet surface, $U_g(x)$, can be evaluated using the theory of the axisymmetric turbulent gas jets (Abramovich 1963; Yarin 2007) as

$$U_g(x)=U_g(0)\frac{2.4d_0}{x+2.4d_0} \tag{8.29}$$

where $d_0 \approx 2a_0$ is the diameter of the coaxial gas-jet nozzle, and $2.4d_0$ is the polar distance of the jet.

The corresponding dimensionless expression becomes

$$U_g(x) = U_g(0)\frac{4.8/\ell}{x + 4.8/\ell} \tag{8.30}$$

where $U_g(x)$ and $U_g(0)$ are rendered dimensionless by $V_{\tau 0}$.

Figure 8.3 depicts the function K(x) of Eq. (8.19), which is obtained from the solution for the unperturbed straight jet in Section 8.2. It is seen that K(x)=0 at $x=x_*=0.146$. This means that at $0 \le x \le 0.146$ bending perturbations are "hyperbolic", whereas at $0.146 \le x \le 1$ they are "elliptic". Two predicted snapshots of the bending jet configurations corresponding to two different time moments are shown in Fig. 8.4. It is seen that in the "hyperbolic" part described by Eq. (8.22) the traveling perturbation wave has the amplitude of the order of $H_{0\omega}$. After the transition to the "elliptic" part, the amplitude of the traveling perturbation wave described by Eq. (8.26) even decreases, but after the bottleneck seen in Fig. 8.4 at about x=0.35, the perturbation amplitude rapidly increases, as is expected for an elliptic problem solved as an initial-value problem. That is the area where the perturbed jet will be drastically stretched and thinned. An accurate description of such thinning can be achieved only in the framework of a fully nonlinear description in the following Section.

The pattern of the perturbation waves predicted for meltblowing in Fig. 8.4 is rather peculiar. It shows that the initial part of the jet attached to the die can be almost straight, since it is stabilized by sufficiently large longitudinal stresses generated in the die and still not fully vanished there. On the other hand, when relaxation of the longitudinal stresses significantly reduces their level, bending perturbations grow and begin to release

the stored energy delivered by the initial perturbations (turbulent pulsations) and are also enhanced by the distributed lift force. A renewed significant liquid stretching is expected because of strong bending, which will be also accompanied by drastic thinning of polymeric jet. This behavior is quite similar to the patterns characteristic of electrospun polymer jets. In the latter case the bending force related to the Coulombic repulsion is formally similar to the distributed aerodynamic lift force here (both are proportional to the local curvature of the jet axis) (Yarin et al., 2001). The presence of significant longitudinal viscoelastic stresses in the initial part of electrospun jets stabilizes them and they stay almost straight. Later on, the stresses fade due to viscoelastic relaxation and strong bending begins (Reneker et al., 2000, 2007; Yarin et al., 2001; Han et al., 2008). Correspondingly, meltblown jets can stay initially almost straight due to stabilization by high longitudinal stress. Only after it fades due to the dominant relaxation, a vigorous bending leading to jet elongation and thinning begins.

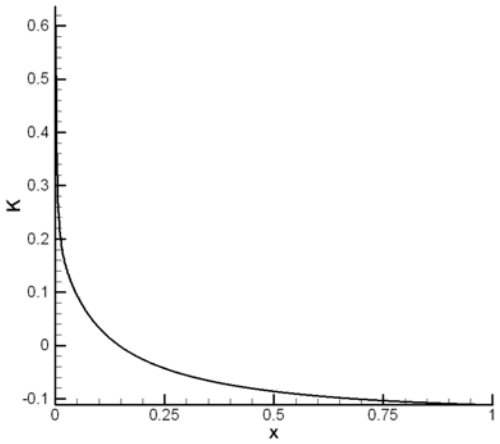

Fig. 8.3. Distribution of K(x).

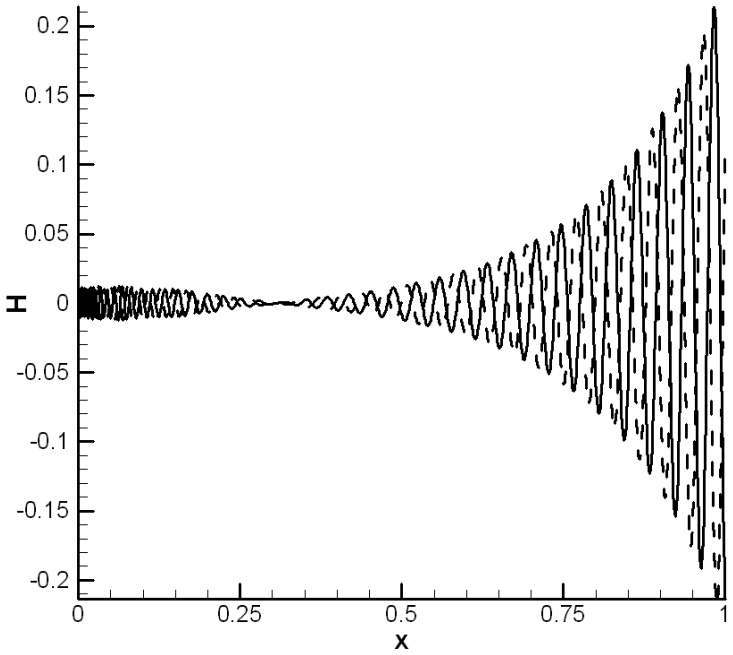

Fig. 8.4. Two snapshots (one shown by solid line, another one by the dashed one) of the predicted traveling wave of the bending perturbations of polymeric jet enhanced by the distributed aerodynamic lift force.

8.4 Nonlinear Behavior: Large-Amplitude Bending Perturbations in the Isothermal Case

In the quasi-one-dimensional theory of liquid jets two types of approaches to describing jet bending (with and without accounting for the bending stiffness) are available (Yarin 1993). In the momentless approximation bending stiffness of very thin liquid jets is neglected compared to the other internal forces affecting bending, since it depends on the cross-sectional jet radius as a^4, while the other forces as a^2 (which is much larger as a tends to zero) (Yarin 1993). In the present section we adopt the momentless approximation and neglect the shearing force in the jet cross-section and the whole moment-of-momentum equation determining it. As a result, the quasi-one-dimensional

equations of the jet dynamics reduce to the autonomous continuity and momentum balance equations in the following form [Eqs. (4.18) on p. 48 in (Yarin 1993)]

$$\frac{\partial \lambda f}{\partial t} + \frac{\partial fW}{\partial s} = 0 \tag{8.31}$$

$$\frac{\partial \lambda f \mathbf{V}}{\partial t} + \frac{\partial fW\mathbf{V}}{\partial s} = \frac{1}{\rho}\frac{\partial P\boldsymbol{\tau}}{\partial s} + \lambda f\mathbf{g} + \frac{\lambda}{\rho}\mathbf{q}_{total} \tag{8.32}$$

In Eqs. (8.31) and (8.32) t is time, s is an arbitrary parameter (coordinate) reckoned along the jet axis, $f(s,t)=\pi a^2$ is the cross-sectional area [the cross-section is assumed to stay circular even in bending jets-a valid approximation according to (Yarin 1993); a(s,t) denotes its radius], W is the liquid velocity along the jet relative to a cross-section with a certain value of s, the stretching factor $\lambda = |\partial \mathbf{R} / \partial s|$, where $\mathbf{R}(s,t)$ is the position vector of the jet axis, $\mathbf{V}(s,t)$ is the absolute velocity in the jet, ρ is liquid density, P(s,t) is the magnitude of the longitudinal internal force of viscoelastic origin in the jet cross-section, $\boldsymbol{\tau}$ is the unit tangent vector of the jet axis, $\mathbf{g}$ is gravity acceleration and $\mathbf{q}_{total}$ is the overall aerodynamic force imposed on unit jet length by the surrounding gas. Boldfaced characters here and hereinafter denote vectors.

Let s be a Lagrangian parameter of liquid elements in the jet (e.g. their initial Cartesian coordinate along the blowing direction). Then, W=0, since the particles keep their Lagrangian coordinate unchanged, and Eq. (31) is integrated to yield

$$\lambda a^2 = \lambda_0 a_0^2 \tag{8.33}$$

where subscript zero denotes the initial values.

Consider for example two-dimensional bending perturbations of the jet (the fully three-dimensional bending can be considered similarly along the same lines(Yarin

1993)). Then, accounting for Eq. (8.33), the two projections of Eq. (8.32) on the directions of the local tangent **τ** and unit normal **n** to the jet axis read

$$\frac{\partial V_\tau}{\partial t} = V_n\left(\frac{1}{\lambda}\frac{\partial V_n}{\partial s} + kV_\tau\right) + \frac{1}{\rho f \lambda}\frac{\partial P}{\partial s} + g_\tau + \frac{q_{total,\tau}}{\rho f} \tag{8.34}$$

$$\frac{\partial V_n}{\partial t} = -V_\tau\left(\frac{1}{\lambda}\frac{\partial V_n}{\partial s} + kV_\tau\right) + \frac{Pk}{\rho f} + g_n + \frac{q_{total,n}}{\rho f} \tag{8.35}$$

where k is the local curvature of the jet axis and subscripts τ and n denote vector projections on the local tangent and normal to the jet axis.

In the case of planar bending, the position vector of the jet axis is described as

$$\mathbf{R} = \mathbf{i}\xi(s,t) + \mathbf{j}H(s,t) \tag{8.36}$$

with **i** and **j** being the unit vectors of the directions of blowing and the directions normal to it, respectively, while the geometric parameters λ and k are given by

$$\lambda = \left(\xi_{,s}^2 + H_{,s}^2\right)^{1/2} \tag{8.37}$$

$$k = \frac{H_{,ss}\xi_{,s} - \xi_{,ss}H_{,s}}{\left(\xi_{,s}^2 + H_{,s}^2\right)^{3/2}} \tag{8.38}$$

The total aerodynamic force is comprised from the distributed longitudinal lift force(Yarin 1993; Entov et al., 1984) [a nonlinear analog of the linearized left force incorporated in Eq. (8.15)], the distributed drag force associate with gas flow across the jet(Yarin 1993; Entov et al., 1984)and the pulling drag force similar to that of Eq. (8.3). Therefore,

$$\mathbf{q}_{\text{total}} = \mathbf{n}q_{\text{total,n}} + \boldsymbol{\tau}q_{\text{total},\tau} =$$
$$-\rho_g U_g^2 \mathbf{n}\left[f\frac{\xi_{,s}^2\left(\mathbf{H}_{,ss}\xi_{,s} - \xi_{,ss}\mathbf{H}_{,s}\right)}{\left(\xi_{,s}^2 + \mathbf{H}_{,s}^2\right)^{5/2}} + a\frac{\left(\mathbf{H}_{,s}/\xi_{,s}\right)^2 \operatorname{sign}\left(\mathbf{H}_{,s}/\xi_{,s}\right)}{1+\left(\mathbf{H}_{,s}/\xi_{,s}\right)^2}\right] \tag{8.39}$$
$$+\pi a\rho_g\left(U_g\tau_\xi - V_\tau\right)^2 0.65\left[\frac{2a\left(U_g\tau_\xi - V_\tau\right)}{\nu_g}\right]^{-0.81}\boldsymbol{\tau}$$

where U_g is the magnitude of the absolute local blowing velocity of gas, and τ_ξ corresponds to its projection on the local direction of the jet axis.

In addition, in Eqs. (8.34) and (8.35) the projections of the gravity acceleration g_τ and g_n are equal to $g_\tau = g\,\tau_\xi$ and $g_n = g n_\xi$ with g being its magnitude and n_ξ the local projection of the unit normal to the jet axis onto the direction of blowing.

The longitudinal internal force of viscoelastic origin in the jet cross-section(Yarin 1993) $P = f(\tau_{\tau\tau} - \tau_{nn})$ where $\tau_{\tau\tau}$ and τ_{nn} are the longitudinal and normal deviatoric stresses in the jet cross-section. As usual, in the case of strong stretching (cf. for example, Section 8.2), $\tau_{\tau\tau} >> \tau_{nn}$ and the latter can be neglected. Then, $P = f\tau_{\tau\tau}$ where the constitutive equation for $\tau_{\tau\tau}$ is provided by the viscoelastic upper-convected Maxwell model (Astarita et al., 1974) (UCM) in the form

$$\frac{\partial\tau_{\tau\tau}}{\partial t} = 2\tau_{\tau\tau}\frac{1}{\lambda}\frac{\partial\lambda}{\partial t} + 2\frac{\mu}{\theta}\frac{1}{\lambda}\frac{\partial\lambda}{\partial t} - \frac{\tau_{\tau\tau}}{\theta} \tag{8.40}$$

Equations (8.33)-(8.35) and (8.37)-(8.40) which describe jet dynamics are supplemented by the following kinematic equations which describe the axis shape

$$\frac{\partial\xi}{\partial t} = V_\tau n_\eta - V_n\tau_\eta \tag{8.41}$$

$$\frac{\partial\mathbf{H}}{\partial t} = V_n\tau_\xi - V_\tau n_\xi \tag{8.42}$$

The projections of the unit vectors associated with the polymer jet axis $\boldsymbol{\tau}$ and $\mathbf{n}$ on the directions of the unit vectors $\mathbf{i}$ and $\mathbf{j}$ associated with the blowing direction and normal to it (ξ and H) are given by the following expressions

$$\tau_{\xi} = n_{\eta} = \left[1 + \left(\mathbf{H}_{,s} / \xi_{,s}\right)^2\right]^{-1/2} \tag{8.43}$$

$$n_{\xi} = -\tau_{\eta} = -\left(\mathbf{H}_{,s} / \xi_{,s}\right)\left[1 + \left(\mathbf{H}_{,s} / \xi_{,s}\right)^2\right]^{-1/2} \tag{8.44}$$

According to the theory of the axisymmetric turbulent gas jets(Abramovich 1963; Yarin 2007), the gas flow field is given by the following expression

$$U_g(\xi, \mathbf{H}) = U_{g0}\varphi(\xi, \mathbf{H}) \tag{8.45}$$

where U_{g0} is the gas velocity of the nozzle exit and the dimensionless function $\varphi(\xi,H)$ is given by

$$\varphi(\xi, \mathbf{H}) = \frac{4.8/\ell}{\left(\xi + 4.8/\ell\right)} \frac{1}{\left(1 + \varsigma^2/8\right)^2}, \quad \varsigma = \varsigma(\xi, \mathbf{H}) = \frac{\mathbf{H}}{0.05\left(\xi + 4.8/\ell\right)} \tag{8.46}$$

In Eq. (8.46) ξ and H are rendered dimensionless by L, the distance between the "initial" cross-section and deposition screen, and ℓ is given by Eq. (8.11).

Neglecting secondary terms, the governing equations of the problem (8.34), (8.35) and (8.40)-(8.42) in the isothermal case can be reduced to the following dimensionless form

$$\frac{\partial^2 \xi}{\partial t^2} = \frac{2}{\mathrm{Re}} \boldsymbol{\Phi} \frac{\partial^2 \xi}{\partial s^2} + \frac{1}{\mathrm{Fr}^2} \tau_{\xi} + J\ell \frac{q_{\mathrm{total},\tau}}{f} \tag{8.47}$$

$$\frac{\partial^2 \mathbf{H}}{\partial t^2} = \left[\frac{\tau_{\tau\tau}}{\mathrm{Re}} - J\varphi^2(\xi, \mathbf{H})\right] \frac{1}{\lambda^2} \frac{\partial^2 \mathbf{H}}{\partial s^2} + \frac{n_{\xi}}{\mathrm{Fr}^2} - J\ell \frac{\varphi^2(\xi, \mathbf{H})}{\pi a} \frac{\left(\mathbf{H}_{,s} / \xi_{,s}\right)^2 \operatorname{sign}\left(\mathbf{H}_{,s} / \xi_{,s}\right)}{1 + \left(\mathbf{H}_{,s} / \xi_{,s}\right)^2} \tag{8.48}$$

where $\boldsymbol{\Phi} = \left(\tau_{\tau\tau} + 1/\mathrm{De}\right)\lambda^{-2}$ satisfies the following equation

$$\frac{\partial \Phi}{\partial t} = -\frac{\tau_{\tau\tau}}{De\lambda^2} \tag{8.49}$$

In Eq. (47)

$$q_{total,\tau} = \pi a\left[\tau_\xi \varphi(\xi, H) - V_\tau\right]^2 0.65\left\{Re_a\, a\left[\tau_\xi \varphi(\xi, H) - V_\tau\right]\right\}^{-0.81} \tag{8.50}$$

The following scales have been used: L/U_{g0} for t; L for s, ξ and H; L^{-1} for k; $\mu\, U_{g0}/L$ for $\tau_{\tau\tau}$ and Φ; U_{g0} for U_g, V_τ and V_n; a_0 for a (and a_0^2 for f); $\rho_g U_{g0}^2 a_0$ for $q_{total,\tau}$; μ/ρ for the kinematic turbulent eddy viscosity ν_t (used below; cf. Chapter 7). As a result, the following dimensionless groups arise in addition to $\ell = L / a_0$

$$Re = \frac{\rho L U_{g0}}{\mu}, \quad J = \frac{\rho_g}{\rho}, \quad Fr = \left(\frac{U_{g0}^2}{gL}\right)^{1/2}, \quad Re_a = \frac{2a_0 U_{g0}}{\nu_g}, \quad De = \frac{\theta U_{g0}}{L} \tag{8.51}$$

where Re and Re_a are the corresponding Reynolds numbers, Fr is the Froude number and De is the Deborah number.

Based on the results in Chapter 7, we assume that turbulent pulsations in the gas jet impose lateral perturbations at the origin of the polymer melt jet at $s=s_{origin}$. Therefore, similarly to Eq. (8.11) and using the results of Chapter 7, the boundary conditions for Eqs. (8.47) and (8.48) are given by the following dimensionless expressions

$$\xi\big|_{s=s_{origin}} = 0, \quad H\big|_{s=s_{origin}} = H_{0\Omega} \exp(i\Omega t) \tag{8.52}$$

where

$$H_{0\Omega} = \left(0.06\, Re^{1/2} / \ell\right)^{1/2} / \tau_{\tau\tau 0}^{1/4}, \qquad \Omega = \frac{\omega L}{U_{g0}} \tag{8.53}$$

with $\tau_{\tau\tau 0}$ being the dimensionless longitudinal stress in the jet inherited from the nozzle. On the other hand, at the free end $s=s_{free\ end}$ the jet is assumed to be fully unloaded, i.e.

$$\xi_{,s}\Big|_{s_{\text{free end}}} = 1, \qquad \mathbf{H}\Big|_{s_{\text{free end}}} = 0 \tag{8.54}$$

The initial condition for Eq. (8.49) at the moment when a liquid element leaves the nozzle and enters the jet t_{birth} reads

$$\boldsymbol{\Phi}\Big|_{t=t_{\text{birth}}} = \left(\tau_{\tau\tau 0} + 1/\mathrm{De}\right)/\lambda_0^2 \tag{8.55}$$

8.5. Nonlinear Behavior: Non-isothermal Case

In the non-isothermal case polymer melt is surrounded by hot gas jet, which is blowing into the space filled with cold gas. As a result, the gas jet is cooled and the encased polymer melt jet is cooled either and solidifies. Following (Yarin 1993), we assume that the viscosity and relaxation time of polymer melt vary with melt temperature T according to the following expressions

$$\mu = \mu_0 \exp\left[\frac{U}{R}\left(\frac{1}{T} - \frac{1}{T_0}\right)\right], \quad \theta = \theta_0 \frac{T_0}{T}\exp\left[\frac{U}{R}\left(\frac{1}{T} - \frac{1}{T_0}\right)\right] \tag{8.56}$$

where T_0 is the melt and gas jet temperature at the origin, μ_0 and θ_0 are the corresponding values of the viscosity and relaxation time, U is the activation energy of viscous flow and R is the absolute gas constant.

The thermal balance equation for a jet element reads

$$\frac{\partial}{\partial t}\left(\rho c T f \lambda\right) = -h\left(T - T_g\right)2\pi a\lambda \tag{8.57}$$

where c is the specific heat, h is the heat transfer coefficient and T_g the local gas temperature.

Using Eq. (8.33) and rendering temperatures T and T_g dimensionless by T_0, rearrange Eq. (8.57) to the following dimensionless form

$$\frac{\partial T}{\partial t} = -2\mathrm{Nu}\ell \frac{JC}{\mathrm{Re}_a \mathrm{Pr}_g} \frac{\lambda}{\lambda_0}\left(T - T_g\right) \tag{8.58}$$

where Pr_g is the molecular Prandtl number for gas, $C=c_{pg}/c$ is the ratio of the specific heat at constant pressure for gas to the specific heat for polymer melt, and the Nusselt number $\mathrm{Nu}=(h2a/k_g)$, with k_g being the molecular thermal conductivity of gas, is given by the following expression(Yarin et al., 2001)

$$\mathrm{Nu} = 0.495\,\mathrm{Re}_a^{1/3}\,\mathrm{Pr}_g^{1/2} \tag{8.59}$$

Substituting Eqs. (8.56) into Eq. (8.40) and using Eq. (8.58), we obtain the following dimensionless rheological constitutive equation replacing Eq. (49)

$$\frac{\partial \Phi}{\partial t} = -\frac{2\mathrm{Nu}\ell JC}{\mathrm{Re}_a \mathrm{Pr}_g \mathrm{De}_0 \lambda_0}\frac{\left(T - T_g\right)}{\lambda} - T\exp\left[-U_A\left(\frac{1}{T}-1\right)\right]\frac{\tau_{\tau\tau}}{\mathrm{De}_0\lambda^2} \tag{8.60}$$

with $\Phi = \left(\tau_{\tau\tau} + T/\mathrm{De}_0\right)/\lambda^2$ and the following two additional dimensionless groups involved

$$\mathrm{De}_0 = \frac{\theta_0 U_{go}}{L}, \quad U_A = \frac{U}{RT_0} \tag{8.61}$$

Using the theory of the axisymmetric turbulent gas jets (Yarin 2007), the temperature field in the gas jet is given by the following expression

$$T_g(\xi, H) = T_{g\infty} + \frac{\left(\mathrm{Pr}_t + 1/2\right)}{0.05\sqrt{6}}\frac{\left(1 - T_{g\infty}\right)}{\ell}\frac{1}{\left(\xi + 4.8/\ell\right)}\frac{1}{\left(1+\varsigma^2/8\right)^{2\mathrm{Pr}_t}} \tag{8.62}$$

where $T_{g\infty}$ is the surrounding cold gas temperature far from the polymer jet rendered dimensionless by T_0, the turbulent Prandtl number $\mathrm{Pr}_t=0.75$, and $\zeta(\xi,H)$ is given by the second Eq. (8.46).

It is emphasized that the other governing equations of the problem, e.g. Eqs. (8.46)-(8.48) and (8.50) do not change in the non-isothermal case.

8.6 Results and Discussion

The governing equation (8.48) is a hyperbolic wave equation for $\xi(s,t)$, which corresponds to propagation of the elastic compression-expansion waves along the jet (the "elastic sound"). The second governing equation (8.49) responsible for the propagation of the bending perturbations H(s,t) is a hyperbolic wave equation if jet is stretched significantly, i.e. $\left[\tau_{\tau\tau}/\mathrm{Re}-\mathrm{J}\varphi^2(\xi,\mathbf{H})\right]>0$. If the longitudinal jet stretching would fade due to the elastic relaxation and the distributed lift force $\mathrm{J}\varphi^2(\xi,\mathbf{H})$ would become dominating, Eq. (8.49) changes type and becomes elliptic, since the factor $\left[\tau_{\tau\tau}/\mathrm{Re}-\mathrm{J}\varphi^2(\xi,\mathbf{H})\right]$ becomes negative. This behavior has already been mentioned in the linearized version of this problem in Section 8.3, which has drastic consequences on perturbation growth.

The following parameter values partially corresponding to those of (Marheineke et al., 2007) were used in the numerical calculations: $a_0=0.2$ cm, L=200 cm, U_{g0}=230 m/s, ρ=1 g/cm^3, $\mu=10^2$ g/(cm s), $\rho_g=1.22\times10^{-3}\,\mathrm{g/cm^3}$. Therefore, the corresponding values of Re, J and ℓ were about Re=46000, J=10^{-3} and $\ell=10^3$. The effect of gravity was excluded, which corresponds to $\mathrm{Fr}=\infty$. The initial longitudinal elastic stress was taken as $\tau_{\tau\tau0}$=10 and λ_0=1. The relaxation time was taken about θ=0.1 s, which corresponds to De=10. In addition, it was taken C=0.25 and Ω=0.3 (the latter corresponds to ω=35 Hz; cf. chapter 7). Also, $T_{g\infty}=0.5$ and U_A=10. The value of $\mathrm{Re_a}$ for air (ν_g=0.15 cm^2/s) is

about 46000. However, at such value of Re_a the pulling aerodynamic drag described by Eq. (8.50) is insufficient to initiate meltblowing. This might be related to the fact that the empirical Eq. (8.50) was established in (Ziabicki et al., 1985) in the experiments with threadlines pulled through stagnant air. However, drag imposed by blowing air may be dramatically increased due to the turbulent eddy viscosity (absent in the experiments (Ziabicki et al., 1985)). To account for that fact, the factor 0.65 in Eq. (8.50) was replaced by 1265. Then, the aerodynamic drag as per Eq. (8.50) became quite sufficient to initiate meltblowing.

The implicit numerical scheme of the generalized Crank-Nicolson type with the central difference special discretisation at three time levels from (Mattheij et al., 2005) (p. 444) was implemented to solve Eqs. (8.47) and (8.48) numerically.

The mean axisymmetric velocity and temperature fields in the central domain close to the jet origin calculated using Eqs. (8.45), (8.46) and (8.62) are presented in Fig. 8.5. Since the turbulent Prandtl number Pr_t is less than 1 (Pr_t=0.75), the temperature profile in the gas jet is wider than the velocity profile.

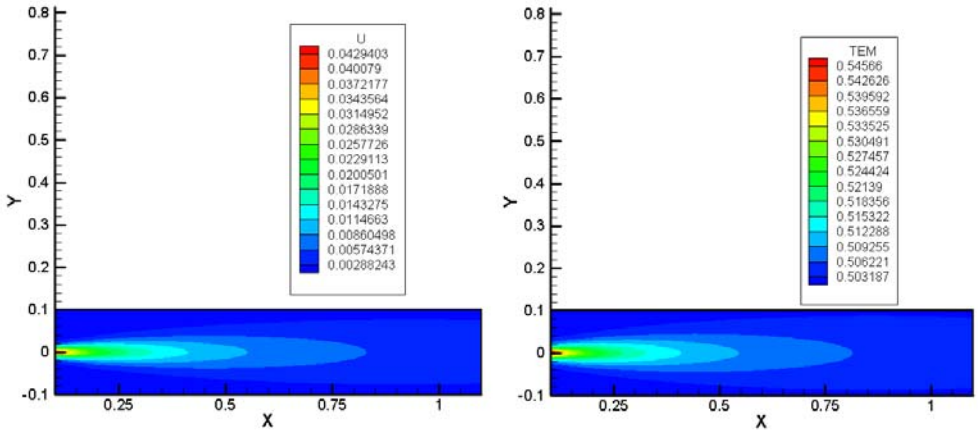

Fig. 8.5. Axisymmetric velocity (left) and temperature (right) fields in the gas jet.

The predicted configurations of the jet axis in the isothermal planar blowing process are depicted in Fig. 8.6. It is seen that the polymer jet is pulled and strongly stretched by the co-flowing gas jet. The polymer jet also experiences lateral perturbations due to turbulent eddies. These bending perturbations are significantly enhanced by the distributed aerodynamic lift force acting on the curved polymer jet. They also propagate along the polymer jet as elastic waves, and are additionally swept by local aerodynamic drag force acting on the jet elements. The configurations of the polymer jet can become rather complicated and self-intersecting in a while (Fig. 8.6a), which is possible for a "phantom" jet but forbidden to a real material one. Still, the evolution similar to that in Fig. 8.6b points at possible self-intersection in meltblowing, even in the case of a single jet considered here.

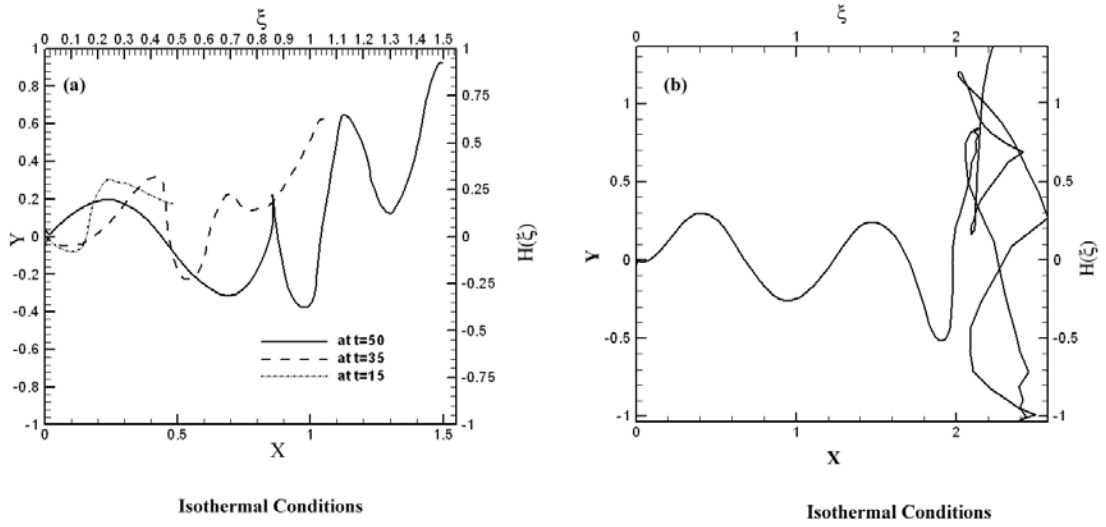

Fig. 8.6. Isothermal planar blowing. (a) Three snapshots of the axis configuration of polymer jet at the dimensionless time t=15, 35 and 50 (the corresponding dimensional times are 0.13 s, 0.3 s and 0.43 s, respectively). (b) The later snapshot of the polymer jet axis corresponding to the dimensionless time t=75 (the corresponding dimensional time is 0.65 s).

If one follows individual material Lagrangian elements of the polymer jet, as we do in our calculations, their distribution along the jet allows visualization of a non-uniform jet stretching**.** Indeed, these material elements are visualized by symbols on the jet axis in Fig. 8.7. The larger is the distance along the jet between two neighboring symbols, the larger is the local stretching of viscoelastic polymer melt in the corresponding jet section. Figure 8.7 clearly shows that initially jet stretching is quite significant and growing in time (from snapshot to snapshot in Fig. 8.7), however, it can deteriorate further on due to the elastic recoil characteristic of viscoelastic polymer melts, as well as a decreasing stretching by the gas jet, which weakens down the flow.

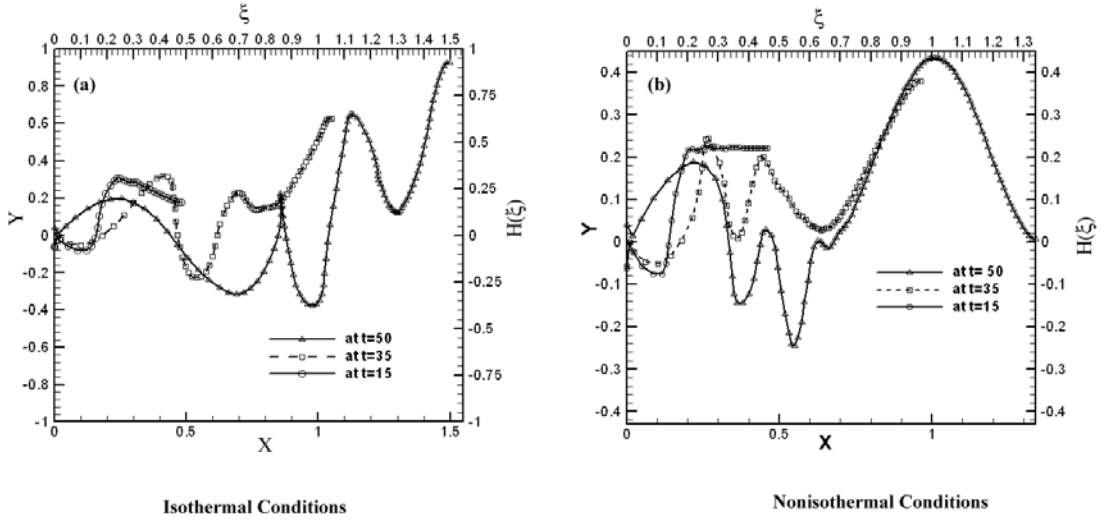

Fig. 8.7. (a) Three snapshots of the polymer jet axis in the isothermal planar blowing at the dimensionless time t=15, 35 and 50 (the corresponding dimensional times are 0.13 s, 0.3 s and 0.43 s, respectively) with the symbols denoting the material elements of the jet. (b) Same in the non-isothermal planar blowing.

Comparison of Figs. 8.7a and 8.7b allows us to visualize the effect of cooling and solidification of the polymer jet. In particular, it is seen that the growth of the bending perturbations of the jet is arrested similarly to the electrospun jets described in (Yarin et al., 2001). However, the jet does not become straight but continues to sustain traveling bending perturbations similarly to the flexible solid threadlines studied in Chapter 7.

The predictions for the isothermal three-dimensional blowing are shown in Fig. 8.8. In this case the configuration of the jet axis is described using the following three projections $\xi = \xi(s)$, $\mathbf{H} = \mathbf{H}(s)$ and $\mathbf{Z} = \mathbf{Z}(s)$ instead of the two, $\xi = \xi(s)$ and $\mathbf{H} = \mathbf{H}(s)$, used in the planar case. The tendency for self-intersection of the polymer jet is clearly seen in the three-dimensional case as well.

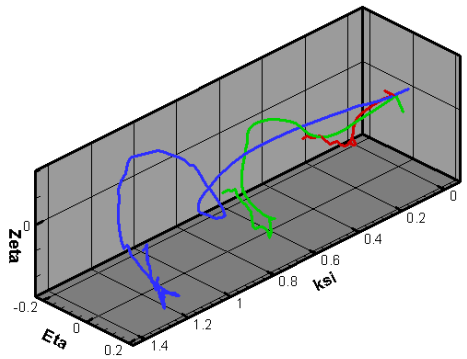

Fig. 8.8. Three snapshots of the polymer jet axis in the isothermal three-dimensional blowing at the dimensional time moments t=15, 30 and 45 (the corresponding dimensional times are 0.13 s, 0.26 and 0.39 s, respectively).

8.7 Conclusion

The linear and nonlinear theory of meltblowing developed in this work explains the physical mechanisms responsible for jet configurations, and in particular the role of the

turbulent pulsations in gas jet, of the aerodynamic lift and drag forces, as well of the longitudinal viscoelastic stress in the polymer jet. The theory produces a plausible pattern of the evolution of the jet in time and allows modeling of not only planar but also three-dimensional jets. The current version of the theory deals with a single polymer jet. The further development will proceed towards calculations of multiple jets and their interaction and even merging with each other-the processes responsible for such defects of meltblown products as roping. Self-intersection of polymer jets visualized by the present results can lead to jet rupture in the case of violent blowing which results in the so-called fly (small jet segments contaminating the surrounding atmosphere). The mechanism of fly formation can also be elucidated by future development of the current model. Formation of the so-called shots resulting from capillary breakup of polymer jets at too high surrounding temperatures will also be targeted after inclusion of capillarity in the model similarly to (Yarin 1993). A comprehensive model of meltblowing requires simulation of polymer flow in die nosepiece, which will be aimed in the future model development. The last but not least goal is in the prediction of the internal structure in the fibers comprising nonwovens resulting from meltblowing. This information can be elucidated relating the predicted longitudinal stresses “frozen” in the jet at the deposition screen to such characteristic features as crystallininty and ultimately strength.

9. MELTBLOWING: MULTIPLE POLYMER JETS AND FIBER-SIZE DISTRIBUTION

9.1 Introduction

The basic theory of meltblowing was outlined in the previous two Chapters (Chapters 7 and 8) where planar bending of a polymeric viscoelastic liquid jet in a high speed gas flow was described in detail. Both isothermal and non-isothermal situations were studied. However, only a single jet was considered and deposition onto a screen was disregarded. Without accounting for the presence of multiple jets and their deposition onto a screen, such practically important questions as fiber-size distribution on the nonwoven and deposition patters cannot be addressed. The latter are the main aim of the present work.

Section 9.2 describes the theoretical framework for the description of the straight part of meltblown polymer jet, while section 9.3 contains the corresponding theoretical results and compares them to the available experimental data. Section 9.4 deals with the governing equations for three-dimensional bending of meltblown jets. Then, section 9.5 describes the results for meltblowing of multiple non-isothermal polymer jets and discusses the results in comparison with the available experimental data. Conclusions are drawn in section 9.6.

9.2 Theoretical: The Initial Straight Part of the Jet

The present section modifies the previous results of Chapter 8 to make them appropriate for the description of the initial part of real jets in meltblowing, which will be

used as a subroutine in the general numerical code for simulations of multiple three-dimensional nonisothermal polymer jets depositing on a moving substrate. In real meltblowing processes polymer jets are issued from dies in a nosepiece at a relatively low speed of about 10 cm/s. They are issued into concentric gas jets with velocities of the order of 100-250 m/s. As a result, polymer jets experience a tremendous pulling force at their initial part (of the order of 1 mm from the die) and rapidly accelerate. The concentric gas jets are formed by oblique impingement of several gas jets surrounding a polymer jet, which produces a significant circular force sustaining straight configuration of the initial part of the latter. In addition, polymer jets at the initial part are still sufficiently thick and possess a significant bending stiffness, which precludes any bending, similarly to the situation encountered in electrospinning (Reneker et al., 2000). It is emphasized that over such a short distance the velocity of the concentric submerged gas jet practically does not fade due to viscous interaction with the surrounding air and will be assumed to be constant in the present section.

The following quasi-one-dimensional stead-state continuity and momentum balance equations are used to describe the initial straight part of the jet in Chapter 8

$$\frac{dfV_\tau}{dx} = 0, \quad f = \pi a^2 \tag{9.1}$$

$$\rho \frac{dfV_\tau^2}{dx} = \frac{d\sigma_{xx} f}{dx} + q_\tau \tag{9.2}$$

where x is the axial coordinate reckoned from the die exit, $f(x)=\pi a^2$ and a(x) are the cross-sectional area and radius, respectively, and $V_\tau(x)$ is the absolute axial velocity of the polymer jet; σ_{xx} is the internal stress in liquid in the jet cross-section.

The stretching aerodynamic drag force per unit jet length q_τ described similarly to Chapters 7 and 8

$$q_\tau = C\pi a\rho_g (U_g - V_\tau)^2 \left[\frac{2\left(U_g - V_\tau\right)a}{\nu_g}\right]^{-0.81} \tag{9.3}$$

In Eq. (9.3), U_g is the absolute velocity of the concentric gas jet, and ρ_g and ν_g are the gas density and kinematic viscosity, respectively.

Equation (9.3) is, in fact, empirically based and stems from the experiments, in which a wire or filament were pulled parallel to itself through stagnant air, as described in (Ziabicki et al., 1985) and references therein. It was used in Chapter 8 with the pre-factor established in the above-mentioned work, C=0.65. While the general structure of Eq (9.3) is physically sound, the modeling in Chapter 8 demonstrated that this value is probably underestimated and should be increased, since otherwise it is impossible to achieve a proper pulling force to stretch viscoelastic polymeric jets. The underestimation of the value of C in the experiments described in (Ziabicki et al., 1985) and references therein, most probably, has deep physical roots. Indeed, the situation where a wire is pulled through stagnant air with a certain speed is not equivalent to the situation where non-moving wire (or a jet, as in meltblowing) is subjected to parallel gas flow with the same speed, since in the latter case turbulent eddy viscosity is expected to be higher and thus the drag force, and thus C, should be higher. An additional circumstance which points out at an additional increase in the value of C is related to the fact that in the experiments where it was established velocities never approached levels characteristic of meltblowing, so sufficiently high turbulence levels were not reached. Due to all these circumstances, while keeping the general structure of Eq. (9.3) with no change, the value of C was

increased to C=100, which was validated a posteriori by the comparison with the experimental data for meltblowing as described below.

Equation (9.1) has an integral which allows one to exclude a from the further consideration via expressing it in terms of V_τ

$$\pi a^2 V_\tau = \pi a_0^2 V_{\tau 0} \tag{9.4}$$

where the subscript 0 corresponds to the die exit where the radius and velocity values are assumed to be given.

Equations (9.1) and (9.2) are supplanted by the rheological constitutive equation for the longitudinal and radial deviatoric stresses τ_{xx} and τ_{yy} in the jet cross-section, while $\sigma_{xx}=\tau_{xx}-\tau_{yy}$. Similarly to (Pinchuk et al., 2002), the upper-convected Maxwell model (UCM) is used as an appropriate rheological constitutive model for viscoelastic polymeric liquids in such strong elongational flows as in meltblown jets.

Following (Pinchuk et al., 2002), Eqs. (9.2)-(9.4) supplemented with the UCM reduce to the following dimensionless equations

$$\frac{dV_\tau}{dx} = \frac{\left[-E(\tau_{xx}-\tau_{yy})/(DeV_\tau^2)+q_\tau\right]}{\left[1-E(\tau_{xx}+2\tau_{yy}+3)/V_\tau^2\right]} \tag{9.5}$$

$$\frac{d\tau_{xx}}{dx} = \frac{1}{V_\tau}\left(2\frac{dV_\tau}{dx}\tau_{xx}+2\frac{dV_\tau}{dx}-\frac{\tau_{xx}}{De}\right) \tag{9.6}$$

$$\frac{d\tau_{yy}}{dx} = \frac{1}{V_\tau}\left(-\frac{dV_\tau}{dx}\tau_{yy}-\frac{dV_\tau}{dx}-\frac{\tau_{yy}}{De}\right) \tag{9.7}$$

where

$$q_\tau = C\left(R\ell/V_\tau^{1/2}\left\{U_g-V_\tau\right\}^2\left[Re(U_g-V_\tau)/V_\tau^{1/2}\right]^{-0.81}\right) \tag{9.8}$$

The equations are rendered dimensionless by the following scales: $V_{\tau 0}$ for V_τ and U_g, the distance of the initial straight part $L_{straight}$ for x, a_0 for a, μ_0/θ_0 (with μ_0 and θ_0 being the viscosity and relaxation time of polymeric liquid at the die temperature T_0) for deviatoric stresses The dimensionless groups involved in Eqs. (9.5)-(9.8) are given by

$$R = \frac{\rho_g}{\rho}, \quad \ell = \frac{L_{straight}}{a_0}, \quad Re = \frac{2V_{\tau 0}a_0}{\nu_g}, \quad De = \frac{\theta_0 V_{\tau 0}}{L_{straight}} \tag{9.9}$$

with Re and De being the Reynolds and Deborah numbers, respectively, with the secondary dimensionless groups being

$$E = \frac{2R}{De\ell Re M}, \quad M = \frac{\mu_g}{\mu_0} \tag{9.10}$$

In Eq. (9.10) μ_g denotes gas viscosity.

9.3 The Initial Straight Part of Meltblown Jets: Numerical Results, Discussion and Comparison with Experimental Data

In the calculations of the initial straight part of the jet the following parameter values corresponding to real practical meltblowing conditions were used. In a typical meltblowing process the polymer throughput through every die in a nosepiece of radius of the order of 100 μm, is of the order of 0.3-1.0 g/min, which means that $V_{\tau 0} \approx 0.17 - 0.5$ m/s. The typical value of gas velocity is of the order of 150 m/s. Using this data, the value of the dimensionless gas velocity $U_g/V_{\tau 0}$ was taken in the experiment as 390, whereas the value of Re used was Re=7.5. The initial length scale of the straight part $L_{straight}$ is of the order of 1 mm, which makes $\ell = 10$. The relaxation time θ_0 is of the order of 10^{-2} s, which might be expected for strong elongational processes, where the leading physical mechanism of relaxation will be associated with the recoil of stretched

macromolecular coils (Yarin 1993; Doi 1980). Then, a reasonable value of the Deborah number De was taken as De=1.59. Following Chapter 8, the values of M and R both were taken to be 0.001. A sufficiently long die channel allows longitudinal elastic stresses acquired in the flow inside to relax. Therefore, the value of the longitudinal deviatoric stress τ_{xx0} was taken to be as low as τ_{xx0}=0.0001. It was found that any further decrease in the value of τ_{xx0} does not affect the results.

Equation (9.5)-(9.8) were solved numerically using the Kutta-Merson method and the predicted distributions of the jet radius and velocity, as well as of the longitudinal deviatoric stress are plotted in Figs. 9.1a-c. As expected, the values of the radial deviatoric stress are practically immaterial compared to τ_{xx}, the result similar to that of Chapter 8, and thus not shown here.

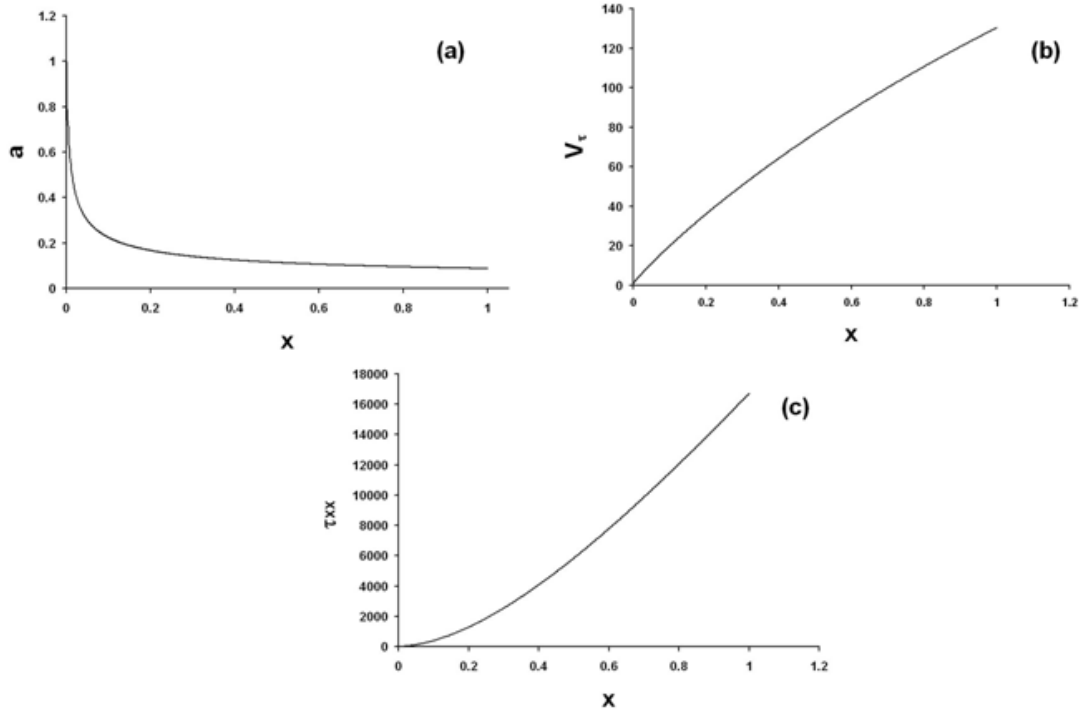

Fig. 9.1. Distributions of (a) dimensionless cross-sectional radius, (b) axial velocity and (c) longitudinal deviatoric stress along the polymer jet.

Figure 9.1a shows that the value of the dimensionless radius at the end becomes 0.0875, which translates into the dimensional value of 8.75 μm. The figure demonstrates that an abrupt decrease in the cross-sectional radius happens close to the exit from a die. Figure 9.1b demonstrates that at the end of the straight part the polymer jet its velocity is already about 30% of the velocity of the surrounding gas jet. In comparison, mention that the experimental data of (Breese et al., 2003) show that at a distance of about 5 mm from the die the velocity of the meltblown polymer jet had already been increased up to 43% of the velocity of the surrounding gas jet, which is the level comparable with our numerical prediction. A more detailed comparison with the experimental data(Breese et al., 2003) is, unfortunately, impossible due to the lack of a number of crucial input parameters characterizing the experimental situation, as well as an insufficient number of the experimental points available. In addition, mention that the experimental data of (Shambaugh 1988) show that at the die to collector distance (DCD) of 6 mm the fiber diameter was 49 μm at the blowing speed of 123.2 m/s, whereas at the DCD of 7 mm the fiber diameter was 117 μm. These value are about 5-10 times higher than our prediction of 8.75 μm. However, the difference can be attributed to the following factors: (a) the lack of the detailed rheological data for the melt blown in (Shambaugh 1988); (b) the unspecified differences in the operating conditions; (c) the as-formed fibers were deposited on screen in (Shambaugh 1988), which allows the fibers to relax and increase their cross-sectional size, which was not considered by the theory here. Nevertheless, the trend observed in the experiments of (Shambaugh 1988) is quite clear. In qualitative

agreement with our predictions, it shows that there was a significant decrease in fiber diameter already at a distance of about 1 mm from the die.

Note also, that Fig. 9.1c that at the end of the straight part the polymer jet already quite significant longitudinal stress, which can be attributed to the strong stretching in the initial part of the jet.

The conditions at the end of the initial straight part of the jet will be been taken as the initial condition for the bending part, which begins from there on and is described in the following section.

9.4 Theoretical: Bending Part of the Jet

After the straight part of the jet becomes sufficiently thin, its bending stiffness becomes very small (since it is proportional to a^4) and small bending perturbations which are imposed on the jet, begin to grow. The description of the bending part of the jet is based on the general momentless quasi-one-dimensional equations of the dynamics of free liquids jets (Chapter 8; Yarin 1993). In distinction from Chapter 8, in the present section we deal not with planar bending of the jet but rather with the fully three-dimensional bending.

The governing equations read

$$\frac{\partial \lambda f}{\partial t} + \frac{\partial f W}{\partial s} = 0 \tag{9.11}$$

$$\frac{\partial \lambda f \mathbf{V}}{\partial t} + \frac{\partial f W \mathbf{V}}{\partial s} = \frac{1}{\rho}\frac{\partial P \boldsymbol{\tau}}{\partial s} + \lambda f \mathbf{g} + \frac{\lambda}{\rho}\mathbf{q}_{\text{total}} \tag{9.12}$$

where Eq. (9.11) expresses the mass balance (the continuity equation) and Eq. (9.12) the momentum balance. Note that Eqs. (9.1) and (9.2) for a straight jet follow from the general Eqs. (9.11) and (9.12).

In Eqs. (9.11) and (9.12) t is time, s is an arbitrary parameter (coordinate) reckoned along the jet axis, $f(s,t)=\pi a^2$ is the cross-sectional area [the cross-section is assumed to stay circular even in bending jets-a valid approximation according to (Chapter 8; Yarin1993) ; a(s,t) denotes its radius], W is the liquid velocity along the jet relative to a cross-section with a certain value of s, the stretching factor $\lambda = |\partial \mathbf{R} / \partial s|$, where **R**(s,t) is the position vector of the jet axis, **V**(s,t) is the absolute liquid velocity in the jet, ρ is liquid density, P(s,t) the magnitude of the longitudinal internal force of viscoelastic origin in the jet cross-section, **τ** is the unit tangent vector of the jet axis, **g** gravity acceleration and $\mathbf{q}_{total}$ is the overall aerodynamic force imposed on unit jet length by the surrounding gas. Boldfaced characters here and hereinafter denote vectors. P(s,t) can be expressed as $f(\tau_{\tau\tau} - \tau_{nn})$, where $\tau_{\tau\tau}$ and τ_{nn} are the are the longitudinal and normal deviatoric stresses in the jet cross-section respectively. In case of strong stretching and in meltblown jets, one can expect that the inequality $\tau_{\tau\tau} >> \tau_{nn}$, holds (cf. section 9.2), and thus $P= f\tau_{\tau\tau}$.

Let s be a Lagrangian parameter of liquid elements in the jet (e.g. their initial Cartesian coordinate along the blowing direction). Then, W=0, since the particles keep their Lagrangian coordinate unchanged, and Eq. (11) after integration reduces to

$$\lambda a^2 = \lambda_{0,straight} a^2_{0,straight} \tag{9.13}$$

where subscript 0,straight denotes the values corresponding to the end of the straight part of the jet predicted in section 9.2.

The local projections of the momentum balance equation (9.12) on the tangent, normal and binormal to the jet axis, after several minor terms are omitted for simplicity, read

$$\frac{\partial V_\tau}{\partial t} = \frac{1}{\rho f \lambda}\frac{\partial \tau_{\tau\tau} f}{\partial s} + g_\tau + \frac{q_{total,\tau}}{\rho f} \tag{9.14}$$

$$\frac{\partial V_n}{\partial t} = \frac{k\tau_{\tau\tau}}{\rho} + g_n + \frac{q_{total,n}}{\rho f} \tag{9.15}$$

$$\frac{\partial V_b}{\partial t} = g_b + \frac{q_{total,b}}{\rho f} \tag{9.16}$$

where k is the local curvature of the jet axis and subscripts τ , n and b denote the projections of the directions of the local unit tangent, normal and binormal, $\boldsymbol{\tau}$, **n** and **b**, respectively.

The position vector **R**(s,t) and the corresponding stretching ratio λ(s,t) are expressed as

$$\mathbf{R}(s,t) = \mathbf{i}\xi(s,t) + \mathbf{j}H(s,t) + \mathbf{k}Z(s,t) \tag{9.17}$$

$$\lambda = \left|\frac{\partial \mathbf{R}}{\partial s}\right| = \left(\xi_{,s}^2 + H_{,s}^2 + Z_{,s}^2\right)^{1/2} \tag{9.18}$$

where ξ, H and Z denote projections of the position vector on the laboratory Cartesian frame with the unit vector **i** corresponding to the direction of blowing and **j** and **k** the other two unit vectors.

The local curvature of the jet axis corresponding to the position vector of Eq. (9.17) is

$$k = \frac{\sqrt{\left(Z_{,ss}H_{,s} - H_{,ss}Z_{,s}\right)^2 + \left(\xi_{,ss}Z_{,s} - Z_{,ss}\xi_{,s}\right)^2 + \left(H_{,ss}\xi_{,s} - \xi_{,ss}H_{,s}\right)^2}}{\lambda^3} \tag{9.19}$$

Each s in the subscript corresponds to differentiation in the s direction.

The velocity components are related with the rate of jet axis evolution according to the following kinematic relations

$$V_n = n_\xi \frac{\partial \xi}{\partial t} + n_\eta \frac{\partial H}{\partial t} + n_\zeta \frac{\partial Z}{\partial t} \tag{9.20}$$

$$V_b = b_\xi \frac{\partial \xi}{\partial t} + b_\eta \frac{\partial H}{\partial t} + b_\zeta \frac{\partial Z}{\partial t} \tag{9.21}$$

$$V_\tau = \tau_\xi \frac{\partial \xi}{\partial t} + \tau_\eta \frac{\partial H}{\partial t} + \tau_\zeta \frac{\partial Z}{\partial t} \tag{9.22}$$

The aerodynamic force (cf. Chapter 8) $\mathbf{q}_{total}$, which consists of the normal, bending component and drag force, as well as the longitudinal pulling component is given by the following expression

$$\mathbf{q}_{total} = -\rho_g U_g^2 fk\mathbf{n} + \rho_g U_g^2 an_\xi^2 sign(n_\xi)\mathbf{n} + C\pi a\rho_g \left(U_g\tau_\xi - V_\tau\right)^2 \left[\frac{2a\left(U_g\tau_\xi - V_\tau\right)}{\nu_g}\right]^{-0.81} \boldsymbol{\tau} \tag{9.23}$$

where U_g is the absolute local velocity of surrounding gas jet, which is given by (cf. Chapter 8)

$$U_g(\xi, \mathbf{H}) = U_{g0}\varphi(\xi, \mathbf{H}) \tag{9.24}$$

In equation (9.24) U_{g0} is the gas velocity of the die exit and the dimensionless function φ(ξ,H) is given by (Yarin 2007; Chapter 8)

$$\varphi(\xi, \mathbf{H}) = \frac{4.8/\ell}{\left(\xi + 4.8/\ell\right)} \frac{1}{\left(1 + \zeta^2/8\right)^2}, \quad \zeta = \zeta(\xi, \mathbf{H}) = \frac{\mathbf{H}}{0.05\left(\xi + 4.8/\ell\right)} \tag{9.25}$$

In Eq. (9.25) ξ and H are rendered dimensionless by L, the distance between the end of the straight part of the jet and the deposition screen, and ℓ is given by $L/a_{0,straight}$.

For the constitutive equation for the longitudinal deviatoric stress similarly to section 9.2 the upper convected Maxwell model (UCM) is used

$$\frac{\partial \tau_{zz}}{\partial t} = 2\tau_{zz}\frac{1}{\lambda}\frac{\partial \lambda}{\partial t} + 2\frac{\mu}{\theta}\frac{1}{\lambda}\frac{\partial \lambda}{\partial t} - \frac{\tau_{zz}}{\theta} \tag{9.26}$$

In the long bending part of the jet variation of the rheological constitutive parameters with the decrease in temperature T is felt and described using the following expressions for the viscosity μ and relaxation time θ similarly to Chapter 8

$$\mu = \mu_0 \exp\left[\frac{U}{R}\left(\frac{1}{T} - \frac{1}{T_0}\right)\right], \quad \theta = \theta_0 \frac{T_0}{T}\exp\left[\frac{U}{R}\left(\frac{1}{T} - \frac{1}{T_0}\right)\right] \tag{9.27}$$

where T_0 is the melt and gas jet temperature at the end of straight part which is practically the same as at the die exit, μ_0 and θ_0 are the corresponding values of the viscosity and relaxation time, U is the activation energy of viscous flow and R is the absolute gas constant.

The thermal balance equation for a jet element reads

$$\frac{\partial}{\partial t}\left(\rho c T f \lambda\right) = -h\left(T - T_g\right)2\pi a\lambda \tag{9.28}$$

where c is the specific heat, h is the heat transfer coefficient and T_g the local gas temperature.

The governing equations are rendered dimensionless using the following scales: U_{g0} for all the velocities, $a_{0,straight}$ for a, $a_{0,straight}^2$ for f, L/U_{g0} for t, $\rho_g U_{g0}^2 a_{0,straight}$ for $\mathbf{q}_{total}$, $\mu_0 U_{g0}/L$ for all the stresses, L for all other lengths except radius. As a result, Eq. (9.28) takes the form

$$\frac{\partial T}{\partial t} = -2\mathrm{Nu}\ell\frac{JK}{\mathrm{Re}_a\,\mathrm{Pr}_g}\frac{\lambda}{\lambda_0}\left(T - T_g\right) \tag{9.29}$$

where is the molecular Prandtl number for gas, $K=c_{pg}/c$ is the ratio of the specific heat at constant pressure for gas to the specific heat for polymer melt, and the Nusselt number $Nu=(h2a/k_g)$, with k_g being the molecular thermal conductivity of gas, is given by the following expression (chapter 8)

$$Nu= 0.495Re_a^{1/3}Pr_g^{1/2} \tag{9.30}$$

Substituting Eq. (9.27) into Eq. (9.26) and using Eq. (9.29), we arrive at the following equation

$$\frac{\partial\Phi}{\partial t} = -\frac{2Nu\ell JK}{Re_a\, Pr_g\, De_0\lambda_0}\frac{\left(T-T_g\right)}{\lambda} - T\exp\left[-U_A\left(\frac{1}{T}-1\right)\right]\frac{\tau_{\tau\tau}}{De_0\lambda^2} \tag{9.31}$$

with $\Phi = \left(\tau_{\tau\tau} + T/De_0\right)/\lambda^2$ and the following two dimensionless groups involved

$$De_0 = \frac{\theta_0 U_{go}}{L}, \quad U_A = \frac{U}{RT_0} \tag{9.32}$$

where De_0 is the Deborah number.

Using the theory of the axisymmetric turbulent gas jets (Yarin 2007), the temperature field in the gas jet is given by the following expression

$$T_g(\xi,H) = T_{g\infty} + \frac{\left(Pr_t+1/2\right)}{0.05\sqrt{6}}\frac{\left(1-T_{g\infty}\right)}{\ell}\frac{1}{\left(\xi+4.8/\ell\right)}\frac{1}{\left(1+\zeta^2/8\right)^{2Pr_t}} \tag{9.33}$$

where $T_{g\infty}$ is the surrounding cold gas temperature far from the polymer jet rendered dimensionless by T_0, the turbulent Prandtl number $Pr_t=0.75$, and $\zeta(\xi,H)$ is given by the second Eq. (9.25).

The projections of the momentum balance equation (9.14)-(9.16) can be transformed to the following dimensionless form (where some of the minor terms are omitted)

$$\frac{\partial^2\xi}{\partial t^2}=\frac{2}{\mathrm{Re}}\Phi\frac{\partial^2\xi}{\partial s^2}+\frac{\tau_\xi}{\mathrm{Fr}^2}+\ell J\frac{q_{\mathrm{total},\tau}}{f} \tag{9.34}$$

$$\frac{\partial^2 H}{\partial t^2}=\left[\frac{\tau_{\tau\tau}}{\mathrm{Re}}-J\varphi^2(\xi,H,Z)\right]\left|b_\zeta\right|\frac{1}{\lambda^2}\frac{\partial^2 H}{\partial s^2}-\frac{\tau_\eta}{\mathrm{Fr}^2}+b_\zeta\ell J\frac{\varphi^2(\xi,H,Z)}{\pi a}n_\xi^2\mathrm{sign}(n_\xi) \tag{9.35}$$

$$\frac{\partial^2 Z}{\partial t^2}=\left[\frac{\tau_{\tau\tau}}{\mathrm{Re}}-J\varphi^2(\xi,H,Z)\right]\left|b_\eta\right|\frac{1}{\lambda^2}\frac{\partial^2 Z}{\partial s^2}+\frac{(b_\eta\tau_\eta+b_\xi)}{b_\eta\mathrm{Fr}^2}-b_\eta\ell J\frac{\varphi^2(\xi,H,Z)}{\pi a}n_\xi^2\mathrm{sign}(n_\xi) \tag{9.36}$$

where

$$q_{\mathrm{total},\tau}=C\pi a\left[\varphi(\xi,H,Z)\tau_\xi-V_\tau\right]^2\left[\mathrm{Re}_a\,a\left(\varphi(\xi,H,Z)\tau_\xi-V_\tau\right)\right]^{-0.81} \tag{9.37}$$

$$\tau_\xi=\frac{\xi_{,s}}{\lambda},\ \tau_\eta=\frac{H_{,s}}{\lambda},\ \tau_\zeta=\frac{Z_{,s}}{\lambda} \tag{9.38}$$

$$n_\xi=\frac{\xi_{,ss}\left(H_{,s}^2+Z_{,s}^2\right)-\xi_{,s}\left(H_{,ss}H_{,s}+Z_{,ss}Z_{,s}\right)}{\lambda\sqrt{\left(Z_{,ss}H_{,s}-H_{,ss}Z_{,s}\right)^2+\left(\xi_{,ss}Z_{,s}-Z_{,ss}\xi_{,s}\right)^2+\left(H_{,ss}\xi_{,s}-\xi_{,ss}H_{,s}\right)^2}}, \tag{9.39}$$

$$n_\eta=\frac{H_{,ss}\left(\xi_{,s}^2+Z_{,s}^2\right)-H_{,s}\left(\xi_{,ss}\xi_{,s}+Z_{,ss}Z_{,s}\right)}{\lambda\sqrt{\left(Z_{,ss}H_{,s}-H_{,ss}Z_{,s}\right)^2+\left(\xi_{,ss}Z_{,s}-Z_{,ss}\xi_{,s}\right)^2+\left(H_{,ss}\xi_{,s}-\xi_{,ss}H_{,s}\right)^2}}, \tag{9.40}$$

$$n_\zeta=\frac{Z_{,ss}\left(\xi_{,s}^2+H_{,s}^2\right)-Z_{,s}\left(\xi_{,ss}\xi_{,s}+H_{,ss}H_{,s}\right)}{\lambda\sqrt{\left(Z_{,ss}H_{,s}-H_{,ss}Z_{,s}\right)^2+\left(\xi_{,ss}Z_{,s}-Z_{,ss}\xi_{,s}\right)^2+\left(H_{,ss}\xi_{,s}-\xi_{,ss}H_{,s}\right)^2}} \tag{9.41}$$

$$b_\xi=\tau_\eta n_\zeta-n_\eta\tau_\zeta,\quad b_\eta=\tau_\zeta n_\xi-n_\zeta\tau_\xi,\quad b_\zeta=\tau_\xi n_\eta-n_\xi\tau_\eta \tag{9.42}$$

$$\mathrm{Re}=\frac{\rho L U_{g0}}{\mu_0},\quad J=\frac{\rho_g}{\rho},\quad \mathrm{Fr}=\left(\frac{U_{g0}^2}{gL}\right)^{1/2},\quad \mathrm{Re}_a=\frac{2a_{0,\mathrm{straight}}U_{g0}}{\nu_g} \tag{9.43}$$

Re and Re_a denote the corresponding Reynolds numbers, Fr is the Froude number.

Following Chapters 7 and 8, the boundary conditions for Eqs. (9.34)-(9.36) at the end of the straight part correspond to the overall effect of turbulent eddies expressed as

$$\xi_{\mathrm{origin}}\approx 0,\ H_{\mathrm{origin}}=H_j+H_{0\Omega}\sin(\Omega_j t),\ Z_{\mathrm{origin}}=H_{0\Omega}\cos(\Omega_j t) \tag{9.44}$$

where H_j were constants monotonously increasing from jet to jet, which corresponds to the nosepiece with the die exits located in the H direction.

In Eqs. (9.44)

$$\mathbf{H}_{0\boldsymbol{\Omega}} = \left(0.06\,\mathrm{Re}^{1/2}/\ell\right)^{1/2} / \boldsymbol{\tau}_{\tau\tau 0}^{1/4}, \qquad \boldsymbol{\Omega}_j = \frac{\boldsymbol{\omega}_j \mathrm{L}}{\mathrm{U}_{g0}} \tag{9.45}$$

where the dimensionless (and the corresponding dimensional) frequencies Ω_j (and ω_j) were chosen randomly from jet to jet, as described in section 9.3.

In Eq. (9.45), $\tau_{\tau\tau 0}$ is related to the dimensionless longitudinal stress at the end of the straight part of the jet predicted in section 9.2, as discussed in section 9.5.

The free end of the jet is practically unloaded, which corresponds to

$$\boldsymbol{\xi}_{,s}\big|_{s=\mathrm{end}} = 1, \quad \mathbf{H}_{,s}\big|_{s=\mathrm{end}} = 0 \text{ and } \quad \mathbf{Z}_{,s}\big|_{s=\mathrm{end}} = 0 \tag{9.46}$$

On the other hand, when a material point of a jet touches the screen moving in the $\mathbf{Z}$-direction, its $\boldsymbol{\xi}$ coordinate stays "frozen" at $\boldsymbol{\xi} = 1$, the $\mathbf{H}$ coordinate stays "frozen" at the value it has had at the moment of touching the screen, while its $\mathbf{Z}$ coordinate increases as

$$\mathbf{Z} = \mathbf{Z}_{\mathrm{touch}} + \mathrm{V}_{\mathrm{screen}}\,\mathrm{t} \tag{9.47}$$

The initial condition for Eq. (31) at the moment when a liquid element the bending part of the jet t_{birth} reads

$$\boldsymbol{\phi}\big|_{\mathrm{t}=\mathrm{t}_{\mathrm{birth}}} = \left(\boldsymbol{\tau}_{\tau\tau 0} + \mathrm{T}_0 / \mathrm{De}_0\right) / \boldsymbol{\lambda}_0^2 \tag{9.48}$$

9.5 The Bending Part of the Jet: Numerical Results, Discussion and Comparison with the Experimental Data

In a typical meltblowing process the die to collector distance (DCD) L is of the order of 10-15 cm and U_{g0} is of the order of 150 cm/s and at the operating temperature T_0= 250-350^{0}C the shear viscosity of polymer melt is within the range 5-20 g/(cm s). Using these values, the Reynolds number Re is of the order of 40000. In the simulations described below, the value of Re was taken as 46000.

At the end of the straight part of the jet the cross-sectional radius was found to be 8.75 μm (cf. section 9.3). This makes the value of $\mathrm{Re}_a = 174$.

The value of the factor C in the expression for the pulling force in Eq. (9.23) was taken as C=14 instead of C=100 used in the calculations for the straight part of the jet in section 9.2. Such reduction in the value of C can be interpreted as the accounting for the fact that jet pulling by air becomes additionally less effective when jet is inclined relative to the gas flow due to bending.

The relaxation time θ_0 =0.1 s was used in the calculations for the bending part instead of θ_0 =0.01 s used in the calculations for the straight part in section 9.2. This corresponds to the fact that the strongest stretching happens in the straight part of the jet, and thus, the fastest relaxation processes are expected there (Yarin 1993; Doi 1980). In the case of a weaker stretching corresponding to the bending part, even reputational relaxation mode (Yarin 1993; Doi 1980)can play role. The corresponding value of De_0 was taken as De_0=400. The effect of gravity was neglected, which corresponds to $\mathrm{Fr} = \infty$. In addition, it was taken K=0.25.

Simulations were done with 62 jets. Each jet was excited by the cumulative effect of the turbulent eddies described using Eqs. (9.44) and (9.45) with the frequencies Ω_j chosen according to the following formula:

$$\boldsymbol{\Omega}_j = \boldsymbol{\Omega}^0 p_j \tag{9.49}$$

where p_j are random numbers from the interval [0,1] generated anew at each time step and initiated by a current time of the computer clock, i.e. non-repeatable.

The basic variants were simulated at the value of Ω^0=0.3 (according to Chapters 7 and 8). For comparison, simulations were also done with Ω^0=0.1 and 0.5.

The value of the stress $\tau_{\tau\tau 0}$ for Eq. (9.45) is found from the value of $\tau_{xx,\text{end straight}}$ calculated in section 9.2. Due to the different scales used for nondimensionalization in sections 9.2 and 9.4, they are related as $\tau_{\tau\tau 0}= \tau_{xx,\text{end straight}}/De_0$, which made $\tau_{\tau\tau 0}$=41.84.

In addition the following values were used as in Chapter 8: $T_{g\infty} = 0.5$, J=10^{-3} and $\ell = 10^3$ and U_A=10.

The deposition screen was located at ξ=1, normal to the direction of blowing and could be moved in the Z direction with a given velocity V_{screen} from 0.015-0.15 (rendered dimensionless by U_{g0}), which corresponds to the dimensional range of 2.25m/s to 22.5 m/s. The jet deposition on the screen was implemented in the following way: at the moment the free end of the jet had reached the screen, its ξ and H coordinates were frozen, whereas its Z coordinate could vary in accordance with the translational motion of the screen in the Z direction. The cross-sectional radius of each jet at the moment it touched the screen was also frozen and used to produce jet-size distributions discussed below. The jet-size distributions were recorded at five different dimensionless time moments t=45, 60, 65, 70 and 75, which corresponds to 0.03 s, 0.04 s, 0.043 s, 0.047 s

and 0.05 s, respectively, for Figs. 9.3, 9.5, 9.7, 9.9 and 9.11. The jet configurations at t=75 corresponding to 0.05 s are shown in Figs. 9.2, 9.4, 9.6, 9.8 and 9.10 for different values of the screen velocity. For the sake of brevity, the radius distribution and jet evolution are illustrated only for Ω^0= 0.3. In addition, a detailed comparison of the maximum fiber diameter, mean fiber diameter, standard deviation and the number of jets reaching the collecting screen for different values of it velocity and Ω^0 is given in Table 9.1 for two dimensionless time moments t= 45 and 75.

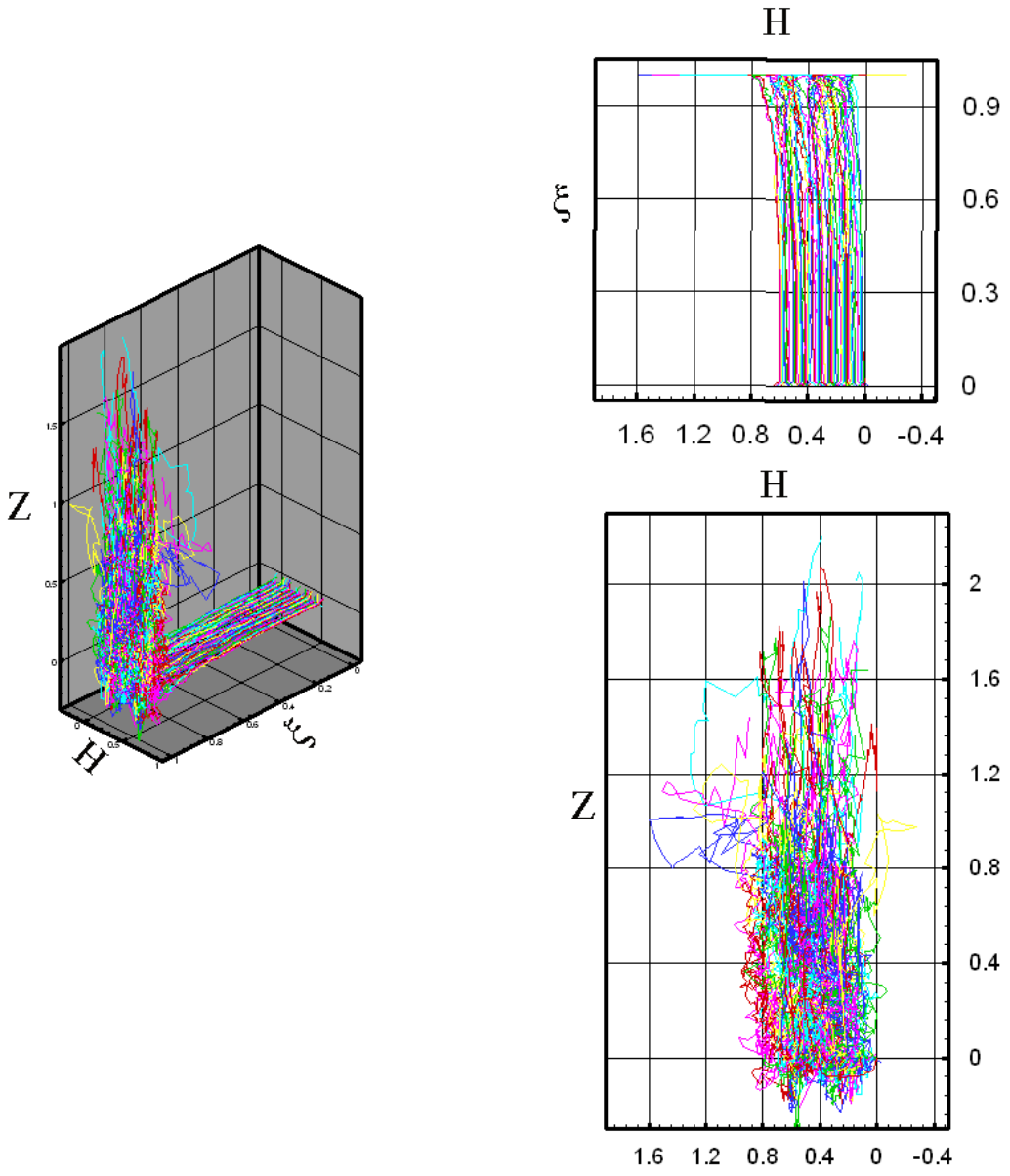

Fig. 9.2. Jet configurations in the case of the dimensionless screen velocity V_{screen}=0.015 (which corresponds to 2.25 m/s) at t=75 (which corresponds to 0.05 s) for Ω^0=0.3.

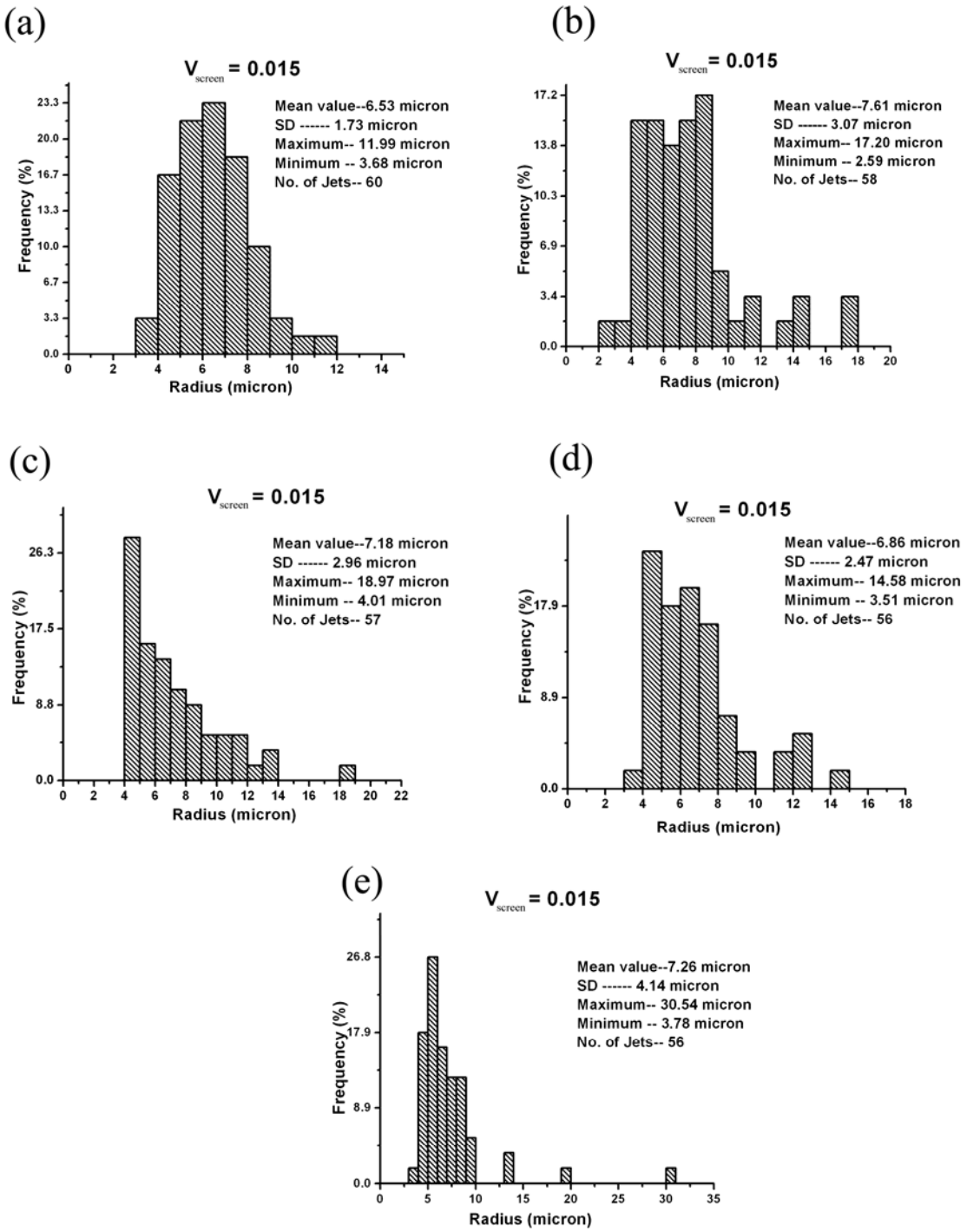

Fig. 9.3. Predicted radius distributions for the screen velocity V_{screen}=0.015 (2.25 m/s) at the time moments (a) t=45 (0.03 s), (b) 60 (0.04 s), (c) 65 (0.043 s), (d) 70 (0.047 s), (e) 75 (0.05 s)for Ω^0=0.3.

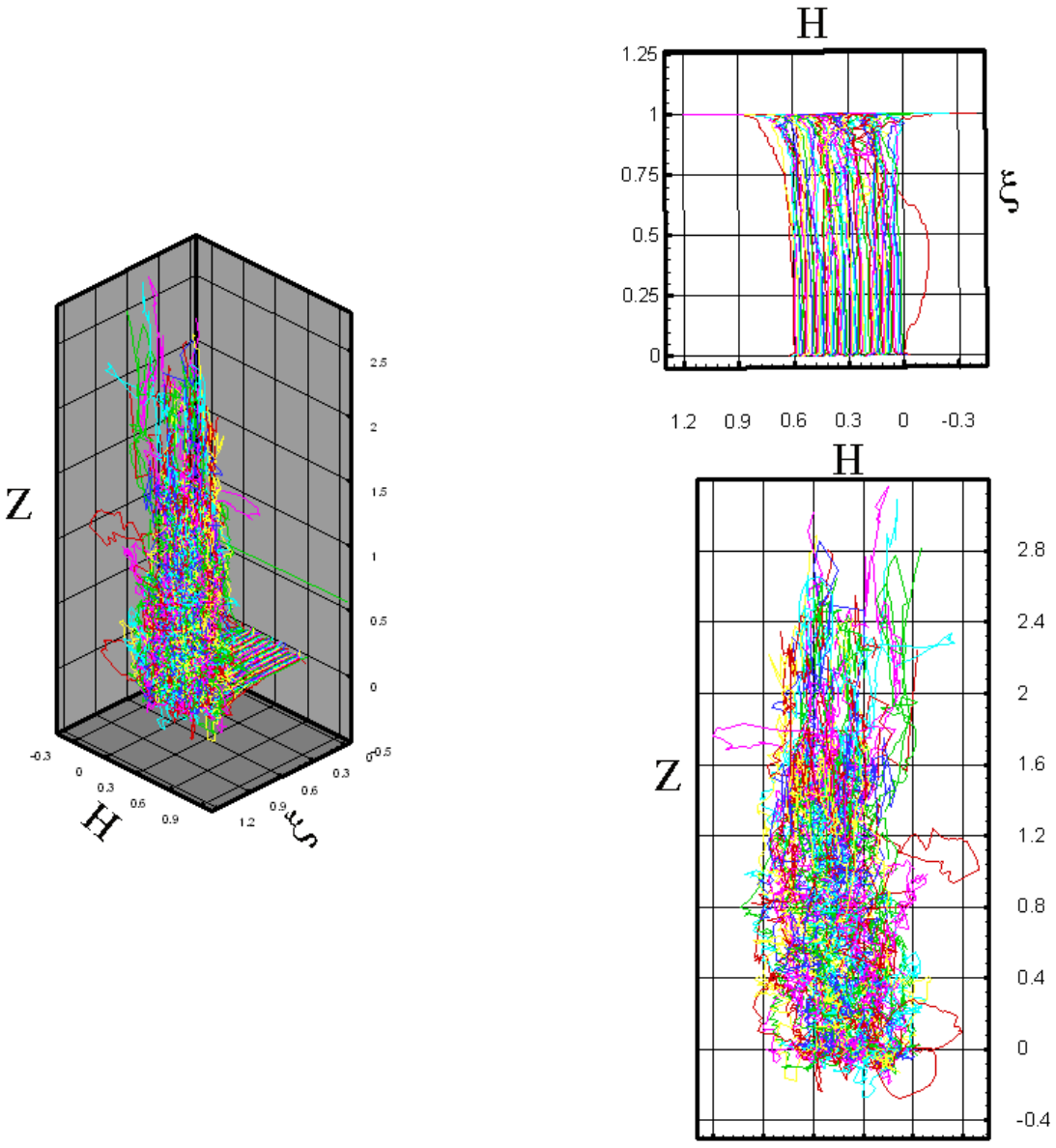

Fig. 9.4. Jet configurations in the case of the dimensionless screen velocity V_{screen}=0.03 (which corresponds to 4.5 m/s) at t=75 (which corresponds to 0.05 s) for Ω^0=0.3.

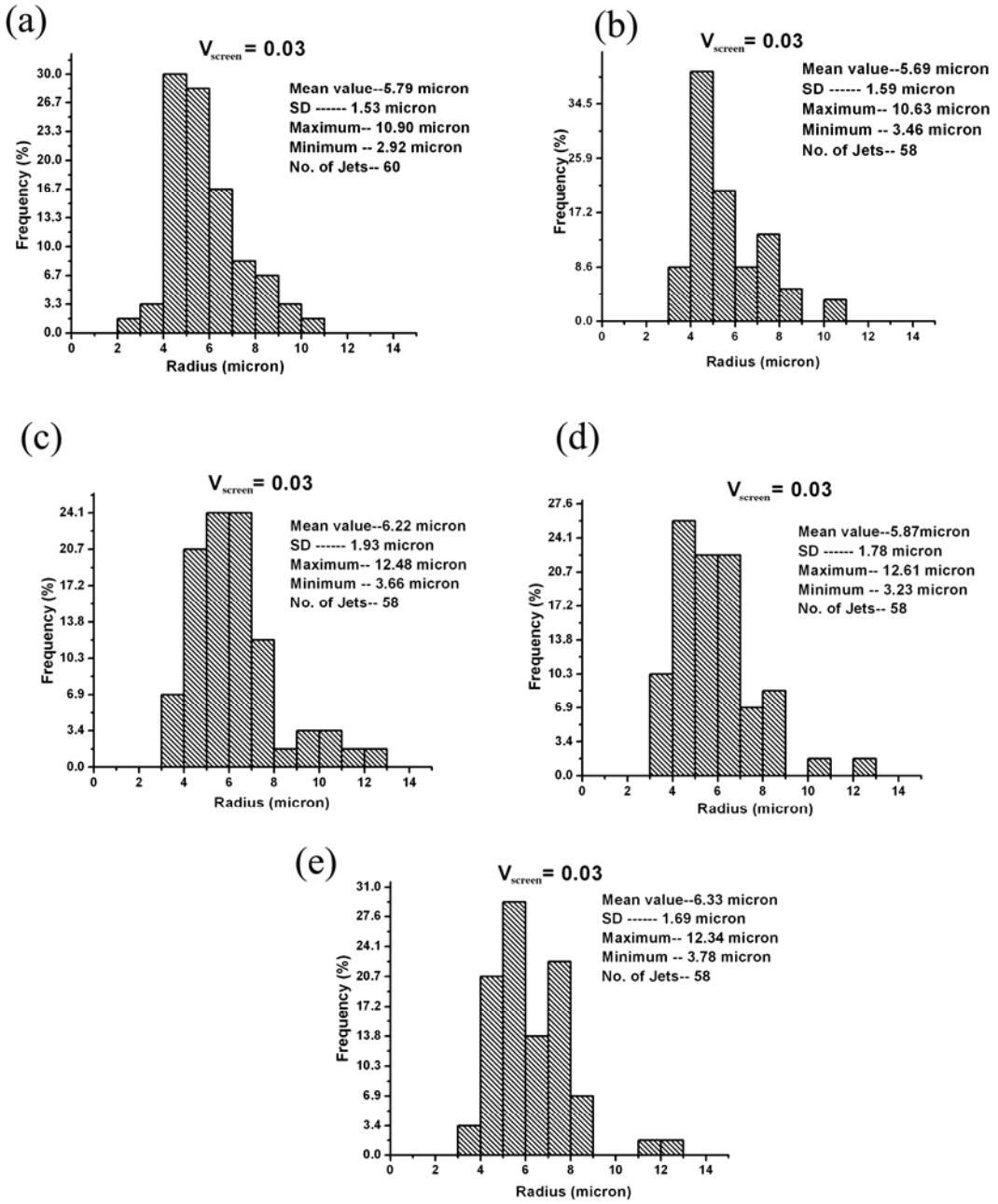

Fig. 9.5. Predicted radius distributions for the screen velocity V_{screen}=0.03 (4.5 m/s) at the time moments (a) t=45 (0.03 s), (b) 60 (0.04 s), (c) 65 (0.043 s), (d) 70 (0.047 s), (e) 75 (0.05 s) for Ω^0=0.3.

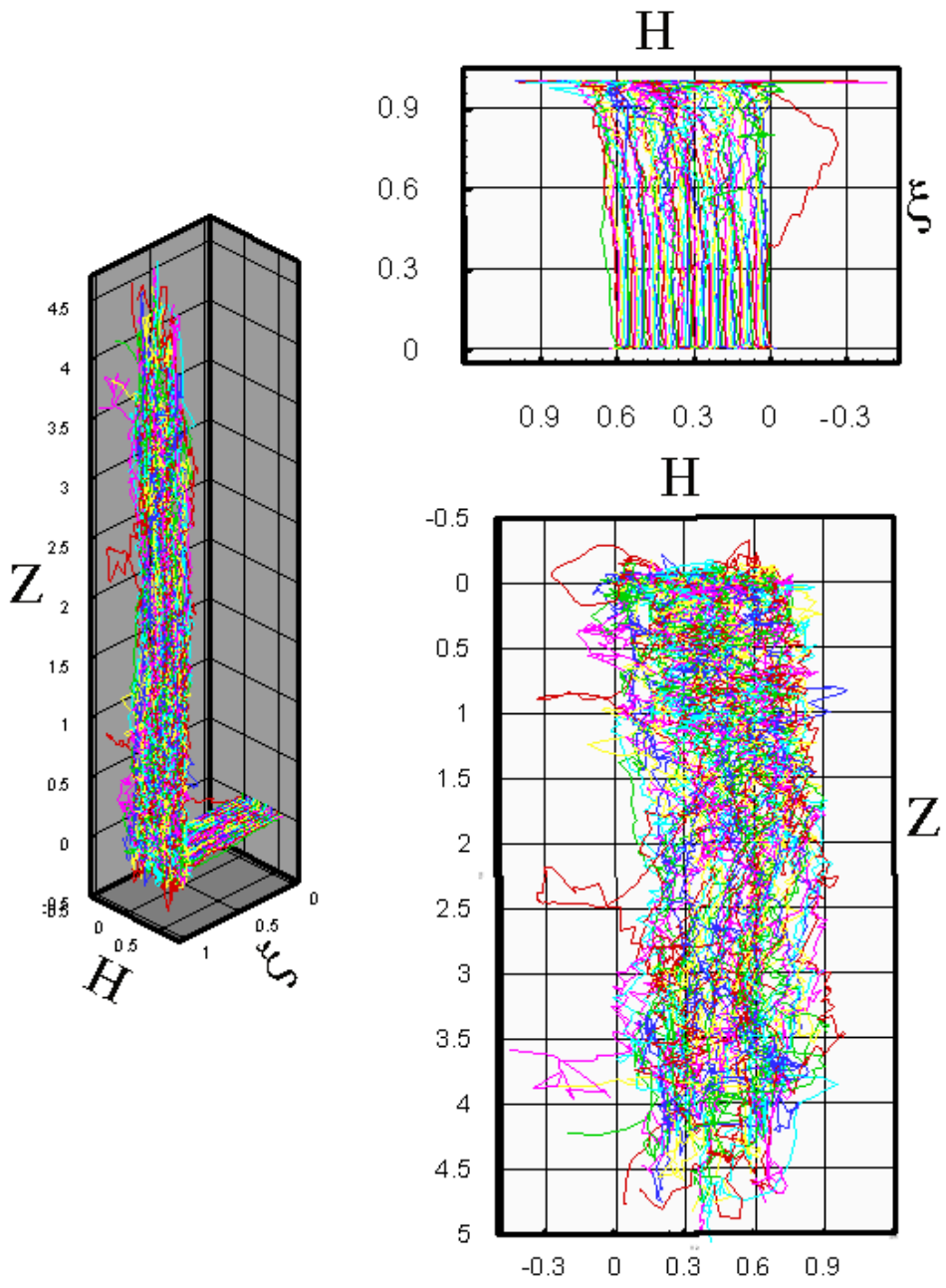

Fig. 9.6. Jet configurations in the case of the dimensionless screen velocity V_{screen}=0.06 (which corresponds to 9 m/s) at t=75 (which corresponds to 0.05 s) for Ω^0=0.3.

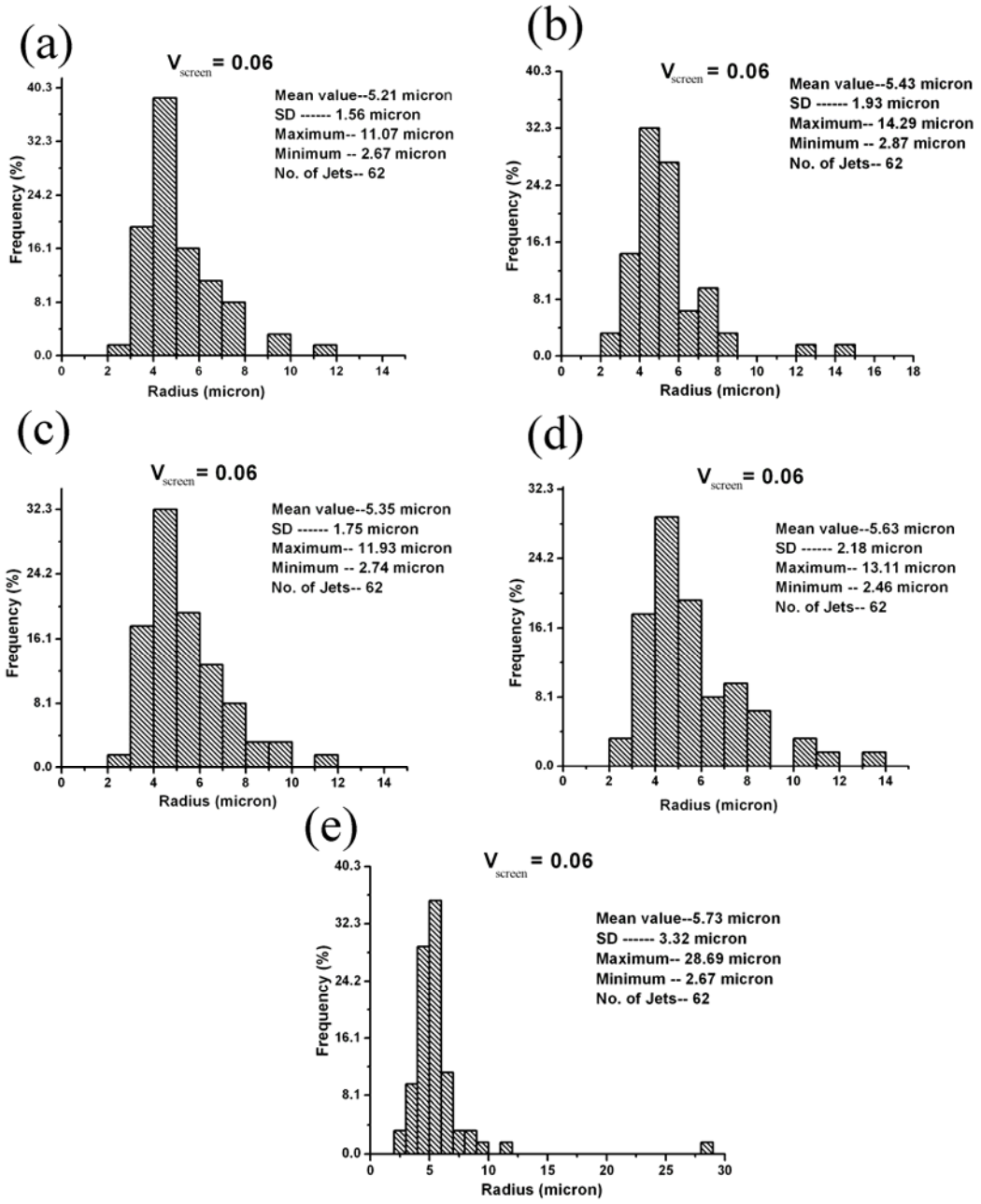

Fig. 9.7. Predicted radius distributions for the screen velocity V_{screen}=0.06 (9 m/s) at the time moments (a) t=45 (0.03 s), (b) 60 (0.04 s), (c) 65 (0.043 s), (d) 70 (0.047 s), (e) 75 (0.05 s) for Ω^0=0.3.

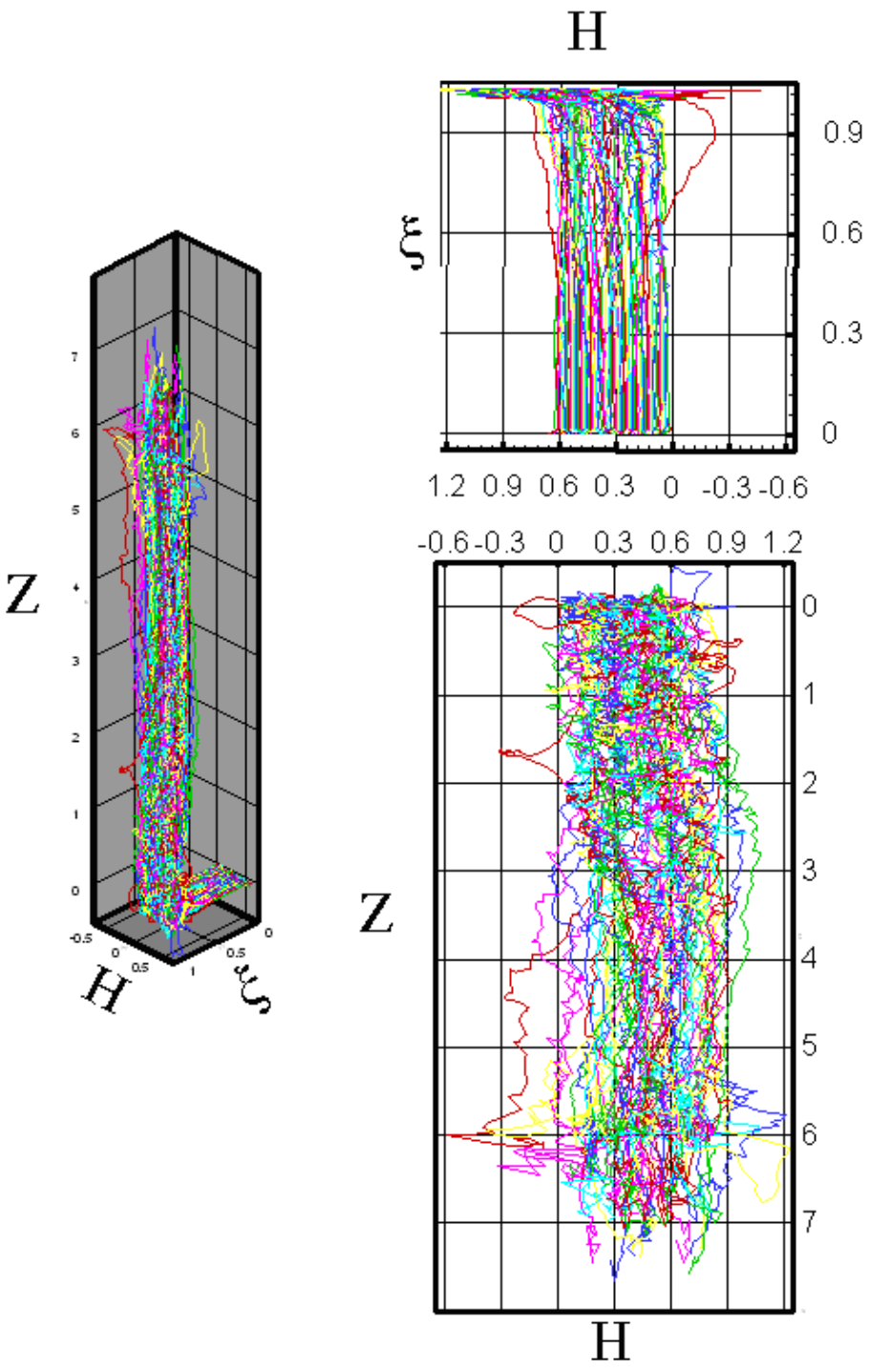

Fig. 9.8. Jet configurations in the case of the dimensionless screen velocity V_{screen}=0.1 (which corresponds to 15 m/s) at t=75 (which corresponds to 0.05 s) for Ω^0=0.3.

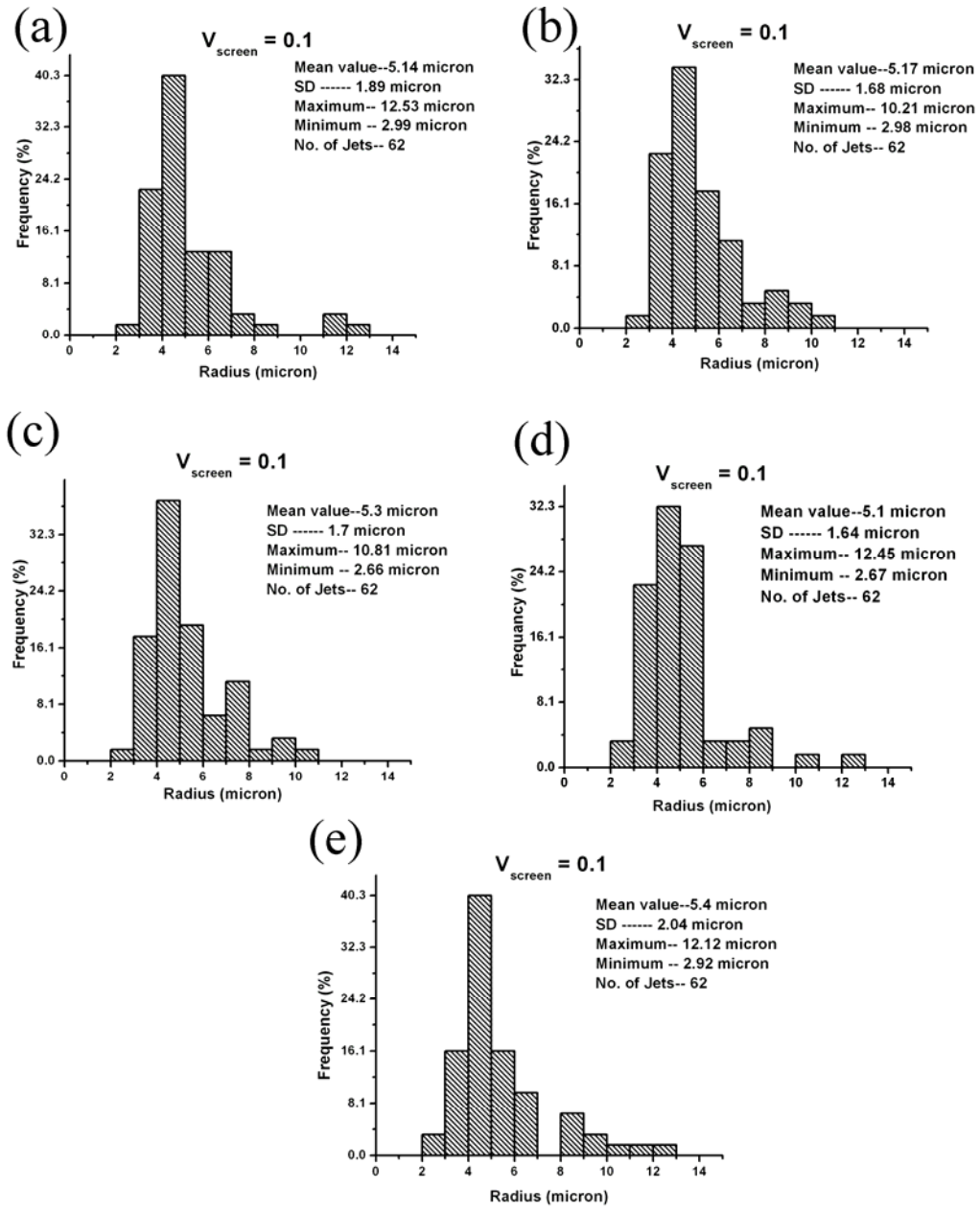

Fig. 9.9. Predicted radius distributions for the screen velocity V_{screen}=0.1 (15 m/s) at the time moments (a) t=45 (0.03 s), (b) 60 (0.04 s), (c) 65 (0.043 s), (d) 70 (0.047 s), (e) 75 (0.05 s) for Ω^0=0.3.

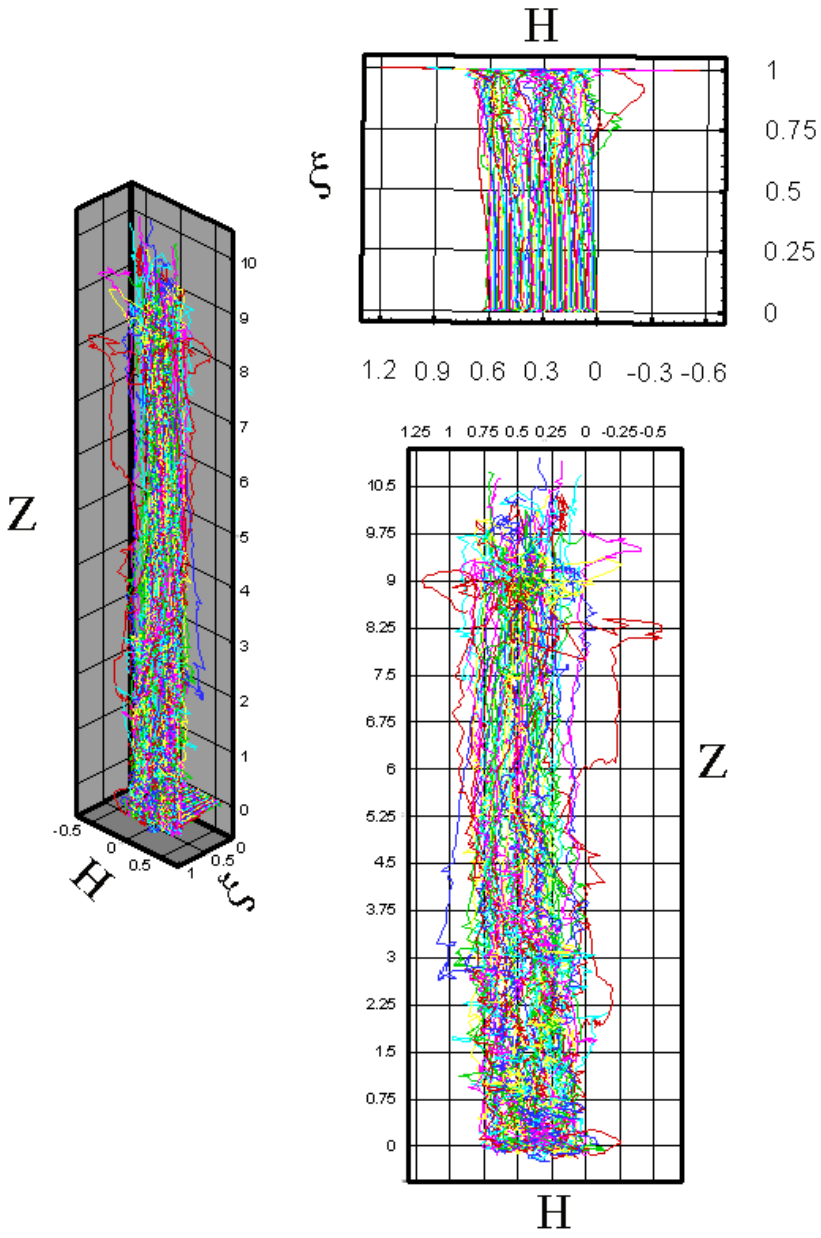

Fig. 9.10. Jet configurations in the case of the dimensionless screen velocity V_{screen}=0.15 (which corresponds to 22.5 m/s) at t=75 (which corresponds to 0.05 s) for Ω^0=0.3.

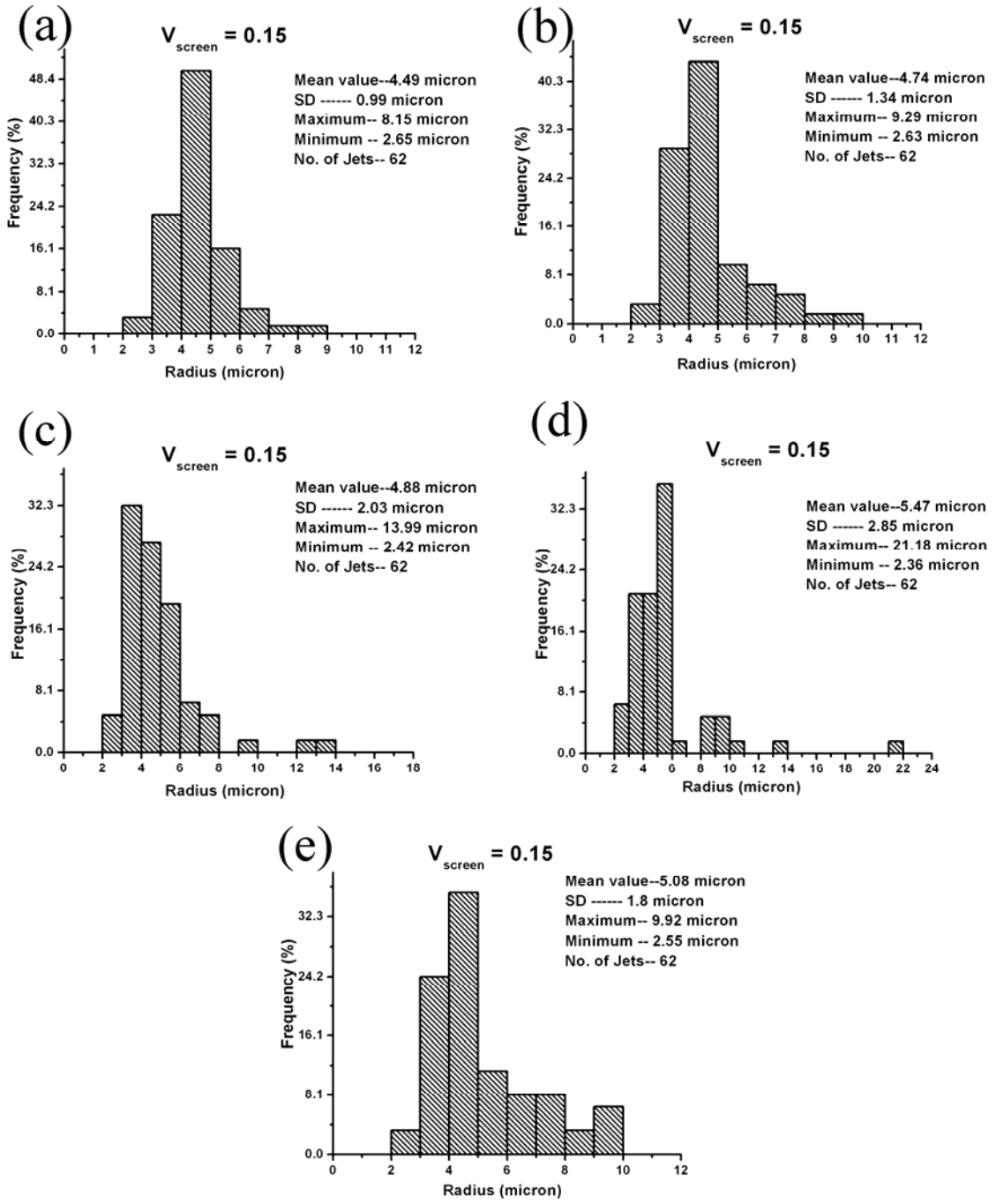

Fig. 9.11. Predicted radius distributions for the screen velocity V_{screen}=0.15 (22.5 m/s) at the time moments (a) t=45 (0.03 s), (b) 60 (0.04 s), (c) 65 (0.043 s), (d) 70 (0.047 s), (e) 75 (0.05 s) for Ω^0=0.3.

Table 9.1. The numerically predicted maximum fiber diameter, mean fiber diameter, standard deviation (SD) and the number of jets reaching the collecting screen for different values of Ω^0. The results for several values of the screen velocity are shown at two dimensionless time moments t= 45 and 75.

Ω^0	V_{screen}	Time moment	Max fiber diameter in μm	Mean fiber diameter in μm	SD in μm	Number of jets reaching the collecting screen
0.1	0.015	45	27.8	14.14	4.96	58
		75	26.9	13.76	4.9	55
	0.03	45	85.44	15.02	10.86	60
		75	29.04	12.18	4.54	56
	0.06	45	37.8	13.04	6.84	62
		75	24.8	10.98	3.74	61
	0.10	45	33.10	12.34	5.86	62
		75	27.50	10.50	3.30	62
	0.15	45	53.14	11.34	6.94	62
		75	27.56	9.2	3.00	62
0.3	0.015	45	23.98	13.06	3.46	60
		75	61.08	14.52	8.28	56
	0.03	45	21.80	11.58	3.06	60
		75	24.68	12.66	3.38	58
	0.06	45	22.14	10.42	3.12	62
		75	57.18	11.46	6.64	62
	0.10	45	25.06	10.28	3.78	62
		75	24.24	10.8	4.08	62
	0.15	45	16.30	8.98	1.98	62
		75	19.84	10.16	3.6	62
0.5	0.015	45	29.84	12.34	4.26	62
		75	35.2	13.8	5.38	62
	0.03	45	53.14	11.34	6.94	62
		75	28.50	13.14	6.64	62
	0.06	45	27.16	10.50	3.92	62
		75	25.14	11.96	3.82	62
	0.10	45	31.04	10.24	3.88	62
		75	34.56	10.92	4.70	62
	0.15	45	17.94	9.48	2.68	62
		75	25	11.02	4.36	62

The experimental data on meltblowing in (Breese et al., 2006) reveal that for a DCD of 22 cm the maximum and mean fiber diameters of 35 μm and 18.3 μm, respectively, for a research line. For a commercial line Ref. 13 reports the maximum and mean fiber diameters of 19 μm and 7.5 μm, respectively. In comparison, Table 9.1 shows that our numerically predicted values of the maximum fiber diameter are within the range of 17.94- 40 μm in reasonable agreement with the experimental data. The experimental data in (Shambaugh 1988) for polypropylene (M_w=175000 and M_n=32000) show that the mean value of the fiber diameter was 6 μm with a standard deviation (SD) of 3 μm, and for polypropylene with a different molecular weight (M_w=120000 and M_n=30000) it was 5 ± 2 μm. In addition, our numerical results listed in Table 9.1 show that the predicted mean fiber diameter is in a range of 8.98-14.52 μm with a range of SD from 1.98 to 10.86 μm. These predictions are in a rather good agreement with the experimental data. It is emphasized that (Shambaugh 1988; Breese et al., 2006) lack many details needed for detailed characterization of the polymer melts and governing parameters used (e.g. the rheological behavior, the initial temperature, polymer flow rate, collector speed, collecting technique, etc.), therefore comparison with these data is inevitably conditional.

In spite of the above-mentioned uncertainty, the experimental data (Shambaugh 1988; Breese et al., 2006) were used for comparison with our numerical predictions in Fig. 9.12. It can be seen that in spite of the above-mentioned uncertainties in the exact experimental conditions, the numerical results are in qualitative agreement with the experimental data.

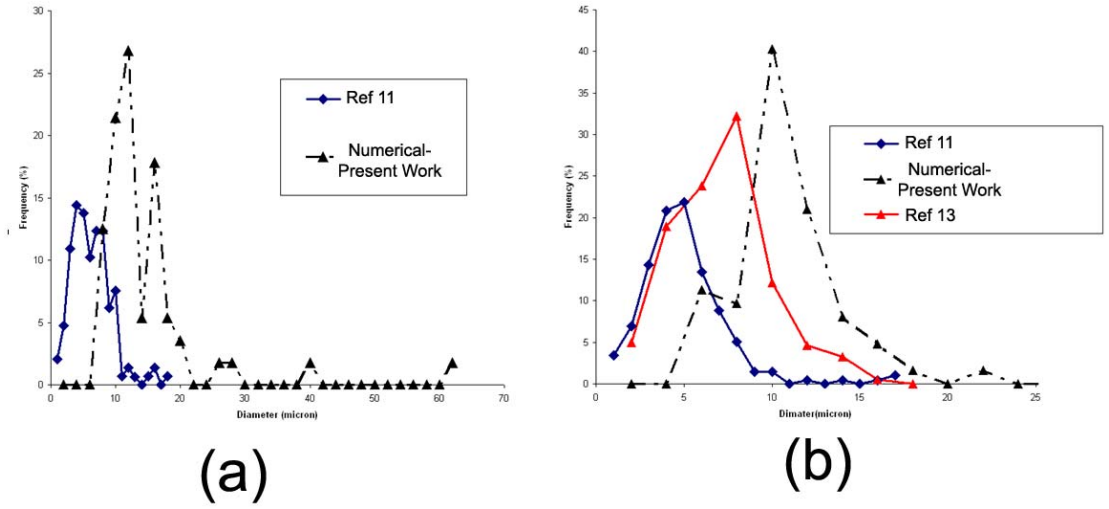

Fig. 9.12. Comparison of the experimental and numerically predicted radius distributions. The numerical results correspond to Ω^0=0.3. In panel (a) V_{screen}=0.015, in (b) V_{screen}=0.06.

Figures 9.3, 9.5, 9.7, 9.9 and 9.11 and Table 9.1 show that the values of the basic frequency Ω^0 and screen velocity V_{screen} do not affect significantly the values of the mean fiber diameter. In regards of the effect of these two parameters no visible trend was found according to the numerical results. As is evident from Figs. 9.3, 9.5, 9.7, 9.9 and 9.11, at Ω^0=0.3 the radius distributions appear to be approaching the normal distribution as the screen velocity V_{screen} increases. A similar approach to the normal distribution at higher values of V_{screen} was observed at the other values of Ω^0 (not shown here).

It is emphasized that the numerical results listed in Table 9.1 show that in a few jets from the initial 62 did not arrive at the collection screen. At a certain moment of time the cross-sectional radius of those few jets became zero at a certain cross-section. This manifests cohesive jet breakup and probably corresponds to the so-called fly formation. The observed cohesive jet breakup is more pronounced at Ω^0=0.1 than at higher values of

Ω^0. Still, the maximum number of broken jets which did not reach the screen was not more than 7 at Ω^0=0.1.

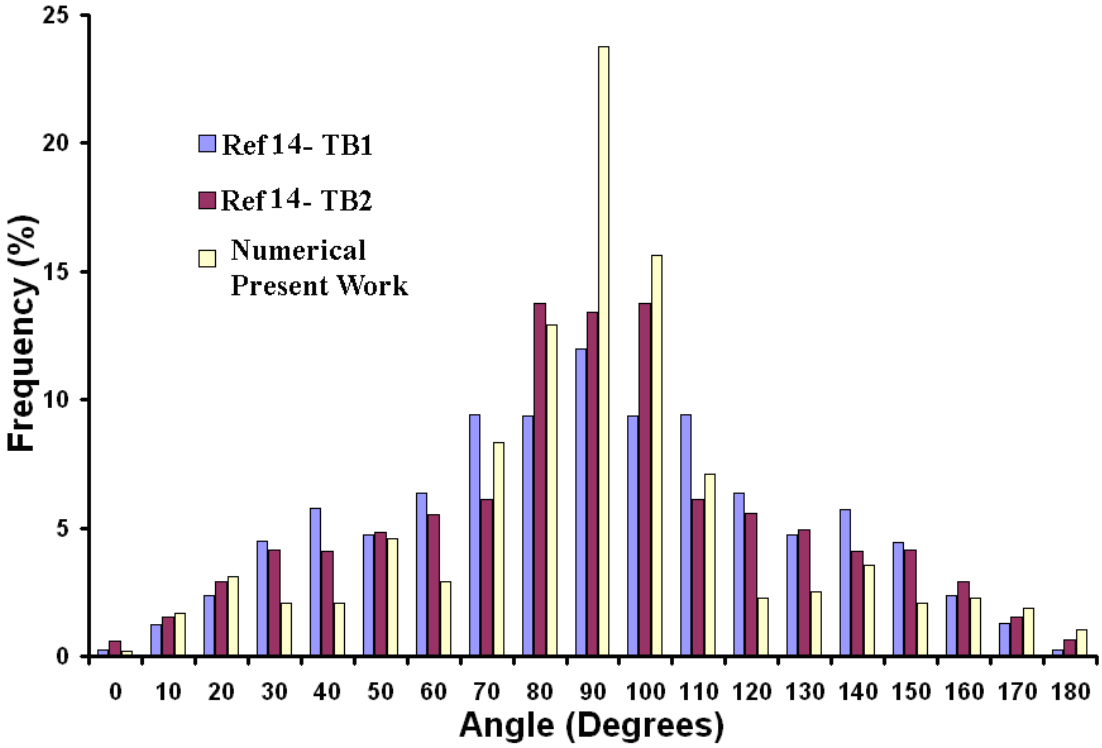

Fig. 9.13. Comparison of the predicted fiber orientation distribution with the experimental data (Rawal et al., 2010). TB1 and TB2 denote two different grades of polyester nonwoven structures meltblown in (Rawal et al., 2010).

The angular distribution in the fiber lay-down on the collecting screen predicted by the present method for a distance of 2 cm from the first touchdown point of the polymer jets in the direction of the collector screen motion is compared to the experimental data (Rawal et al., 2010) in Fig. 9.13. In this particular case the relaxation time value of θ_0 = 0.025 s was used which corresponds to the Deborah number De_0 =100. It is emphasized that in (Rawal et al., 2010) the velocity of the collector screen was not reported.

Therefore, in the simulations it was taken as in (Begenir 2008) as 30 m/min (which corresponds to the dimensionless value of 0.0033). Note that in (Rawal et al., 2010), in the lay-down nonwoven 0^0 corresponded to the machine direction. In the present work, however, the machine direction corresponds to 90^0, and the data of (Rawal et al., 2010) was transformed accordingly. Figure 9.13 shown that the numerical predictions slightly overestimate fiber orientation in the machine direction, albeit in general show a pattern similar to the experimental one.

9.6 Conclusion

The comprehensive quasi-one-dimensional model of the dynamics of three-dimensional excursions of polymer jets in meltblowing outlined in the present work and implemented with 62 jets was used to simulate a number of characteristic cases and compare the results with the available experimental data. The results obtained revealed the following. The model is capable of predicting reasonable patterns of fiber deposition in nonwovens formed on a moving screen, as well as the fiber-size distributions for different operation conditions. The predicted values of the mean fiber diameter and its standard deviations were found to be in a fairly good agreement with the experimental data from literature, even though the experimental reports do not specify rheological behavior of polymer solutions, as well as a detailed pattern of the initial interaction of gas and polymer jets. It was also found that the model reveals both bimodal and normal types of fiber-size distributions in nonwovens in qualitative agreement with the experimental data. The numerical predictions also suggest that the effect of the turbulence spectrum in gas flow, as well as the screen speed, do not affect significantly the values of the mean

diameter of deposited fibers, since no visible trend was found. It was also predicted that the fiber-size distribution approaches the normal one as the screen velocity increases. The numerical results also demonstrated cohesive breakup of several jets before they reach the screen, which might be kindred to the so-called fly formation.

10. PRODUCTION OF 100 NM DIAMETER CARBON TUBES BY SOLUTION BLOWING AND CARBONIZATION OF CORE-SHELL NANOFIBERS AND SOLUTION BLOWN THREE-DIMENSIONAL CARBON FIBER NONWOVENS FOR APPLICATION AS ELECTRODES IN MICROBIAL FUEL CELLS

10.1 Introduction

The present work introduces a modified solution blowing process as a route for making mesoscopic carbon tubes. It deals first with solution blowing of monolithic Polyacrylonitrile nanofibers and then introduces a novel process of solution co-blowing of core-shell Polymethyl Methacrylate- Polyacrylonitrile (PMMA-PAN) fibers, as well as a post-treatment resulting in mesoscopic carbon tubes [with bores in the range of 50-150 nm and outer diameter of 400-600 nm]. In a sense, the co-blowing of core-shell nanofibers, as well as their transformation into mesoscopic carbon tubes, are kindred to co-electrospinning of core-shell polymer nanofibers and mesoscopic carbon tubes in (Zussman et al., 2006; Bazilecsky et al., 2007) albeit being driven by different forces (aerodynamic drag and electric forces, respectively).

In this Chapter we also aim a development of high surface area solution-blown carbonized nonwovens to further enhance the current density of BES anodes which were tested in microbial fuel cells by our German collaborators (the U. Schroder group).

Section 10.2 describes the experimental and section 10.3 deals with the solution blown polymer nanofiber mats and carbon nanotubes. Section 10.4 puts describes the results obtained using solution blown carbonized nanofiber electrodes implemented in microbial fuel cell. Conclusions are listed in section 10.5.

10.2 Experimental

Two polymers were used in these experiments: Polymethyl Methacrylate (PMMA) with molecular weight M_W=996 kDa obtained from Sigma-Aldrich, and Polyacrylonitrile (PAN) - M_W =150 kDa obtained from Polymer Inc. The following two solvents were used: N,N-Dimethyl Formamide (DMF) anhydrous-99.8% and Dichloro Methane (MC) and were obtained from Sigma-Aldrich. Solutions used in the blowing and co-blowing experiments described below were 6 wt% PMMA solution in w/w 60:40 DMF:MC, and 8% PAN solution in DMF. For preparation of carbon nanofiber based microbial fuel cells in addition to 8% PAN solution in DMF blends of PAN and Carbon Black (CB) solution was prepared as follows. The blends were prepared using the following steps. Initially a 12% PAN solution in DMF was prepared. Then, 1 g of 12 wt% PAN solution, 0.12 g of CB and 4 g of DMF in a 20 mL vial were sonicated for 45 min. During sonication CB clusters were broken, dispersed and coated by PAN, which prevented coalescence of particulates. Then, 4.32 g of DMF and 0.68 g of PAN were added to the vial and kept on a hotplate overnight under permanent stirring. In this way a blend of 8 wt% PAN solution with 15 wt% CB was prepared.

The experimental setups used for solution blowing and co-blowing experiments are depicted in Fig. 10.1. In particular, the setup for solution blowing used to form monolithic PAN nanofibers and PAN nanofibers with CB is shown in Fig. 10.1(a). Polymer solution was delivered from a syringe pump at a rate of 5 mL/h to a reservoir attached to a core nozzle. The core nozzle was surrounded by a concentric annular nozzle. Polymer solution from the reservoir was issued through the core nozzle into the surrounding high speed nitrogen jet flow (at 230-250 m/s) from the annular nozzle, which

delivered gas from a high pressure cylinder at a pressure of 20-30 bar [Fig. 10.1(a)]. The nitrogen jet accelerated and stretched the core jet of PAN solution with and without carbon black. The latter was undergoing not only stretching but a substantial bending instability (Reneker et al., 2000). Stretching and bending instability resulted in significant thinning of the polymer solution jet, while solvent was gradually evaporating. At a certain stage, polymer precipitated, nanofibers solidified, and were collected at a solid collector at a distance of 19 cm below the nozzle exit.

The setup used for co-blowing of core-shell PMMA-PAN nanofibers is sketched in Fig. 10.1(b). In this case two different polymer solutions were supplied by two different syringe pumps. The core solution (PMMA) was supplied into a core nozzle. The core nozzle was surrounded by a reservoir, to which the shell (PAN) solution was supplied. PMMA solution was issued through the core nozzle surrounded by an annular orifice through which the shell solution could flow, i.e. at the reservoir exit a core-shell polymer jet was formed. The flow rates of the core and shell polymer solutions were 5 and 2 mL/h, respectively. The core-shell polymer jet was issued inside a concentric nozzle, which issued nitrogen jet surrounding the core-shell polymer jet. The upstream nitrogen pressure in the high pressure cylinder was 35 bar. Initially, the core nozzle was kept slightly protruding from the annular shell nozzle, as it is recommended for co-electrospinning (Zussman et al., 2006). However, it was found that the protrusion was hampering the flow and the nozzle end was clogging up rapidly as the polymer had started drying. To avoid that, the core nozzle was moved slightly into the annular shell nozzle. That was still not enough to avoid an intermittent process, even though the clogging was reduced. Therefore, both polymers were electrified through the core-shell

nozzle, so that a potential difference of 3 kV was applied between the nozzle and a grounded nanofiber collector, which was an Al foil. The application of the electric field, which makes the process kindred to co-electrospinning (Zussman et al., 2006), resulted in its stabilization.

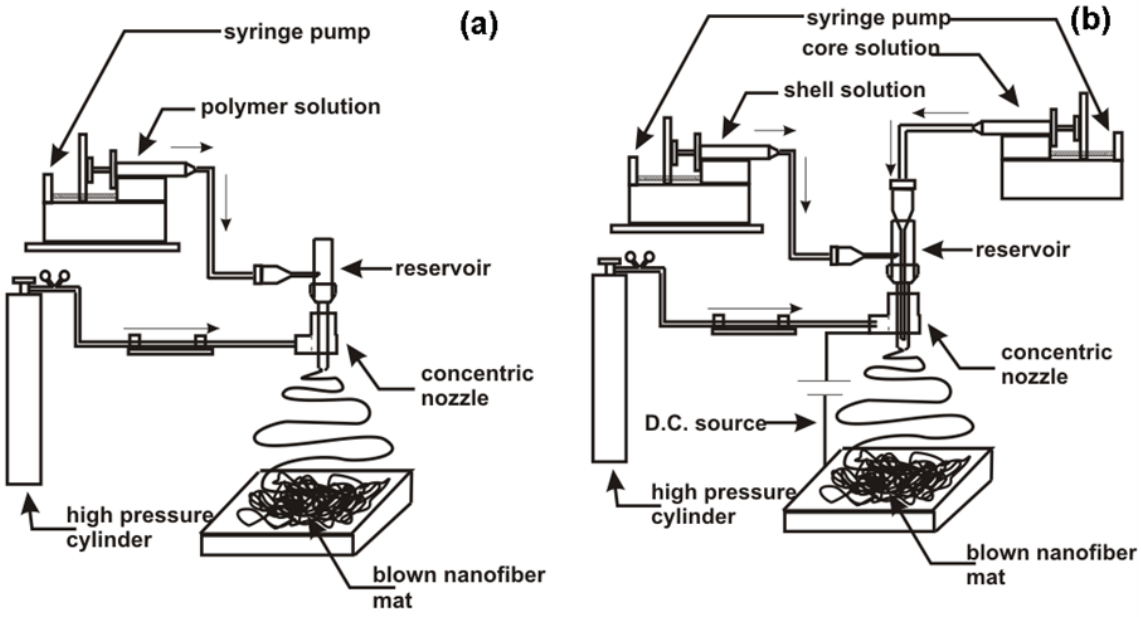

Fig. 10.1. Schematic drawing of the setup for (a) solution blowing of monolithic nanofibers and (b) for the electrically-assisted co-blowing of core-shell nanofibers.

Core-shell nanofibers and carbon nanofiber mats were heat treated to transform them into hollow mesoscopic amorphous carbon tubes. Following (Zussman et al., 2006; Bazilevsky et al., 2008a) the as-blown fiber mat removed from the collector was heated at 350 ^{0}C for 3 h under air atmosphere to destroy PMMA cores in the fibers. Then, it was heated at 750 ^{0}C under nitrogen atmosphere for 1 h. The latter stage led to carbonization of the PAN resulting in carbonized shell for core-shell nanofiber and carbon nanofiber for the monolithic as blown fiber mat.

For the observations of the blown monolithic nanofibers scanning electron microscopy (SEM) was used. In particular, SEM images were prepared using JEOL-JEM 6320 F. Prior to observation with SEM, all samples were sputter-coated with Pt-Pd to a thickness of 5 nm. For the observation of the co-blown core-shell nanofibers optical microscope Olympus BX51 was used prior to carbonization. After carbonization, the carbonized mesoscopic tube mat was sonicated in ethanol. The sonication fractured and dispersed the carbonized tube mats, and then the suspension in ethanol was deposited on TEM grids for observations. TEM images were obtained using JEOL JEM-3010.

For using carbonized PAN nanofibers with CB as microbial fuel cells setup used as described in (Chen et al., 2011) in Dr. U. Schroder's group in Institute of Environmental and Sustainable Chemistry, Technische Universitat Braunschweig, Germany.

10.3 Solution Blown Polymer Nanofiber Mat and Production of Carbon Nanotubes

A long-exposition photograph of a solution blown jet in flight taken by DSLR Nikon D-70s camera [Fig. 10.2(a)] clearly shows large amplitude bending similar, albeit more vigorous than that of the blown solid flexible threadline observed in Chapter 7. Figure 10.2(b) shows a snapshot of the jet in flight taken by CCD camera.

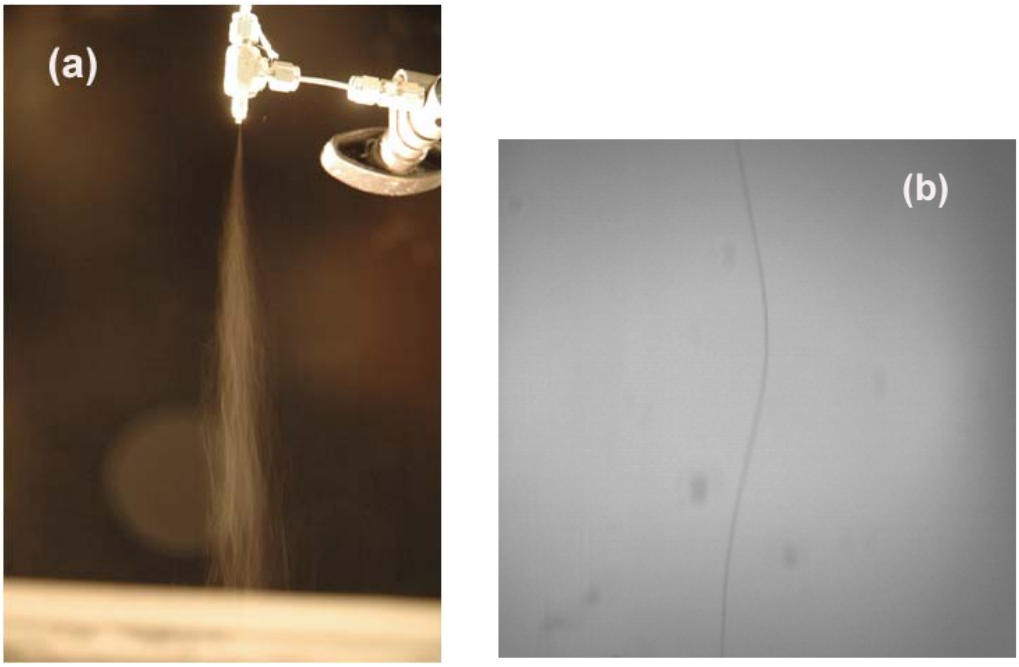

Fig. 10.2. Solution blown polymer jet at 25 bar. (a) The envelope and (b) a snapshot.

SEM images of solution blown monolithic PAN nanofibers are shown in Fig. 10.3. It can be seen that the nanofiber diameter range is within 150-250 nm [Fig. 10.3(b)] and the individual nanofibers are quite uniform in the longitudinal direction.

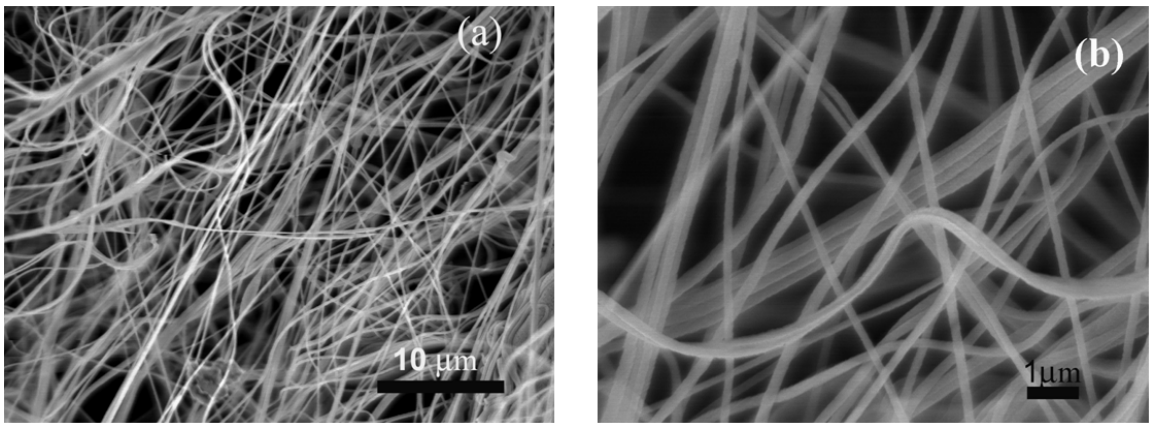

Fig. 10.3. (a) The overall view of PAN nanofiber mat produced using solution blowing. (b) A zoomed-in area of the PAN nanofiber mat. PAN solution was supplied at the rate of

5 mL/h; nitrogen was supplied from a high pressure cylinder with stagnation pressure of 25 bar.

An example of the optical images of co-blown PMMA-PAN core-shell fibers obtained using the optical microscope is shown in Fig. 10.5a. The image clearly demonstrates the core of 0.54 μm in diameter surrounded by the shell of 2 μm.

Formation of core-shell instead of monolithic fibers in co-blowing, and their transformation into hollow mesoscopic carbon tubes after heat treatment can be also elucidated with the help of TEM images. Such images are shown in Figs. 10.4b,c. They demonstrate that carbonized fibers in co-blown core-shell mats are indeed hollow, with a through bore of about 50-150 nm in diameter. It is emphasized that the optical images of the as-blown core-shell fibers in Fig. 10.3a showed the outer diameters of about 2 μm, whereas the TEM images of the carbonized fibers revealed shrinkage, which resulted in the outer diameters in the range 400-600 nm. It is emphasized that sonication flattened the amorphous carbon tubes, which can be seen from the TEM images in Figs. 10.4-b,c.

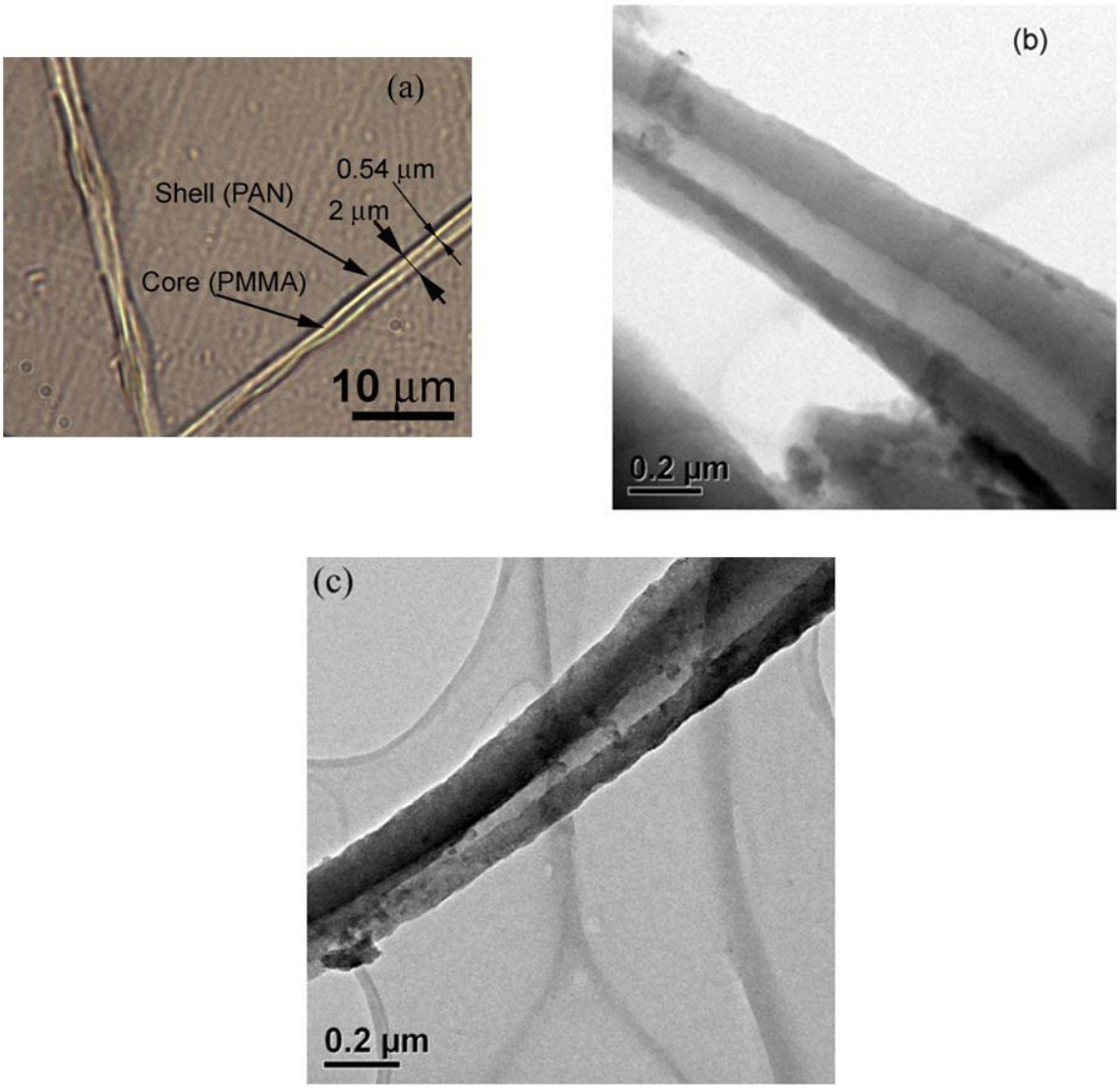

Fig. 10.4. (a) An optical image of the core-shell (PMMA-PAN) fibers. (b) and (c) TEM images of mesoscopic carbon tubes formed from carbonized PMMA-PAN core-shell fibers.

10.4 Electrochemical Results of Solution Blown Carbon Nanofiber Mat

The solution blown carbon nanofiber mat prepared in this work were tested by U. Schroder as an electrode in microbial fuel cell. The current density data corresponding to the maxima of the respective semi-batch experiment were averaged over at least three

independent experimental sets. The results thus obtained is summarized in Table 10.1. From the experiments it was found that for the conventional carbon graphite felt the maximum projected current density obtained was 13 Am^{-2}, which is still quite high and can be attributed to the fact that preselected (secondary) biofilms were with an optimized performance (Liu et al., 2008) in combination with the reaction temperature of 35 ^0C (Patil et al., 2010). For solution blown carbon nanofiber mat prepared in the present work the projected current density showed a higher value of 17-21 Am^{-2}. In addition, it was found that addition of 15% CB increased the current density from 17 A m^{-2} to 21 A m^{-2}. However, the reasoning behind such behaviour is not clear from the experiments and it requires further investigation.

Table 10.1 Cumulative data on electrocatalytic current densities obtained at different electrode materials. The substrate was 10 mM acetate.

Electrode material	**Projected (geometric) Current Density ($A\ m^{-2}$)**
Polycrystalline graphite	13
Solution Blown Carbon Nanofiber Mat	17
Solution Blown Carbon Nanofiber Mat + Carbon Black	21

10.5 Conclusion

In summary, solution blowing and co-blowing resulted in monolithic PAN and core-shell PMMA-PAN polymer nanofibers, respectively. After heat treatment of core-shell nanofiber mats the PMMA core was eliminated, whereas the PAN shell was carbonized. As a result, mesoscopic carbon tubes were obtained with a through bore of about 50-150 nm in diameter and the outer diameters in the range 400-600 nm. The preliminary testing of our solution blown carbonized electrodes conducted by U. Schroder group showed our materials also provide a better alternative to standard microbial fuel cell, which can be fine tuned and optimized for even better results in future.

11. SOLUTION BLOWING OF SOY PROTEIN FIBERS

11.1. Introduction

In the present work we employed solution blowing as described in Chapter 10 - to produce monolithic and core-shell nanofibers containing soy protein. We denote as monolithic the fibers made of sp/polymer blends and distinguish them from core-shell fibers where sp is located in the core, and a polymer is predominantly in the shell. It is emphasized that in this work it was impossible to form pure sp fibers. The monolithic nanofibers made from sp/nylon-6 blends were basically non-porous in the scale of 10-100 nm. The core-shell sp/nylon-6 fibers had pores in the shell in the scale of 10 nm.

The structure of this Chapter is as follows. Section 11.2 describes the experimental methods, section 11.3 is devoted to the results and discussion. Conclusion are drawn in section 11.4.

11.2 Experimental

For solution blowing of monolithic and core-shell nanofibers containing soy protein two different polymers were used: polyamide-6 (nylon-6) obtained from BASF (Mw= 65.2 KDa). The solvent used was formic acid, grade >95%, obtained from Sigma-Aldrich. The soy protein isolate PRO-FAM 955 (sp 955) was generously donated by ADM Specialty Food Ingredients. They were used to obtain all the results reported in this work except those in Figs. 11.2 c,d and Fig. 11.3 where soy protein isolate PRO-FAM 974 was used for comparison. All the materials were used as received. For fluorescent imaging the following materials were used: phosphate-buffered saline (PBS), bovine serum albumin (BSA; Sigma A7906), a rabbit anti-soy antibody (S 2519; Sigma-Aldrich,

Steinheim, Germany) and a goat anti-rabbit IgG FITC antibody (Cat. No.10004302, Cayman, USA).

For solution blowing (Rangavajhyala et al., 1997) of monolithic nanofibers, blends of nylon-6 and sp 955 in formic acid were used. Solutions based on formic acid were prepared as follows. First, 1 g of soy protein sp 955 was mixed with 8.5 g of formic acid and left on a hotplate at 60-65 ^{0}C for 24 hours. Next, 1.5 g of nylon-6 was added to the solution. For comparison (cf. Figs. 11.2 c,d and 11.3 below), the additional blends of soy protein sp 974 and nylon-6 in formic acid were prepared with the sp/nylon-6 ratio of 40/60 (w/w). It is emphasized that soy protein was completely dissolved in the acid. It should be mentioned that the pH of formic acid is 2, which is significantly lower than pH 4.5 corresponding to the isoelectric point of soy protein. The color of the soy protein solution changed to transparent brownish instead of opaque, which corresponds to a complete denaturation of soy protein as explained in (Gennadios et al., 1993). Note also that solubility of soy protein at pH 2 was reported in (Rangavajhyala et al., 1997).

For the solution blowing of core-shell fibers (Chapter 10) the shell was formed from a 20 wt% nylon-6 solution in formic acid. The core was prepared as follows: 1.3 g of sp 955 was completely dissolved in 8.7 g of formic acid. After that, 1g of nylon 6 was also dissolved in that solution. The addition of nylon-6 to the core was also done to increase viscoelasticity which facilitates solution blowing.

Solutions used for blowing experiments were characterized rheologically in a simple shear experiment. The shear measurements were carried out using a Brookfield DV-II+ PRO cone-and-plate viscometer. Figure 11.1 depicts the data corresponding to two solutions: (i) a solution of sp 955 in formic acid (1 g of sp 955 in 8.5 g of formic

acid), and (ii) a solution of sp 955 and nylon-6 in formic acid (described in the previous subsection). In both cases the flow curves show an expressed shear-thinning behavior, albeit shear viscosity of the sp solution is by two to three orders of magnitude lower than that of the sp/nylon-6 solution.

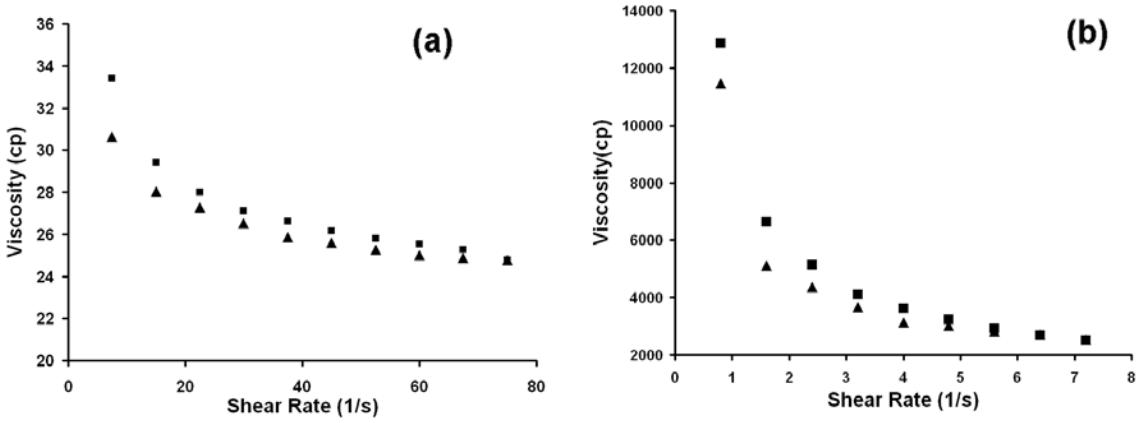

Fig. 11.1. Shear viscosity vs. shear rate of two solutions: (a) soy protein (sp 955) solution in formic acid, (b) sp 955 and nylon-6 solution in formic acid. Triangles correspond to the data acquired when ramping up in shear rate, while squares - when ramping down.

The setup used for solution blowing in this work is described in detail in chapter 10. However, depending on the polymer solutions used minor adjustments were done in the size of the nozzle issuing them. In particular, a 13 gauge needle was used for blowing blends of soy protein with nylon-6 to prevent clogging. For blowing core-shell fibers the needle sizes were initially chosen as in Chapter 10 where a 25 gauge needle was used as a core and a 16 gauge needle was used as a shell. The shell flow rate tested first was 5 mL/h and the core flow rate was 1.6 mL/h. However, as the core diameter was relatively small, the flow in it was frequently interrupted and required cleaning. Then it was established that the best choice for blowing core-shell fibers is to issue the shell solution through a 13 gauge needle and the core solution through an 18 gauge needle. These sizes

were sufficient to prevent clogging and sustain a continuous blowing process. It is emphasized that similarly to Chapter 10, a continuous blowing process was achieved when the core needle did not protrude from the concentric outer needle. In distinction from Chapter 10, no electric field was used in the present work. This can be attributed to the fact that in Chapter 10 the core was a poly(methylmethacrylate), PMMA (M_w=996 kDa), solution, which was highly viscoelastic and required an extra pulling force (the electric force resulting from the Maxwell electric stresses). On the other hand, the core soy protein blends (even with a small amount of nylon-6 added) had a low enough elasticity, for which the aerodynamic drag imposed by the blowing gas was sufficient to sustain a continuous process. It should be also mentioned that it was found that a mismatch in the solvents in the core (e.g. water) and shell (formic acid) immediately led to precipitation of the shell polymer and interruption of the process. For this reason, formic acid was used not only in the shell but also in the core.

For blowing of monolithic fibers, the flow rates of the blends in all cases were varied in the range 4-5 mL/h and the stagnation pressure of the compressed gas was varied in the range 20-25 bar. For blowing of nylon-6 based core-shell fibers, the shell flow rate was set as 5 mL/h. The flow rate of the core was kept constant at 6 mL/h and the stagnation pressure of the compressed gas was varied in the range 20-25 bar.

All the optical observations were done using optical microscope Olympus BX-51. SEM images were obtained using JEOL 6320F. Fluorescent images were recorded using a Nikon microscope (Eclipse E800).

11.3 Results and Discussion

Blends of Soy Protein and Polymer: Monolithic Fibers. The fibers obtained from the blend of soy protein and nylon-6 are shown in Figure 11.2. They have no visible grains of protein, as it was completely dissolved in formic acid. A macroscale web image corresponding to Fig. 11.2a-c is shown in Fig. 11.2d.

In dry monolithic nanofibers formed using solution blowing of soy protein (PRO-FAM 955) blends with nylon-6 the protein/polymer ratio of sp/nylon=40/60 was achieved.

Core-shell Nanofibers of Soy Protein and Polymer. The SEM images in Figure 11.3 show the cross-sectional view (Fig. 11.3a) and side view (Fig. 11.3b) of the nylon-6 based core-shell nanofibers. Denaturation of soy protein by formic acid results in complete solubilization of the former, while the evaporation of the latter after fibers were formed leaves a porous nylon-6 shell seen in Fig. 11.3b (as discussed in Dror et al., 2007; Srikar et al., 2008). The image in Fig. 11.3a shows a significant grayness gradient between the core and the shell, which is attributed to a significant electron contrast of soy protein in the core and nylon-6 in the shell.

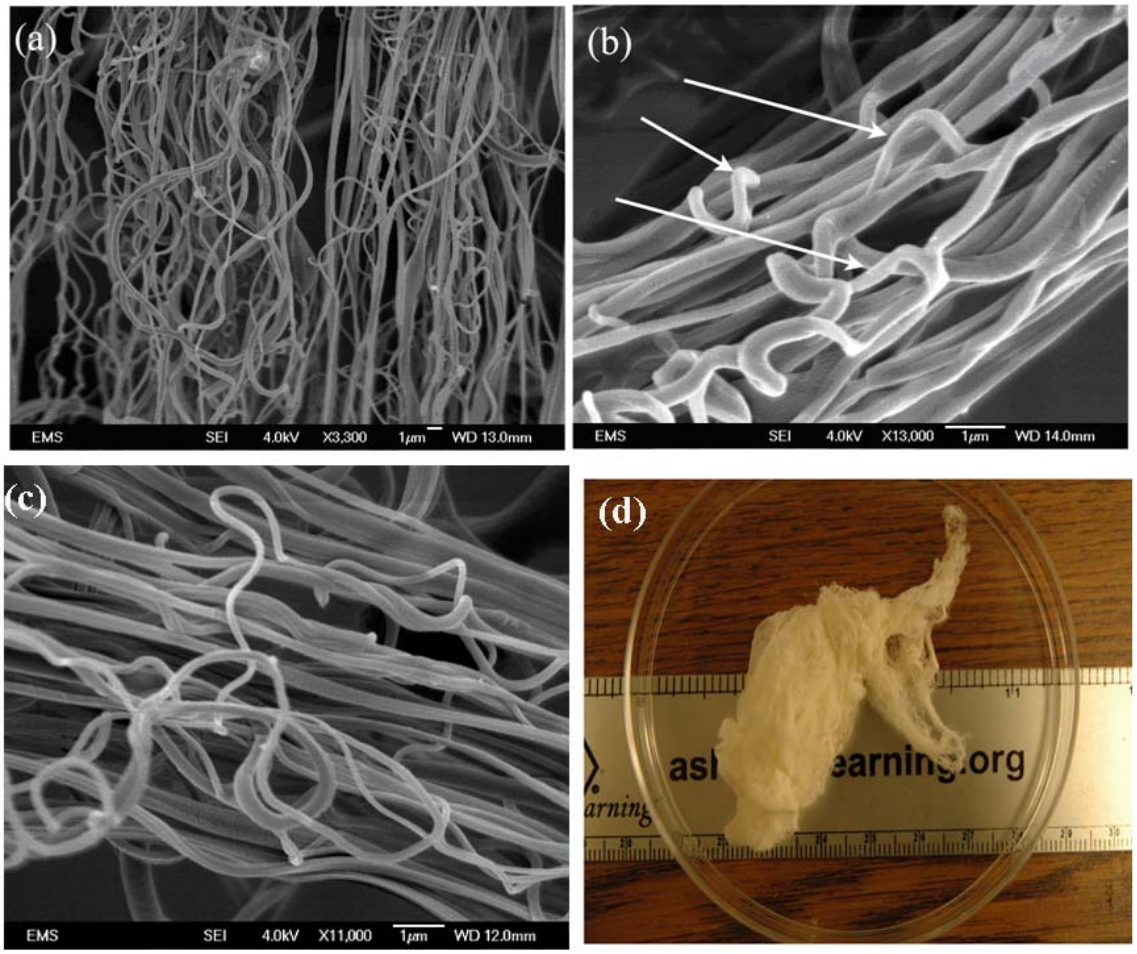

Fig. 11.2. Panels (a) and (b) show SEM images of the monolithic fibers formed by blowing a blend of nylon 6 and soy protein PRO-FAM 955 in formic acid. The zoomed-in view of a section of (a) is shown in panel (b) and (c). The fibers are rather curly. The macroscale web shown in panel (d) corresponds to the nanofibers of panel (a)-(c).

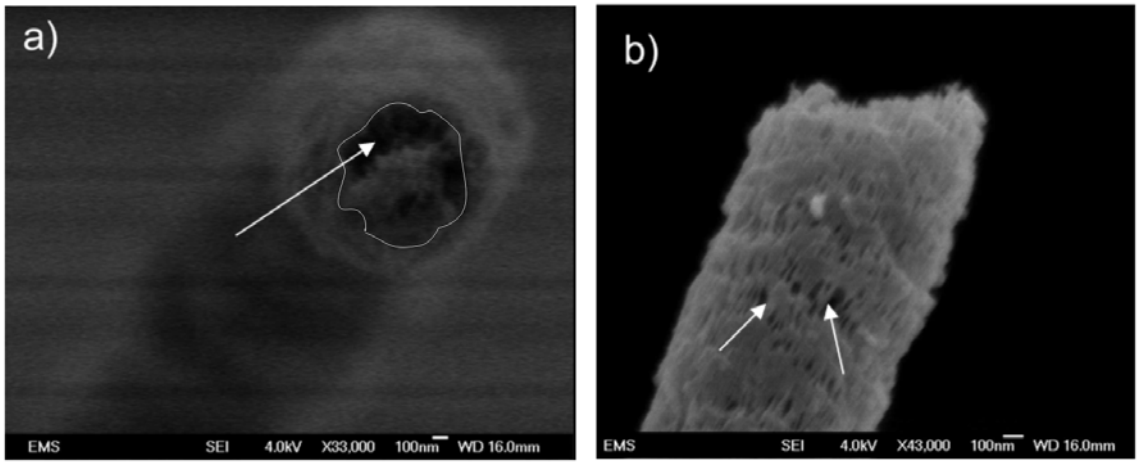

Fig. 11.3. Panels (a) and (b) show SEM images of core-shell fibers made with fully denaturated soy protein and nylon 6. The core is clearly visible in the cross-sectional view in panel (a) because of a significant electron contrast between soy protein and nylon-6. The core boundary in panel (a) is also traced by a white contour to make it more visible in printed reproduction and marked by the arrow. The side view (b) shows that the nylon 6 shell of this core-shell fiber is porous.

In dry core-shell nanofibers the sp/nylon-6 ratio was 32/68.

Fluorescence Microscope Imaging. Fluorescence imaging done by Yiyun Zhang revealed the presence of soy protein in blend and core-shell nanofibers.

Statistical Image Analysis. Nonwovens produced by solution blowing are comprised of the entangled individual fibers. They practically never end until the process is stopped. In this sense, they are similar to electrospun nanofiber mats. Therefore, measurements of fiber lengths and aspect ratios are meaningless. On the other hand, cross-sectional diameter can vary even along the individual fibers due to the effect of the turbulent pulsations in gas and elastic wave propagation (Chapters 7 and 8). Therefore,

measurements of fiber diameter distribution can be important for the structural characterization of the solution-blown nonwovens and their further applications. Figure 11.4 depicts the diameter distributions measured from SEM images of sp/nylon-6 fibers blown from blends, while Fig. 11.5 contains the corresponding data for sp/nylon-6 core-shell fibers. It is emphasized that the blend-blown (monolithic) fibers all belong to the submicron range, whereas the core-shell fibers can involve infrequent outliers as large as 2 μm. Still the core-shell fibers are submicron in average.

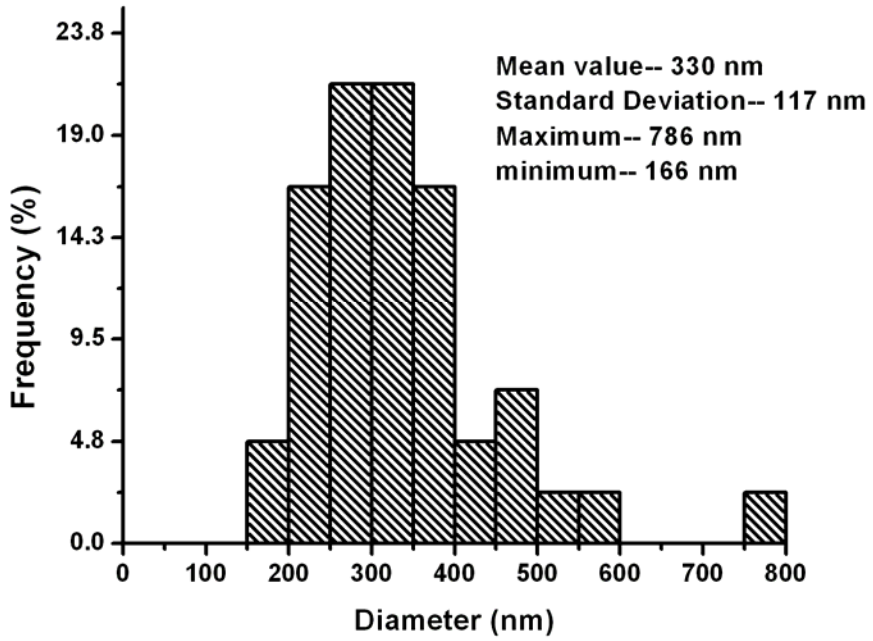

Fig. 11.4. Diameter distribution in sp/nylon-6 blend solution blown nanofibers.

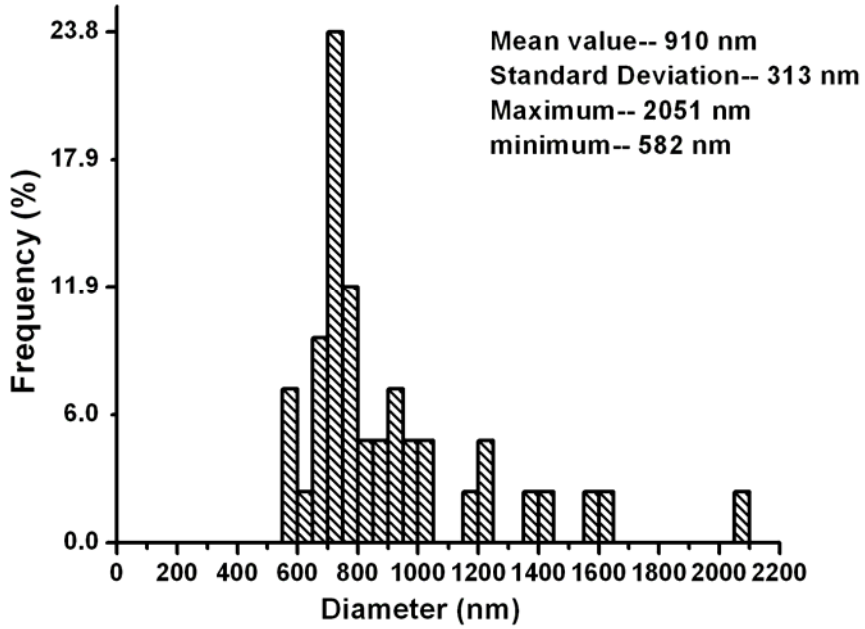

Fig. 11.5. Diameter distribution in sp/nylon-6 core-shell solution blown fibers.

11.4 Conclusion

Solution blowing of monolithic and core-shell soy protein-polymer fibers was demonstrated. The blend fibers were produced from soy protein and nylon-6. They had a protein/polymer ratio of 40/60 in the dry sp/nylon-6 fibers. The core-shell fibers were produced from protein/nylon-6 in the core and nylon-6 in the shell. They had a protein/polymer ratio of 32/68 in the dry core-shell fibers. The individual fibers and their nonwovens were analyzed using optical and scanning electron microscopy (with EDS). Soy protein and nylon-6 provided a significant electron contrast to make the protein core clearly distinguishable from the polymer shell. It was also observed that the shell is typically porous, which probably allows low molecular weight fluids to communicate with the core when core-shell fibers are submerged into them, which makes them

attractive for many applications. The monolithic (blend-blown) fibers all belong to the submicron range, whereas the core-shell fibers can involve infrequent outliers as large as 2 μm. Nevertheless, the core-shell fibers are submicron in average.

The monolithic and core-shell nano- and micro-fibers containing significant amounts of soy protein developed in this work hold great potential as an effective method of utilizing of the one of the most abundant natural materials. In particular, it is foreseen as an effective method of utilization and valorisation of residual material left by SoyDiesel production, which can be useful in various applications of nonwovens.

12. THORNY DEVIL NANO-TEXTURED FIBERS: THE WAY TO COOLING RATES OF THE ORDER OF 1 KW/CM^2

12.1 Introduction

In the present work high-heat flux surfaces, which should serve at temperatures up to 200 ^{0}C, were covered by electrospun polymer nanofiber mats of thicknesses of about 30 μm. Then, four different metals were electroplated on separate polymer mats, namely, copper, silver, nickel and gold. As a result, copper-plated nanofiber mats took an appearance resembling that of a small Australian thorny devil lizard, i.e. became very rough (on the nano-scale), as well as acquired high thermal diffusivity. Silver-plated nanofiber mats also became very rough due to the dendrite-like and cactus-like nano-structures on their surfaces. On the other hand, nickel-plated nanofibers were only partially rough, while their mats incorporated large domains of smooth nickel-plated fibers, and gold-plate nanofibers were practically smooth. Drop impacts on the hot surfaces coated with copper-plated and silver-plated nanofibers revealed tremendously high values of heat removal rates up to 0.6 kW/cm^2. Such high values of heat flux are more than an order of magnitude higher that the currently available ones, and probably can be increased even more using the same technique. They open some intriguing perspectives for cooling of high-heat flux micro- and opto-electronics and for further miniaturization of such devices, especially for such applications as UAVs and UGVs.

Section 12.2 describes the experimental and section 12.3 - the result and discussion. Section 12.4 exposes theoretical background. Conclusions are drawn in section 12.5.

12.2 Experimental

Polyacylonitrile (PAN; M_w=150 kDa) was obtained from Polymer Inc. N-Dimethyl formamide (DMF) anhydrous-99.8%, sulfuric acid, hydrochloric acid, copper sulfate, formaldehyde, silver nitrate, potassium hydroxide, ammonium hydroxide, nitric acid, nickel sulfamate, boracic acid, sodium hydroxide, triammonium citrate, potassium aurochlorate, and sodium sulfite were obtained from Sigma-Aldrich. Copper plates obtained from McMaster-Carr were cut into 1''×1'' square pieces used as substrates. The substrates were polished and cleaned with acetone by sonication prior to use.

For electrospinning, 12 wt% PAN solution in DMF was prepared. Electroplating protocols were developed by Yiyun Zhang and will be described in detail in her thesis (also, cf. Sinha-Ray et al. 2011**)**

Polymer nanofiber mats were prepared by electrospinning PAN solution using a standard electrospinning setup described elsewhere (Reneker et al., 2000, 2007, 2008). Randomly oriented nanofibers were collected on thin copper substrates. Fibers were electrospun for 5-7 minutes, while keeping the flow rate of 0.8 mL/hr and the electric field about 1 kV/cm, which resulted in the nanofiber thicknesses of the order of 20-30 μm. The nanofiber mats adhered to the copper substrates and were used as templates for the further electroplating.

For the electroplating nanofiber mats had to be sensitized to make them conducting. For that purpose the nanofiber mats were sputter-coated with Pt-Pd to a thickness of 15 nm by using Cressington Sputter Controller.

All scanning electron microscopy of metal-plated nanofiber mats was done using JEOL JSM-6320F with a cold emission source.

For the investigation of drop impacts, three different variants of the experimental setup depicted in Figure 12.1 were used. In this setup substrates were kept on a hot plate at a constant temperature. Water was supplied to the needle end using a syringe pump. As a result, a single drop had been growing at the needle edge, then disconnected and dripped due to gravity. After that, the pump had been stopped. Water drops were dripped from a height, which could be varied. For visualization of drop impacts on metal-plated nanofiber mats, two cameras were used in the basic setup in Fig. 12.1. For high speed photography a Redlake Motion Pro camera was used at a recording speed of 2000 fps, and for capturing top views an ordinary CCD video camera Pulnix 7M at a recording speed of 30 fps was used. In the second variant of the setup, the low speed CCD camera was removed and only the high speed CCD camera was used. In the third variant of the setup, the low speed CCD camera was used only.

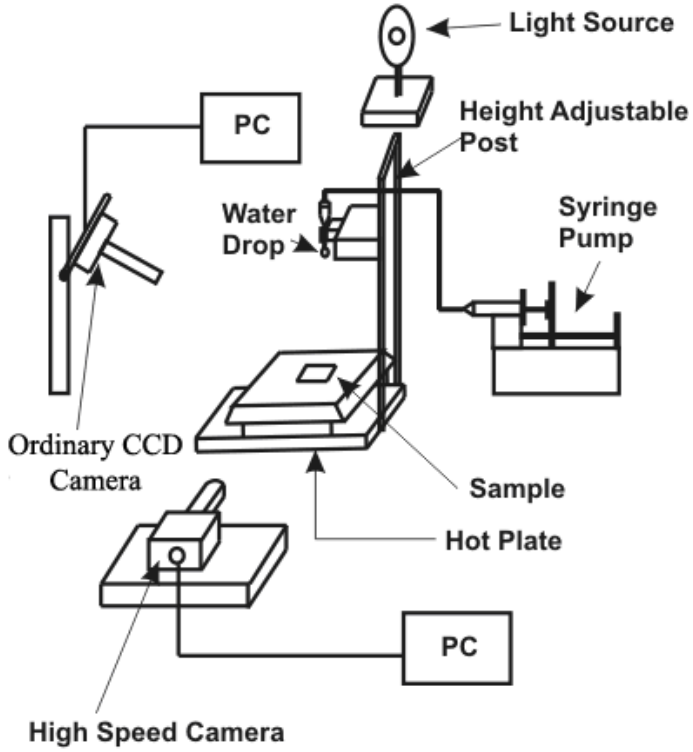

Fig. 12.1. Schematic of the experimental setup.

It is emphasized that the temperature on the display of the hotplate is not exactly the same as that of the sample on top of it. Therefore, measurements of the sample temperature were done separately and the calibration of the temperature versus that of the display is shown in Table 12.1. The thin copper substrates used in this work were covered by metal-plated nanofiber mats of thicknesses of about 30 μm. In this case the substrate steady-state temperature distribution is uniform and accurately represented by its base temperature measured by a thermocouple. The latter represents itself the whole sample temperature (including nanofibers) given in Table 12.1.

Table 12.1. Sample temperature versus the display temperature.

Display temperature (^{0}C)	Sample temperature (^{0}C)
40	34
50	41
60	50.3
70	57.5
80	68.4
90	73.6
100	83.7
110	93.5
125	102.7
150	125.6
200	172.2

12.3 Results and Discussion

Metal-plated Nanofiber Mats. SEM images of the electroplated nanofiber mats produced by Yiyun Zhang are shown in Figs. 12.2-12.5. The individual copper-plated fibers possess thorny (Fig. 12.2c) and grainy (Fig. 12.2d) nano-texture, which makes them reminiscent of the Australian thorny devil lizards. Silver-plated nanofibers are equally rough but show predominantly dendrite-like or cactus-like structures (Fig. 12.3). The nickel-plated nanofibers reveal an additional type of nano-texture, namely, the distinct domains of smooth and rough fibers (Fig. 12.4). In contrast to the other cases, gold-plated fibers are smoother and possess only infrequent spheroidal appendices or their small clusters (Fig. 12.5). The comparison of the images with the same magnification (Figures 12.2c,d, 12.3c,d, 12.4c,d and 12.5c,d) shows that copper –plated fibers possess the roughest nano-texture uniformly. Moreover, even though only the upper layer of the nanofibers appears to be rough in Figs. 12.2 and 12.3, this is only an artifact related to the electron beam focusing in SEM. The images of a cut copper-plated nanofiber mat in Figure 12.6 show that the fibers at the mat bottom in contact with the underlying substrate are as thorny-devil-like as those near the mat surface in Fig. 12.2. Therefore, the fibers are rough throughout the whole mat depth.

Similarly, the nickel-plated fibers possess a mosaic of smooth and rough domains, and gold-plated fibers are practically smooth throughout the mat depth. The gold-plated nanofibers in Fig. 12.5 are relatively smooth.

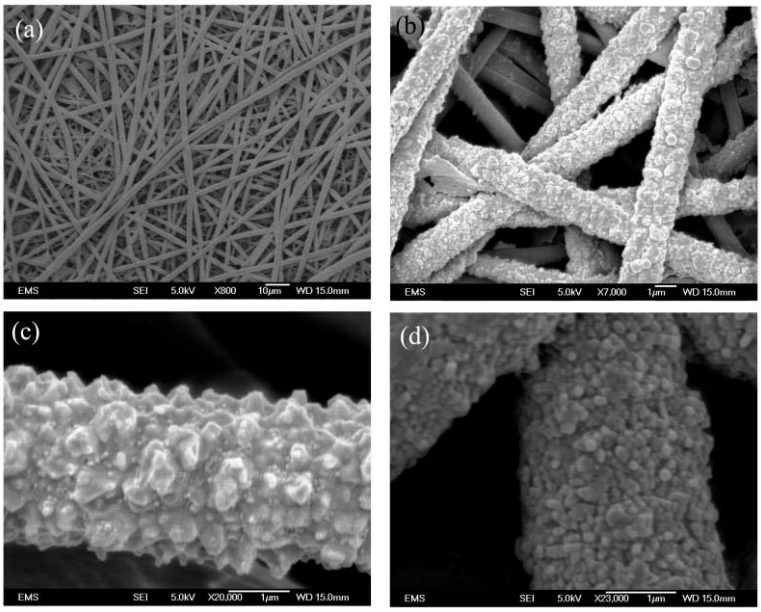

Fig. 12.2. SEM images of the thorny devil copper-plated fibers. (a) The overall view of the copper-plated fiber mat. (b) The zoomed-in view of the top layer. The individual fibers at different locations: (c) thorny and (d) grainy nano-textures.

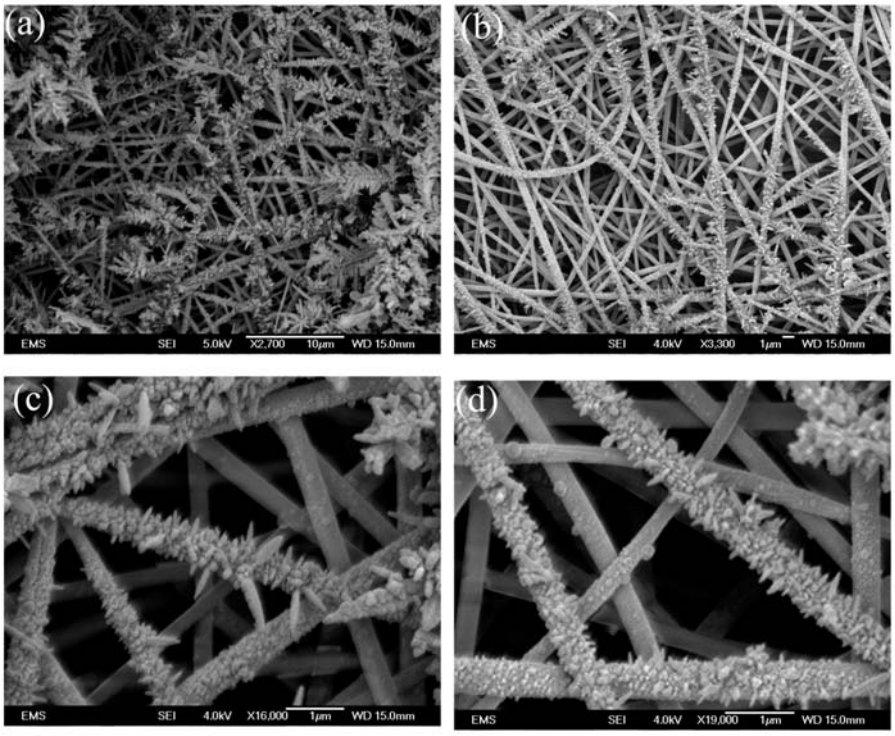

Fig. 12.3. SEM images of the dendrite-like and cactus-like silver-plated nanofiber mats. Panels (a) and (b) show the overall view of the silver-plated nanofiber mat at two different locations. The fibers look like dendrites or fern leaves in (a) and more cactus-like in (b). Panels (c) and (d) show cactus-like nanofibers in more detail.

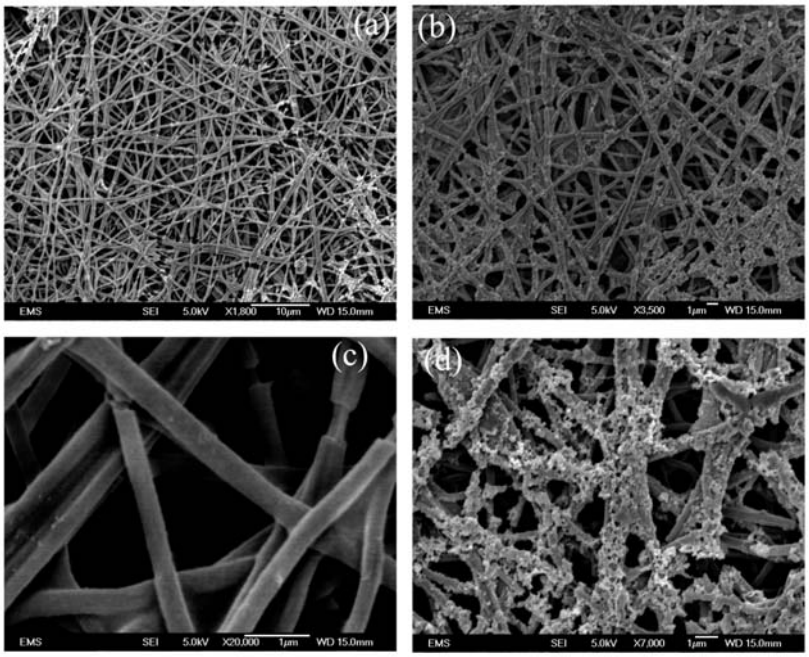

Fig. 12.4. SEM images of nickel-plated nanofibers. Panels (a) and (b) show the overall view of nickel-plated nanofibers at two different locations. (c) Smooth nano-texture of the individual nickel-plated nanofibers. At some places the coating broke due to rough handling exposing the skeletal template polymer. (d) Rough nano-texture of the individual nickel-plated nanofibers.

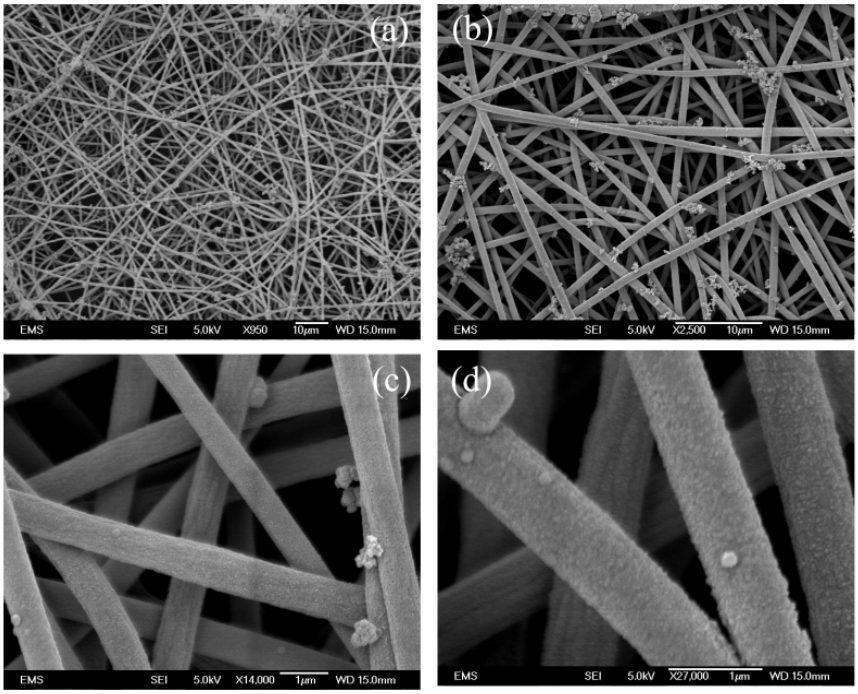

Fig. 12.5. SEM images of gold-plated nanofibers. (a) The overall view of the gold-plated nanofiber mat. (b) The zoomed-in view of the upper layers with the visible appendices scattered over the fibers. (c) and (d) Several individual fibers: almost smooth coatings with some appendices at two different locations.

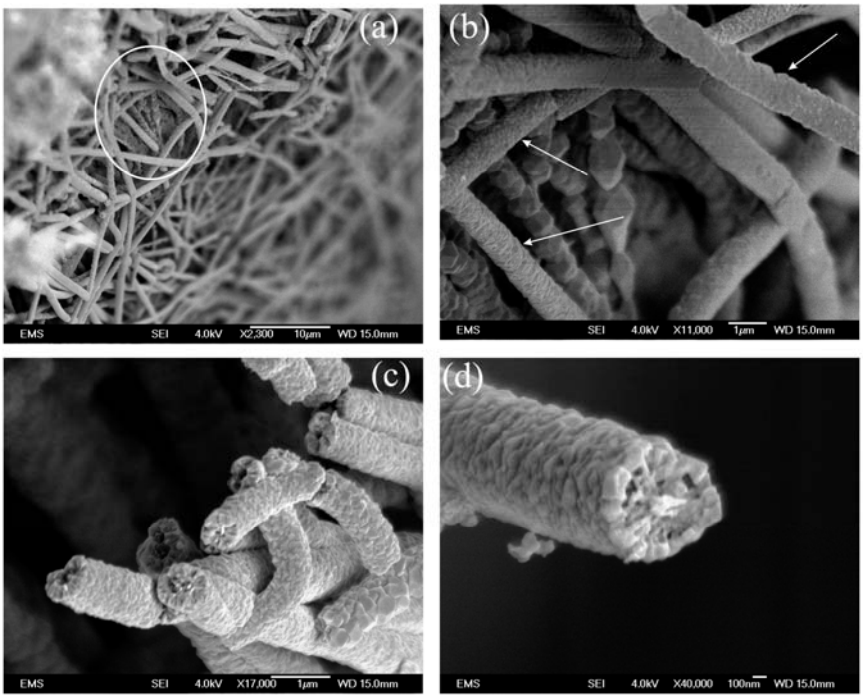

Fig. 12.6. SEM images of a cut copper-pated nanofiber mat. (a) The overall view of the cut mat near the underlying substrate. The encircled area seemingly shows that some copper-plated nanofibers are rough, whereas some others seem to be smooth. The latter is just an artifact, since these smooth-like nanofibers are just out of focus. Indeed, the zoomed-in image of the encircled area in panel (b) shows that the previously "smooth" nanofibers indicated by arrows, in reality have rough structure as well. Panels (c) and (d) show a detailed structure of the copper-plated fiber mat near the substrate in some other place.

Surface Enhancement Factor. The surface enhancement factor α is defined as a ratio of the overall surface area including that of the fibers on a unit area of a substrate to that of the bare substrate. It is emphasized that in the general case the bare substrate used for comparison might be made of a different metal than the one coated with nanofibers, since

in the experiments described in the present section the expectation is that the surface enhancement factor is a pure geometric parameter. For the evaluation of the surface enhancement factor the following experiment was conducted. A water drop was dripped from a fixed height of 10.64 cm on either bare copper substrate or a copper substrate covered with copper-plated nanofiber mat. The bare substrate and the fiber-mat-coated substrate were kept at the same fixed temperature when drop evaporation was observed. In different experiments a fixed temperature was chosen from the range from 40 ^{0}C to 110 ^{0}C (the display temperature, which corresponds to 34 ^{0}C to 93.5 ^{0}C sample temperature) with a 10 ^{0}C step (the display temperature). The evaporation time Δt of water drops was recorded using the ordinary CCD camera. The thermal balances for a bare substrate and a nanofiber-coated substrate read

$$LV_1 = \frac{k_{w1}}{\delta_{w1}} \Delta T S_1 \Delta t_1 \tag{12.1}$$

$$LV_2 = \frac{k_{w2}}{\delta_{w2}} \Delta T S_2 \Delta t_2 \tag{12.2}$$

where subscripts 1 and 2 refer to a bare substrate and a nanofiber-coated substrate, respectively. Also, L is the latent heat of evaporation, V is the drop volume, k_w and δ_w are the thermal conductivity and thickness of a substrate, respectively, S is the wetted surface area, and ΔT is the excess temperature of the substrates relative to the room temperature.

The area S_2 can be represented as the sum of the wetted substrate area S_{20} and the wetted nanofiber area on the substrate ΔS

$$S_2 = S_{20} + \Delta S \tag{12.3}$$

In the experiments it was $k_{w1}=k_{w2}$ and $\delta_{w1}=\delta_{w2}$, i.e. two substrates of the same material and thickness were used. Also, two drops were identical, i.e. $V_1=V_2=3.053$ mm^3, which corresponds to the initial drop radius of 0.9 mm Then, Eqs. (12.1)-(12.3) reduce to

$$\alpha = 1+\frac{\Delta S}{S_{20}} = \frac{\Delta t_1}{\Delta t_2}\frac{S_1}{S_{20}} \tag{12.4}$$

The values of Δt_1, Δt_2 and S_1/S_{20} measured experimentally are listed in Table 12.2 together with the surface enhancement factor α found from Eq. (12.4). The relative surface area of the nanofibers was determined from Eq. (12.4) as

$$\frac{\Delta S}{S_{20}} = \alpha - 1 \tag{12.5}$$

which is also presented in Table 12.2.

Table 12.2. Surface enhancement factor α

Temperature (^{0}C) Display/sample	Δt_1 (sec)	Δt_2 (sec)	$\Delta t_1/\Delta t_2$	S_1/S_{20}	α	Relative surface area of nanofibers, $\Delta S/S_{20}$
40/34	255	30	8.5	0.873	7.42	6.42
50/41	195	21	9.3	0.852	7.91	6.91
60/50.3	100	18	5.56	0.933	5.18	4.18
70/57.5	60	15	4	0.804	3.22	2.22
80/68.4	39	13	3	0.833	2.50	1.50
90/73.6	25	9	2.78	0.717	1.99	0.99
100/83.7	18	7	2.57	0.934	2.40	1.40
110/93.5	16	5	3.2	0.908	2.90	1.90

It is emphasized that the experimental data in Table 12.2 fully support Eqs. (12.1) and (12.2). Indeed, taking for the room temperature the value of 20 ^{0}C and taking the sample temperature from Table 12.1, one can plot the measured value of the evaporation time on metal-plated nanofiber mats Δt_2 versus ΔT. The result plotted in Fig. 12.7 fully supports the linear dependence of Δt_2 on ΔT^{-1} anticipated from Eq. (12.2).

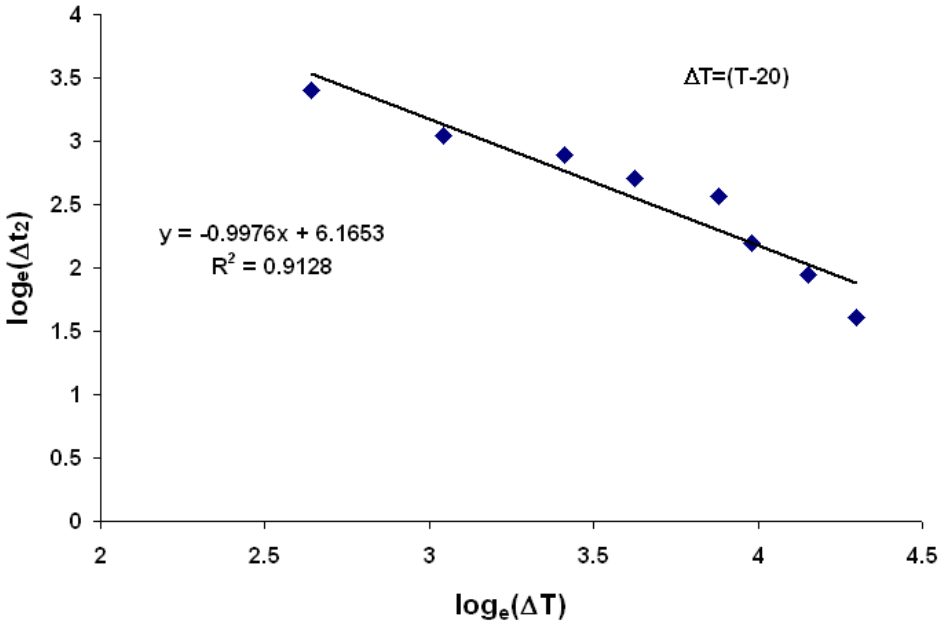

Fig. 12.7. Dependence of drop evaporation time on metal-plated nanofiber mat on ΔT at the room temperature of 20 ^{0}C. The slope is equal to -0.9976 in log-log coordinates; from Eq. (2) the slope -1 is anticipated. The coefficient of determination R^2=0.9128.

The data in Table 12.2 and Fig. 12.7 show that at elevated temperatures the linear dependence of t_2 on ΔT deteriorates and the effective value of α decreases, which probably can be attributed to the effect of rapid evaporation and boiling inside the

copper-plated nanofiber mat. Therefore, only the values at the lowest two temperatures are relevant to determine such purely geometric parameter as the surface enhancement factor α. Then, the surface enhancement factor due to the presence of nanofibers is in the range $\alpha \approx 7.5-8$.

Morphology of Drop Impact Cooling Through Copper-plated Mats. Copper substrates coated with metal-plated nanofiber mats, as well as bare copper uncoated substrates used for control, were located on a hot plate at different fixed elevated temperatures. Water drops released from different heights were used to locally cool them to evaluate the corresponding cooling rate. In these experiments the setup depicted in Figure 12.1 was initially employed. A substrate coated with copper-plated nanofiber mat was placed on a hot plate at a fixed temperature of 150 ^{0}C (the display temperature corresponding to 125.6 ^{0}C of the sample). A single water drop of radius a_0=0.9 mm **(**was dripped from various heights. The whole process (drop approach, spreading, and evaporation at the nanofiber mat) was captured simultaneously by the ordinary CCD camera (recording at 30 fps) and the high speed camera (at 2000 fps). The ordinary CCD camera recorded the process from top, whereas the high speed camera recorded the process from a side. Drops fell onto nanofiber mats from the following heights h=3.55 cm, 6.15, 8.75, 11.15, 13.75 and 17.95 cm, which correspond to the impact velocities V_0= 83.46, 109.85, 131.02, 147.91, 164.25 and 187.66 cm/s respectively, (evaluated as $V_0 = \sqrt{2gh}$, where g is gravity acceleration).

The top and side view images of drop impact from the height of 3.55 cm, spreading and evaporating on a copper-plated nanofiber mat are shown in Figs. 12.8 and 12.9,

respectively. Figure 12.8a depicts the moment of drop impact (t=0) at the nanofiber surface. Figure 12.8b shows that at the moment t =32.5 ms water boiling is visible at the surface, whereas Fig. 12.8c demonstrates that boiling seemingly ceased at t=66 ms and there is no visible activity at the surface anymore. In panel (a) in Fig. 12.9 the area surrounded by the white tracing contour corresponds to the projection of the oncoming drop onto the nanofiber mat surface. This image corresponds approximately to the top view of the situation similar to that of Fig. 12.8a. In panel (b) in Fig. 12.9 the area surrounded by the white tracing contour is still covered by water visible in the side view of the corresponding Fig. 12.8b. Water was either partially evaporated or penetrated into the copper-plated mat between the images in Figs. 12.9a and 12.9b. In panel (c) in Fig. 12.9 the area surrounded by the white tracing contour is still wetted, even though the active boiling at the surface and probably inside the mat has already ended according to the corresponding Fig. 12.8c. From that time on, the wet area begins rapidly loosing its visible contrast, which probably corresponds to the ultimate drying. It should be mentioned that when the images recorded by the CCD camera for the longer times were analyzed, some minor contrast variations were observed for the next 4-5 frames, which corresponds to t=132-165 ms. However, the contrast variation was so small that no visible activity was recorded by the high speed camera in this time range. Therefore, it was concluded that the above-mentioned minor contrast variations resulted most probably from condensation of water vapor onto nanofiber mat, which followed the cessation of the cooling stage. Due to the low time resolution of the CCD camera used, it could not resolve the time frame t<33 ms in Figure 12.9. However, Fig. 12.9 shows that the water drop impacted onto the surface between the panels (a) and (b) in Fig. 12.9, which

corresponds to $0 \le t \le 33$ ms and that it fully evaporated sometime between the panels (c) and (d), which corresponds to $66 \le t \le 99$ ms. On the other hand, Fig. 12.8 shows that the activity at the surface of the nanofiber mat ceased at 66 ms, which is close to the time frame suggested by Fig. 12.9. Similar observations were done for drop impacts from the other heights.

Cooling Rates with Copper-plated Nanofiber Mats. As in (Srikar et al., 2009b) the heat flux j was evaluated from the experimental data using the following expression: $j = \rho(4\pi a_0^3/3)(1-p)L/\pi a^2 \Delta t$, where ρ is the liquid density, a_0 the initial drop radius, a the full spread-our radius after drop impact onto nanofiber mat, L the latent heat of evaporation of water, and Δt is the duration of drop evaporation. The above expression also involves the "atomization" volume ratio p. The value of p corresponds to mass lost due to "atomization" from the mat surface, which accompanied the evaporation process in some cases. The direct measurements of p are discussed below. Using the side view images, it is practically impossible to resolve the spread-out radius a. The top view images showed that the maximum spread factor $\xi = a/a_0$ for water drops on the copper-plated mats was close to $\xi = 2$. Then, the values of the spread-out radius a (and thus, of ξ) were evaluated using the following widely used expression (Scheller et al., 1995; Yarin 2006) $\xi = 0.61(We/Oh)^{0.166}$, where the Weber and Ohnesorge numbers are defined as $We = \rho 2a_0 V_0^2/\sigma$ and $Oh = \mu/(\rho\sigma 2a_0)^{1/2}$, with μ and σ being viscosity and surface tension of water. Such values of ξ correspond to the maximum spread-out on a surface at room temperature, and thus lead to an underestimation of the cooling rate j. Note also, that the evaporation time Δt and the "atomization" volume ratio p could be accurately

evaluated from the side view images recorded by the high speed camera, therefore the top view images recorded by the CCD camera should not be used for this purpose.

The corresponding results for the spread factor ξ and the cooling rate j are presented in Table 12.3. It is emphasized that the underestimated values of the cooling rate are close or exceeding the tremendous value of $j \approx 0.57$ kW/cm^2. It is worth noting, that no clear dependence of j on the impact velocity is visible in Table 12.3.

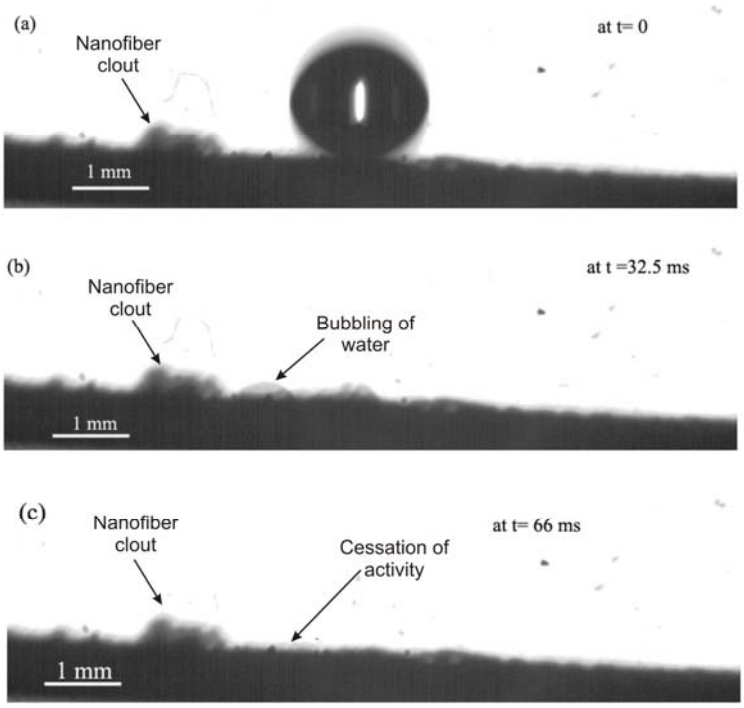

Fig. 12.8. Drop impact from the height of 3.55 cm (V_0=83.46 cm/s) onto a copper-plated nanofiber mat at 150 ^{0}C (the display temperature corresponding to 125.6 ^{0}C of the sample). (a) 0 ms-at the moment of impact; (b) 32.5 ms, (c) 66 ms.

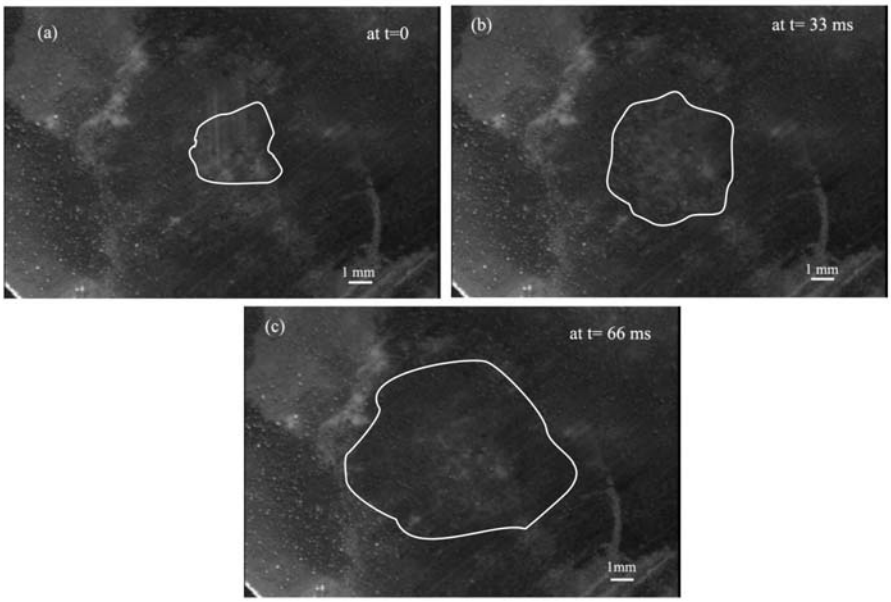

Fig. 12.9. Top view of drop impact onto a copper-plated nanofiber mat corresponding to that of Figure 7 [at 150 ^{0}C (the display temperature corresponding to 125.6 ^{0}C of the sample)].Panel (a) corresponds to t=0 ms, (b)-to 33 ms (the closest to 32.5 ms of Fig. 8b the ordinary CCD could resolve), (c)-to 66 ms.

Table 12.3. The maximum drop spread factor and the cooling rates corresponding to water drop impact on copper-plated nanofiber mats at 150 ^{0}C (the display temperature corresponding to 125.6 ^{0}C of the sample). No visible "atomization" was recorded, therefore p=0.

H (cm)	**V_0 (cm/s)**	**Δt (ms)**	**ξ**	**p**	**j (kW/cm^2)**
3.55	83.46	66	2.6	0	0.607
6.15	109.85	58	2.85	0	0.575
8.75	131.02	53.5	3.02	0	0.555
11.15	147.91	52.5	3.15	0	0.521
13.75	164.25	47	3.25	0	0.543

Comparison of Drop Impacts and Cooling Rates for Copper-plated, Silver-plated, Nickel-plated and Gold-plated Nanofiber Mats. Drop impact morphologies and the corresponding cooling rates through different metal-plated nanofiber mats (and a bare copper substrate used as a control) were studied at a fixed height of water drop release at h=17.95 cm. The latter corresponds to the drop impact velocity V_0=187.66 cm/s and the overestimated spread factor of ξ=3.407. The fixed hot plate temperatures were chosen as 125 ^{0}C, 150 ^{0}C and 200 ^{0}C (the display temperatures corresponding to 102.7 ^{0}C, 125.6 ^{0}C and 172.2 ^{0}C of the sample, respectively). Drop impact morphologies at different metal-plated nanofiber mats are shown in Figs. 12.10-12.12, which correspond to 125 ^{0}C, 150 ^{0}C and 200 ^{0}C (the display temperatures), respectively. It is clearly seen that on all metal-

plated nanofibers water drop evaporates faster than on the bare copper substrate used for control. Moreover, at higher temperatures of 150 ^{0}C and 200 ^{0}C (the display temperatures corresponding to 125.6 ^{0}C and 172.2 ^{0}C of the samples, respectively) the water drop bounces back and levitates over the bare copper substrate, which corresponds to the Leidenfrost effect.

The comparison and discussion of the results for the different metal-plated nanofiber mats are facilitated by the values of the thermal diffusivities of these metals. According to (Rohsenow et al., 1998), the values of the thermal diffusivity are as follows: for copper α_{Cu}=1.1 cm^2/s, for silver α_{Ag}=1.7 cm^2/s, for nickel α_{Ni}=0.19 cm^2/s and for gold α_{Au}=1.23 cm^2/s. The most effective fibers yielding the fastest evaporation according to Figs. 12.9-12.11 are the copper-plated fibers, with the silver-plated fibers being the second and producing close evaporation times. The highest efficiency of copper and silver could be expected based on their high values of the thermal diffusivity and highly developed thorny-devil-like or dendrite-like roughness depicted for these fibers in Figs. 12.2 (copper) and 12.3 (silver). The fact that the nickel-plated fibers lag behind the copper-plated and silver-plated ones is not surprising given an order of magnitude lower thermal diffusivity of nickel compared to that of copper and silver, and the lower fiber roughness (cf. Fig. 12.4 with Figs. 12.2 and 12.3). The most striking fact visible in Figs. 12.10-12.12 is that the gold-plated fibers lag far behind the copper-plated fibers, even though the thermal diffusivities of copper and gold are close. The latter inevitably leads to the conclusion that thorny-devil-like copper-plated fibers are much more effective in drop cooling than the smooth gold-plated ones (cf. Figs. 12.2 and 12.5) just because the surface area of the former is dramatically higher than that of the latter. It is emphasized

that gold-plated nanofibers yield the evaporation time as long as that on the nickel-plated fibers (cf. Table 12.3), even though the disparity in the corresponding thermal diffusivities is of the order of one order of magnitude in favor of gold. It is also worth mentioning that the evaporation times on metal-plated nanofiber mats are dramatically shorter than those reported before for the polymer mats (Srikar et al, 2009b). In particular, the shortest evaporation times measured in the present work are about 400 times shorter than the shortest times reported in (Briones et al., 2010) for the comparable temperatures.

The results for the cooling rate j reported in Table 12.4 are based on the directly measured values of the loss fraction p evaluated from a careful analysis of the "atomization" during boiling using multiple video images similar to several frames depicted in Figs. 12.13-12.16. The latter figures also contain the measured values of p during the whole process and the final plateau value. For the copper-plated mats the largest value of p does not exceed 0.1, i.e. is less than 10% (Fig. 12.13). For the bare copper substrate mass losses during boiling are quite dramatic, with p being of the order of 0.3 (Fig. 12.14), which means that about 30% of the initial drop was "atomized" and lost. For the silver-plated nanofibers p is about 0.03 (relatively low losses, Fig. 12.15), however, for the nickel-plated fibers losses might be as high as 20% (Fig. 12.16). Note, that there was no water "atomization" and thus, no losses, when boiling took place in gold-plated nanofiber mats.

The results for the cooling rate presented in Table 12.4 are based on the measured values of p. The non-zero values of p in Table 12.4 led to lower values of j for copper-

plated fibers listed there compared to the case in Table 12.3 (probably due to sample-to-sample variability). Still, these values are close to a tremendous value of 0.4 kW/cm^2.

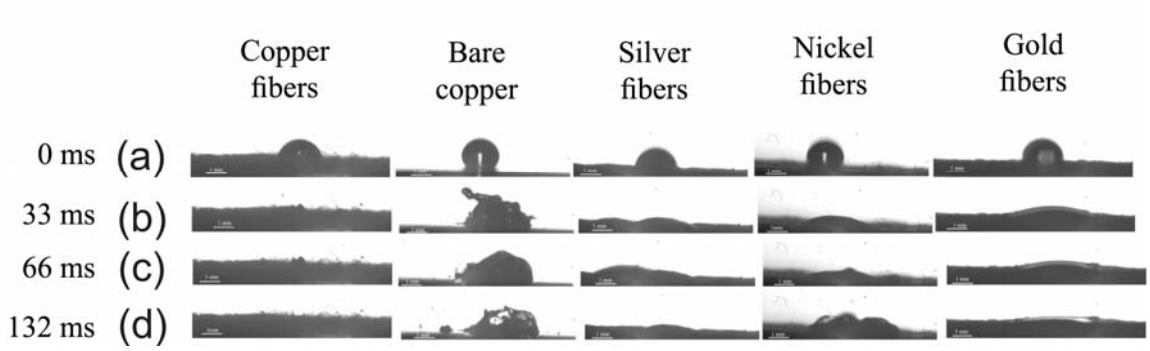

Fig. 12.10. Drop impact onto thorny devil nanofibers at 125 ^{0}C (the display temperature corresponding to 102.7 ^{0}C of the samples). The five columns correspond (from left to right) to copper-plated fibers, a bare copper substrate, silver-plated fibers, nickel-plated fibers and gold-plated fibers, respectively. The four rows (a), (b), (c) and (d) correspond to t=0, 33, 66 and 132 ms, respectively.

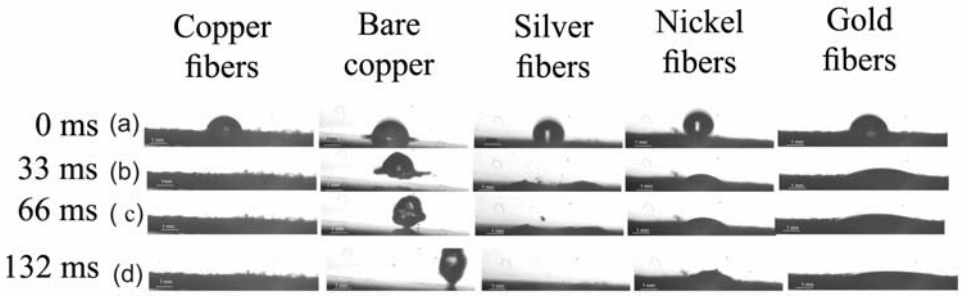

Fig. 12.11. Drop impact onto thorny devil nanofibers at 150 ^{0}C (the display temperature corresponding to 125.6 ^{0}C of the samples). The five columns correspond (from left to right) to copper-plated fibers, a bare copper substrate, silver-plated fibers, nickel-plated fibers and gold-plated fibers, respectively. The four rows (a), (b), (c) and (d) correspond to t=0, 33, 66 and 132 ms, respectively. Note that the surface of the bare copper substrate

looks as being inclined because shining illuminating light makes a part of its surface too shiny and thus invisible. This is an optical artifact.

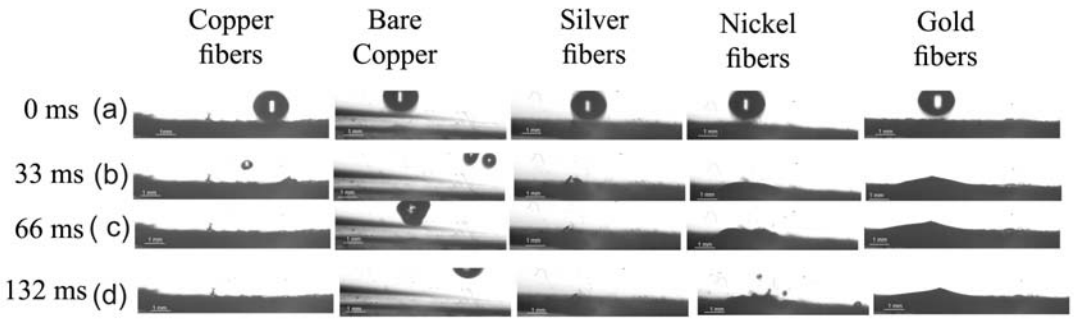

Fig. 12.12. Drop impact onto thorny devil nanofibers at 200 ^{0}C (the display temperature corresponding to 172.2 ^{0}C of the samples). The five columns correspond (from left to right) to copper-plated fibers, a bare copper substrate, silver-plated fibers, nickel-plated fibers and gold-plated fibers, respectively. The four rows (a), (b), (c) and (d) correspond to t=0, 33, 66 and 132 ms, respectively.

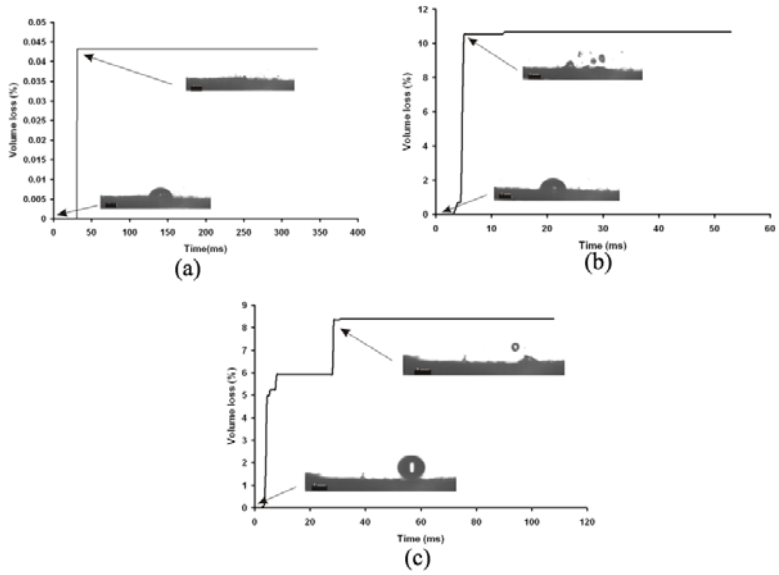

Fig. 12.13. Mass losses due to the "atomization" during cooling through copper-plated nanofiber mats. (a) 125 ^{0}C, (b) 150 ^{0}C, (c) 200 ^{0}C. (The display temperatures corresponding to 102.7 ^{0}C, 125.6 ^{0}C and 172.2 ^{0}C of the samples, respectively).

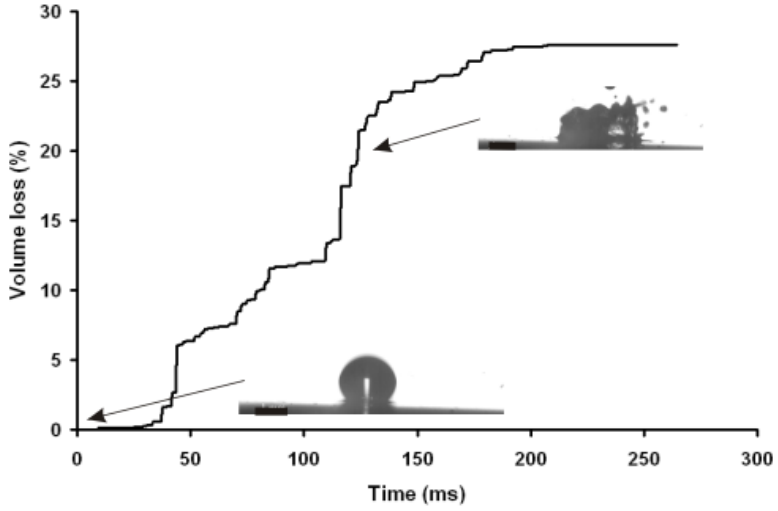

Fig. 12.14. Mass losses due to the "atomization" during cooling of a bare copper substrate at 125 ^{0}C (the display temperature corresponding to 102.7 ^{0}C of the sample).

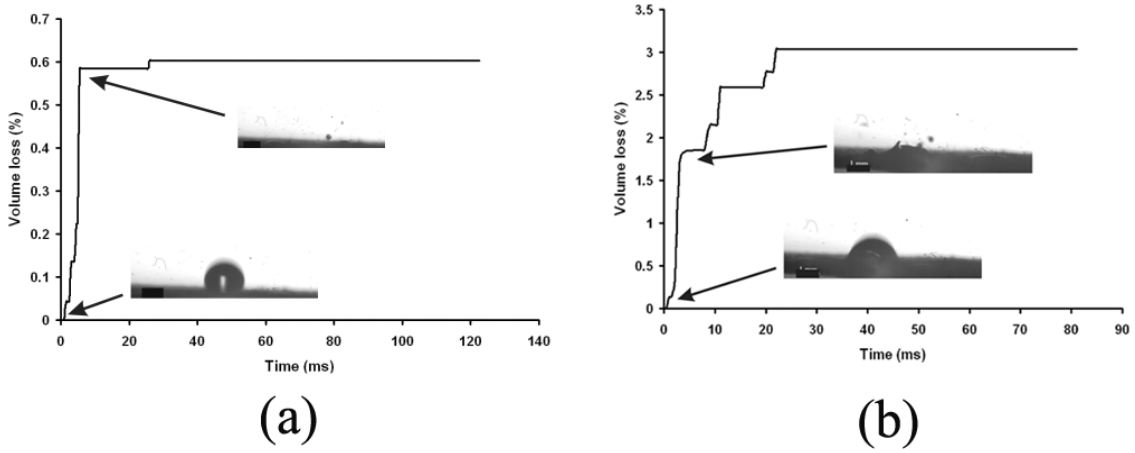

Fig. 12.15. Mass losses due to the "atomization" during cooling through silver-platted nanofiber mats. (a) 150 ^{0}C, (b) 200 ^{0}C. (The display temperatures corresponding to 125.6 ^{0}C and 172.2 ^{0}C of the samples, respectively).

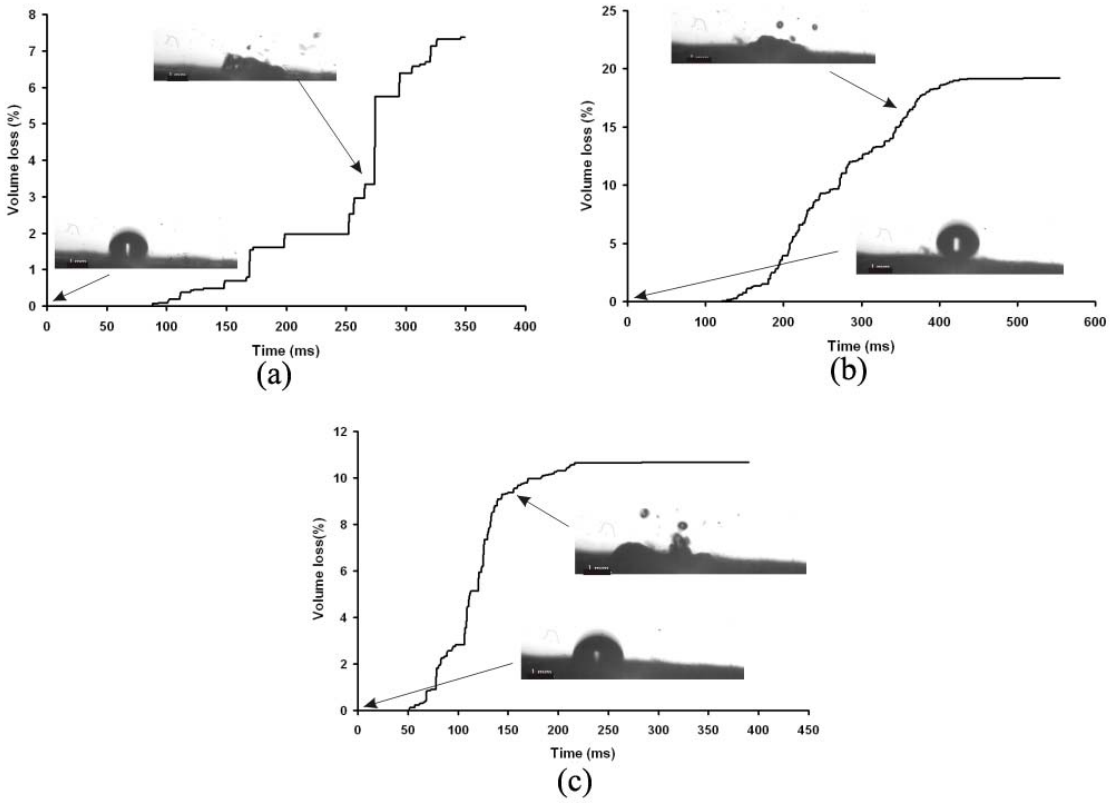

Fig. 12.16. Mass losses due to the "atomization" during cooling through nickel nanofiber mats. (a) 125 ^{0}C, (b) 150 ^{0}C, (c) 200 ^{0}C. (The display temperatures corresponding to 102.7 ^{0}C , 125.6 ^{0}C and 172.2 ^{0}C of the samples, respectively).

Table 12.4. The evaporation times and cooling rates for different metal-plated nanofiber mats and a bare copper substrate. For the bare copper substrate the value of the spreading ratio used to calculate the corresponding heat flux j was directly measured from the top view images.

Material	**Temperature (^{0}C)**	Δt **(ms)**	**p**	**j (kW/ cm^2)**
Bare copper	125	264	0.27	0.256
	150	N/A	N/A	N/A
	200	N/A	N/A	N/A
Copper nanofibers	125	172.5	0.04	0.136
	150	53	0.11	0.392
	200	52	0.09	0.408
Silver nanofibers	125	170	0	0.138
	150	128.5	0.006	0.181
	200	55.5	0.03	0.407
Nickel nanofibers	125	355	0.074	0.061
	150	600	0.20	0.031
	200	388	0.10	0.054
Gold nanofiber	125	495	0	0.047
	150	633.5	0	0.037
	200	468	0	0.049

12.4 Theoretical Evaluation of Evaporation Time

In addition to measuring the evaporation time Δt of water drops inside metal-plated nanofiber mats, it is worth of theoretically estimating it for comparison with the data. That will allow verification of the fact that complete evaporation inside nanofiber mats can happen indeed approximately at the same moment when visible signs of water presence on the mat surface disappear. According to (Kenning 1977), we can expect that bubble nucleation responsible for evaporation happens predominantly at the nanofiber surfaces in contact with water in the pores instead of bulk evaporation inside water body in the pores. When evaporation into a vapor embryo begins, the embryo practically contains only air (and no vapor), and vapor concentration c inside it might be described in the first approximation by the self-similar distribution near a plane surface

$$\frac{c}{c_s(T)} = 1 - \mathrm{erf}\left(\frac{y}{2\sqrt{Dt}}\right) \tag{12.6}$$

where $c_s(T)$ is the saturated vapor concentration near liquid/vapor interface inside the embryo determined by the current local temperature T, y is the distance from the interface (with larger values of y, in fact, corresponding to the embryo center), D is the diffusion coefficient of vapor, and t is time.

In an almost flash-like evaporation we are dealing with inside the pores in the metal-plated nanofiber mats, vapor bubbles almost instantaneously fill the whole pore. Therefore, their size can be taken as the pores size δ. According to Eq. (12.6), the vapor mass flux into a vapor embryo is then equal to

$$\dot{M} = \delta^2 c_s(T)\sqrt{\frac{D}{\pi t}} \tag{12.7}$$

Using the Clapeyron equation and the equation of state (assuming vapor to behave as an ideal gas), we find that

$$c_s(T) = k_0 \exp\left(-\frac{E}{RT}\right) \tag{12.8}$$

where R is the absolute gas constant and

$$E = L\mu_m, \quad k_0 = \frac{p_{s0}\mu_m}{RT_w}\exp\left(\frac{E}{RT_0}\right) \tag{12.9}$$

In the latter equations μ_m is the molecular weight of vapor, p_{s0} is the saturated vapor pressure at temperature T_0, and T_w is the substrate temperature, which is assumed to be equal to the metal-plated nanofiber temperature. The Eqs. (12.9) shows that E plays the role of the evaporation activation energy and k_0 is a pre-exponential.

The average magnitude of the heat removal rate as a latent heat of evaporation in a pore during the characteristic evaporation time Δt is equal to

$$\dot{Q}_I = L\frac{1}{\Delta t}\int_0^{\Delta t}\dot{M}dt \tag{12.10}$$

Using Eqs. (12.7)-(12.9), the latter yields

$$\dot{Q}_I = A\exp\left(-\frac{E}{RT}\right) \tag{12.11}$$

where the pre-exponential is given by

$$A = \frac{2L\delta^2\mu_m}{PT_w}p_{s0}\exp\left(\frac{E}{RT_0}\right)\sqrt{\frac{D}{\pi\Delta t}} \tag{12.12}$$

On the other hand, heat is supplied through a metal substrate plate (wall) to the nanofiber mat attached to it and thus to water in the pore by thermal conduction. The corresponding heat flux is

$$\dot{Q}_{II} = \frac{k_w}{\delta_w}\left(T_w - T\right)\delta^2 \tag{12.13}$$

In a zero-dimensional model (Yarin et al., 1999), the equality

$$\dot{Q}_I = \dot{Q}_{II} \tag{12.14}$$

determines the evaporation temperature T_{ev}. According to Eqs. (12.11), (12.13) and (12.14), it can be found from the following equation

$$A\exp\left(-\frac{E}{RT_{ev}}\right) = \frac{k_w}{\delta_w}\left(T_w - T_{ev}\right)\delta^2 \tag{12.15}$$

On the other hand, the evaporation time Δt is evaluated as

$$\Delta t = \frac{\rho\delta^3}{(A/L)\exp(-E/RT_{ev})} \tag{12.16}$$

where ρ is the liquid (water) density.

Substituting Eq. (12.12) in Eq. (12.16), we arrive at

$$\Delta t = \frac{\pi}{D}\left\{\frac{\rho\delta RT_w \exp\left[E(T_{ev}^{-1} - T_w^{-1})/R\right]}{2\mu_m p_{sw}}\right\}^2 \tag{12.17}$$

where p_{sw} is vapor pressure at the substrate temperature T_w.

It is emphasized that T_{ev} on the right hand side of Eq. (12.17) depends on Δt through Eq. (12.16). Therefore, Eq. (12.17) represents itself a highly nonlinear equation for Δt. A significant simplification, however, is possible. Namely, it is possible to show using the Frank-Kamenetskii transformation familiar from the combustion theory (Zeldovich et al., 1985) that when the inequality

$$\frac{(k_w/\delta_w)R^2T_w^3}{2E^2p_{sw}\left[D/(\pi\Delta t)\right]^{1/2}} >> 1 \tag{12.18}$$

holds, the temperature $T_{ev} \approx T_w$, and Eq. (12.17) reduces to the following expression for the evaporation time Δt

$$\Delta t = \frac{\pi}{D}\left(\frac{\rho \delta R T_w}{2\mu_m p_{sw}}\right)^2 \tag{12.19}$$

Taking for the estimate ρ=1 g/cm^3, the pore size $\delta=10^{-4}$ cm, T_w=373 ^{0}K, μ_m=18 g/mol and D=0.21 cm^2/s, and using the standard expression for the saturation pressure of water as a function of temperature to evaluate p_{sw} from (Seaver et al., 1989; Yarin et al., 1999), we find from Eq. (12.19) that $\Delta t = 0.11\,\text{s}$. Then, we check a posteriori that the left hand side of Eq. (12.18) is equal to 5.4×10^6, for such a wall as a copper nanofiber, i.e. the inequality (12.18) holds indeed.

It is emphasized that the predicted value of Δt of the order of 100 ms is close to the values of the evaporation time measured experimentally for copper and silver nanofiber mats and listed in Tables 12.3 and 12.4. The agreement between the predicted and measured values corroborates the latter ones and supports the conclusion based on processing the experimental data in the experimental section that cooling rates in the range of 0.4-0.6 kW/cm^2 were achieved using such nanofiber mats.

12.5. Conclusion

A new method of electroplating of electrospun nanofiber mats allowed us to prepare copper-, silver-, nickel-, and gold-plated mats. The copper- and silver-plated individual nanofibers revealed high surface roughnesses, which made them similar to thorny devil

lizards and dendrites/cactuses, respectively. In addition, these nanofibers and their mats possess high thermal diffusivities.

Copper substrates with deposited metal-plated nanofiber mats of thicknesses of about 30 μm were heated to constant temperatures up to 200 ^{0}C, and single water drop impacts on them were used for localized cooling. The results reveal the following. The presence of nanofiber mats dramatically reduces water losses due to boiling-associated "atomization" (zero or several percent loss on copper-plated nanofiber mats on a copper substrate compared to about 30% on a bare copper substrate). Moreover, the presence of nanofiber mats completely eliminated drop bouncing characteristic of bare hot surfaces, i.e. suppressed the Leidenfrost effect. It was shown that nanofiber surface roughness plays a more significant role than its thermal diffusivity for the enhancement of drop evaporation rate, and thus the heat removal rate. As a result, with copper-plated nanofiber mats cooling rates close to 0.6 kW/cm^2 were demonstrated, which is an impressive value in comparison with the previously achieved values reported in the literature. The experimentally measured evaporation times on metal-plated nanofiber mats were supported by the theoretical estimates.

13. NANO-ENCAPSULATED SMART TUNABLE PHASE CHANGE MATERIALS

13.1 Introduction

In this work we achieve the intercalation of different types of paraffins and their mixtures with triglycerides inside carbon nanotubes (CNTs) by means of self-sustained diffusion followed by a proper rinsing. The CNTs were investigated using TEM, which showed that they were intercalated inside and clean outside. For the mixtures melting can be realized in an interval of about 20 ^{0}C, which opens new opportunities for Phase Change Materials (PCM) attracting attention in relation to solar energy storage, cooling of power electronic devices and the energy-saving technologies.

Section 13.2 describes the experimental, section 13.3 contains the results and discussions and section 13.4-summary. This Chapter contains joint results with Rakesh P. Sahu, which is mentioned individually.

13.2 Experimental

Two different paraffin waxes (W1 and W2) with different melting points – (1) 44-46 ^{0}C (W1) and (2) 53-57 ^{0}C (W2) (both with M_w ~400 Da)- and benzene (anhydrous 99.8%) were purchased from Sigma-Aldrich. Commercial, as-grown, highly graphitic carbon nanotubes (PR-24, Pyrograph III) were purchased from Pyrograph Products Inc. Ethanol (200 proof) was obtained from Pharmco Inc. Household butter (M_w~ 300 Da) was used in these experiments. Syringe filter with pore size of 0.2 μm was purchased from Cole-Parmer. All materials were used without any further purification.

Two paraffin waxes, wax W1, with melting point of 44-46 ^{0}C, and wax W2, with melting point of 53-57 ^{0}C (the average M_w ~ 400 Da) and household butter (B1, the average M_w ~ 300 Da) were dissolved in benzene as described below. Commercial, as-grown, highly graphitic carbon nanotubes (PR-24, Pyrograph III) constitute the CNTs employed in this study. They contained some iron (<14,000 ppm), and less than 5% moisture, and had the inner diameters close to 50-100 nm and lengths in the range 10-100 μm.

Five different solutions were prepared using benzene as a solvent. Solution A contained W1 ; solution B- W2; solution C – a 1:1 (w/w) blend of W1 and W2; solution D- a 2:1 (w/w) blend of W1 and B and solution E- a 2:1 (w/w) blend of W2 and B. In all these cases the overall amount of solute was kept equal to 0.3 g per 20 g of solvent. After the addition of the solutes to solvents, they were sonicated for 35-40 min until a clear solution was prepared.

For the intercalation of the solutes into CNTs, 0.018- 0.022 g of CNTs was added to each solution and sonicated for 30 min, which resulted in homogeneous suspensions. After that, the vial cap was kept open in a chemical hood until complete evaporation of benzene. During this process the self-sustained diffusion (Bazilevsky et al., 2007b; 2008a) of solutes into CNTs took place (as discussed below). Then, benzene was added to the deposit and sonicated for 3-4 min to rinse any solute which possibly could have been deposited outside the CNTs. It is emphasized that if sonication was continued longer than 4 min, some solute could be already lost from inside the CNTs. Following sonication, the dispersion was filtered through a syringe filter. After that, fresh benzene was passed 2-3 times to rinse any residual solute deposited on the outside of the CNTs.

All the optical observations were done using JEOL JEM 3010 Transmission Electron Microscopy (TEM).

All the DSC measurements were done using DSC-Q200, TA Instruments. All the DSC measurements were done by Rakesh P. Sahu.

13.3 Results and Discussion

According to (Bazilevsky et al., 2007b, 2008a), the intercalation of solutes (which might be molecular dispersions as in the present case, or particulates) is driven by diffusion through solvent bulk. However, in distinction from the ordinary diffusion where a solute content equilibration is rapidly achieved everywhere, in the case of self-sustained diffusion the simultaneous solvent evaporation permanently sustains solute gradient between the solution bulk and the inner space of CNTs. That leads to a practically 100% intercalation of CNTs with chosen solutes at room temperature and normal pressure. The process is fully scalable and transformative to the industrial applications.

Figures 13.1 A-E show several TEM micrographs of the intercalated CNTs densely filled inside and clean outside. Holey carbon grids were used for support, and all the observations were done with the CNT sections freely suspended over the grid holes. Thus, we avoided the interference with the imaging of any residual materials which could be present at the holey carbon surface. A careful examination of the images in Fig. 13.1 reveals that some ordered striations (marked by arrows; several of them highlighted in Fig. 13.1C) are visible in the intercalated deposits inside the CNTs. As Fig. 13.2 shows, the inner surface of these CNTs is rather rough, which probably makes wax deposition

non-uniform and maybe even unstable according to the mechanism described in (Srikar et al., 2009a).

The contrast of deposits in TEM micrographs is mostly determined by the molecular weights. This makes impossible to distinguish W1, W2 and B in Figs. 13.1 D-E. It is emphasized that paraffin waxes W1 and W2 represent themselves conglomerates of different alkanes (C_nH_{2n+2}, with $20 \le n \le 40$), whereas butter B is mostly triglycerides ($C_nH_{2n-2}O_2$, with n= 14-20). Therefore, the only difference between W1 and W2 on the one hand, and B on the other hand, involves the presence of oxygen, which is impossible to quantify conclusively even using the Energy Dispersive X-ray (EDX) patterns in the present case. Nevertheless, the presence of W1 and B, as well as W2 and B in the intercalated deposits in Figures 1D-E was fully elucidated by means of Differential Scanning Calorimetry (by using DSC-Q200, TA Instruments). For all the DSC measurements the samples were cooled to 20 ^{0}C, then they were heated up to 80 ^{0}C at a ramp rate of 5 ^{0}C/min, held at 80 ^{0}C for 5 min, and then back to 20 ^{0}C at a ramp rate of -5 ^{0}C/min.

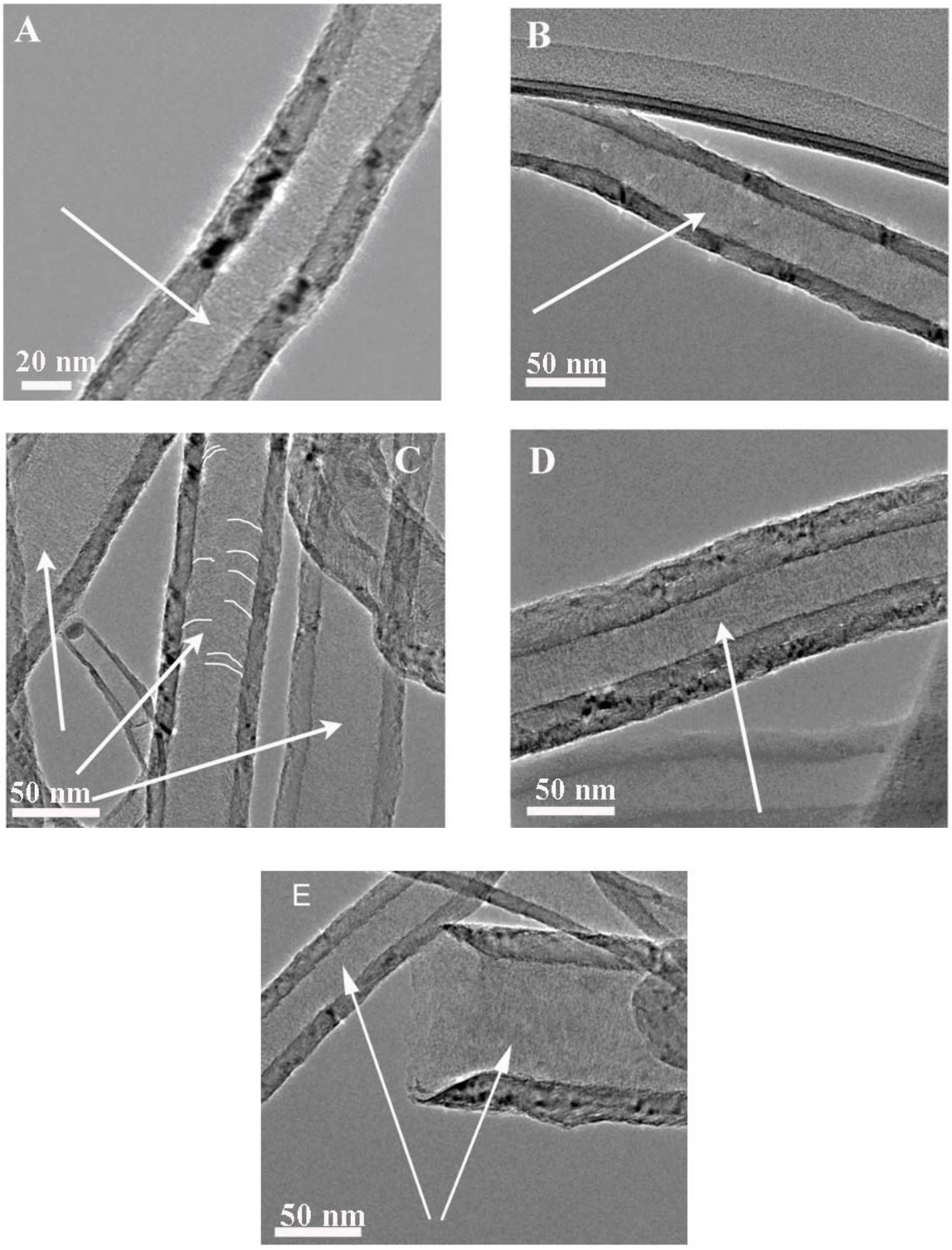

Fig. 13.1. TEM (JEOL JEM 3010) micrographs of carbon nanotubes intercalated by solutes A-E, respectively. The arrows point at the striations that can be seen inside the

deposits in the CNTs. The solutes are deposited only inside the tubes, with no residual solutes visible outside. Panels A-E correspond to the samples intercalated with solutions A-E, respectively. Several characteristic striations are highlighted in panel C.

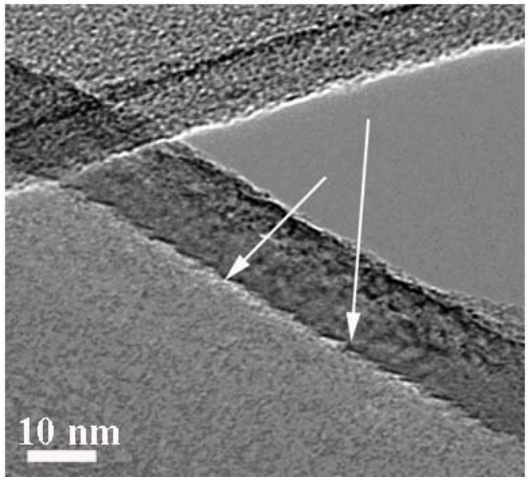

Fig. 13.2. TEM image of an empty CNT. The arrows point at the roughness of the inner wall.

The thermograms of bulk samples of W1, W2 and B separately were measured first (Fig. 13.3). The thermograms reveal that W1 has glass transition temperature (T_g) and melting point (T_m) close to 27 ^{0}C and 46.2 ^{0}C, respectively, whereas for W2 they are 36 ^{0}C and 56 ^{0}C, respectively. The latent heat of melting of W1 and W2 was close to 140-141 J/g and 144-148 J/g, respectively. On the other hand, in the temperature range studied, butter revealed only one endothermic peak close to 24 ^{0}C, which corresponds to its melting point, with the latent heat of melting being ~2 J/g .

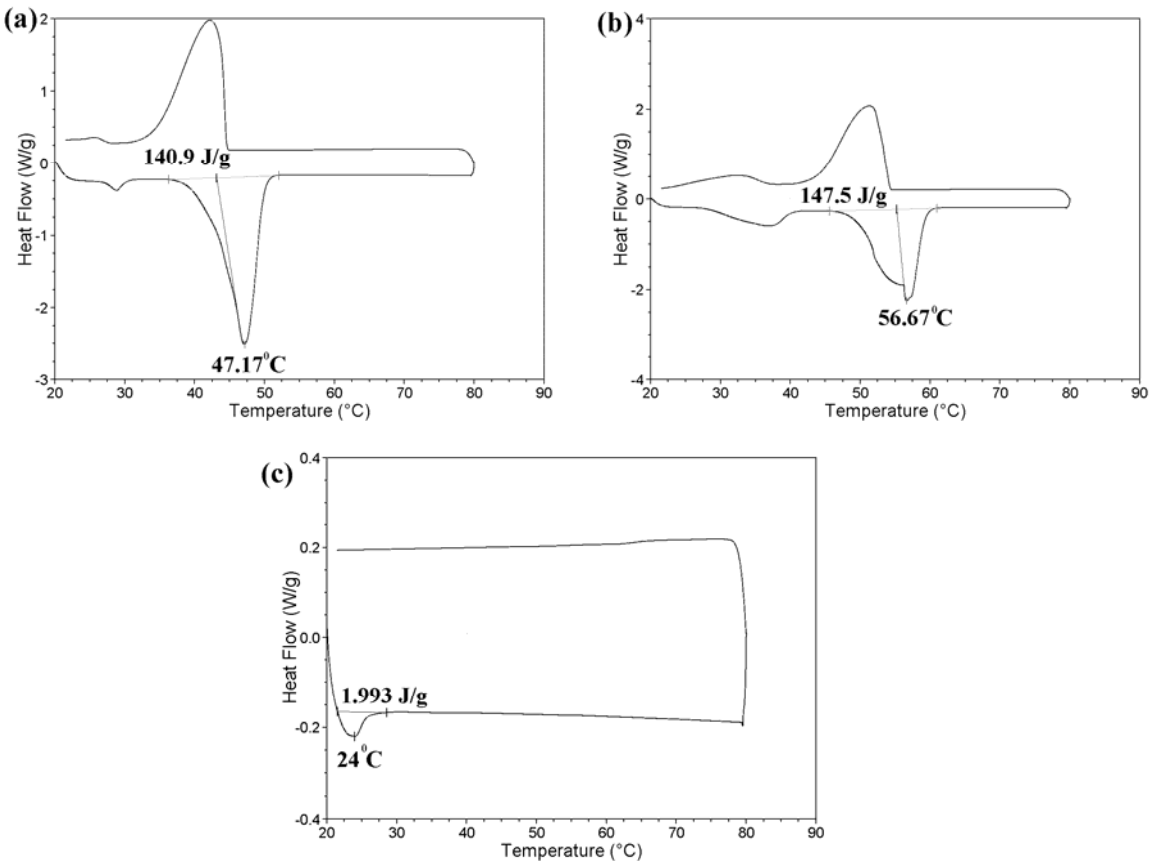

Fig. 13.3. Thermograms of bulk samples of (a) W1, (b) W2 and (c) B. (Rakesh P. Sahu).

Then DSC of the intercalated samples of Fig. 13.1 was performed next. In each case samples from three different locations were used for control. The corresponding thermograms are shown in Figs. 13.4-13.6. Comparing the thermograms for bulk samples of W1 (Fig. 13.3 a) with that of W1 encapsulated inside CNT (Fig. 13.4a), one can observe that in the latter case the endothermic peak corresponding to the glass transition temperature of the bulk sample disappeared. Moreover, the melting point of the bulk sample of W1 of 47.17 ^{0}C (Fig. 13.3a) is replaced by 44.24 ^{0}C for the intercalated W1 (Fig. 13.4a). A similar trend was found for W2: the bulk melting point of 56.67 ^{0}C (Fig. 13.3b) was shifted to 52.64 ^{0}C for the intercalated sample (Fig. 13.4b). The thermograms

show that for W2 the glass transition in the temperature range studied has not disappeared completely, albeit deteriorated significantly. The reduction of the melt temperature in the intercalated samples is attributed to changes in the confined crystalline structure formed inside CNT (Bazilevsky et al., 2008b).

Figures 13.5 a and b correspond to the intercalated blends of W1 and B, as well as W2 and B (both in the 2:1 ratio). They reveal heat absorption in a much wider temperature range than that for pure W1 and W2. Indeed, W1 and B revealed heat absorption in the range of 28 ^{0}C- 52 ^{0}C (Fig. 13.5a) versus that of pure W1 only in the range of 35 ^{0}C- 52 ^{0}C in Fig. 13.3a. Similarly for W2 and B in CNTs in Figure 13.5b the heat absorption range of 26 ^{0}C- 62 ^{0}C is wider than for pure W2- 36 ^{0}C- 62 ^{0}C in Fig. 13.4b. In addition, the intercalated blend samples of two different waxes, W1 and W2, demonstrate the heat absorption range of 35 ^{0}C- 62 ^{0}C (Fig. 13.6), which is an overlap of the heat absorption ranges of these waxes separately (Figs. 13.4 a and b). All these results show that the temperature range of PCM heat absorption can be tuned by tailoring the composition of the intercalated materials in CNTs. This effectively solves problem (i) mentioned above. In addition, it should be noted that the intercalated B occupies some space and makes wax confinement even smaller, which can affect and change its crystalline structure even more. This, in turn, determines its melting in a wider temperature “window”.

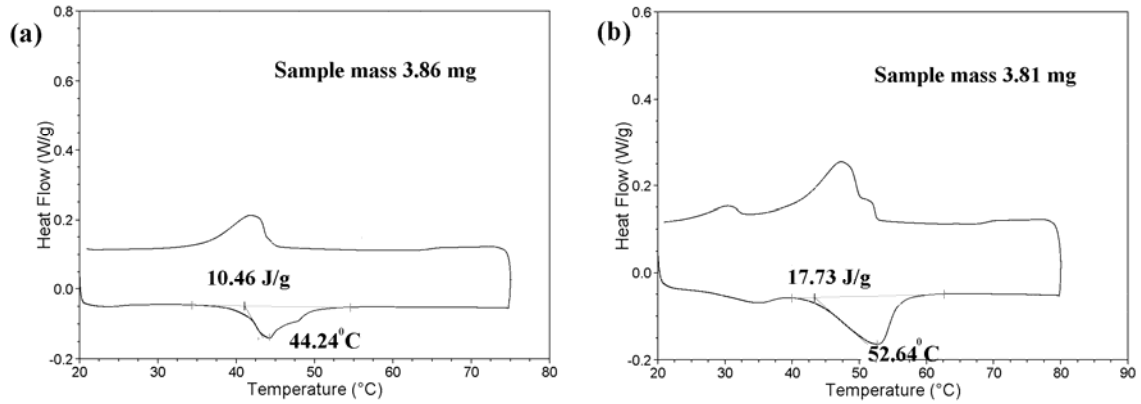

Fig. 13.4. Thermograms of the intercalated wax in CNT: (a) Pure W1; and (b) Pure W2. (Rakesh P. Sahu).

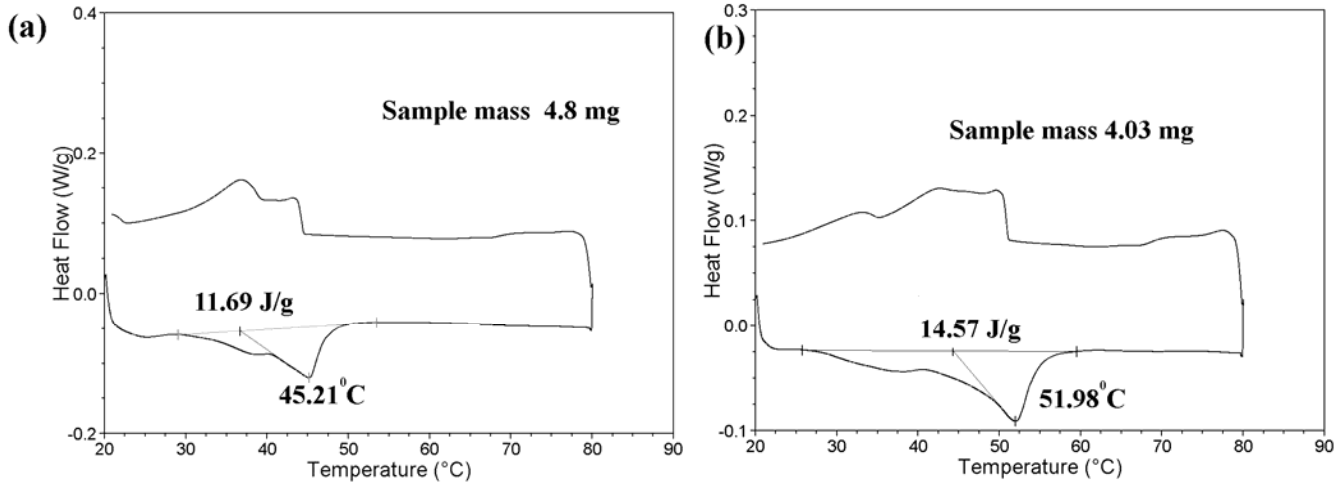

Fig. 13.5. Thermograms of the intercalated blended deposits in CNT: (a) 2:1 blend of W1 and B; (b) 2:1 blend of W2 and B. (Rakesh P. Sahu).

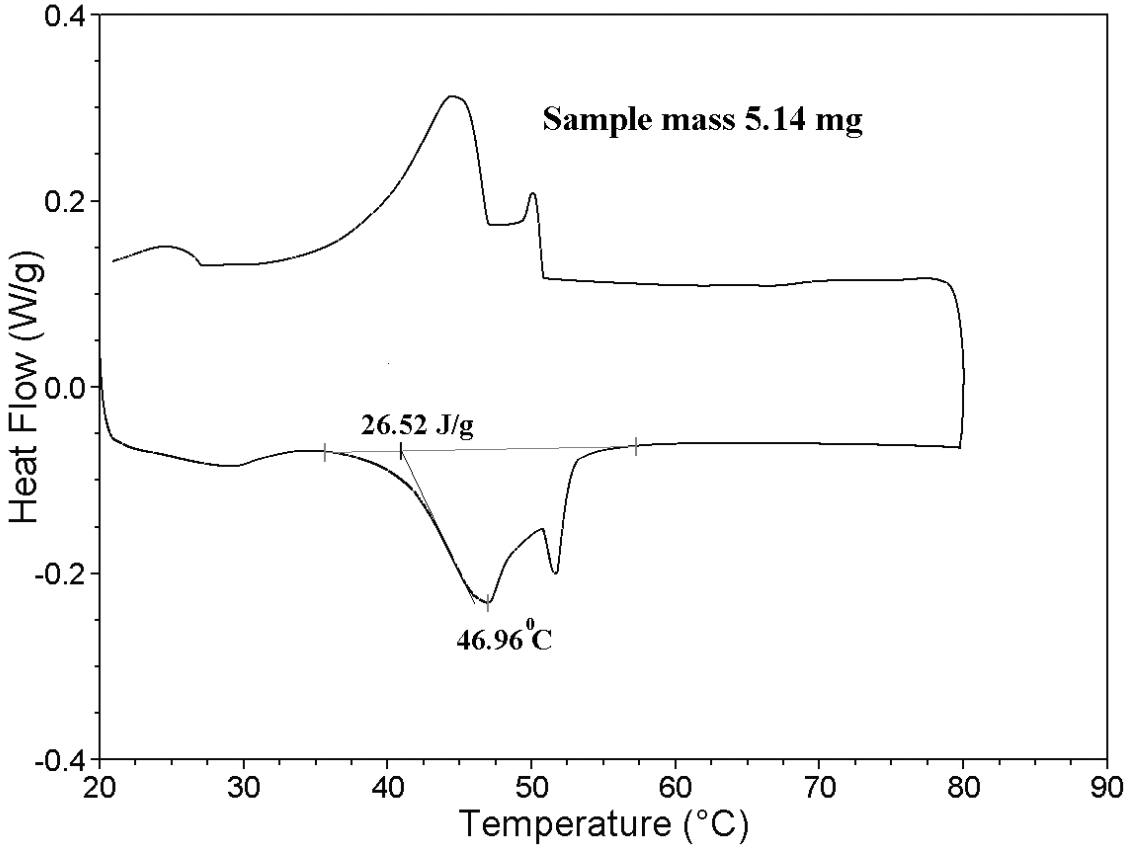

Fig. 13.6. Thermogram of 1:1 blend of W1 and W2 intercalated in CNT. (Rakesh P. Sahu).

The latent heat of melting is known for both W1 and W2. Their molecular weights are approximately the same. Then, the thermogram in Fig. 13.6 can be used to evaluate the masses of W1 and W2 intercalated into a given CNT sample. As a result, we find that in the case of a 1:1 blend of W1 and W2, the intercalated overall mass was close to 20% of the encasing CNTs mass. Moreover, the proportion of W1 to W2 in the original solution (C) was practically replicated into the composition inside CNTs, since with the close molecular weights, molecules of these two waxes had close gyration radii, and thus close

diffusion rates (Bazilevsky et al., 2007a). Therefore, the masses of W1 and W2 in CNTs were approximately 10% each of the mass of the encasing CNTs.

However, W1 (or W2) and B had different molecular weights, so one cannot expect that their proportion in a binary solution (W1+B or W2+B) will be replicated in the intercalated deposit. On the other hand, the latent heat of melting of B is negligibly small compared to that of W1 or W2. Therefore, the thermograms of Fig. 13.5 reveal the intercalated masses of W1 or W2 directly. This shows that for the intercalated samples from solutions D-E the amount of wax inside CNTs is of the order of 8.8% and 11.08% of the mass of the CNTs samples, respectively.

The thermal diffusivity α of wax is known to be of the order 10^{-7} m^2/s (Totten et al., 2003). Taking for the estimate the average CNT diameter D of the order of 100 nm, we estimate the characteristic thermal response time as $D^2/\alpha \sim 10^{-7}$ s. This shows that the thermal response time in the nano-encapsulated PCM is immaterial, which effectively solves problem (ii) mentioned above and eliminates the need in the intercalation of copper nanoparticles. Since the encapsulated wax cannot solidify on heat exchanger surfaces, problem (iii) can also be effectively eliminated.

13.4 Conclusion

In summary, we have demonstrated a novel technique to intercalate paraffin waxes, as well as their blends with triglycerides inside carbon nanotubes using self-sustained diffusion. The nano-scale phase change materials (PCM) obtained using this route can be tailored to possess a relatively wide working temperature range, as well as a negligible thermal response time. The method allows a straightforward scale up and can

be used for mass production of PCM for solar energy storage, cooling of power electronic devices and the energy-saving technologies.

14. SHEAR AND ELONGATIONAL RHEOLOGY OF GYPSUM SLURRIES

14.1 Introduction

In this work, elongational rheometry of gypsum slurries is studied, which was compared with shear rheometry done by Raman Srikar. The article is organized as follows. Materials and methods used for preparing slurries are described in section 14.2. Section 14.3 describes results and discussion. After that, conclusions are drawn in section 14.4.

14.2 Materials and Methods

Stucco- β-hemihydrate form of synthetic gypsum (cf. Fig. 14.1)- and all the additives were supplied by US Gypsum Corporation, IL. Deionized water was used for preparing slurries in all the cases.

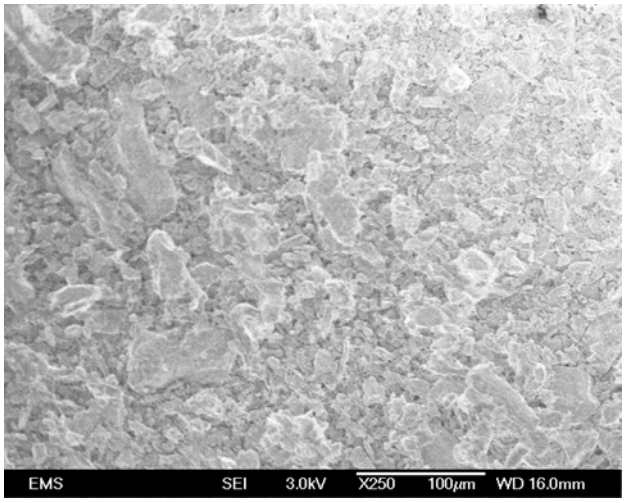

Fig. 14.1 SEM image of stucco particles as received.

Stucco with additives was allowed soaking in water for 15 sec. After that, the suspensions were mixed vigorously for additional 15 sec using a rotary mixer. Deionized

water was used for slurry preparation. The water-to-stucco ratio ranged from 70 to100 (by weight). The slurry was then poured into the shear rheometer and measurements were carried out. The shear rate and time scale of the measurements were set up corresponding to the experiment requirements. The slurry density for different compositions was measured. The density is given in Table 14.1. The notation 75WSR represents 75 parts of water to 100 parts of stucco by weight. The compositions listed in Table 14.1 varied not only by water content but also by the other density control agents.

In the present work all the shear experiments for the rheological characterization of gypsum slurries were carried out using the shear viscometer, TA Instruments AR 2000ex.

Surface tension measurements for stucco slurries were carried out using the Kruss Bubble Pressure tensiometer Model BP2. A diluted stucco slurry (concentration of water in slurry > 75WSR-water to stucco ratio) was prepared and investigated using the tensiometer. The measurements were carried out several times to ensure repeatability. Prior to these measurements, the capillary diameter used for measuring the bubble pressure was found using water as a standard whose physical parameters was known.

The elongational rheometer was similar to that of (Yarin et al. 2004). The schematic of the experimental setup is shown in Fig. 14.2. The elongational rheometer consisted of a stationary lower plate and a movable spindle-like upper contact, whose motion was

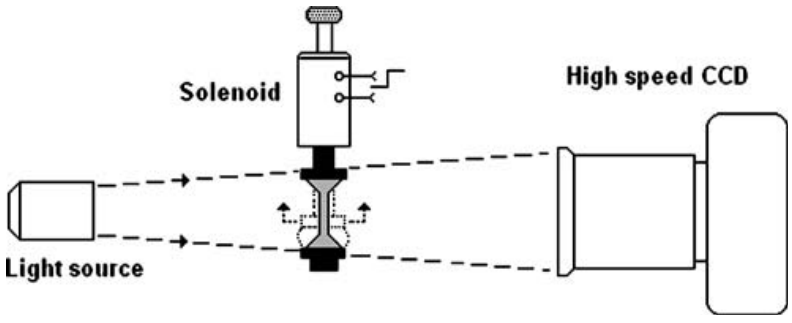

Fig. 14.2 Schematic of the elongational rheometer used in the present study.

controlled by a solenoid. Elongational rheometry of 75 WSR (composition 11 in Table 14.1) is done only. Stucco with additives was allowed soaking in water for 15 sec. After that, the suspensions were mixed vigorously for additional 15 sec. Then, a single droplet of the prepared slurry was rapidly (in 5-10 sec) transferred to the elongational rheometer. Droplets were used in the elongational experiments. They were stretched by the spindle-like contact, and then experienced capillary self-thinning, the later being the observation stage. The experiments were repeated with the same droplet for 2-3 times to elucidate the effect of the water evaporation and hydration reactions in the slurry (ultimately leading to solidification) on the rheological parameters. The evolution of diameter of pinching threads was recorded using a high speed digital camera (Redlake- Motion Pro) equipped with a 185 mm macrolens at the frame rate of 500 fps. The images thus obtained were analyzed using the image analysis software developed on the platform of MATLAB R-2007A. The complete process starting from slurry mixing to the end of thread self-stretching experiment was recorded using a digital camcorder to quantify the timing involved in every single operation.

Table 14.1. Slurry density

Sample	Density
	g/ml
75 WSR- composition 1	0.862
80 WSR- composition 2	0.878
85 WSR- composition 3	0.863
90 WSR- composition 4	0.887
80 WSR- composition 5	0.878
80 WSR- composition 6	0.865
80 WSR- composition 7	1.046
75 WSR- composition 8	0.863
75 WSR- composition 9	0.862
70 WSR- composition 10	1.590
75 WSR- composition 11	1.560
85 WSR- composition 12	0.863

14.3 Results and Discussion

Preliminary observations and theoretical framework

The measured effective shear viscosity versus shear rate reveals that the rheological properties of gypsum slurries are strongly affected by their composition. For example, the effective shear viscosity decreased with the increase of the water-to-stucco ratio, WSR. The preliminary experiments suggested that gypsum slurries are non-Newtonian fluids and the first rheological constitutive equation to be applied to them should be the Ostwald–de Waele power law (Astarita and Marrucci 1974)

$$\boldsymbol{\sigma} = -p\mathbf{I} + \boldsymbol{\tau}, \quad \boldsymbol{\tau} = 2K\left[2\mathrm{tr}\left(\mathbf{D}^2\right)\right]^{(n-1)/2}\mathbf{D} \tag{14.1}$$

where $\boldsymbol{\sigma}$ is the stress tensor, $\boldsymbol{\tau}$ is the stress deviator tensor, p is pressure, **D** is the rate–of-strain tensor, **I** is unit tensor, K is the consistency index and n is the exponent (the flow behavior index).

In simple shear flows Eq. (14.1) reduces to

$$\mu_{shear} = K\dot{\gamma}^{(n-1)} \tag{14.2}$$

where μ_{shear} is equal to $\mu_{shear} = \tau_{xy} / \dot{\gamma}$, with τ_{xy} being the shear stress, and $\dot{\gamma}$ the shear rate.

Simple shear flows in rheometry are typically employed at a constant shear rate $\dot{\gamma}$ (which values can be chosen different)**.** Then, measurements of shear viscosity are conducted after transients have faded. In the present experiments this shear rheometer was operated with a gradually increasing shear rate. Therefore, the value of $\dot{\gamma}$ was not set in the present experiments but was linearly increasing in time. The interpretation of such experimental data requires a fully transient description which is provided below. The momentum balance equation for shear flow of slurry under the assumption that the power-law model (14.1) is applicable is given by

$$\rho\frac{\partial u}{\partial t} = \frac{\partial}{\partial y}\left[K\left(\frac{\partial u}{\partial y}\right)^{n}\right] \tag{14.3}$$

where u(y) is the velocity profile, and y is the coordinate normal to the wall, ρ is the density and t is time.

The initial and boundary conditions imposed are as follows

$$\begin{aligned} &t = 0: \quad u = 0 \\ &t > 0: \quad \begin{cases} y = 0, u = 0 \\ y = h, u = At \end{cases} \end{aligned} \tag{14.4}$$

where h is the gap and A is the acceleration.

The effective shear viscosity $\mu_{shear} = \tau_{xy} / \dot{\gamma}$, with τ_{xy} being the shear stress, and $\dot{\gamma}$ the shear rate. According to Eq. (14.1), it is given by

$$\mu_{shear} = K\left(\frac{\partial u}{\partial y}\right)^{n-1} \tag{14.5}$$

The problem (14.3) and (14.4) was solved numerically by the method of finite differences. The results were compared to the experimental data for various water-stucco ratios in gypsum slurries to determine the corresponding values of K and n.

Rheological characteristics of slurries found in shear flows

The results of some of our shear experiments conducted by Dr. R. Srikar are compared to the theoretical flow curves as shown in Figs. 14.3 (a), (b) and (c). The experimental data is plotted by symbols and the theoretical curve is depicted by lines. The model predicts that during the initial shear rates, the flow is underdeveloped, the velocity profile is not triangular, as is assumed by the rheometer software, and hence no meaningful agreement can be achieved. According to the theoretical predictions, the flow becomes fully developed beyond the shear rate of 10-100 1/s. In that range fitting of the theory to the measured data is possible and produces meaningful values of the rheological parameters K and n. Their values corresponding to all the compositions studied are given in Table 14.2. The successful comparison in the range above 10-100 1/s shows that the effects of water evaporation and slurry solidification due to the chemical reaction (1) are still negligible in the present experiments.

Similar comparisons of the measurements and the theoretical predictions were done for a range of slurry compositions. Table 14.2 lists the results for the values of the rheological parameters K and n found in all the cases.

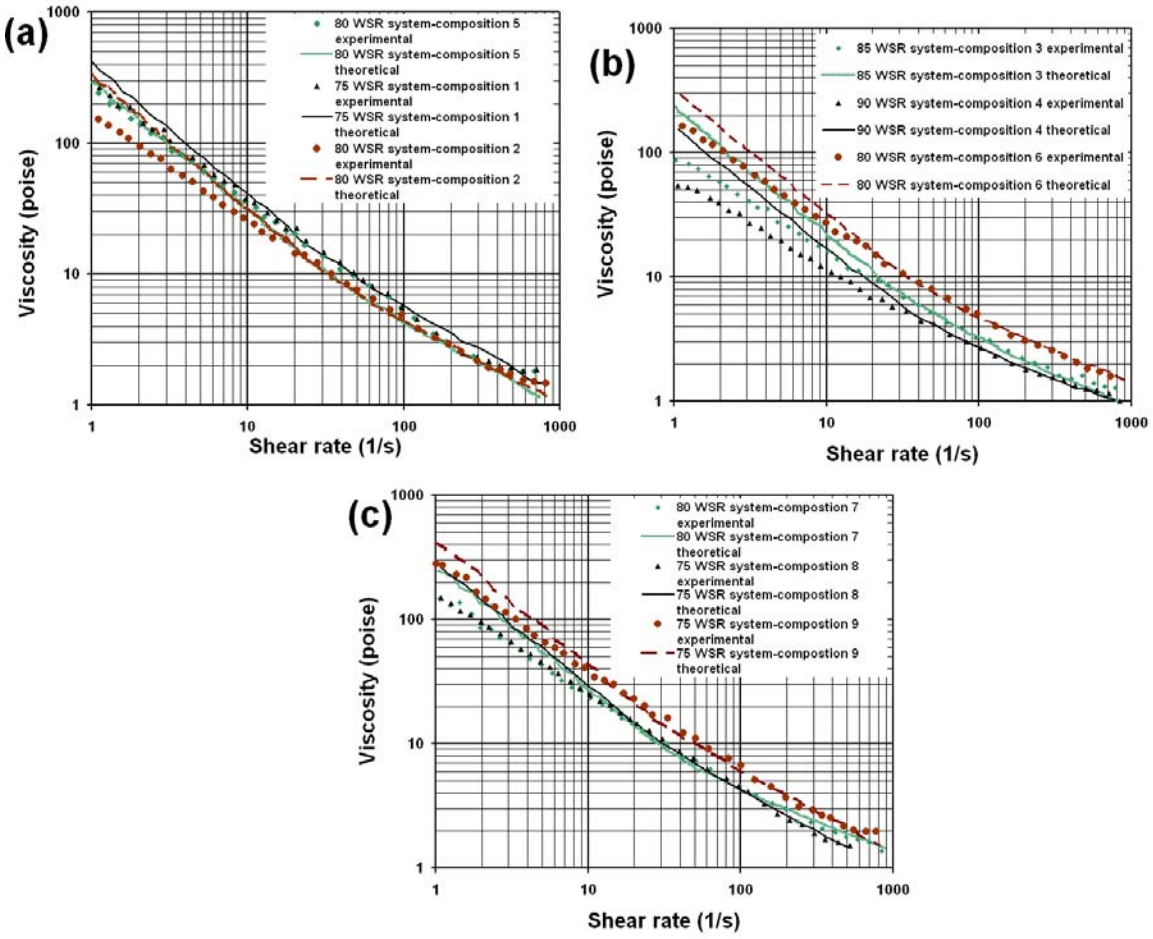

Fig. 14.3 The effective shear viscosity (flow curve) for: 80 WSR system-composition 5; 75 WSR system-composition 1; 80 WSR system-composition 2; 85 WSR system-composition 3; 90 WSR system-composition 4; 80 WSR system-composition 6; 80 WSR system-composition 7; 75 WSR system-composition 8; 75 WSR system-composition 9.

In order to ensure repeatability, all the experiments were carried out more than once. The values of the consistency index and the corresponding average errors for four compositions are shown in Figs. 4 (a) and (b).

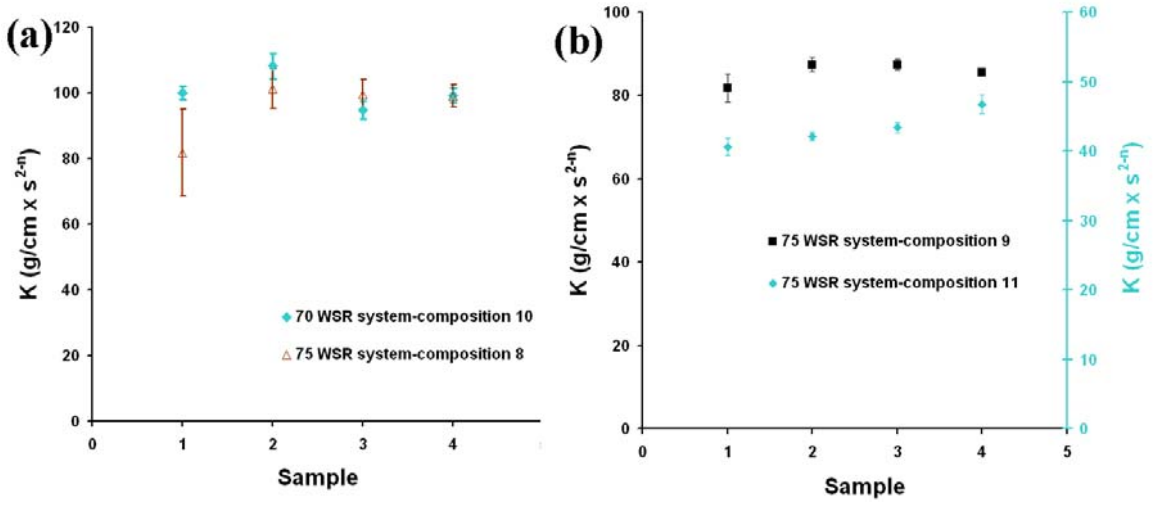

Fig. 14.4. (a) Consistency index for 70 WSR system-composition 10. The error bars represent the average error = ± 6.13 % maximum; consistency index for 75 WSR-composition 8. The error bar represents the average error = ± 16.25 % maximum. (b) Consistency index for 75 WSR system-composition 11. The error bar represents the average error = ± 6.978 % maximum; consistency index for 75 WSR-composition 9. The error bar represents the average error = ± 4.225 %.

An additional benchmark for comparison of the theory with the experimental data is provided by the case of viscous Newtonian test fluids with independently verified viscosity values. The comparison of the measurements and the theory for one such fluid, a standard solution S600 was done. Fitting the theory to the experimental data revealed the viscosity value of 18.6 Poise, whereas the standard independently measured value is reported as 20.45 Poise. This is quite close given the fact that the data were obtained

using the rheometer with a cross-like rotor (as is required for testing gypsum slurries for their easy pouring and removal) and thus, pronounced three-dimensional effects.

Table 14.2. Rheological parameters of gypsum slurries

Sample	n	K
		$g/cm \times s^{2-n}$
70 WSR-composition 10	0.46	118.86
75 WSR-composition 11	0.55	51.61
75 WSR-composition 1	0.38	105.10
80 WSR-composition 2	0.44	61.71
85 WSR-composition 3	0.5	35.23
90 WSR-composition 4	0.56	21.60
80 WSR-composition 5	0.44	50.57
80 WSR-composition 6	0.44	63.31
75 WSR-composition 9	0.42	85.85
75 WSR-composition 8	0.35	92.84
80 WSR-composition 7	0.56	34.22

The results in Table 14.2 show the following general trends for the consistency index and power law exponent with variations in system composition. The value of n increases with the increase in water content relative to that of stucco. However, even at 90% of water in the system, it still does not approach Newtonian behavior, and stays significantly pseudoplastic (with n=0.56). The value of the consistency index K increases with the decrease in water content in the slurry. Therefore, lower water content results in a higher effective viscosity of slurries. Also, lower water content enables faster solidification of slurries, which manifests itself in a dramatic increase in K. This dramatic increase in K is expressed by the data in Table 14.2, which shows that the increase in K value is almost 100% when the system changes from 75 WSR to 70 WSR (a 5% water content reduction).

An analytical correlation of the experimental data on shear rheology of stucco slurries is desirable to be able to extrapolate the results towards compositions for which measurements are extremely difficult due to the rapid setting time. The experimental results for the consistency index K are plotted versus the water-to-stucco ratio (WSR) in Fig. 14.5. The data can be fitted using the linear correlation $K = (-5.54 \times WSR) + 512.9$. A similar fit for the exponent value yields $n = (0.012 \times WSR) - 0.52$.

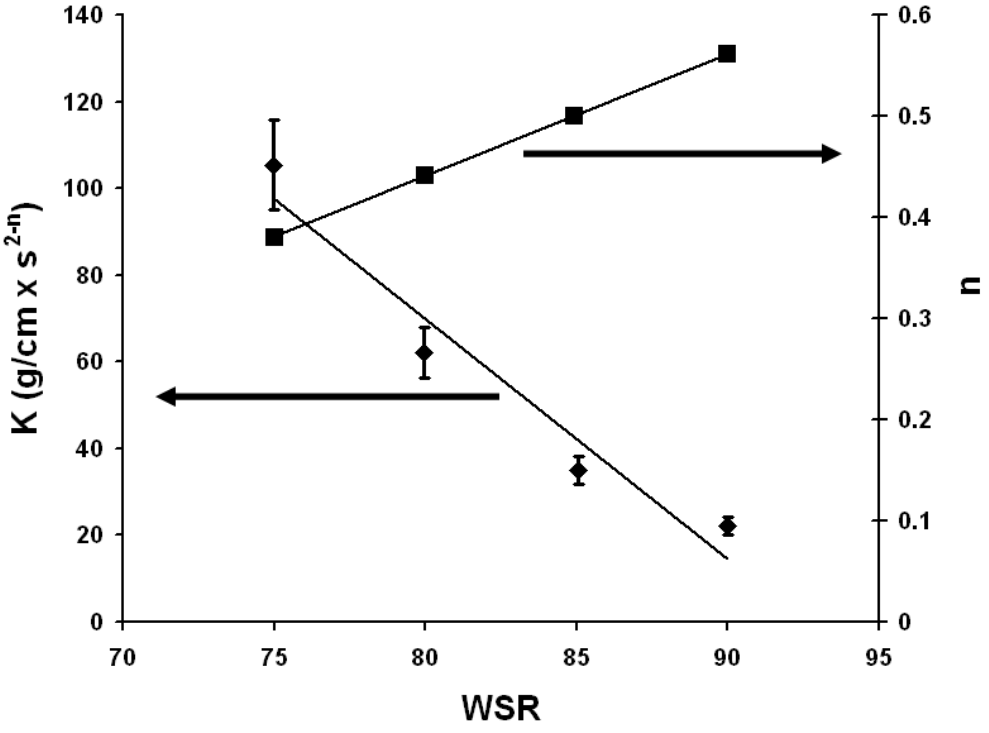

Fig. 14.5 The consistency index and flow behavior index versus WSR. The symbols represent the experimental data and the solid line -the linear fit.

Surface tension measurements for slurries

The values of surface tension coefficient measured in this sub-section will be used in the processing of the results of elongational experiments described in the following section. The data for the stucco slurry is presented in Table 14.3. The average value of surface tension for the slurry was found to be 110.81 mN/m which is significantly higher than that of water. The increase in the effective surface tension is a manifestation of surface solidification processes proceeding in an accelerated manner at the free surface due to water evaporation.

Table 14.3. Surface tension of diluted stucco slurry (concentration of water in slurry > 75WSR)

Sample	Surface tension mN/m
1	118.07
2	121.65
3	102.72

Another step towards measuring surface tension of the slurry was implemented employing contact angle measurements using NRL Contact Angle Goniometer Model 100-00. The instrument incorporated a camera which allows for accurate measurements of contact angles. A slurry drop was placed gently onto a horizontal surface (glass) aligned to the camera and the contact angle measurements were then conducted. It was found that for 75 WSR (composition 11) slurry the average contact angle was

approximately 55.81^{o}, and for 85 WSR (composition 12) slurry the average contact angle was 43.5^{o}. The error in both cases was less than 10%.

According to Young's equation, $\gamma_{SG} = \gamma_{SL} + \gamma_{LG}\cos\theta_c$, where γ_{SG} represents the surface tension between glass (solid) and air (gas), γ_{SL} represents the surface tension between glass (solid) and liquid, γ_{LG} represents the surface tension between liquid and air (gas), and θ_c represents the contact angle. For pure water droplet, correspondingly, $\gamma_{SG} = \gamma_{SL} + \gamma_W\cos\theta_{cW}$, where γ_W and θ_{cW} are the surface tension and contact angle of water, respectively. It is emphasized that we assume γ_{SG} and γ_{SL} to be the same for both water and slurries on glass. Also, it is known that γ_W = 72.1 mN/m and θ_{cW}=18^{o}. Therefore, $\gamma_{LG} = \gamma_W\cos\theta_{cW} / \cos\theta_c$, which yields the surface tension of 75 WSR (composition 11) slurry as γ_{LG75} = 122.02 mN/m, and the surface tension of 85 WSR composition 12) slurry as γ_{LG85} = 94.53 mN/m. Both values are relatively close to the average value of the surface tension of the diluted slurry in Table 3, 110.81 mN/m, which corroborates the latter. We can conclude that the effective surface tension of slurries is significantly higher than that of water.

Elongational rheology of gypsum slurries

Shear rheology alone is incapable to fully uncover true rheological behavior of complex non-Newtonian fluids (Yarin et al. 2004). The shear mode measurements typically are insufficient to shed light on the rheological behavior of the same non-Newtonian fluid in elongational flow. In the present work, an elongational rheometer developed in previous works (Yarin et al. 2004; Stelter et al. 1999, 2000, 2002; Brenn et al. 2006; Tiwari et al. 2009) is applied to study the rheological behavior of gypsum

slurries. In order to ascertain rheological description of a fluid, the constitutive equation in question should consistently fit both the elongational and shear measurements with the same set of parameters. The elucidation of the capability of the power-law constitutive equation (14.1) to describe both shear and elongational behavior of gypsum slurries in both shear and elongational flows is aimed in the present section.

The elongational rheometry is based on the observation of flow in a self-thinning liquid thread driven by capillary forces (self-pinching; Fig. 14.6). It is described in the framework of the quasi-one dimensional equations of the dynamics of liquid jets and threads (Yarin 1993) and in the case of the power-law Eq. (14.1) reduces to the following equation for the evolution of the thread diameter as a function of time

$$d = d_0\left(\frac{t_s - t}{t_s}\right)^n \left(\frac{t_s^n}{d_0\kappa}\right)\frac{1}{3^{(n-1)/2}}\frac{1}{6n\left(1+\beta_1\right)} \tag{14.6}$$

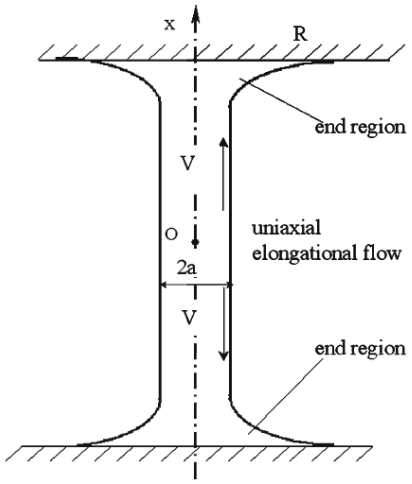

Fig. 14.6 Self-pinching cylindrical liquid thread.

where d is the diameter of the pinching thread, d_0 is the initial diameter of the thread, t_s is the time of pinching, t is time, β_1 is a theoretically established constant (0.175) required

to account for the thread non-uniformity (Yarin et al. 2004), and $\kappa = K/\sigma$, where σ is the surface tension. The value of σ used in this work was measured in the previous section (110.81 mN/m).

Equation (14.6) can be written as

$$\log\frac{d}{d_0} = n\log\left(\frac{t_s - t}{t_s}\right) + C(n,\kappa) \tag{14.7}$$

where

$$C(n,\boldsymbol{\kappa}) = \log\left[\left(\frac{t_s^n}{d_0\kappa}\right)\frac{1}{3^{(n-1)/2}}\frac{1}{6n\left(1+\beta_1\right)}\right] \tag{14.8}$$

The results of the elongational experiments for d(t) were processed by fitting Eq. (14.7) using the least square method which allows for the evaluation of the values of K and n.

It is emphasized that due to the fast solidification of gypsum slurries not every experiment was considered to be successful. For the 1st elongational experiment with any droplet the following two criteria were established for segregation of successful experiments: (i) the initial diameter of the thread at the centre should be at least 1.2 mm, and (b) there should be at least 12 data points recorded before complete thread pinching. To achieve statistically sound results (with respect to the Gaussian probability density function), data from 34 successful experiments were used for the evaluation of the rheological parameters K and n corresponding to the 1st elongational experiment. Of these 34 experiments, only 14 led to successful 2nd stretching experiments with the same droplet. A more relaxed segregation criterion was formulated for the 2nd experiment. Namely, the successful 2nd stretching experiment is the one, which provided at least 12 data points. The relaxation in the criterion for the 2nd stretching experiment was dictated

by rapid evaporation of water from the surface of small slurry droplets employed in the elongation experiments, which accelerated slurry setting. Accordingly, no successful experiments were found for the 3rd stretching of the same droplet.

One of the 34 successful experiments on the 1st stretching is shown in Fig. 14.7. The theory, Eq. (14.7) was fitted to the experimental data using the least square method and the corresponding values of the rheological parameters are shown in Figure 14.8 (a) and (b). Using the measured value of the surface tension of slurry (110.81 mN/m), the value of the consistency index K is found out to be 48.07 $g/cm \times s^{2-n}$, while n=0.57. Values of K and n for the other successful experiments of this series are combined in Fig. 8. The average values of n and K are $n=0.6 \pm 0.064$ and $K=32.42 \pm 16.18$ $g/cm \times s^{2-n}$. The large standard deviation in the value of K can be attributed to variability in slurry mixing and non-uniformity of slurries, which are ultimately related to irregular shapes and sizes of the stucco particles (Fig. 14.1), as well as some inevitable variation in size of the initial droplets used in the elongational tests. In Fig. 14.8 (b) the red point corresponds to the value of n for the encircled point in Fig. 14.8 (a). For this data point, the 1st stretching of slurry droplet was done in 60 sec after the moment when water was added to stucco at the stage of slurry preparation, whereas for all the other data points-only in 52-55 sec. This was done on purpose, to evaluate the effect of slurry setting on the results. The comparison of the red data point with the other data points shows that slurry setting results in increasing the consistency index K and decreasing the value of n-both trends in the direction of a more pronounced pseudoplasticity. When the values of the rheological parameters n and K presented in Fig. 14.8 ($n=0.6 \pm 0.064$ and $K=32.42 \pm 16.18$ $g/cm \times s^{2-n}$ for elongation of 75 WSR-composition 11) are compared to the values obtained in shear

experiments (Table 2: n=0.55 and K= 51.61 g/cm× s^{2-n} for shear of 75 WSR-composition 11), it can be seen that the values of n are rather close, whereas there is a difference in the values of K. This might be due to an inaccuracy in the value of the surface tension coefficient used to process the data of the elongational experiments.

The rheological parameter values evaluated from the 14 successful 2nd stretching experiments are plotted in Fig. 14.9. The data in Fig. 14.9 show a clear tendency of the value of n to decrease and the value of K to increase for the 2nd stretching of the same droplet compared to the 1st one. This shows a clear tendency toward the enhancement of pseudoplasticity of slurry due to water evaporation and hydration chemical reactions, similarly to the finding related to different delay times in the 1st stretching experiment discussed before.

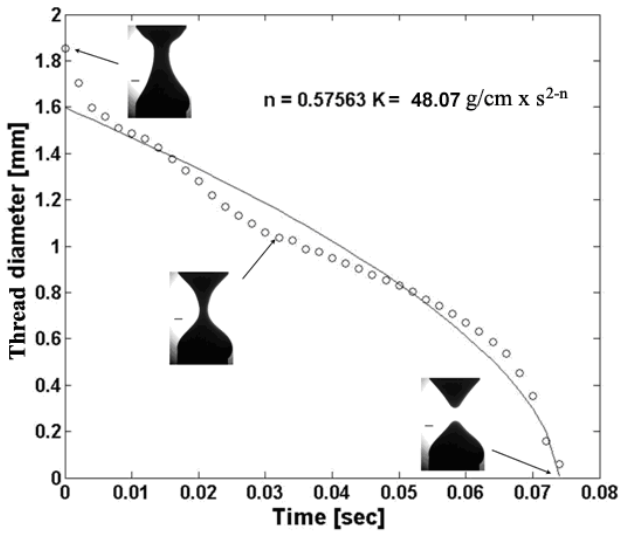

Fig. 14.7 Thread diameter vs. time in the 1st stretching experiment; slurry 75 WSR-composition 11. The inserted images show the slurry thread at different moments during its capillary self-pinching. The scale bar in the images is 1 mm. The experimental data is

shown by symbols, the curve was plotted according to Eq. (8), the corresponding values of the consistency index K and power n are also shown.

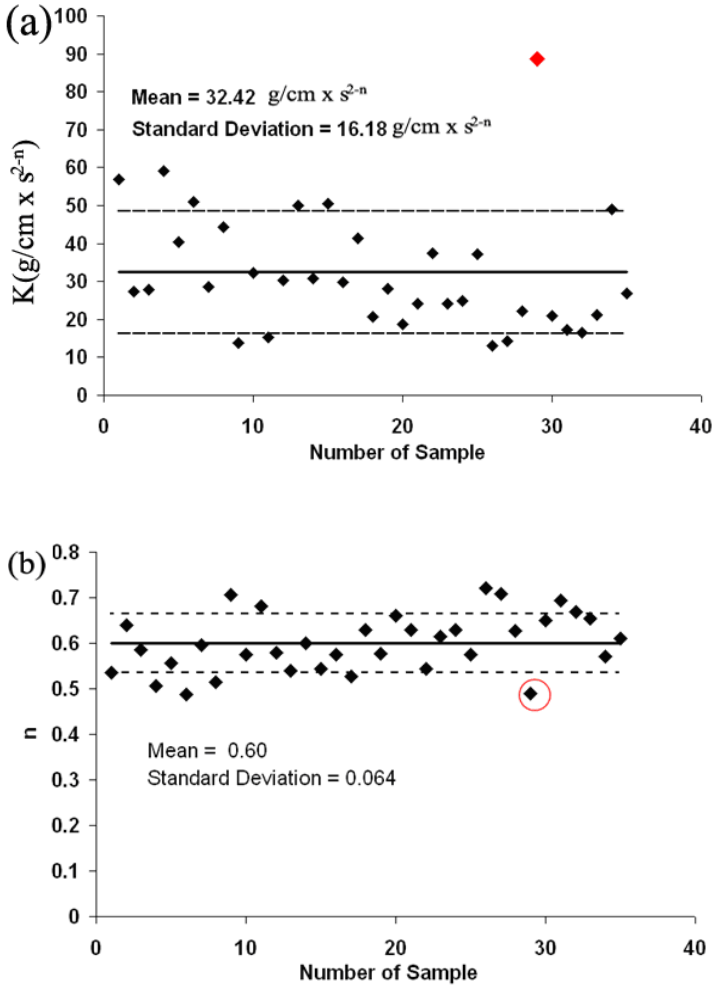

Fig. 14.8 (a) Values of K, and (b) values of n found for all 34 successful experiments on the 1st stretching; slurry 75 WSR-composition 11. The solid lines correspond to the averaged values, the dotted lines to the standard deviations.

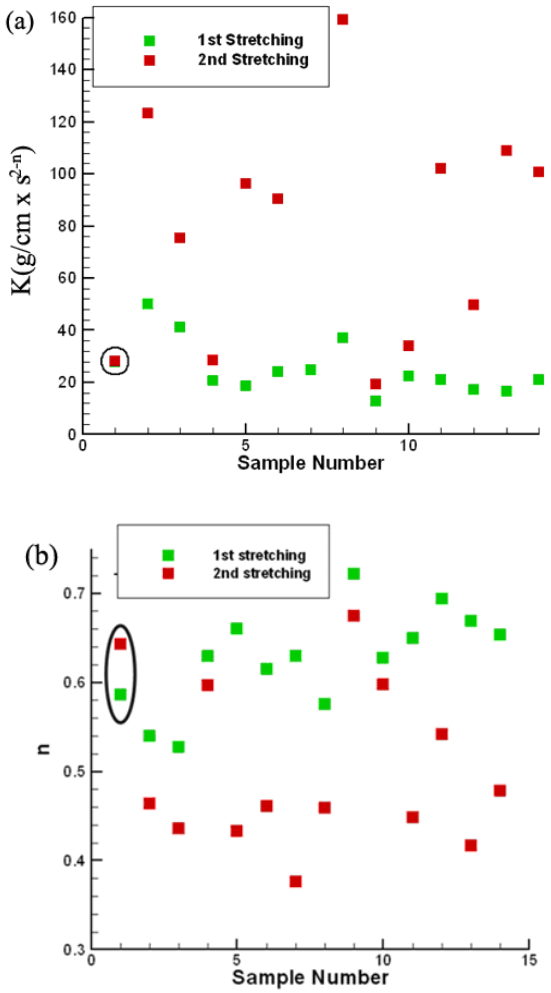

Fig. 14.9 (a) Values of K and (b) values of n found in the 14 successful 2nd stretching experiments with the same droplet (the data for the 1st stretching is also shown for comparison); 75 WSR-composition 11. Except one case (the encircled data points), in all the other cases the value of n decreased and the value of K increased in the 2nd stretching compared to the first one.

14.4 Conclusion

Using the shear and elongational viscometry, it is shown that concentrated gypsum slurries can be roughly characterized as materials following the tensorial

Ostwald–de Waele (power law) constitutive equation. The other known examples of materials which follow the tensorial power law constitutive equation in both shear and elongation with roughly the same values of the rheological parameters (the consistency index K and flow behavior index n) also include suspensions of needle-like γ-Fe_2O_3 particles in oil and gelled propellant simulants (Yarin et al. 2004). However, the family of such materials is not wide. Indeed, the power law model is frequently used to fit the shear data but very rarely efforts are directed to simultaneous elongational testing, which in many cases would disprove applicability of the tensorial model, as for example, in the case of polymer solutions and melts. In the present work the tensorial power-law rheological behavior was established for gypsum slurries with different water content and compositions. In particular, the values of the rheological parameters n and K found in elongation of slurry with water-to-stucco ratio of 75 (composition 11) were: $n=0.6\pm0.064$ and $K=32.42\pm16.18$ g/cm$\times$ s^{2-n}, whereas for shear of the same slurry it was found that n=0.55 and K= 51.61 g/cm$\times s^{2-n}$, which is sufficiently close.

15. CONCLUSION

In this dissertation a broad scope of nanochannels, nanoparticles, nano- and/or micro-fibers and gypsum slurries was subjected to detailed experimental and theoretical investigations having in mind a wide scope of potential applications. These include nanofluidics, drug carriers, electrospinning and blowing of novel types of fibers, in particular, those incorporating such natural biodegradable biopolymers as soy protein. The range of potential applications also incorporates cooling high-heat-flux surfaces in microelectronics and avionic applications and phase change materials potentially important for the enhanced heat transfer systems. The rheological results of the present work related to gypsum slurries have already resulted in modifications of the existing methods of wallboard production with a goal to achieve the better ones.

In addition to its important technological aspects, the present work revealed some novel unusual physical phenomena, such as the giant pseudo-slip in nanochannels and the anti-Leidenfrost effect of nano-textured surfaces. The work discovered PNIPAM hydrogel nano-“raisins” of the order of 2 nm embedded in polymer nanofibers.

The work resulted in 11 publications in several high-profile peer-reviewed journals, several additional submitted papers and 2 patent disclosures.

CITED LITERATURE

Astarita, G, Marrucci, G. Principles of Non-Newtonian Fluid Mechanics; 1974; London: McGraw-Hill.

Abhat A. Low temperature latent heat thermal energy storage: heat storage materials; 1983; Solar Energy;30;313–32.

Abramovich, GN, The Theory of Turbulent Jets; 1963; Boston: The MIT Press.

Ahmed I, Decker J, Morris D. How Much Does it Take to Make a Gallon of Soydiesel? Report for the National SoyDiesel Development Board, Jefferson, Missouri, 1994.

Akgun M, Aydın O, Kaygusuz K. Thermal energy storage performance of paraffin in a novel tube-in-shell system; 2008;Appl. Therm. Eng.; 28(5-6), 405-13.

Alemdar A, Sain M. Isolation and characterization of nanofibers from agricultural residues – Wheat straw and soy hulls; 2008; Bioresource Technology; 99; 1664-71.

Alexandrou A N, Bazilevskii A V, Entov V M, Rozhkov A N, Sharaf A; Breakup of a capillary bridge of suspensions; 2010; Fluid Dyn.; 45; 952-64.

Alexis F., Rhee J., Richie J P., Radovic-Moreno A F., Langer R., Farokhzad O C. New frontiers in nanotechnology for cancer treatment; 2008;Urologic Oncology: Seminars and Original Investigations 26, 74-85.

Anna S L, Bontoux N, Stone H A.Formation of dispersions using “flow focusing” in microchannels; 2003; Applied Physics Letters; 82; 364-66.

Antonia, RA, Satyaprakash, BR, Hussain AKMF. Measurement of dissipation rate and some other characteristics of turbulent plane and circular jets; 1980; Phys. Fluids; 23;695-700.

Antonietti M, Landfester K. Polyreactions in miniemulsions; 2002; Prog. Polym. Sci.; 27; 689-757.

Argentina, M, Mahadevan, L, Fluid-flow-induced flutter of a flag;2005; PNAS; 102;1829-34.

Aruna S T, Diwakar S, Jain A, Rajam K S. Comparative study on the effect of current density on Ni and Ni–Al2O3 nanocomposite coatings produced by electrolytic deposition; 2005; Surf. Eng.; 21; 209-14.

Ashcroft S J, Ben Isa M. Effect of dissolved gases on the densities of hydrocarbons 1997; J. Chem. Eng. Data; 42; 1244–8.

Asua J.M. Miniemulsion polymerization; 2002; Prog. Polym. Sci.; 27; 1283-1346.

Bal L M, Satya S, Naik S N, Meda V. Review of solar dryers with latent heat storage systems for agricultural products; 2011; Renewable and Sustainable Energy Reviews; 15; 876–80.

Banfill P F G; The rheology of fresh cement and concrete-A review; 2003; Proc 11th Int Cement Chem Congress. Durban.

Baret J C, Kleinschmidt F, El Harrak A, Griffiths A D. Kinetic aspects of emulsion stabilization by surfactants: a microfluidic analysis; 2009; Langmuir; 25; 6088-93.

Barnes H A; Thixotropy, rheopexy, yield stress; 2007; Chapter 9.2 in Springer Handbook of Experimental Fluid Mechanics, Springer-Verlag, Berlin, Heidelberg.

Bazilevsky A V, Sun K, Yarin A L, Megaridis C M [a]. Selective intercalation of polymers in carbon nanotubes; 2007; Langmuir; 23; 7451-55.

Bazilevsky A V, Yarin A L, Megaridis C M [b].Co-electrospinning of core-shell fibersusing a single-nozzle technique; 2007; Langmuir; 23; 2311–4.

Bazilevsky A V, Yarin A L, Megaridis C M [a]. Pressure-driven fluidic delivery through carbon tube bundles; 2008; Lab Chip; 8; 152–60.

Bazilevsky A V, Sun K, Yarin A L, Megaridis C M [b]. Room-temperature, open-air, wet intercalation of liquids, surfactants, polymers and nanoparticles within nanotubes and microchannels; 2008; J. Mater. Chem.; 18; 696-702.

Begenir A. Structure-process-property relationships in elastic nonwovens made from multi-block elastomers (PhD Thesis); 2008; Fiber and Polymer Science, North Carolina State University.

Berenson P J. Film boiling heat transfer from a horizontal surface; 1961; ASME Journal of Heat Transfer; 83; 351-58.

Bernardin J D, Mudawar I. The leidenfrost point: experimental study and assessment of existing models; 1999; 121; 894-903.

Blaiszik B J., Sottos N R., White S R.Nanocapsules for self-healing materials; 2008; Composites Science and Technology; 68, 978-86.

Bonilla L L, Gotz T, Klar A, Marheineke N, Wegener R. Hydrodynamic limit of a Fokker-Planck equation describing fiber lay-down processes;2007; SIAM J. Appl. Math.;68 :648-65.

Brahim S, Narinesingh D, Guiseppi-Elie A. Bio-smart hydrogels: co-joined molecular recognition and signal transduction in biosensor fabrication and drug delivery; 2002; Biosensors and Bioelectronics; 17; 973-81.

Breese RR, Ko WC. Fiber formation during melt blowing; 2003; International Nonwovens Journal;Summer; 21-28.

Breese RR, Qureshi UA. Influence of process conditions on melt blown web structure; 2006; Part IV - Fiber Diameter. Journal of Engineered Fibers and Fabrics; 1;32-46.

Briones A M, Ervin J S, Putnam S A, Byrd L W, Gschwender L. Micrometer-Sized Water Droplet Impingement Dynamics and Evaporation on a Flat Dry Surface;2010; Langmuir;26; 13272-86.

Chabba S, Netravali A N.'Green' composites Part 2: Characterization of flax yarn and glutaraldehyde/poly(vinyl alcohol) modified soy protein concentrate composites; 2005; J. Mater. Sci.; 40; 6275-82.

Chalencon F, Orgeas L, Dumont P J J, Foray G, Cavaille J Y, Maire E, Rolland du Roscot S; Lubricated compression and X-ray microtomography to analyse the rheology of a fibre-reinforced mortar; 2010; Rheol. Acta; 49; 221-235.

Chen H, Hsieh Y L.Ultrafine hydrogel fibers with dual temperature- and pH-responsive swelling behaviors; 2004; J. Polym. Sci., A: Polym. Chem; 42; 6331–39.

Chen YY, Yu B-Y; Wang J H; Cochran R E; Shuye J J. Template-based fabrication of SrTiO3 and BaTiO3 nanotubes; 2009; Inorganic Chemistry; 48; 681-86.

Chhabra R, Shambaugh R L. Probabilistic model development of web structure formation in the melt blowing process; 2004; Int. Nonwovens J. Fall; 24-34.

Cho E C, Kim J W, Fernandez-Nieves A, Weitz D A. Highly responsive hydrogel scaffolds formed by three-dimensional organization of microgel nanoparticles; 2008; Nano Letters; 8; 168-72.

Cho D, Nnadi O, Netravali A, Joo Y L. Electrospun hybrid soy protein/PVA fibers; 2010; Macromol. Mater. Eng.; 295; 763-73.

Choi E, Cho Y I.Local friction and heat transfer behavior of water in a turbulent pipe flow with a large heat flux at the wall; 1995;Trans. ASME, J. Heat Transfer; 117; 283-88.

Chu L.Y., Utada A.S., Shah R.K., Kim J.W., Weitz, D.A. Controllable monodisperse multiple emulsions; 2007; Angew. Chem. Int. Ed.; 46; 8970-74.

Connell, BSH, Yue, DKP, Flapping dynamics of a flag in a uniform stream; 2007; J. Fluid Mech. 581; 33-67.

Debye, P, Daen, J., Stability considerations on nonviscous jets exhibiting surface or body tension; 1959; Phys. Fluids; 2; 416-21.

Dersch R, Steinhart M, Boudriot U, Greiner A, Wendorff J H. Nanoprocessing of polymers: applications in medicine, sensors, catalysis, photonics;2005 ;Polym. Adv. Technol.; 16; 276-82.

Doi M. Molecular rheology of concentrated polymer systems;1980; Journal of Polymer Science, Polym. Phys. Ed. ; 18: 1005-20.

Dror Y, Salalha W, Avrahami R, Zussman E, Yarin A L, Dersch R, Greiner A, Wendorff J H.One-step production of polymeric microtubes by co-electrospinning; 2007; Small; 3; 1064-73.

Duracher D, Elaissari A, Mallet F, Pichot C.Adsorption of modified HIV-1 capsid p24 protein onto thermosensitive and cationic core−shell Poly(styrene)−Poly(N-isopropylacrylamide) particles; 2000; Langmuir; 16; 9002-08.

Egres R G, Nettesheim F, Wagner N J; Rheo-SANS investigation of acicular-precipitated calcium carbonate colloidal suspensions through the shear thickening transition; 2005; J. Rheol.; 50; 685-709.

Egres R G, Wagner N J ; The rheology and microstructure of acicular precipitated calcium carbonate colloidal suspensions through the shear thickening transition; 2005; J. Rheol.; 49 ; 719-746.

EkechukwuOV O V, Norton B.Review of solar-energy drying systems II: an overview of solar drying technology; 1999; Energy Convers Manage; 40; 615-55.

El-Aasser M S., Miller C M. In polymeric dispersions: principles and applications; 1997; NATO ASI Series E Applied Sciences; 335; 109.

Entov V M, Yarin, AL, The dynamics of thin liquid jets in air; 1984; J. Fluid Mech., 140,91-111.

Entov V M, Kestenboim, KS. Mechanics of formation of fibers; 1987; Fluid Dyn.; 22; 677-86.

Ewing M, Wallingford R A, Olefirowicz T M. Capillary electrophoresis;1989; Analytical Chemistry 1989; 61; 292A-303A.

Farnell DJJ, David, T, Barton, DC, Coupled states of flapping flags. J. Fluids and Structures;2004; 19; 29-36.

Feng Q Y, Li T J, Zhang Z T, Zhang J, Liu M, Jin J Z. Preparation of nanostructured Ni/Al2O3 composite coatings in high magnetic field; 2007; Surf. Coat. Technol.; 201, 6247-52.

Ferrari M. Cancer nanotechnology: opportunities and challenges ;2005; Nature Reviews; Cancer 5; 161- 71.

Ferraris C F; Measurement of the rheological properties of high performance concrete: state of the art report; 1999; J Res NIST; 104; 461-478.

Fricke K, Harnisch F, Schröder U. On the use of cyclic voltammetry for the study of anodic electron transfer in microbial fuel cells; 2008; Energy & Environmental Science, 1; 144-47.

Frost, W, Moulden, TH (Editors). Handbook of Turbulence; 1977; v. 1.; New York: Plenum Press.

Fung W, Yuen K, Liong M. Characterization of fibrous residues from agrowastes and the production of nanofibers; 2010; J. Agri. Food Chem.;58; 8077-84.

Gandhi M, Srikar R, Yarin A L, Megaridis C M, Gemeinhart R A. Mechanistic examination of protein release from polymer nanofibers; 2009; Molec. Pharm.; 6; 641-47.

Garstecki P, Fuerstman M J, Stone H A, Whitesides G M.Formation of droplets and bubbles in a microfluidic T-junction—scaling and mechanism of break-up; 2006; Lab on a Chip; 6; 437-46.

Garstecki P, Gitlin I, DiLuzio W, Whitesides G M, Kumacheva E, Stone H A. Formation of monodisperse bubbles in a microfluidic flow-focusing device; 2004; Applied Physics Letters; 85; 2649-51.

Goel M, Sengupta S, Roy S K. The performance of liquid heat sinks with phase change material suspensions; 1993; Int. Comm. Heat Mass Transfer; 20; 69-77.

Gong X, Wen, W, Sheng P. Microfluidic fabrication of porous polymer microspheres: dual reactions in single droplets; 2009; Langmuir; 25; 7072-7.

Gotz T, Klar A, Marheineke N, Wegener R. A stochastic model and associated Fokker-Planck equation for the fiber lay-down process in nonwoven production processes; 2007 SIAM J. Appl. Math.; 67: 1704-17.

Graham A K. Electroplating Engineering Handbook (3nd edition); 1971; New York: VNR.

Graves S, Meleson K, Wilking J, Lin M Y, Mason T G. Structure of concentrated nanoemulsions; 2005; Journal of Chemical Physics; 122; 134703.

Greene J. Biodegradation of compostable plastics in green yard-Waste compost environment; 2007; J. Polym. Environ.; 15; 269-73.

Gunther A, Jensen K F. Multiphase microfluidics: from flow characteristics to chemical and materials synthesis; 2006; Lab on a Chip; 6; 1487-1503.

Guo L J, Cheng X, Chou C. Fabrication of size-controllable nanofluidic channels by nanoimprinting and its application for DNA stretching; 2004; Nano Letters; 4; 69-73.

Gutiérrez J M, González C, Maestro A, Solè I, Pey C M, Nolla J.Nano-emulsions: New applications and optimization of their preparation; 2008; Current Opinion in Colloid & Interface Science 13, 245-51.

Han, T, Yarin, AL, Reneker, DH. Viscoelastic electrospun jets: initial stresses and elongational rheometry; 2008; Polymer; 49; 1651-58.

Heath J R,Davis M E. Nanotechnology and cancer ;2008 ; Annu. Rev. Med.; 59, 251-65.

Hettiarachchy N S, Kalapathy U, Myers D J. Alkali-modified soy protein with improved adhesive and hydrophobic properties; 1995; J. Am. Oil Chem. Soc.; 72; 1461-64.

Hoffman A S. Applications of thermally reversible polymers and hydrogels in therapeutics and diagnostics; 1987; J. Controlled Release; 6; 297-305.

Hossain M A, Woods J L, Bala B K.Optimization of solar tunnel drier for drying of chilli without color loss;2005; Renew Energy; 30; 729-42.

Huang X, Netravali A A N.Environmentally friendly green materials from plant-based resources: modification of soy protein using gellan and micro/nano-fibrillated cellulose; 2008; J. Macromol. Sci., Part A: Pure Appl. Chem.; 45; 899-906.

Huang X, Netravali A A N.Characterization of flax fiber reinforced soy protein resin based green composites modified with nano-clay particles; 2007; J. Compos. Sci. Technol.; 67; 2005-14.

Huang Y, Agrawal B, Sun D D, Kuo J S, Williams J C. Microfluidics-based devices: New tools for studying cancer and cancer stem cell migration; 2011; Biomicrofluidics; 5; 013412.

Hulicova D, Sato F, Okabe K, Koishi M, Oya A. An attempt to prepare carbon nanotubes by the spinning of microcapsules; 2001; Carbon; 39; 1438-42.

Ijima S. Helical microtubules of graphitic carbon; 1991; Nature; 354; 56-58.

Inaba H.New challenge in advanced thermal energy transportation using functionally thermal fluids; 2000; Int. J. Therm. Sci.; 39; 991-1003.

Izquierdo P, Esquena J, Tadros T F, Dederen C, Garcia-Celma M J, Azemar N, Solans C. Formation and stability of nano-emulsions prepared using the phase inversion temperature method; 2002; Langmuir; 18; 26-30.

Izquierdo P, Esquena J, Tadros T F, Dederen J C, Feng J, Garcia M J, Azemar N,Solans C. Phase behavior and nano-emulsion formation by the phase inversion temperature method; 2004; Langmuir; 20; 6594-98.

Izquierdo P, Feng J, Esquena J, Tadros T F, Dederen J C, Garcia M J, Azemar N,Solans C. The influence of surfactant mixing ratio on nano-emulsion formation by the pit method; 2005; J. Colloid Interface Sci.; 285; 388-94.

Jafari S M, He Y, Bhandari B. Nano-emulsion production by sonication and microfluidization—a comparison; 2006; International Journal of Food Properties; 9; 475-85.

Johnson L A, Myers D J, Burden D. Early uses of soy protein in far east; 1984; US Inform; 3; 282-84.

Joseph, DD. Fluid Dynamics of Viscoelastic Liquids; 1990; Berlin: Springer.

Kalapathy U, Hettiarachchy N S, Myers D, Hanna M A. Modification of soy proteins and their adhesive properties on woods;1995; J. Am. Oil Chem. Soc.; 72; 507-10.

Kanczler, J M, Ginty P J, Bany J A, Clarke N M P, Howdle, S M, Shakesheff K M, Oreffo R O C.The effect of mesenchymal populations and vascular endothelial growth factor delivered from biodegradable polymer scaffolds on bone formation ;2009;Biomaterials; 29; 1892-1900.

Karaipekli A, Sari A. Capric–myristic acid/vermiculite composite as form-stable phase change material for thermal energy storage; 2009; Sol. Energy; 83; 323-32.

Kenning D B R. In Two-Phase Flow and Heat Transfer. (Butterworth, D.,Hewitt, G.F., Eds.); 1977; Oxford: Oxford Univ. Press.

Kim C W, Frey M W, Marquez M, Joo Y L.Preparation of submicron-scale, electrospun cellulose fibers via direct dissolution; 2005; J. Polym. Sci., Part B: Polym. Phys.; 43; 1673-83.

Kim C W, Frey M W, Marquez M, Joo Y L.Structural studies of electrospun cellulose nanofibers;2006; Polymer; 47, 5097-107.

Kim J, Utada A S, Nieves A F, Hu Z, Weitz D A.Fabrication of Monodisperse Gel Shells and Functional Microgels in Microfluidic Devices; 2007; Angew. Chem. Int. Ed.; 46; 1819-1822.

Kim J. Spray cooling heat transfer: The state of the art; 2007; International Journal of Heat and Fluid Flow; 28; 753–767.

Kim S J, Park S J, Kim S I.Properties of smart hydrogels composed of polyacrylic acid/poly(vinyl sulfonic acid) responsive to external stimuli; 2004; Smart Mater. Struct.; 13; 317.

Klass D L. Biomass for renewable energy, fuels, and chemicals; 1998; New York: Academic Press.

Kohli P, Harrell C C, Cao Z H, Gasparac R, Tan W H, Martin C R. DNA-functionalized nanotube membranes with single-base mismatch selectivity;2004; Science; 305; 984-86.

Kondo A, Kaneko T,Higashitani K. Development and application of thermo-sensitive immunomicrospheres for antibody purification; 1994; Biotechnol. Bioeng.; 44; 1-6.

Kunieda H, Friberg S E. Critical phenomena in a surfactant/water/oil system. basic study on the correlation between solubilization, microemulsion, and ultralow interfacial tensions; 1981; Bull. Chem. Soc. Jpn.; 54; 1010-14.

Kunieda H, Fukui H, Uchiyama H, Solans C.spontaneous formation of highly concentrated water-in-oil emulsions (gel-emulsions); 1996; Langmuir; 12, 2136-140.

Kuntze R A; Gypsum. Connecting Science and Technology; 2009; West Conshohocken: ASTM International.

Kuznik F, David D, Johannes K, Roux J J.A review on phase change materials integrated in building walls; 2011; Renewable and Sustainable Energy Reviews; 15; 379–91.

Lauga E, Brenner M P, Stone H A. Microfluidics: the no-slip boundary condition; 2007; Springer Handbook of Experimental Fluid Mechanics ed C Tropea, A L Yarin and J Foss; Berlin: Springer chapter 19, pp 1219–40.

Laulicht B, Cheifetz P, Mathiowitz E, Tripathi A. Evaluation of Continuous Flow Nanosphere Formation by Controlled Microfluidic Transport; 2008; Langmuir; 24; 9717-26.

Lee K H, Ryu H S, Rhee K C. Protein solubility characteristics of commercial soy protein products; 2003; J. Am. Oil Chem. Soc; 80; 85-90.

Lembach A, Tan H B, Roisman I V, Gambaryan-Roisman T, Zhang Y, Tropea C, Yarin A L.Drop impact, spreading, splashing, and penetration into electrospun nanofiber mats; 2010; Langmuir; 26; 9516-23.

Li H, Wan Y, Liang H, Li X, Huang Y, He F. Composite electroplating of Cu–SiO2 nano particles on carbon fiber reinforced epoxy composites; 2009; Appl. Surf. Sci.; 256; 1614-16.

Liu Y, Harnisch F, Fricke K, Sietmann R, Schröder U. Improvement of the anodic bioelectrocatalytic activity of mixed culture biofilms by a simple consecutive electrochemical selection procedure; 2008; Biosens Bioelectron.; 24; 1012-17.

Loitsyanskii L G. Mechanics of liquids and gases; 1966; Oxford: Pergamon.

Lord Rayleigh. 1945; Theory of sound; New York: Dover.

Mahapatra A K, Imre L. Role of solar-agricultural-drying in developing countries. International Journal of Ambient Energy ; 1990; J Ambient Energy; 2; 205–10.

Marheineke N,Wegener R. Fiber dynamics in turbulent flows: General modeling framework; 2006; SIAM J. Appl. Math; 66;1703-26.

Marheineke N, Wegener R. Fiber dynamics in turbulent flows: Specific Taylor drag; 2007; SIAM J. Appl. Math; 68; 1-23.

Marla V T, Shambaugh R L. Three-dimensional model of melt-blowing process; Industrial & Engineering Chemistry Research; 2003; 42; 6993-7005.

Marla VT, Shambaugh RL. Modeling of the melt blowing performance of slot dies;2004; Ind. Eng. Chem. Res; 43; 2789-97.

Mathiowitz E, Jacob Y S, Jong Y S, Carino G P, Chickering D E, Chaturvedi P, Santos C A, Vijayaraghavan K, Montgomery S, Bassett M, Morrell C.Biologically erodable microspheres as potential oral drug delivery systems Nature; 1997; 386; 410-14.

Mattheij R M M,Rienstra S W,Boonkkamp J H M ten Thije. Partial Differential Equations; 2005;Philadelphia: SIAM.

Mattia D, Gogotsi Y. Review: static and dynamic behavior of liquids inside carbon nanotubes; 2008; Microfluidics and Nanofluidics; 5: 289-305.

McCabe, WL, Smith, JC, Harriott, P. Unit Operations in Chemical Engineering; 1993; 5th Ed.; New York: McGraw-Hill.

Medeiros E S, Glenn G M, Klamczynski A P, Orts W J, Mattoso L H C. Solution blow spinning: A new method to produce micro- and nanofibers from polymer solutions; 2009;Journal of Applied Polymer Science; 113 : 2322- 30 .

Menon, ES. Piping Calculations Manual; 2005; New York: McGraw-Hill.

Mudawar I, Estes K A. Optimizing and predicting CHF in spray cooling of a square surface; 1996; Journal of Heat Transfer; 118; 672–79.

Mudawar I.Assessment of high-heat-flux thermal management schemes; 2001; IEEE Transactions on Components and Packaging Technologies;24; 122-41.

Nie Z H, Xu S Q, Seo M, Lewis P C, Kumacheva E. Polymer particles with various shapes and morphologies produced in continuous microfluidic reactors; 2005; Journal of the American Chemical Society; 127; 8058-63.

Nisisako T, Okushima S, Torii T. Controlled formulation of monodisperse double emulsions in a multiple-phase microfluidic system ;2005; Soft Matter; 1; 23-27.

Ochanda F, Jones W E. Sub-Micrometer-Sized metal tubes from electrospun fiber templates; 2005; Langmuir; 21; 10791-96.

Ochanda F, Jones W E. Fabrication and thermal analysis of submicron silver tubes prepared from electrospun fiber templates;2007; Langmuir; 23; 795-801.

Pai, SI, Fluid Dynamics of Jets. Van Nostrand Company, Macmillan Toronto, 1954.
Paidoussis, MP, Dynamics of flexible cylinders in axial flow;1966;J. Fluid Mech.; 26, 717-51.

Patil S A, Harnisch F, Kapadnis B, Schröder U; Electroactive mixed culture biofilms in microbial bioelectrochemical systems: the role of temperature for biofilm formation and performance; 2010; Biosens Bioelectron.; 26; 803-08.

Phiriyawirut M, Rodchanacheewa N, Nensiri N, Supaphol P. Morphology of electrospun mats of soy protein isolate and its blend; 2008; Adv. Mat. Res.; 55-57; 733-36.

Pinchuk L C, Goldade V A, Makarevich A V, Kestelman V N. Meltblowing, equipment, technology and polymer fibrous materials;2002; Berlin: Springer.

Pinto N J, Carrion P, Quinones J X. Electroless deposition of nickel on electrospun fibers of 2-acrylamido-2-methyl-1-propanesulfonic acid doped polyaniline; 2004; Mater. Sci. Eng. A; 366; 1-5.

Pope, SB, Turbulent Flows; 2000; Cambridge: Cambridge University Press.

Rangavajhyala N, Ghorpade V, Hanna M. Solubility and molecular properties of heat-cured soy protein films; 1997; J. Agric. Food Chem. 1997, 45, 4204-08.

Rawal A, Priyadarshi A, Lomov SV, Verpoest I, Vankerrebrouck J. Tensile behaviour of thermally bonded nonwoven structures: model description; 2010; J Mater Sci.;45;2274-84.

Reneker D H, Yarin A L, Fong H, Koombhongse S. Bending instability of electrically charged liquid jets of polymer solutions in electrospinning; 2000; Journal of Applied Physics ; 87: 4531-47.

Reneker, DH, Yarin, AL, Zussman, E, Xu, H, Electrospinning of nanofibers from polymer solutions and melts;2007; Advances in Applied Mechanics; 41; 43-195.

Reneker D H, Yarin A L. Electrospinning jets and polymer nanofibers; 2008; Polymer; 49; 2387-425.

Reznik S N, Yarin A L, Zussman E, Bercovici L. Evolution of a compound droplet attached to a core-shell nozzle under the action of a strong electric field; 2006; Phys.Fluids;18; 062101.

Rohsenow W M, Hartnett J P, Cho Y I. Handbook of Heat Transfer (3rd edition);1998; New York:McGraw-Hill.

Ruiz-Agudo E, Rodriguez-Navarro C; Microstructure and rheology of lime putty; 2009; Langmuir; 26; 3868-3877.

Sabbah R, Farid M M, Al-Hallaj S. Micro-channel heat sink with slurry of water with micro-encapsulated phase change material: 3D-numerical study; 2009; Appl. Therm. Eng.; 29(2-3); 445-54.

Saeki D, Sugiura S, Kanamori T, Sato S, Mukataka S, Ichikawa S. Highly productive droplet formation by anisotropic elongation of a thread flow in a microchannel; 2008; Langmuir; 24; 13809-13.

Sandou T, Oya A. Preparation of carbon nanotubes by centrifugal spinning of coreshell polymer particles; 2005; Carbon; 43; 2013-32.

Sarkar K, Gomez C, Zambrano S, Ramirez M, Hoyos E D, Vasquez H, Lozano K;Electrospinning to Forcespinning; 2010; Materials Today; November; 12-14.

Scheller B L, Bousfield D W.Newtonian drop impact with a solid surface; 1995; AIChE J.; 41; 1357-67.

Schlesinger M, Paunovic M. Modern Electroplating (4th edition);2000; New York: Wiley.

Schossig P, Henning H M, GschwanderS, Haussmann T. Micro-encapsulated phase-change materials integrated into construction materials; 2005; Solar Energy Materials & Solar Cells; 89; 297–306.

Seaver M, Galloway A, Manuccia T J. Acoustic levitation in a free□jet wind tunnel; 1989; Rev. Sci. Instrum.; 60; 3452-59.

Seo M, Paquet C, Nie Z H, Xu S Q, Kumacheva E. Microfluidic consecutive flow-focusing droplet generators; 2007; Soft Matter; 3; 986-92.

Shah R K, Shum H C, Rowat A C, Lee D, Agresti J J, Utada A S, Chu L Y, Kim J W,Fernandez-Nieves A, Martinez C J, Weitz D A. Designer emulsions using microfluidics; 2008; Materials Today; 11; 18-27.

Shambaugh RL. A macroscopic view of the melt-blowing process for producing microfibers; 1988; Industrial & Engineering Chemistry Research; 27: 2363-72.

Shelley, M, Vandenberghe, N, Zhang J, Heavy flags undergo spontaneous oscillations in flowing water; 2005; Phys. Rev. Lett.; 94; 094302.

Shenoy S S, Wagner N J; Influence of medium viscosity and adsorbed polymer on the reversible shear thickening transition in concentrated colloidal dispersions; 2005; Rheol. Acta; 44; 360-371.

Sigmund W, Yuh J, Park H, Maneeratan V, Pyrgiotakis G, Daga A, Taylor J, Nino J C. Processing and structure relationships in electrospinning of ceramic fiber systems; 2006; J. Am. Ceram. Soc.; 89 [2]; 395–407.

Sikder A K, Misra D S, Singhbal D, Chakravorty S. Surface engineering of metal–diamond composite coatings on steel substrates using chemical vapour deposition and electroplating routes; 1999; Surf. Coat. Technol.; 114; 230-34.

Silk E A, Golliher E L,Paneer Selvam R;Spray cooling heat transfer: Technology overview and assessment of future challenges for micro-gravity application; 2008; Energy Conversion and Management; 49; 453-68.

Silk E, Kim J, Kiger K T. Investigation of enhanced surface spray cooling; 2004; Proceedings of the ASME IMECE, Anaheim, CA,Paper No. IMECE2004-61753.

Silk E A, Kim J, Kiger K ;Spray cooling of enhanced surfaces: Impact of structured surface geometry and spray axis inclination; 2006; International Journal of Heat and Mass Transfer; 49; 4910-20.

Sinha Ray S, Chando P, Yarin A L.Enhanced release of liquid from carbon nanotubes due to entrainment by an air layer; 2009; Nanotechnology; 20; 095711.

Sinha-Ray S, Yarin A L, Pourdeyhimi B [a]. Meltblowing: I-Basic physical mechanisms and threadline model; 2010; Journal of Applied Physics; 108; 034912.

Sinha-Ray S, Yarin A L, Pourdeyhimi B [b].The production of 100/400 nm inner/outer diameter carbon tubes by solution blowing and carbonization of core–shell nanofibers;2010 ; Carbon; 48; 3575-78.

Sinha-Ray S, Zhang Y, Placke D, Megaridis C M, Yarin A L [c]. Resins with Nano-Raisins; 2010; Langmuir; 26; 10243-49.

Sinha-Ray S, Zhang Y, Yarin A L . Thorny Devil Nanotextured Fibers: The Way to Cooling Rates on the Order of 1 kW/cm2; 2011; Langmuir; 27; 215-26.

Sodha M S, Chandra R. Solar drying systems and their testing procedures: A review; 1994;Energy Convers Manage; 35 ;219-67.

Solans C., Izquierdo P., Nolla J., Azemar N., Garcia-Celma M.J. Nano-emulsions; 2005; Current Opinion in Colloid & Interface Science; 10; 102-10.

Springer G F, Schwick H G, Fletcher M A.Relation of the influenza virus inhibitory activity of glycoproteins to their molecular size and sialic acid content; 1969; Biochemistry; 64; 634-41.

Srikar R, Yarin A L, Megaridis C M, Bazilevsky A V, Kelley E.Desorption-limited mechanism of release from polymer nanofibers; 2008; Langmuir; 24; 965-74.

Srikar R, Yarin A L, Megaridis C M [a]. Fluidic delivery of homogeneous solutions through carbon tube bundles; 2009; Nanotechnology; 20; 275706.

Srikar R, Gambaryan-Roisman T, Steffes C, Stephan P, Tropea C, Yarin A L [b].Nanofiber coating of surfaces for intensification of drop or spray impact cooling; 2009; Int. J. Heat and Mass Transf; 52; 5814-26.

Sun Z, Zussman E, Yarin AL, Wendorff JH, Greiner A. Compound core-shell polymer nanofibers by co-electrospinning; 2003 Advanced Materials; 15; 1929-32.

Tanaka T, Fillimore D J.Kinetics of swelling of gels; 1979; J. Chem. Phys.; 70; 1214-18.
Taylor G I. The formation of emulsions in definable fields of flow; 1934; Proc. Roy. Soc. London; A146, 501-23.

Taylor G I. The instability of liquid surfaces when accelerated in a direction perpendicular to their plane; 1950; Proc. Of Royal Soc. Of London, A201,192.

Telkes M, Raymond E. Storing solar heat in chemicals—a report on the Dover house; 1949; Heat Vent;46; 80–6.

Terrones M. Science and technology of the twenty-first century: Synthesis, properties, and applications of carbon nanotubes; 2003; Annual Review of Materials Research; 33; 419-501.

Theron A, Zussman E, Yarin A L.Electrostatic field-assisted alignment of electrospun nanofibre; 2001; Nanotechnology; 12; 384–90.

Thompson CJ, Chase GG, Yarin AL, Reneker DH. Effect of parameters on nanofiber diameter determined from electrospinning model; 2007; Polymer; 48; 6913-22.

Tiwari M K, Bazilevsky A V, Yarin A L, Megaridis C M; Elongational and shear rheology of carbon nanotube suspensions-fluids with yield stress; 2009; Rheol. Acta; 48; 597-609.

Tong R, Cheng J. Anticancer polymeric nanomedicines polymer reviews; 2007; Polymer Reviews; 47; 345-81.

Totten G E, Westbrook S R, Shah R J. Fuels and Lubricants Handbook: Technology, Properties, Performance and Testing; Vol. 1. ASTM International: Glen Burnie, MD, 2003.

Triantafyllou, GS, Physical condition for absolute instability in inviscid hydroelastic coupling; 1992; Phys. Fluids A; 4; 544-52.

Utada A S, Lorenceau E, Link D R, Kaplan P D, Stone H A, Weitz, D A. Monodisperse double emulsions generated from a microcapillary device ; 2005; Science; 308; 537-41.

Uyttendaele M A J, Shambaugh R L. General equation development and experimental verification; 1990; AIChE Journal; 36;175-86.

Vaezi M R, Sadrnezhaad S K, Nikzad L. Electrodeposition of Ni–SiC nano-composite coatings and evaluation of wear and corrosion resistance and electroplating characteristics; 2008; Colloids Surf. A; 315; 176-82.

Vega-Lugo, A, Lim L. Controlled release of allyl isothiocyanate using soy protein and poly(lactic acid) electrospun fibers; 2009; Food Res. Int.; 42; 933-40.

Wan J, Bick A, Sullivan M, Stone H A. Controllable microfluidic production of microbubbles in Water-in-Oil emulsions and the formation of porous microparticles; 2008; Advanced Materials; 20; 3314-18.

Weber, C. Zum Zerfall eines Fluessigkeitsstrahles; 1931; ZAMM; 11; 136-54.

Wente V A. Superfine Thermoplastic Fibers; 1956; Ind. Eng. Chem.; 48; 1342-1346.

Whitesides G M, Grzybowski B. Self-Assembly at All Scales; 2002; Science; 295; 2418-21.

Williamson, CHK, Govardhan, R, Vortex-induced vibrations; 2004; Annu. Rev. Fluid Mech.; 36; 413-55.

Wu S, Zhu D, Zhang X, Huang J. Preparation and melting/freezing characteristics of Cu/paraffin nanofluid as phase-change material (PCM); 2010; Energy Fuels; 24; 1894-98.

Xu R D, Wang J L, He L F, Guo Z C.Study on the characteristics of Ni–W–P composite coatings containing nano-SiO2 and nano-CeO2 particles; 2008; Surf. Coat. Technol.; 202; 1574-79.

Yao S C, Henry R E. An investigation of minimum film boiling temperature on horizontal surface; 1978; Transactions of the ASME; 100; 263-66.

Yarin A L, Oron A, Rosenau Ph. Capillary instability of thin liquid film on a cylinder; 1993; Phys. Fluids; A5; 91–8.

Yarin A L. 1993; Free liquid jets and films: hydrodynamicsand rheology; New York: Wiley.

Yarin A L, Brenn G, Kastner O, Rensink D, Tropea C. J. Fluid Mech. 1999,399, 151-204.

Yarin AL, Koombhongse S, Reneker DH. Bending instability in electrospinning of nanofibers; 2001; Journal of Applied Physics; 89; 3018-26.

Yarin A L, Yazicioglu A G, Megaridis C M, Pia Rossi M, Gogotsi Y. Theoretical and experimental investigation of aqueous liquids contained in carbon nanotubes; 2005; J. Appl. Phys.; 97; 124309.

Yarin A L. Drop impact dynamics: splashing, spreading, receding, bouncing;2006;Annu. Rev. Fluid Mech.; 38; 159-192.

Yarin A L, Zussman E, Wendorff J H, Greiner A. Material encapsulation and transport in core-shell micro/nanofibers, polymer and carbon nanotubes and micro/nanochannels; 2007; J. Mater. Chem. ;17; 2585-99.

Yarin AL. Self-similarity. Section 2.3 in Springer Handbook of Experimental Fluid Mechanics (Eds. Tropea, C, Yarin, AL, Foss, J);2007; pp. 57-82; Berlin:Springer.

Yarin A L. Stimuli-responsive polymers in nanotechnology: deposition and possible effect on drug release; 2008; Math. Modell. Nat. Phenom.; 3; 1-15.

Yarin L P, Mosyak A, Hetsroni G. Fluid flow,heat transfer and boiling in micro-channels;2009; Berlin: Springer.

Yarin A L, Sinha-Ray S, Pourdeyhimi B. Meltblowing: II-Linear and nonlinear waves on viscoelastic polymer jets; 2010 Journal of Applied Physics; 108: 034913.

Yu G, Fan Y. Preparation of poly(D,L-lactic acid) scaffolds using alginate particles; 2008;J. Biomater. Sci. Polym. Ed.; 19; 87-98.

Zeldovich Ya B, Barenblatt G I, Librovich V B, Makhviladze G M. The mathematical theory of combustion and explosions; 1985;New York: Consultants Bureau.

Zhang H, Tumarkin E, Peerani R, Nie Z, Sullan R M A, Walker G C, Kumacheva E. Microfluidic production of biopolymer microcapsules with controlled morphology; 2006; Journal of the American Chemical Society; 128; 12205-10.

Zhang X, Min B G, Kumar S. Solution spinning and characterization of poly(vinyl alcohol)/soybean protein blend fibers; 2003;J. Appl. Polym. Sci.; 90; 716-21.

Zhang Y, Yarin A L. Stimuli-responsive copolymers of n-isopropyl acrylamide with enhanced longevity in water for micro- and nanofluidics, drug delivery and non-woven applications; 2009; J. Mater. Chem.; 19; 4732-39.

Zhiqiang Y. Development of solar thermal systems in China;2005;Solar Energy Mater Solar Cell; 86; 427- 42.

Zhirnov V V, Cavin R K, Hutchby J A, Bourianoff G I; Limits to binary logic switch scaling – a Gedanken model; 2003; Proceedings of the IEEE; 91; 1934–39.

Ziabicki, A. Fundamentals of Fibre Formation; 1976; London:Wiley.

Ziabicki A, Kawai H (Editors). High-Speed Fiber Spinning; 1985; New York:Wiley.

Zussman E, Theron A, Yarin A L. Formation of nanofiber crossbars in electrospinning; 2003 ;Applied Physics Letters; 82; 973-75.

Zussman E, Yarin A L, Bazilevsky A V, Avrahami R, Feldman M. Electrospun polyacrylonitrile/poly(methyl methacrylate)-derived turbostratic carbon micro/-nanotubes; 2006; Adv. Mater.; 18; 348–53.

VITA

NAME: Suman Sinha Ray

EDUCATION: Bachelor of Mechanical Engineering, Jadavpur University, Kolkata, West Bengal, India, 2007

Ph. D., Mechanical Engineering, University of Illinois at Chicago, Chicago, Illinois, USA, 2011

TEACHING: Teaching Assistant in the Department of Mechanical and Industrial Engineering, University of Illinois at Chicago, Illinois: Heat Transfer (ME 321), Combustion Engine (ME 429), Experimental Methods in Mechanical Engineering (ME 341) and Fluid Mechanics (ME 211)

HONORS: Chicago Consular Corps Scholarship, University of Illinois at Chicago, 2010

Provost Award, University of Illinois at Chicago, 2010

Best Poster Presentation, Nano for the 3rd Millennium, Raleigh, North Carolina, 2010

Dean's Fellowship, University of Illinois at Chicago, 2010-11

Silver Medal winner for 1st place in the third year of Mechanical Engineering, Jadavpur University, Kolkata, India, 2007.

PROFESSIONAL MEMBERSHIP: Materials Research Society
Americal Physical Society

PUBLICATIONS: Patents and Disclosures

Sinha-Ray S, Zhang Y, Yarin A L. Thorny devil nano-textured fibers: the way to cooling rates of the order of 1 kw/cm^2; 2010.

Journals

1. Sinha-Ray S, Chando P, Yarin A L. Enhanced release of liquid from carbon nanotubes due to entrainment by an air layer; 2009; Nanotechnology; 20; 095711.

2. Sinha-Ray S, Yarin A L. Flow from macroscopically long straight carbon nanopores for generation of thermoresponsive nanoparticles; 2010; Journal of Applied Physics; 107; 024903.

3. Sinha-Ray S, Zhang Y, Placke D, Megaridis C M, Yarin A L. Resins with “Nano-Raisins”; 2010; Langmuir; 26; 10243-49.

4. Sinha-Ray S, Yarin A L, Pourdeyhimi B. Meltblowing: I-basic physical mechanisms and threadline model; 2010; Journal of Applied Physics; 108; 034912.

5. Yarin A L, Sinha-Ray S, Pourdeyhimi B. Meltblowing: II-linear and nonlinear waves on viscoelastic polymer jets; 2010; Journal of Applied Physics; 108; 034913.

6. Sinha-Ray S, Yarin A L, Pourdeyhimi B. The production of 100/400 nm inner/outer diameter carbon tubes by solution blowing and carbonization of core-shell nanofibers; 2010; Carbon; 48; 3575-78.

7. Sinha-Ray S, Zhang Y, Yarin A L; Thorny Devil Nanotextured Fibers: The Way to Cooling Rates on the Order of 1 kW/cm^2; 2011; Langmuir; 27; 215-26.

8. Chen S, Hou H, Harnisch F, Patil S A, Carmona-Martinez A A, Agarwal S, Zhang Y, Sinha-Ray S, Yarin A L, Greiner A, Schroder U.Electrospun and solution blown three-dimensional carbon fiber nonwovens for application as electrodes in microbial fuel cells; 2011; 4; 1417-21.

9. Yarin A L, Sinha-Ray S, Pourdeyhimi B. Meltblowing: multiple polymer jets and fiber-size distribution and lay-down patterns; 2011; Polymer; 52; 2929-38.

10. Sinha-Ray S, Zhang Y, Yarin A L, Davis S C, Pourdeyhimi B. Solution blowing of soy protein fibers; 2011; Biomacromolecules; 12; 2357-63.

11. Zhang Y, Sinha-Ray S, Yarin A L. Mechanoresponsive polymer nanoparticles, nanofibers and coatings as drug carriers and components of microfluidic devices; 2011; Journal of Materials Chemistry; 21; 8269-81.